



Provided by the author(s) and University of Galway in accordance with publisher policies. Please cite the published version when available.

Title	Photoacoustic imaging with clinical, preclinical, and quantitative applications
Author(s)	Breathnach, Aedán
Publication Date	2020-11-20
Publisher	NUI Galway
Item record	<a href="http://hdl.handle.net/10379/16611">http://hdl.handle.net/10379/16611</a>

Downloaded 2024-04-26T13:03:05Z

Some rights reserved. For more information, please see the item record link above.



# **Photoacoustic imaging with clinical, preclinical, and quantitative applications**

by

Aedán Earnán Breathnach

A thesis submitted in partial fulfilment of the requirements for the  
degree of

**Doctor of Philosophy**

Supervisor: Prof. Martin J Leahy



Tissue Optics and Microcirculation Imaging (TOMI) group,

School of Physics,

National University of Ireland Galway, Ireland

March 2020



# Abstract

Photoacoustic (PA) imaging (PAI) is an emerging biomedical imaging modality that combines optical absorption contrast with ultrasonic resolution and imaging depth. Major research has been carried out into PAI in recent years, and as a result PAI is rapidly being established as a mainstream imaging modality in both biological research and clinical practice.

In this thesis, three main areas of PAI application were studied: clinical, preclinical, and quantitative PAI.

Handheld linear-array PAI was introduced to the clinic for breast and melanoma imaging applications. For the breast study, PAI using was assessed in terms of its ability to image the morphology and oxygenation status of breast lesions suspicious for cancer. PAI was found to image the morphology of superficial lesions with high contrast, while functional imaging found strong evidence of tumour hypoxia indicating malignancy. For the melanoma imaging study, PAI was applied to preoperatively measure lesion thickness of pigmented cutaneous lesions suspicious for melanoma. The PAI measured lesion thickness was found to correlate strongly with the histologically measured lesion thickness, indicating the efficacy of PAI in guiding biopsy depth and sample location. Additionally, PAI was found to be effective at imaging intradermal lesion growth which has important implications for melanoma staging.

A method of correcting for the effects of spectral fluence attenuation on quantitative PA measurements was introduced in chapter 3. The method uses arteries as a known optical calibration standard to estimate optical fluence at nearby veins and to quantify venous blood oxygen saturation. The method was experimentally validated in coupled Monte-Carlo-PA simulations, phantom, and *in vivo* tests.

Finally, the PA image contrast capabilities of novel gold nanostars (GNS) were tested in phantom and *in vivo* studies. The results showed the addition of a silica coating increased photothermal transfer and hence PAI contrast, while the *in vivo* study showed the strong photostability and low tissue clearance of the particles after GNS-mediated photothermal therapy in a mouse-tumour model.

# Table of Contents

Declaration.....	v
Acknowledgements.....	vi
List of Publications.....	vii
Acronyms & Abbreviations.....	ix
List of figures.....	xi
List of tables.....	xx
Chapter 1: Introduction.....	1
Chapter 2: Background theory.....	6
2.1 Photoacoustic imaging.....	6
2.2 Initial photoacoustic pressure generation.....	7
2.3 Photoacoustic wave equation.....	9
2.4 Penetration depth and spatial resolution.....	11
2.5 Quantitative photoacoustic Imaging.....	14
2.6 Tissue optical properties.....	15
2.6.1 Absorption in biological tissues.....	15
2.6.2 Scattering in biological tissues.....	17
2.7 Diffusion theory.....	20
2.8 Monte Carlo simulations of light transport in biological tissue.....	22
2.9 Photoacoustic simulations.....	24
2.10 Vevo LAZR PAI system.....	26
Chapter 3: Fluence-corrected venous blood oxygen saturation measurement using arterial fluence calibration.....	30
3.1 Importance of blood oxygenation measurements: motivation.....	30
3.2 Currently available techniques for measuring blood oxygenation.....	34
3.3 Quantification blood oxygen saturation with PA imaging.....	36
3.4 Fluence-corrected venous blood oxygen saturation measurement using arterial fluence calibration.....	41
3.4.1 Method overview.....	41
3.5 Methodology.....	44
3.5.1 Coupled MC-PA simulations.....	44
3.5.2 Phantom experiments.....	47

3.5.3 <i>In vivo</i> experiments.....	51
3.6 Results and discussion.....	52
3.6.1 Coupled Monte Carlo and PA simulation results .....	52
3.6.2 Phantom results.....	57
3.6.3 <i>In vivo</i> results.....	58
3.7 Conclusion.....	62
Chapter 4: Preoperative measurement of cutaneous melanoma and nevi thickness with photoacoustic imaging. ....	63
4.1 Introduction .....	63
4.2 Materials and Methods .....	65
4.3 Results .....	67
4.4 Discussion .....	71
4.5 Acknowledgements .....	73
Chapter 5: Photoacoustic imaging of tumour oxygenation level in breast cancer and neoadjuvant chemotherapy patients. ....	74
5.1 Introduction .....	74
5.2 Materials and methods. ....	82
5.3 Results and discussion.....	86
5.3.1 Benign lesions.....	86
5.3.2. Malignant tumours and NAC patients .....	89
5.4 Conclusion.....	95
Chapter 6: Silica enhanced dual plasmonic gold nanostars for photoacoustic imaging and photothermal therapy .....	97
6.1 Introduction .....	97
6.2 Materials and Methods .....	100
6.2.1 Synthesis & surface modification of DPGNS .....	100
6.2.2 PAI of phantoms .....	101
6.2.3 <i>In vivo</i> PAI of DPGNS .....	102
6.2.4 PTT of tumours <i>in vivo</i> .....	103
6.3 Results and Discussion.....	105
6.3.1 Initial PA characterisation of DPGNS.....	105
6.3.2 Initial PA and photothermal characterisation of silica-coated DPGNS .....	107
6.3.3 PA monitoring of PTT in a mouse-tumour model.....	111
6.4 Conclusion.....	119

Chapter 7: Conclusion and future work .....	121
Chapter 8: References .....	126

## **Declaration**

The work in this thesis is based on research carried out at the Tissue Optics and Microcirculation Imaging Group, School of Physics, National University of Ireland, Galway. No part of this thesis has been submitted elsewhere for any other degree or qualification, it is all my own work, unless otherwise stated in the text.

Aedán Breathnach

# Acknowledgements

In submitting this thesis, I would like to acknowledge the following people for their support and guidance along the way. I would like to start by thanking my supervisor, Professor Martin Leahy, for his guidance, support, and sharing of knowledge that has enabled me to complete my PhD studies and submit this thesis.

I would like to thank Professor Steve Jacques for his advice and guidance which proved to be of great help and assistance during times of uncertainty, and Dr Hrebesh Molly Subhash for his guidance and support during the early years of my PhD.

I would like to thank the many great and lifelong friends I have made during my time in NUIG. Particular thanks are owed to Colm, Shane, Allen, Adam, VJ, Mark, Aonghus, Mags, Niamh, and Conor, who were always on hand for support and some much-needed distraction at times.

I would also like to acknowledge my group-mates Seán, James, Kai, Gillian, Roshan, Cerine and Haroon for their help along the way.

I would like to thank my family for the encouragement they have shown me during this process.

Finally, I would like to particularly thank my partner, Mary-Rose, who has consistently encouraged and supported me from the beginning to the end of my PhD studies, and my daughter, Aoibhinn, who came into the world towards the end of my PhD journey. Aoibhinn has given me the motivation and determination to finish this thesis, without which it would not have been possible.

# List of Publications

## Journal publications

A. Breathnach, E. Concannon, J.J. Dorairaj, S. Shaharan, J. McGrath, J. Jose, J.L. Kelly, M.J. Leahy, Preoperative measurement of cutaneous melanoma and nevi thickness with photoacoustic imaging, *Journal of Medical Imaging*. 5 (2018) 015004.

H. Zafar, A. Breathnach, H.M. Subhash, M.J. Leahy, Linear-array-based photoacoustic imaging of human microcirculation with a range of high frequency transducer probes, *Journal of Biomedical Optics*. 20 (2014) 051021.

V. Raghavan, C. O'Flatharta, R. Dwyer, A. Breathnach, H. Zafar, P. Dockery, A. Wheatley, I. Keogh, M. Leahy, M. Olivo, Dual plasmonic gold nanostars for photoacoustic imaging and photothermal therapy, *Nanomedicine*. 12 (2017) 457–471.

## Conference publications

M.J. Leahy, H. Zafar, S. O'Gorman, A. Breathnach, H.M. Subhash, Microcirculation Imaging with Light and Sound, (n.d.).

V. Raghavan, H. Subhash, A. Breathnach, M. Leahy, P. Dockery, M. Olivo, Dual plasmonic gold nanoparticles for multispectral photoacoustic imaging application, in: *Photons Plus Ultrasound: Imaging and Sensing 2014*, International Society for Optics and Photonics, 2014: p. 89434J.

A. Breathnach, L. Concannon, L. Aalto, J. Dorairaj, H.M. Subhash, J. Kelly, M.J. Leahy, Assessment of cutaneous melanoma and pigmented skin lesions with photoacoustic imaging, in: *Photonic Therapeutics and Diagnostics XI*, International Society for Optics and Photonics, 2015: p. 930303.

A. Breathnach, H. Subhash, and M. Leahy, Quantification of absolute blood oxygen saturation in veins with photoacoustic imaging, in: *Photons Plus Ultrasound: Imaging and Sensing*, International Society for Optics and Photonics, 2016.

A. Breathnach, M. Leahy, and Michael Kerin, Detection of oxyhaemoglobin flare response from neoadjuvant chemotherapy in breast cancer patients with photoacoustic imaging, in: *Biophotonics and Imaging Graduate Summer School*, 2016.

### **Manuscripts submitted at the time of thesis submission**

A. Breathnach, M. Leahy, Fluence-corrected photoacoustic quantification of blood oxygen saturation using arterial fluence calibration, *Journal of Photoacoustics*, 2020.

## Acronyms & Abbreviations

ANOVA	Analysis of variance
ANSI	American national standards institute
BOLD	blood oxygen level-dependent
CC	Correlation coefficient
CW	Continuous wave
DOT	Diffuse optical tomography
DPGNS	dual-plasmonic gold nanostars
EM	Electromagnetic
EPRI	Electron paramagnetic resonance imaging
FEM	Finite element method
GNP	Gold nanoparticle
GNS	Gold nanostars
H&E	Haematoxylin and eosin
LED	Light-emitting diode
MPE	Maximum permissible exposure
MC	Monte Carlo
MCML	Monte Carlo multi-layered
MCxyz	Monte Carlo xyz
MRI	Magnetic resonance imaging
NIR	Near infrared
NIRS	Near infrared spectroscopy

NS	Nanostars
OPO	Optical parametric oscillator
OR-PAM	Optical-resolution photoacoustic microscopy
PA	Photoacoustic
PACT	Photoacoustic computed tomography
PAI	Photoacoustic imaging
PAM	Photoacoustic microscopy
PBS	Phosphate buffered saline
PET	Positron emission tomography
PPG	Photoplethysmography
PTT	Photothermal therapy
RTE	Radiative transport equation
SBU	Symptomatic breast unit
SERS	Surface-enhanced Raman scattering
SHG	Second harmonic generator
SNR	Signal-to-noise ratio
SPECT	Single photon emission computed tomography
SPR	Surface plasmon resonance
SU	Spectral Unmixing
SWNT	Single-walled carbon nanotubes
TEM	Transmission electron microscopy
US	Ultrasound

## List of figures

<b>Figure 2.1.</b> (a) The PA waves arriving at a point detector at time $t$ are modelled as coming from sources over a spherical shell with a constant radius of $v_s t$ , centered at the detector position $P(\mathbf{r}, t)$ . (b) An example of a PA signal generated from a uniform spherical PA source. .....	10
<b>Figure 2.2.</b> Absorption coefficients of endogenous biological chromophores in the visible and NIR spectral regions at concentrations typically found in the human body. Oxy- and deoxyhaemoglobin, 150 g/L. Water 60% by weight. Melanin concentration corresponds to that in skin (adapted from [26]). .....	14
<b>Figure 2.3.</b> Optical absorption process by a chromophore with geometric cross-section $A_a$ and effective cross-section $\sigma_a$ .....	16
<b>Figure 2.4.</b> Optical scattering process by a scattering particle with a given geometric cross-section $A_s$ and effective cross-section $\sigma_s$ .....	18
<b>Figure 2.5.</b> Reduced scattering coefficients of various tissues based on empirical formulas. Blue line: bloodless rat skin [33]. Red line: in vitro human skin [34]. Black line: in vitro subcutaneous adipose (fat) tissue [34]. For skin, the reduced scattering coefficients of the epidermis and dermis are assumed to be the same and an averaged $\mu'_s$ value is used. ....	19
<b>Figure 2.6.</b> Time resolved diffusion of fluence rate $\phi$ [ $\text{W}/\text{cm}^2$ ] after the deposition of a point source of radiant energy of 1 J at $r = 0$ and $t = 0$ at various timepoints in an absorbing and scattering tissue medium at 800 nm, with $\mu_a = 0.017 \text{ cm}^{-1}$ and $\mu'_s = 14.25 \text{ cm}^{-1}$ . ....	21
<b>Figure 2.7.</b> A MC simulation of light transport. (a) Propagation of a single photon in a light-scattering tissue. When the photon is totally internally reflected at the air/tissue surface, a fraction of the photon weight is allowed to escape as reflectance and the remaining photon weight continues to propagate in the tissue where it can be scattered and absorbed. (b) Example MC simulation of relative fluence rate [ $\text{W}/\text{cm}^2/\text{W}$ delivered] at 800 nm on a tissue phantom composed of two highly absorbing blood vessels with a diameter of 0.25 cm and centred at a depth of 0.3 cm, placed in a medium with low scattering and absorption. The light source is a 2.5 cm diameter collimated circular beam in the $+z$ direction. The low scattering properties of the water results in an extended shadowing underneath the highly absorbing blood vessels..	22
<b>Figure 2.8.</b> Example of a coupled MC-PA simulation. (a) Tissue model consisting of a 1 cm diameter blood vessel in a layer of fat centred at a depth of 1.5 cm. (b) MC simulation of optical	

energy deposition from wide-beam laser source at 800 nm. (c) PA pressure recorded by detector shown in (a) and (b). (d) Velocity potential recorded by detector shown in (a) and (b). .....25

**Figure 2.9.** Acoustic attenuation factor with depth for an acoustic attenuation coefficient of 0.75 dB/cm/MHz.....26

**Figure 2.10.** (Left) Schematic of PA system showing laser source, signal processing procedure, and linear-array PA probe (viewed from elevational direction). (Right) View of the PA probe head (enclosed by dashed box on left) showing crossed laser beam geometry (lateral direction). .....27

**Figure 2.11.** Photo of the 21 MHz PA probe illuminating a scattering medium (polystyrene insulation) showing diffusion of the light beam in the lateral (left) and elevation (right) directions.....28

**Figure 2.12.** Laser-source setup, consisting of a flashlamp pumped Q-switched ND:YAG laser operating at 1064 nm directed into the SHG where 532 nm light was produced via frequency doubling. The SHG output was then used to pump the OPO which was tunable in the wavelength range of 680-970 nm. The laser power was measured with an energy meter to ensure the laser energy pulse did not exceed the ANSI standard of 20 mJ/cm<sup>2</sup>. The laser output ports, marked 1, 2, 3, provided 1064 nm light for port 1, the OPO output for port 2, and green 532 nm light for port 3. The laser output source could be changed by manually coupling the probe fibre optical cable to either port. The system configuration allowed for spectroscopic scans to be taken across the OPO output range in steps of 1 nm.....29

**Figure 3.1.** Blood vessels of the microcirculation. Arterioles extend out from arteries and transition to capillaries. The capillaries convey blood from the arterioles to the venules and are the smallest blood vessels in the body (diameter ≈ 5-10 μm), with vessel walls that are one endothelial cell thick. The thin walls and small diameter of capillaries allow for the exchange of nutrients such as oxygen, water, and glucose, and waste products such as carbon dioxide, with the surrounding interstitial fluid. Cells are typically located within 100 μm from a capillary, a distance known as the oxygen diffusion limit [52]. The capillary beds then drain into venules and then to veins.....31

**Figure 3.2.** Schematic of a pulse oximeter. The pulse oximeter revolutionised modern medicine with its ability to noninvasively and transcutaneously measure  $sO_2^A$ . Pulse oximetry is a NIR spectroscopic technique that takes advantage of the spectrally distinct absorption profiles of oxy- and deoxyhaemoglobin to quantify  $sO_2^A$ . Pulse oximeters employ a pair of small light-emitting diodes (LEDs) facing a photo sensor through a translucent part of the patient’s body,

usually a fingertip or earlobe. The wavelength pair of 660 nm and 940 nm is typically used as the optical absorption difference between oxy- and deoxyhaemoglobin differs significantly at these wavelengths. The sensitivity of pulse oximetry to arterial blood only is based on photoplethysmography (PPG) - the principle that the degree of optical absorption varies due to the cardiac induced changes in blood volume. The arterial blood volume reaches a maximum during systole and reaches a minimum during diastole. In contrast, the blood volume in the capillary beds, veins, and surrounding tissues remains relatively constant. This allows the time-varying portion of the detected signal to be isolated, allowing the oxygenation level of the arterial compartment to be quantified. ....32

**Figure 3.3.** 2D and 3D parametric  $sO_2$  images. (a) Coupled 2D B-mode US and PA  $sO_2$  scan of a tumour on the hindlimb of a mouse obtained using a linear PA quantification algorithm at two wavelengths (750 and 850 nm). (b) Coupled 3D US and PA  $sO_2$  scan of the tumour volume. Image reproduced from [121] with permission. ....37

**Figure 3.4.** Tissue models used in MC-PA simulations, showing (a) the singlelayer model and (b) the multilayer model in the xz plane ( $y=0$ ). Time resolved PA signals were recorded from point detectors placed on the surface of each model directly above the center of the vein and artery, respectively.....45

**Figure 3.5.** (a) Optical absorption and (b) reduced scattering coefficients of the tissue types in figure 3.4 (including water). The scattering properties of venous and arterial blood, and fat, are the same. Optical properties are based on data from [26].....45

**Figure 3.6.** MC simulation results on the multilayer model at 800 nm. (a) and (b), optical fluence distribution in the xz ( $y=0$ ) and yz ( $x=0$ ) planes, respectively. (c) Optical energy deposition in the xz plane ( $y=0$ ), showing high absorption in the blood vessels compared to the surrounding fat layer. (d) Optical fluence distribution in the xy plane ( $z=0$ ), showing the rectangular-beam illumination profile. ....46

**Figure 3.7.** PA signals plotted against tissue depth for detectors placed over the vein and artery, respectively, for the singlelayer model at 680 nm and with  $sO_2^V = 55\%$  and  $sO_2^A = 97\%$ . The relative difference in PA signal amplitude for the blood vessels can be observed at  $\approx 0.45$  cm, caused by the different oxygenation levels. A secondary set of peaks caused by the blood vessel furthest away from each detector can be observed at  $\approx 1.25$  cm, with a reduced PA amplitude caused by the angular sensitivity of the detector and acoustic attenuation.....47

<b>Figure 3.8.</b> (a) Schematic of phantom structure. (b) Mass extinction coefficients of the 740, 780, and 832 nm dyes ( $\epsilon_{740}$ , $\epsilon_{780}$ , $\epsilon_{832}$ ), and scattering efficiency (dimensionless) of polystyrene microspheres contained in the upper and lower layers. ....	48
<b>Figure 3.9.</b> Dye mixtures for various $R_{dye}$ values. ....	49
<b>Figure 3.10.</b> Tissue phantoms in 3D-printed phantom moulds at different stages of manufacture, in (a) with the lower layer added, and (b) with the upper layer added. The clear silicon tubing can be seen protruding from the mould wall in (a) and (b), as well as the plastic film separating the layers. ....	50
<b>Figure 3.11.</b> Scanning setup used for tissue phantom scans (gel pad attachment not shown). ....	51
<b>Figure 3.12.</b> Scan region on ventral aspect of the wrist. ....	51
<b>Figure 3.13.</b> Peak PA amplitude spectra from the vein and artery from the singlelayer model for each simulated $sO_2^V$ and $sO_2^A$ value. The error bars represent the standard deviation of points from repeated simulations. ....	53
<b>Figure 3.14.</b> Fluence-corrected and uncorrected $sO_2^V$ values plotted against the known values for the singlelayer model. ....	54
<b>Figure 3.15.</b> Fluence-corrected and uncorrected $sO_2^V$ values plotted against the known values for the multilayer model. ....	55
<b>Figure 3.16.</b> Simulated arterial PA spectra plotted alongside the arterial spectra calculated using the calibrated fluence model. ....	56
<b>Figure 3.17.</b> (a) PA scan of a 0%-100% $R_{dye}$ phantom taken at 780 nm, showing the 100% tube (left) and 0% dye tube (right), centred at a depth of $\approx 10$ mm. The upper layer boundaries can be seen between $\approx 6$ -8 mm. (b) Averaged PA amplitude spectra from the two marked regions in (a). ....	57
<b>Figure 3.18.</b> Fluence-corrected and uncorrected $R_{dye}$ values plotted against the known values. ....	58
<b>Figure 3.19.</b> (a) Coregistered PA-US image at 800 nm of the scan region showing the targeted veins marked 1, 2, and 3. (b) PA amplitude spectra normalised at 800 nm from veins 1, 2, and 3, as well as from the artery used for calibration. ....	59
<b>Figure 4.1.</b> Coregistered PAI image of <i>in situ</i> melanoma on upper left extremity. Handheld linear-array based PAI was able to image pigmented lesion and skin architecture with high contrast, speed, and resolution. ....	68

**Figure 4.2.** Coregistered linear-array based PAI of melanoma and benign skin lesions. (a) Coregistered PAI image of in situ melanoma with a PA depth of 0.3 mm. (b) In situ melanoma on chest. (c) Histology of excised melanoma, with Breslow depth of 0.15 mm. Original magnification  $\times 4$ . (d) Coregistered PAI image of invasive melanoma on back, showing signs of dermal invasion, with a PA depth of 1.85 mm. (e) Invasive melanoma on back. (f) Histology after full excision, with a Breslow depth of 1.6 mm and Clarke level IV. Original magnification  $\times 4$ . (g) SU image of dysplastic nevus showing adnexal extension, with a PA depth of 0.36 mm and adnexal depth of 1.6 mm. (h) Dysplastic nevus on lower left extremity. (i) Histology of excised nevus, with a histological depth of 0.39 mm and adnexal depth of 2.08 mm. Original magnification  $\times 4$ . ..... 68

**Figure 4.3.** Correlation between *in vivo* measurements of melanomas (black circles) and benign lesions (clear circles) and histological measurements from biopsied samples (black line shows 1:1 agreement for PAI measurements and histological measurements). (a) Plot of primary lesion thickness measured with PAI against histological thickness. (b) Plot of adnexal tumour extension measured with SU against histological depths..... 70

**Figure 4.4.** Rendered 3-D PA images of pigmented skin lesions taken using a stepper motor. (a) Large diameter melanoma in situ located on ventral aspect of wrist. (b) 3-D PAI scan (area 14 mm  $\times$  235 mm) of dashed region in (a) showing complex pigmentation pattern. (c) Compound melanocytic nevus located on lower left extremity. (d) 3-D PAI scan (area 4 mm  $\times$  4 mm) of lesion in (c). 3-D PA scans assessed lesion volume and allowed for the thickest portion to be registered to the surface, which can potentially guide incisional biopsy location and depth. .... 71

**Figure 5.1.** Schematic diagram of LOIS optoacoustic imaging system. Reproduced with permission from [200]..... 77

**Figure 5.2.** Schematic diagram of the Twente photoacoustic mamoscope showing parallel plate geometry. Reproduced from [201] with permission. .... 78

**Figure 5.3.** Drawing of 3D PA mammography system hemispherical detection array mounted on an XY translation stage. Reproduced from [204] with permission. .... 80

**Figure 5.4.** Change in oxygenation level of responding and non-responding tumours on days 1-7. Reproduced from [196] with permission. .... 81

**Figure 5.5.** Vevo® LAZR PAI system setup in the SBU, showing laser cart, computer station, and examination table. .... 83

**Figure 5.6.** (Left) PA imaging probe (15 MHz) with US gel pad showing a section of the pad cut out to fit the shape of the probe head. (Right) PA probe with Gel pad attached at the head

and held in place with clear plastic film wrapped over the probe and secured with tape on the body of the probe. ....85

**Figure 5.7.** Coregistered PA (right) and US (left) images of a fibroadenoma (shown marked) at an image depth of  $\approx 21$  mm. The highly absorbing region on the PA image at an image depth of  $\approx 27$  mm is an image artefact caused by an air bubble in the gel pad. ....88

**Figure 5.8.** Coregistered parametric  $sO_2$  map (right) and US (left) image of the fibroadenoma shown in figure 5.7. The average intratumoural  $sO_2$  is measured in the yellow region. ....88

**Figure 5.9.** Coregistered parametric  $sO_2$  map (right) and US (left) image of a healthy breast patient. The average tissue  $sO_2$  is measured in the yellow region. ....89

**Figure 5.10.** Coregistered PA (right) and US (left) images of a malignant breast tumour (shown marked) in patient 8 at an image depth of  $\approx 22$  mm. The highly absorbing region on the PA image at an image depth of  $\approx 27$  mm is an image artefact caused by an air bubble in the gel pad. ....90

**Figure 5.11.** Coregistered parametric  $sO_2$  map (right) and US (left) image of the same malignant breast tumour shown in figure 5.10. The green and yellow regions show the average  $sO_2$  and average haemoglobin concentrations (relative units) in the intertumoral and extratumoural regions, respectively. ....91

**Figure 5.12.** Coregistered PA (right) and US (left) images of a malignant breast tumour (shown marked) in patient 9 at an image depth of  $\approx 20$  mm. ....92

**Figure 5.13.** Coregistered parametric  $sO_2$  map (right) and US (left) image of the same malignant breast tumour shown in figure 5.12. The green and yellow regions show the average  $sO_2$  and average haemoglobin concentrations (relative units) in the intertumoral and extratumoural regions, respectively. ....92

**Figure 5.14.** Coregistered parametric  $sO_2$  map (right) and US (left) image of a malignant breast tumour in patient 10. The green and yellow regions show the average  $sO_2$  and average haemoglobin concentrations (relative units) in the intertumoral and extratumoural regions, respectively .....93

**Figure 5.15.** Coregistered parametric  $sO_2$  map (right) and US (left) image of a malignant breast tumour in patient 11. The green and yellow regions show the average  $sO_2$  and average haemoglobin concentrations (relative units) in the intertumoral and extratumoural regions, respectively. ....94

**Figure 6.1.** Absorption spectrum (a.u.) of DPGNS tuned to absorb in the 650–700 nm and 1000-1350 nm wavelength ranges. .... 101

**Figure 6.2.** (A) Schematic of PTT and PAI experimental setup. (B) Timeline of the *in vivo* study..... 104

**Figure 6.3.** Experimental setup, showing the PAI system, consisting of the PA laser source, imaging station, and PA imaging probe. Also shown is the PTT laser source (right), thermal camera, and animal stage with mouse attached. During treatment/PAI, the mouse vital signs, including heart rate, respiration rate, and temperature, were monitored. The 1064 nm PTT laser source is shown directed onto the target with a fibre optical cable. .... 104

**Figure 6.4.** B-mode PA and US scans of an optical phantom consisting of 4 agarose tubes ( $\approx$  5 mm in diameter) arranged from left to right in order of increasing concentration of DPGNS. Panels (A) and (B) show PA scans taken at 700 and 1064 nm, respectively. The agarose tubes were placed in US gel to provide coupling to the PA-US probe. .... 106

**Figure 6.5.** B-mode PA and US scans of a euthanised mouse thigh taken at 1064 nm, showing the injection of 10  $\mu$ L of DPGNS at a concentration of 50  $\mu$ M. Panel A and panel B show the mouse thigh before injection and post injection, respectively..... 107

**Figure 6.6.** TEM image of non-silica-coated and silica-coated DPGNS in panels A and B, respectively. The silica coating in panel B is approximately 10 nm on average. The scale bar in both panels is 100 nm. .... 108

**Figure 6.7.** Coregistered PA-US scans of an agarose-intralipid phantom containing two capillary tubes filled with an aqueous solution of silica-coated DPGNS (right) and non-silica-coated DPGNS (left). Panels A and B show scans taken at 700 and 1064 nm, respectively. 108

**Figure 6.8.** Photothermal efficiency of DPGNS. Thermal camera images of cuvettes filled with aqueous solutions of silica-coated (A) and non-silica-coated (B) DPGNS, irradiated by a 1064 nm laser with an irradiance ranging from 0.5 to 2 W/cm<sup>2</sup>. (C) Temperature plot vs time of the cuvettes undergoing laser heating in (A) and (B), as well as water. (D) Absorption spectra (via spectrophotometer) of non-silica coated DPGNS, as well as silica-coated DPGNS after exposure to laser irradiation ranging from 1 to 4 W/cm<sup>2</sup> (spot size 1 mm<sup>2</sup>). .... 110

**Figure 6.9.** *In vivo* PAI of silica-coated DPGNS. Coregistered PA-US images of mice tumours for (A) untreated tumour at 700 nm, while (B) and (C) show tumours injected with silica-coated DPGNS imaged at 700 and 1064 nm, respectively. (D) Plot of the relative, average PA amplitude inside the tumour volume corresponding to the images (A), (B), and (C). Student Newman-Keuls Multiple Comparison post hoc test found an increase in laser wavelength to cause a significant difference in PA amplitude at 700 and 1064 nm ( $p < 0.001$ ). Data are expressed as means and SDs. \*\*\* $p < 0.001$  versus control; ^^ $p < 0.001$  versus 1064 nm wavelength. .... 112

**Figure 6.10.** PTT treatment of mice tumours. (A) photo of mouse with tumours on each flank circled. (B) Thermal image of mouse in the treatment group (with tumours containing silica-coated DPGNS) undergoing laser irradiation (CW laser operating at 1064 nm and 0.5 W/cm<sup>2</sup> for 10 minutes), where a rapid increase in temperature of 8-9°C in the tumour (marked area) was observed compared with the surrounding tissue (baseline temperature 35°C). (C) Thermal image of control group mouse undergoing laser treatment showing no temperature increase in the tumour (marked area). (D) Tumour-growth curve of the 4 different study groups, consisting of: treatment group containing DPGNS and undergoing PTT, tumours containing DPGNS but without PTT, tumours containing PBS and given laser irradiation, and the untreated control group. No significant difference in mean relative tumour volume was found for the treatment group ( $F(3, 24) = 0.397, p > 0.05$ ) or measurement day ( $F(3, 72) = 1.581, p > 0.05$ ). Error bars represent the standard deviation (n = 7). (NS = nanostars). ..... 113

**Figure 6.11.** *In vivo* PA spectra of silica-coated DPGNS. (A) Average photoacoustic amplitude spectra (680-970 nm, relative units) from DPGNS administered tumour from scan region marked in yellow. (B-D) Coregistered PA-US images (700 nm) of a DPGNS administered tumour (from treatment group) at days 3, 7, and 14 post-treatment, respectively..... 115

**Figure 6.12.** (A-B) Coregistered PA-US scans taken at 1064 nm of a representative silica-coated DPGNS administered tumour from the treatment group (A) and the untreated group (no PTT) (B). (C) Plot of average PA signal amplitude from inside the tumours shown in (A) and (B) at each study timepoint. Post hoc analysis of PA signal amplitudes using a two-sided dependent samples t-test found a significant difference in PA signal amplitude for all measurement days post DPGNS administration compared with the baseline measurement (Day -1) for both the treated and untreated group ( $p < 0.05$ ). Data are presented as means and standard error of mean. \*\* $p < 0.01$  vs Day -1, \*\*\* $p < 0.001$  vs Day -1, # $p = 0.066$  vs Day -1, ^ $p < 0.05$  vs Day -1, ^^ $p < 0.001$  vs Day -1. .... 116

**Figure 6.13.** Histological sections with H&E staining from tumours from each study group at magnifications of x10 and x40, respectively, for (A) the treatment group (DPGNS + PTT), (B) DPGNS and no PTT, (C) PBS and PTT, and (D) control group (no DPGNS, PBS, or PTT). ..... 117

**Figure 6.14.** Quantification of tumour cellular area post treatment. (A) A one-way ANOVA test found the percentage difference in total cellular area to be significant between different groups ( $F(3,7) = 21.75, p < 0.01$ ). A student's Newman-Keuls Multiple Comparisons post hoc test found the tumours in the treatment group to a significantly lower cellular area compared to the other groups. Data are expressed as means and SDs. \*\* $p < 0.01$  vs control, ^ $p < 0.01$

DPGNS + Laser; (B) H&E stained histological section from a tumour in the treatment group with apoptotic cells with fragmented nuclei marked with arrows. .... 118

## List of tables

<b>Table 3.1.</b> Values of $c_m$ , $c_b^D$ , $sO_2^D$ , $c_b^F$ , and $sO_2^F$ , used in the tissue models in figure 3.4. ....	45
<b>Table 3.2.</b> Average values of $c_b^F$ and $sO_2^F$ obtained from the arterial fluence calibration procedure for each simulation on the singlelayer model, as well as the corresponding average error and uncertainty. ....	53
<b>Table 3.3.</b> Average values of $c_m$ , $c_b^D$ , $sO_2^D$ , $c_b^F$ , and $sO_2^F$ obtained from the arterial fluence calibration procedure for each simulation on the multilayer model, as well as the corresponding average error and uncertainty for each parameter. ....	53
<b>Table 3.4.</b> Average values of $c_{780}^U$ and $c_{832}^L$ determined from the arterial fluence calibration procedure on each phantom, as well as the corresponding average error and uncertainty. ....	57
<b>Table 3.5.</b> Values of $c_m$ , $c_b^D$ , $sO_2^D$ , $c_b^F$ , and $sO_2^F$ determined from the arterial fluence calibration procedure, as well as the corresponding average error and uncertainty for each parameter. ..	59
<b>Table 3.6.</b> Fluence corrected and uncorrected $sO_2^V$ values determined for veins 1, 2, and 3, as well as the corresponding average accuracy and uncertainty. ....	60
<b>Table 4.1.</b> CC, median percentage errors, and statistical significance of PAI and SU measurements of lesion thickness and adnexal depths, for melanomas and benign lesions....	69
<b>Table 5.1.</b> Average $sO_2$ values measured from within the fibroadenomas (intratumoural) and from the contralateral breasts (control), for patients 1-3. ....	87
<b>Table 5.2.</b> Average $sO_2$ values measured from within healthy breasts for patients 4-7.....	87
<b>Table 5.3.</b> Average $sO_2$ values measured from within the tumour (intratumoural), outside the tumour in the same breast (extratumoural), and from the contralateral breast (control) for patients 8-11. ....	90

# Chapter 1: Introduction

Photoacoustic (PA) imaging (PAI) is a hybrid biomedical imaging modality that merges ultrasonic detection with optical absorption contrast for high-speed, high-resolution imaging in deep tissue. Within the last two decades, major research into PAI has been carried out for various clinical and preclinical imaging applications. PAI overcomes the limitations of optical scattering in biological tissue by detecting ultrasonic waves generated by the photoacoustic effect. The absorption of a pulse of electromagnetic radiation by molecules creates a thermally induced expansion and contraction that launches ultrasonic waves which are detected by ultrasonic transducers to form images. The combination of light and sound gives PAI the unique capability to scale its spatial resolution and penetration depth across both the optical and ultrasonic domains, giving it a versatile range of applications. Using the intrinsic optical absorption of biological chromophores such as haemoglobin, melanin, lipids, and water, PAI provides functional, anatomical, and genetic contrasts of vasculature, blood haemodynamics, oxygen saturation level, and oxygen metabolism. Furthermore, exogenous contrast agents, such as organic dyes, nanoparticles, and reporter gene products, extend PAI capability to allow for targeted molecular imaging, drug release, and genetic process monitoring in complex biological systems. Preclinical studies on animals have been extensively carried out over the past decade, particularly on cancer models, providing a basis for the translation of positive results to the clinic. As a result, PAI is rapidly expanding in clinical fields, with major developments in breast cancer detection, dermatological imaging, vascular imaging, carotid artery imaging, and musculoskeletal imaging, using various PAI system configurations.

This thesis seeks to add to the expansion of PAI into the clinic in the areas of breast cancer and melanoma imaging, and to add to the molecular imaging capabilities of PAI through the validation of the PA contrast capabilities of novel gold nanoparticles. In addition, a novel method of correcting for the effects of wavelength-dependent fluence attenuation on measured PA spectra for the purposes of quantifying blood oxygen saturation is developed and implemented.

The contents of the thesis are as follows:

Chapter 2 covers the relevant background theory of PAI and tissue optics.

Chapter 3 deals with the development and implementation of the method of fluence-corrected venous sO<sub>2</sub> quantification using *arterial fluence calibration*. The method involves using arteries as a known optical calibration standard *in vivo* using the fact that the arterial absorption coefficient can be estimated from arterial sO<sub>2</sub> level measured with pulse oximetry. The method makes use of the fact that arterial sO<sub>2</sub> is systemic and the fact that arteries and arterioles are ubiquitous in biological tissue, meaning it can be applied at any location where an artery or arteriole can be resolved. The method was demonstrated by incorporating a multilayer model of optical diffusion into a PA forward model and fitted to the arterial PA spectrum to yield the volume fraction of melanosome in the epidermis, and the blood volume fraction and sO<sub>2</sub> level in the dermis and subcutaneous fat layers – the parameters that govern the extent of tissue-optical interference. The determined parameters were then used in the same model to correct the venous PA signal for the degrading effects of optical fluence attenuation. The method was demonstrated with coupled Monte Carlo (MC) and PA simulations, phantom studies, and an *in vivo* demonstration on human vasculature.

Chapter 4 deals with a clinical study where a handheld 40 MHz linear-array PA probe was used to preoperatively measure the thickness of pigmented skin lesions with suspicion of melanoma skin cancer. Melanoma is the most lethal form of skin cancer and accounts for 75% of skin cancer related deaths despite accounting for less than 5% of all cases. The histopathologically measured melanoma thickness, known as the Breslow thickness, is the most important factor for melanoma staging and determining treatment course and prognosis. Currently, the recommended technique for sampling lesions suspicious for cutaneous melanoma is excisional biopsy with narrow margins, however, partial biopsy techniques, which have a high incidence of microstaging inaccuracies due to undersampling of the primary lesion, are still used in up to 27% of melanoma diagnoses. Moreover, current surgical guidelines suggest the most pigmented part of the lesion is the most invasive and thus the most favourable for sampling, however, this does not always correspond to the most histologically advanced region, and therefore the full lesion thickness is unavailable to the pathologist in many cases. A noninvasive method of preoperatively determining lesion thickness could therefore guide sampling location, improve microstaging accuracy, save time, and prevent the need for additional surgeries.

PAI, with its high sensitivity, contrast, and penetration depth, is uniquely suited to imaging pigmented lesion morphology and measuring lesion thickness. To test its efficacy, 27 patients (with 32 lesions in total) with pigmented skin lesions suspicious for melanoma were recruited

from Galway University Hospital to undergo PA scans of the lesion with a handheld linear-array probe. Histology confirmed 6 cases of melanoma with the rest being various types of benign melanocytic nevi. PAI was able to image the lower lesion morphology in all cases except for 3 (benign lesions). The PA measured lesion thicknesses were compared with the histologically measured thicknesses from the excised lesion samples. The results showed the PA measurements accurately correlated with the histological measurements, however, there was a tendency of PAI to overestimate lesion thickness due to dehydration occurring in the histological sectioning process resulting in sample shrinkage.

In chapter 5, the efficacy of a 15 MHz handheld linear-array PA probe for imaging suspect breast cancer lesions in the clinic is described. Breast cancer is the most common malignancy occurring in women worldwide and is the leading cause of cancer-related death. Noninvasive imaging technologies play an important role in breast cancer screening and diagnosis, however, no one technology has sufficient sensitivity for standalone application. The gold standard technology, X-ray mammography, while demonstrating excellent sensitivity and specificity in many cases, lacks sufficient sensitivity in dense breasts, common in younger women. PAI, with its scalable imaging depth and high sensitivity to haemoglobin, possesses a means of detecting and diagnosing malignant tumours in deep tissue by imaging the increased blood concentration and lower  $sO_2$  level associated with pathological angiogenesis, using endogenous biological contrast alone. Handheld linear-array PAI holds promise for eventual integration in breast cancer screening alongside ultrasound (US) imaging, given that they can both be performed simultaneously and with the same imaging probe, with the added benefit of providing molecular imaging contrast which US lacks.

To test its efficacy, 31 patients from the Symptomatic Breast Unit in GUH were recruited to undergo linear-array PAI at 15 MHz. The criteria for patient selection were that the patient be able to provide informed consent and that the suspect lesion be relatively close to the skin surface (2-3 cm) so as to be within the imaging depth range of the system. Handheld linear-array PAI was assessed in terms of its ability to image lesion morphology and intratumoural oxygenation level. The results showed an ability to image the upper lesion morphology for lesions less than 13 mm deep, while the  $sO_2$  scans showed clear differences in intratumoural  $sO_2$  between malignant and benign lesions in the majority of cases.

In addition to the above assessment, the study also included an assessment of patient response to neoadjuvant chemotherapy - a standard treatment for locally advanced breast cancer prior to

definitive surgery. Between 8% and 20% of patients undergoing neoadjuvant chemotherapy experience no clinical or pathologic response and therefore undergo the stress of chemotherapy for months without any therapeutic benefit. However, previous studies using diffuse optical imaging (DOI) to monitor patient response have shown that responding patients experience a statistically significant intratumoural oxyhaemoglobin flair compared with nonresponding patients on the first day of treatment, thereby providing an early biomarker that could alter treatment strategy and improve therapeutic management. To test the efficacy of PAI in monitoring same, a number of neoadjuvant chemotherapy patients were recruited to undergo PAI to monitor intratumoural sO<sub>2</sub> level before and after the administration of chemotherapy. However, due to logistical reasons, follow-up scans from the baseline measurements (pre-treatment) were not possible and the study is still ongoing.

In chapter 6, the PAI image contrast capabilities of silica-coated dual-plasmonic gold nanostars (DPGNS) were evaluated in *in vivo* and phantom studies. Gold nanostars (GNS) serve as excellent contrast agents for PAI due to their high acoustic-to-optical conversation efficiency and can be tuned to absorb in the visible and NIR wavelength range (700-1000 nm). GNS coupled with targeted antibodies offer a range of biomedical applications such as cancer diagnosis, lesion localisation, and molecular typing of disease. DPGNS, synthesised to produce absorption bands in the second biological window (1000-1350 nm), offer additional advantages due to the lower optical scattering and increased penetration depth found in this wavelength region. Moreover, the addition of a silica coating on the particle surface serves to enhance the PA image contrast by increasing the photothermal conversion efficiency. To test this, PA scans at 700 and 1064 nm on an agar and intralipid phantom containing both silica-coated and non-silica coated DPGNS were carried out, with the results showing an increased PA signal amplitude for the former. Illumination of both groups of particles with a 1064 nm laser further confirmed this, showing an increase in the photothermal conversion efficiency of the silica-coated DPGNS, as evidenced by a 2-3°C temperature rise measured with a thermal camera.

In an *in vivo* study, the spatial distribution and relative concentration of DPGNS in mice tumours undergoing photothermal therapy (PTT) was assessed with PAI at various study timepoints. Mice injected with MDA-MB-213 tumour cells in the hind legs to initiate tumour growth were divided into 4 study groups containing 7 mice each, consisting of a treatment group and 3 control groups. Mice tumours in the treatment group were injected intratumorally with silica-coated DPGNS and underwent PTT using a 1064 nm continuous-wave laser for 10 minutes to bring about thermal-induced cell destruction. The 3 control groups consisted of

tumours injected with silica-coated DPGNS but receiving no PTT, tumours injected with phosphate buffered saline (PBS) and receiving PTT, and a group with no DPGNS, PBS or PTT. PAI scans at 700 and 1064 nm on each group were taken before treatment on day -1, and post treatment on days 3, 7, 14 and 21. The intratumoural PA amplitude from tumours containing silica-coated DPGNS undergoing laser treatment and the control group containing same but undergoing no treatment were found to be very similar, indicating the photostability of the particles and showing that additional laser treatment sessions with higher laser power are possible future studies, possibly bringing about further therapeutic benefit and reduction in tumour volume.

Finally, chapter 7 deals with the thesis conclusion and future work.

## Chapter 2: Background theory

### 2.1 Photoacoustic imaging

PAI is a hybrid biomedical imaging technique that uses optically generated ultrasonic waves to form *in vivo* images of tissue [1–6]. PA imaging is based on the PA effect, which relates how pulsed electromagnetic (EM) radiation is used to generate ultrasound (US) waves in optically absorbing media. The PA effect was first discovered by Alexander Graham Bell in 1880 [7], who found that acoustic waves could be generated by objects being illuminated by chopped sunlight. However, PA imaging did not emerge as an imaging modality until the 1970s, after the invention of laser light sources, acoustic transducers, and computers.

PA imaging combines the advantages of high optical absorption contrast with the low scattering of acoustic waves in soft tissue. Unlike optical imaging techniques, PA imaging is capable of imaging past the optical diffusion regime with high spatial resolution, as it indirectly detects diffuse optical absorption through US detection. Since US scattering is 2 to 3 times less than optical scattering in biological tissue, ultrasonic imaging is capable of achieving higher spatial resolution than optical imaging at depths greater than  $\sim 1$  mm. However, pure US imaging is only sensitive to the mechanical properties of tissue, which have a 10% variation, giving it weak image contrast. Moreover, US is insensitive to molecules like oxy- and deoxyhaemoglobin, which provide important physiological and functional information. PA imaging overcomes the above disadvantages and yields high optical absorption contrast with high ultrasonic resolution for deep tissue imaging.

When biological tissue is irradiated with a pulsed light source, the photons propagate through the tissue and quickly become diffuse. Some of this light is absorbed by optically absorbing molecules and is partially converted into heat, which results in a rapid expansion and contraction of the tissue, called thermoelastic expansion. This transient thermoelastic expansion propagates outwards from the source in all directions as a wideband US wave, called the PA wave or PA signal. The PA waves from the initial acoustic source reach the surface of the tissue with various time delays and can be detected with the coupling of an acoustic transducer, and subsequently used to reconstruct an image of the spatial distribution of absorbed optical energy within the tissue.

## 2.2 Initial photoacoustic pressure generation

To generate an acoustic impulse response from laser heating in tissue and achieve a high spatial resolution in a PA image, two important illumination conditions must be satisfied: thermal and stress confinement [8–10,4].

### 1. Thermal confinement

The laser pulse used to generate PA waves must have a temporal width shorter than the thermal relaxation time, so that the effects of thermal diffusion can be neglected. The thermal relaxation time,  $\tau_{th}$ , is estimated by

$$\tau_{th} = \frac{d_c^2}{\alpha_{th}}, \quad 2.1$$

where  $\alpha_{th}$  is the thermal diffusivity [m<sup>2</sup>/s], and  $d_c$  is the characteristic dimension [m] (targeted spatial resolution).

### 2. Stress confinement

The laser pulse width must be shorter than the stress relaxation time, so that stress propagation is negligible during laser heating. The stress relaxation time is given by

$$\tau_s = \frac{d_c}{v_s}, \quad 2.2$$

where  $v_s$  is the speed of sound ( $\approx 1500$  m/s in soft tissue).

The light energy deposition or absorption,  $A(\mathbf{r})$  [J/cm<sup>3</sup>], at a position  $\mathbf{r}$  as a result of an incident short-pulsed laser on an absorbing tissue can be expressed as

$$A(\mathbf{r}) = \mu_a(\mathbf{r})\phi(\mathbf{r}), \quad 2.3$$

where  $\mu_a(\mathbf{r})$  [cm<sup>-1</sup>] is the local optical absorption coefficient and  $\phi(\mathbf{r})$  [J/cm<sup>2</sup>] is the local optical fluence (light energy per meter squared), at location  $\mathbf{r}$ , respectively. A fraction of the optical energy deposited is converted into thermal energy, which results in a local temperature rise  $T(\mathbf{r})$  [K] which is given by

$$T(\mathbf{r}) = \frac{\mu_a(\mathbf{r})\phi(\mathbf{r})}{\rho C_p}, \quad 2.4$$

where  $\rho$  denotes the mass density ( $\sim 1000 \text{ kg/m}^3$  for water and soft tissue [8]) and  $C_p$  denotes the specific heat at constant pressure ( $\sim 3600$  to  $3900 \text{ J/(kg}\cdot\text{K)}$  for soft tissue [11]). The rise in temperature produces a strain  $S(\mathbf{r})$  [dimensionless] via thermoelastic expansion defined as

$$S(\mathbf{r}) = \frac{\beta\mu_a(\mathbf{r})\phi(\mathbf{r})}{\rho C_p}, \quad 2.5$$

where  $\beta$  is the thermal expansivity ( $\sim 4 \times 10^{-4} \text{ K}^{-1}$  for muscle [8]). If the laser pulse duration is less than both the thermal and stress confinement times, this produces a transient pressure wave with a peak amplitude  $P_0(\mathbf{r})$  [Pa], given by

$$P_0(\mathbf{r}) = \frac{M\beta}{\rho C_p} \mu_a(\mathbf{r})\phi(\mathbf{r}), \quad 2.6$$

where  $M$  is the bulk modulus [Pa per strain]. For most PA applications, it can be assumed that the heating effect dominates the absorption interaction, and that fluorescence effects are negligible for the source spectra typically used (visible and near infrared (NIR)) in biomedical applications. Furthermore, the radiation intensity used in PA imaging should be below the maximum permissible exposure (MPE) level on humans defined by the American national standards institute (ANSI) of 20–100  $\text{mJ/cm}^2$  at the wavelengths ranging from 400 to 1500 nm [12], guaranteeing no chemical reactions or thermal damage in the tissue. Equation 2.6 can be used to relate *in vivo* tissue chromophore concentrations, to the peak PA signal amplitude and can incorporate forward models that account for variations in optical fluence at the measuring site.

The Grüneisen parameter  $\Gamma$  [dimensionless] [13], which represents the efficiency of the tissue in converting absorbed EM energy to sound, can be inferred from equation 2.6 as

$$\Gamma = \frac{M\beta}{\rho C_p}. \quad 2.7$$

For water and aqueous based solutions,  $\Gamma$  can be estimated by the following empirical formula:

$$\Gamma_w(T_0) = 0.0043 + 0.0053T_0, \quad 2.8$$

where  $T_0$  is the temperature in degrees Celsius. For soft tissue at body temperature,  $\Gamma_w(37^\circ C) = 0.20$ . The temperature dependence of the Grüneisen parameter allows the PA technique to monitor *in vivo* temperature distribution in real-time with submillimetre resolution [14].

### 2.3 Photoacoustic wave equation

The generation and propagation of PA pressure waves in an acoustically homogenous and non-viscous medium is described by the following general PA wave equation [8] [15]:

$$\left(\nabla^2 - \frac{1}{v_s^2} \frac{\delta^2}{\delta t^2}\right) p(\mathbf{r}, t) = -\frac{\beta}{\kappa v_s^2} \frac{\delta^2 T(\mathbf{r}, t)}{\delta t^2}, \quad 2.9$$

where  $p(\mathbf{r}, t)$  denotes the acoustic pressure variation (from equilibrium), and  $T(\mathbf{r}, t)$  denotes the temperature rise due to optical absorption, at location  $\mathbf{r}$  and time  $t$ , respectively. The left-hand side of equation 2.9 describes the acoustic wave propagation from the source point, and the right-hand side describes the source term.

The general forward solution of the PA wave equation, which satisfies thermal confinement, can be solved by the Green's function approach, to yield the PA pressure as

$$p(\mathbf{r}, t) = \frac{\beta}{4\pi C_p} \frac{\delta}{\delta t} \int \frac{d\mathbf{r}'}{|\mathbf{r} - \mathbf{r}'|} S\left(\mathbf{r}', t - \frac{|\mathbf{r} - \mathbf{r}'|}{v_s}\right). \quad 2.10$$

For a short EM pulse that satisfies the acoustic-stress confinement, a delta heating response can be assumed and the heat generation function  $H(\mathbf{r}', t')$  can be written in terms of the spatial absorption function and the temporal illumination function as

$$H(\mathbf{r}', t') = A(\mathbf{r}') H_t(t'), \quad 2.11$$

where  $H_t(t') = \delta(t')$ . Equation 2.10 can then be written as

$$p(\mathbf{r}, t) = \frac{\beta}{4\pi C_p} \frac{\delta}{\delta t} \left[ \frac{1}{v_s t} \int d\mathbf{r}' A(\mathbf{r}') \delta\left(t - \frac{|\mathbf{r} - \mathbf{r}'|}{v_s}\right) \right]. \quad 2.12$$

The quantity in the square brackets is the step heating response of an arbitrary absorbing object, and its time differentiation gives the delta heating response. Equation 2.12 can be written in terms of the initial pressure amplitude by inserting equation 2.6 to give

$$p(\mathbf{r}, t) = \frac{1}{4\pi v_s^2} \frac{\delta}{\delta t} \left[ \frac{1}{v_s t} \int dr' P_0(\mathbf{r}') \delta \left( t - \frac{|\mathbf{r} - \mathbf{r}'|}{v_s} \right) \right]. \quad 2.13$$

Equation 2.13 indicates that the detected PA pressure at time  $t$  arrives from sources over a spherical shell centred at the detector position  $\mathbf{r}$  and with a radius of  $v_s t$ , as depicted in figure 2.1 (a). Figure 2.1 (b) shows a typical example of a PA wave emitted from a spherical source which has undergone a uniform instantaneous energy deposition. The familiar bipolar shape arises from two parts. The initial positive pressure rise results from the thermoelastic expansion of the heated object and propagates outward from the source as a diverging spherical compression wave. When the object contracts it emits an inward travelling compression wave that upon reaching the object centre becomes a diverging spherical rarefaction wave that arrives at the detector at a later time and registers as a negative pressure.

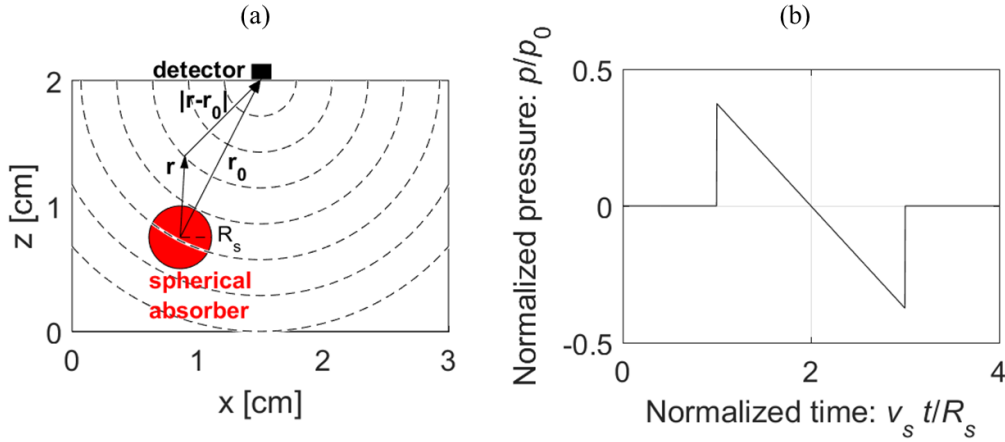


**Figure 2.1.** (a) The PA waves arriving at a point detector (a) at time  $t$  are modelled as coming from sources over a spherical shell with a constant radius of  $v_s t$ , centered at the detector position  $P(\mathbf{r}, t)$ . (b) An example of a PA signal generated from a uniform spherical PA source.

At far away distances, a number of physical characteristics about the source object can be interpreted from the PA waveform:

1. The amplitude of the PA wave is approximately proportional to the radius of the source object, but inversely proportional to the distance from the source object.

2. The temporal width of the PA wave is proportional to the radius of the source. This indicates that smaller objects produce higher frequency component PA signals, which influences the required detection bandwidth and imaging depth.
3. The zero point of the PA waveform indicates its distance from the source object.

Sometimes, the PA pressure is represented by the velocity potential,  $\Phi_v(\mathbf{r}, t)$  [ $\text{m}^2/\text{s}$ ], which is given by the negative of the time-resolved integration of PA pressure:

$$\Phi_v(\mathbf{r}, t) = -\frac{1}{\rho} \int p(\mathbf{r}, t') dt'. \quad 2.14$$

Conversely, the PA pressure is equal to the negative of the time derivative of the velocity potential. For a delta heating response  $\Phi_v(\mathbf{r}, t)$  is given by

$$\Phi_v(\mathbf{r}, t) = -\frac{\beta}{4\pi\rho C_p} \int \frac{dr'}{|\mathbf{r} - \mathbf{r}'|} A(\mathbf{r}') \delta\left(t - \frac{|\mathbf{r} - \mathbf{r}'|}{v_s}\right). \quad 2.15$$

Equation 2.15 is an integral of the optical energy deposition of a shell of radius  $v_s t$  centred around the detector at position  $\mathbf{r}$ . The energy deposition  $A(\mathbf{r}')$  [ $\text{J}/\text{m}^2$ ] makes a positive contribution to the negative velocity potential at position  $\mathbf{r}$ , and correspondingly,  $\Phi_v(\mathbf{r}, t)$  drops to zero in areas where no optical absorption occurs. The velocity potential in equation 2.15 represents a spherical Radon transformation, thus the corresponding back projection algorithm to obtain the original spatial distribution of optical energy density at time zero becomes an inverse Radon transformation.

## ***2.4 Penetration depth and spatial resolution***

### **Penetration depth**

One of the main advantages of PA imaging is its ability to overcome optical diffusion and image past the ballistic regime with high spatial resolution. However, PA penetration depth is still limited by optical and acoustic attenuation. In biological tissue, optical attenuation effects dominate owing to the strong optical absorption from endogenous tissue chromophores and light scattering from collagen fibres and small-scale cell structures [16–18].

Optical attenuation in highly scattering media which satisfy the requirements of diffusion theory is best characterised by the effective attenuation coefficient  $\mu_{eff}$  [ $\text{cm}^{-1}$ ], given as

$$\mu_{eff} = \sqrt{3\mu_a(\mu_a + \mu'_s)}, \quad 2.16$$

where  $\mu_a$  and  $\mu'_s$  are the absorption and reduced scattering coefficients, respectively (defined in section 2.6).  $\mu_{eff}$  defines the probability of photon interaction via absorption and scattering per unit infinitesimal pathlength under isotropic radiance. The effective penetration depth,  $\delta_{eff}$  [ $\text{cm}$ ], can therefore be calculated by inverting  $\mu_{eff}$  as

$$\delta_{eff} = \frac{1}{\mu_{eff}}. \quad 2.17$$

$\delta_{eff}$  is therefore the depth at which the incident light intensity drops by  $1/e$  of its initial value. The greatest optical penetration depth is achieved in the wavelength range of 700-900 nm, termed the ‘biological window’, due to the reduction in optical scattering and absorption coefficients.

Acoustic waves in biological tissue are similarly attenuated by absorption and scattering. In the low megahertz frequency range, US waves are highly penetrating and are weakly absorbed by soft tissue. Acoustic attenuation follows a frequency dependent power law given by

$$\mu = af^b, \quad 2.18$$

where  $\mu$  is the acoustic attenuation coefficient [ $\text{dB cm}^{-1} \text{MHz}^{-1}$ ],  $f$  is the US frequency, and  $a$  and  $b$  are constants. A mean value of  $\mu$  in soft tissues for an US frequency of 10 MHz is  $\sim 0.75 \text{ dB cm}^{-1} \text{MHz}^{-1}$  [6]. It follows from equation 2.16 that higher penetration depths can be achieved at lower US frequencies, and conversely, acoustic attenuation is higher for higher US frequencies.

The combined effects of optical and acoustic attenuation results in at least one order of magnitude of the reduction of light intensity per centimetre. This proves challenging for deep-tissue imaging over several centimetres, as exponential signal attenuation requires the detection of very weak US signals. However, since PA imaging relies on the detection of US waves and not on emission (as in US imaging), the emission efficiency of dedicated PA probes can be disregarded, and transducers used in PA imaging applications can be specifically designed for detector sensitivity. Coupled with this, through optimum selection of laser wavelength, and

optimisation of light delivery and signal processing, penetration depths of several centimetres *in vivo* have been achieved. An imaging depth of 4 cm was achieved in human breast tissue [19], while other studies on *ex vivo* samples and tissue phantoms have suggested a penetration depth of 5-6 cm can be achieved with the use of endogenous contrast agents [20,21]. In addition, imaging at longer wavelengths, such as 1064 nm, where tissue is more transparent due to the drop in the optical absorption coefficient of blood, can increase penetration depth with the use of appropriate contrast agents [22]. Imaging at 1064 nm also allows for a higher ANSI MPE in the skin due to the lower absorption by melanin.

### **Spatial resolution**

The PA effect results in the emission of broadband US waves with frequencies in the range of 10-100 MHz, depending on the length-scale of the optical absorbers. Since the acoustic attenuation coefficient in equation 2.18 is dependent on frequency, biological tissue acts as a low-pass filter and disproportionately attenuates high-frequency components as the PA signal travels. The net effect of this is to degrade PA spatial resolution with depth. Acoustic attenuation is thus the main factor in determining the spatial resolution limit. Acoustic attenuation varies considerably with tissue type and composition, however, an approximate rule of thumb for scaling spatial resolution is that for centimetre penetration depths, sub-millimetre resolution is achievable, which decreases to sub-100  $\mu\text{m}$  for millimetre penetration depths and sub-10  $\mu\text{m}$  spatial resolution to for depths of a few hundred micrometres [6]. Spatial resolution is also dependent on the temporal width of the laser pulse, according to equations 2.1 and 2.2. For example, to achieve a spatial resolution of 100  $\mu\text{m}$ , the laser pulse must be shorter than 18 ns for temporal confinement, and shorter than 64 ns for stress confinement.

Characteristics of the US transducer also have a significant effect on spatial resolution, such as detection bandwidth, numerical aperture, and transducer element size. Transducer bandwidth effects the lateral and axial resolution, while the numerical aperture mainly effects the lateral resolution [23]. Transducer bandwidth is particularly important when imaging small-scale superficial features which emit wideband US signals with high frequency components which have not been lost to acoustic attenuation. Additionally, reconstruction algorithms which model acoustic transducers as ideal point-like detectors with a wide acceptance angle and infinite bandwidth, such as the universal back-projection [24] and time-reversal algorithms [25], can induce reconstruction errors if applied directly to experimental data.

## 2.5 Quantitative photoacoustic Imaging

Multiwavelength PA imaging can be used to extract functional information from tissue such as tissue oxygenation level and oxygen consumption rate, and to quantify chromophore concentrations. Figure 2.2 shows the absorption spectra of the primary endogenous biological chromophores in the visible-NIR wavelength region, consisting of melanin, oxy- and deoxyhaemoglobin, and water. Since the peak PA signal amplitude is proportional to optical absorption, PA amplitude spectra obtained by scanning at multiple wavelengths are proportional to the absorption spectra of a given chromophore. This fact can be used to quantify chromophore concentrations, which has various clinical and research applications. Of major physiological interest is the quantification of blood oxygen saturation ( $sO_2$ , the percentage of total haemoglobin bound with molecular oxygen) and total haemoglobin concentration ( $c_{HbT}$  [g/L]), which are primary indicators of tissue health and function. PA quantification of  $sO_2$  and  $c_{HbT}$  is dealt with in greater detail in section 3.3.

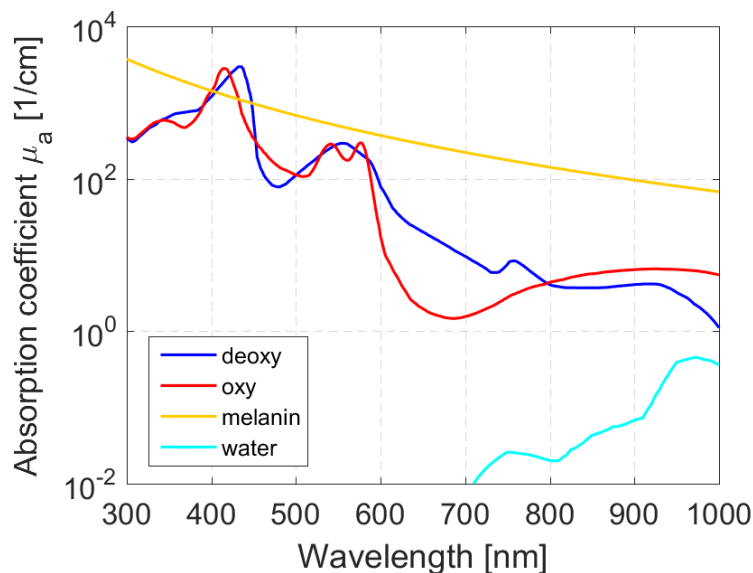


**Figure 2.2.** Absorption coefficients of endogenous biological chromophores in the visible and NIR spectral regions at concentrations typically found in the human body. Oxy- and deoxyhaemoglobin, 150 g/L. Water 60% by weight. Melanin concentration corresponds to that in skin (adapted from [26]).

## 2.6 Tissue optical properties

As light passes through biological tissue, it is absorbed, scattered, and reflected according to the tissue optical properties. The optical properties of biological tissues are described in terms of the absorption coefficient  $\mu_a$  [ $\text{cm}^{-1}$ ], the scattering coefficient  $\mu_s$  [ $\text{cm}^{-1}$ ], the anisotropy of scattering  $g$ , and the real refractive index  $n$ . The rate of optical attenuation of a beam of light as it propagates through biological tissue and the resulting spatial distribution of the absorbed energy density are directly influenced by the tissue optical properties.

In the visible (400-700 nm) and near-infrared (700-1000 nm) wavelength regions most biological tissues are characterised by high optical scattering ( $\mu_s \approx 100 \text{ cm}^{-1}$ ) and are referred to as scattering or turbid media. By contrast, optical absorption is comparatively weak ( $\mu_a \approx 0.1 \text{ cm}^{-1}$ ) which allows for deep optical penetration. Optical scattering properties can reveal structural changes at the cellular and subcellular level, while optical absorption properties can reveal functional information such as haemoglobin oxygen saturation and concentration.

### 2.6.1 Absorption in biological tissues

Biological tissue is composed of optical chromophores that absorb light and give tissue its colour. Optical absorption is measured by the absorption coefficient  $\mu_a$ , which is defined as the probability of photon absorption per unit infinitesimal pathlength. Figure 2.2 shows the wavelength dependent optical absorption coefficients of the main biological absorbers in tissue in the visible and NIR spectral regions.

Optical absorption can be modelled by considering a chromophore as an idealised sphere with a given geometrical size, as shown in figure 2.3. Light incident on the sphere is blocked by absorption and casts a shadow, the size of which is called the effective cross section  $\sigma_a(\lambda)$  [ $\text{cm}^2$ ]. The effective cross section is related to the geometrical size of the sphere  $A_a$  [ $\text{cm}^2$ ] by the proportionality factor  $Q_a(\lambda)$  [dimensionless]:

$$\sigma_a(\lambda) = Q_a(\lambda)A_a. \quad 2.19$$

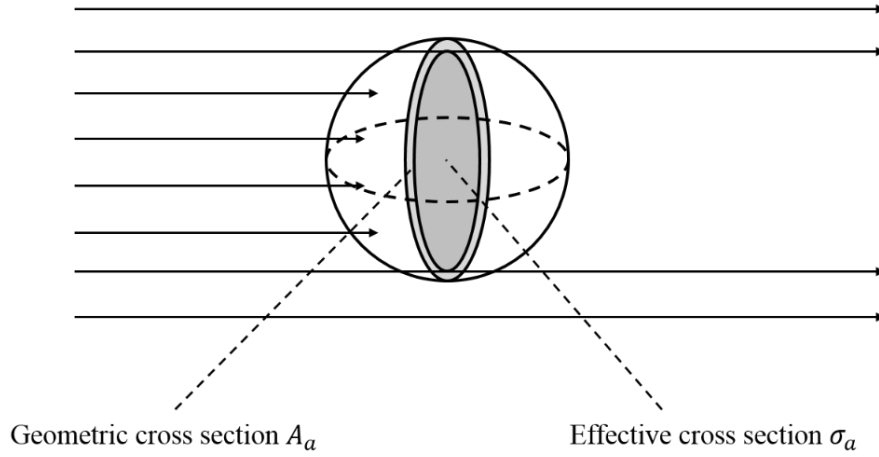


**Figure 2.3.** Optical absorption process by a chromophore with geometric cross-section  $A_a$  and effective cross-section  $\sigma_a$ .

In a medium containing many chromophores with a number density  $\rho_a$  [ $\text{cm}^{-3}$ ], the absorption coefficient can be considered as the total cross-sectional area of absorbers per unit volume of the medium as

$$\mu_a(\lambda) = \rho_a \sigma_a(\lambda). \quad 2.20$$

The absorption coefficient of biological tissues can be calculated based on the concentrations of the various optical chromophores present. For most tissues, it can be assumed that oxyhaemoglobin, deoxyhaemoglobin, and water are the dominant absorbing compounds in the visible-NIR spectral region, and  $\mu_a(\lambda)$  can be written as

$$\mu_a(\lambda) = \ln(10) (\varepsilon_{HbO_2}(\lambda)c_{HbO_2} + \varepsilon_{Hb}(\lambda)c_{Hb} + \varepsilon_{H_2O}(\lambda)c_{H_2O}), \quad 2.21$$

where  $\varepsilon_{Hb}(\lambda)$ ,  $\varepsilon_{HbO_2}(\lambda)$ , and  $\varepsilon_{H_2O}(\lambda)$  are the known molar extinction coefficients [ $\text{L}/\text{cm mol}$ ] of oxyhaemoglobin, deoxyhaemoglobin, and water, respectively, and  $c_{Hb}$ ,  $c_{HbO_2}$ , and  $c_{H_2O}$  are the concentrations [ $\text{mol}/\text{L}$ ] of same, respectively. The other main biological absorber is melanin; however, it is highly localised in the stratum basale of the epidermis, or in the retina, and does not need to be considered when calculating the absorption coefficient of the dermis or subcutaneous tissues.

If the concentrations of oxy- and deoxyhaemoglobin are known, then the haemoglobin or blood oxygen saturation,  $sO_2$ , can be calculated as

$$sO_2 = \frac{c_{HbO_2}}{c_{HbO_2} + c_{Hb}} \times 100, \quad 2.22$$

and the total haemoglobin concentration,  $c_{HbT}$ , as

$$c_{HbT} = c_{HbO_2} + c_{Hb}. \quad 2.23$$

Equation 2.22. shows that absolute values of blood oxygen saturation can be calculated from relative values of  $c_{HbO_2}$  and  $c_{Hb}$ . The absorption coefficient of tissue or blood vessels can then be written in terms of  $sO_2$  and  $c_{HbT}$  to give

$$\mu_a(\lambda) = \ln(10) (\varepsilon_{HbO_2}(\lambda)c_{HbT}sO_2 + \varepsilon_{Hb}(\lambda)c_{HbT}(1 - sO_2) + \varepsilon_{H_2O}(\lambda)c_{H_2O}). \quad 2.24$$

The absorption coefficients of oxy- and deoxyhaemoglobin are distinct but share a few intersection points, called isosbestic points. At these points the absorption coefficient is independent of the blood oxygen saturation level.

## 2.6.2 Scattering in biological tissues

Optical scattering results from photon interaction with small-scale biological structures such as cells and organelles. Optical scattering is described by Mie theory [27–29], which models scatterers as homogenous spheres with a given radius. Mie theory applies in situations where the characteristic size of the scattering sphere,  $r$ , is on the order of or greater than the wavelength of light  $\lambda$ . In the case of  $r \ll \lambda$ , Mie scattering is approximated by Rayleigh scattering. In tissue, cell nuclei and whole organelles scatter light in the Mie regime, while the organelles and cell membranes scatter light in the Rayleigh regime [30]. Photons are scattered most strongly by structures whose size is similar to the photon wavelength and whose refractive index mismatches with that of the surrounding tissue.

Single scattering by a scattering structure idealised as a sphere with a given geometrical size is depicted in figure 2.4. Incident photons are redirected by scattering and thereby cast a shadow, the size of which is called the effective cross-section,  $\sigma_s$  [ $cm^2$ ], which can be smaller or larger than the geometric size of the sphere. The effective cross section is related to the geometric size of the sphere  $A_s$  [ $cm^2$ ] by the proportionality factor called the scattering efficiency  $Q_s$  [dimensionless]:

$$\sigma_s(\lambda) = Q_s(\lambda)A_s. \quad 2.25$$

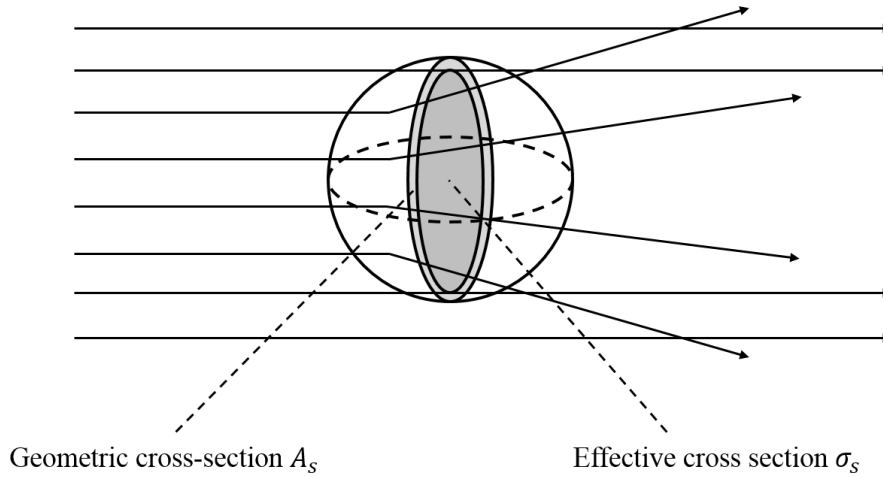


**Figure 2.4.** Optical scattering process by a scattering particle with a given geometric cross-section  $A_s$  and effective cross-section  $\sigma_s$ .

The scattering coefficient is then related to the number density  $\rho_s$  [ $\text{cm}^{-3}$ ] of scattering particles as

$$\mu_s(\lambda) = \rho_s \sigma_s(\lambda). \quad 2.26$$

Similar to the absorption coefficient, the scattering coefficient is defined as the probability of photon scattering per unit infinitesimal pathlength. Equation 2.26 defines  $\mu_s$  as the cross-sectional area of scatterers per unit volume of the medium. The reduced scattering coefficient  $\mu'_s$  [ $\text{cm}^{-1}$ ] can then be defined using the anisotropy factor  $g$  as

$$\mu'_s(\lambda) = \mu_s(\lambda)(1 - g), \quad 2.27$$

where  $g$  [dimensionless] is a measure of the amount of forward direction retained after a single scattering event and is defined as the mean value of the cosine of the deflection angle,  $\cos(\theta)$ . Typical values for  $g$  are in the range of 0.7-0.95 for skin [18,31,32]. The wavelength dependence of the reduced scattering coefficients for the skin and subcutaneous fat are shown given by empirical formulas in figure 2.5.

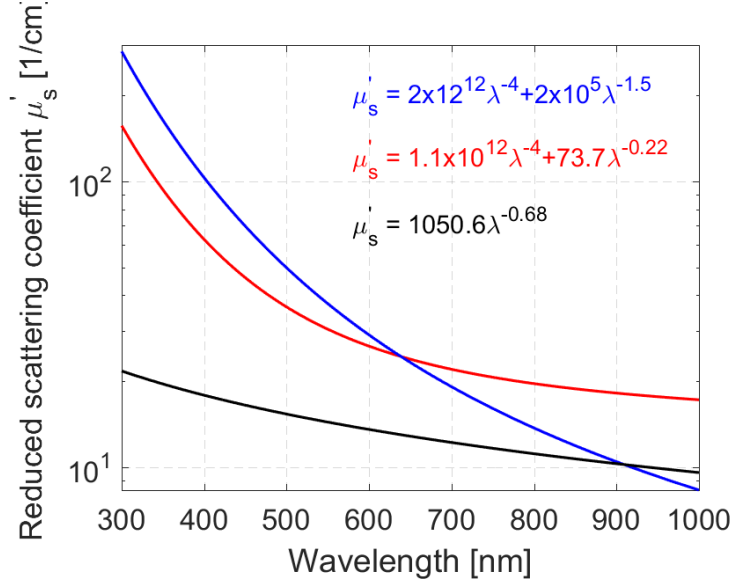


**Figure 2.5.** Reduced scattering coefficients of various tissues based on empirical formulas. Blue line: bloodless rat skin [33]. Red line: in vitro human skin [34]. Black line: in vitro subcutaneous adipose (fat) tissue [34]. For skin, the reduced scattering coefficients of the epidermis and dermis are assumed to be the same and an averaged  $\mu'_s$  value is used.

The probability of photon transmission  $T$  [dimensionless] without scattering in a clear medium after a path length  $x$  [cm] has been travelled is given by the Beer–Lambert law as:

$$T(x) = \exp(-\mu_s x). \quad 2.28$$

Equation 2.28 can also be written similarly for optical absorption. The total attenuation coefficient,  $\mu_t$ , can be defined as by the sum of  $\mu_a$  and  $\mu_s$  as

$$\mu_t = \mu_a + \mu_s, \quad 2.29$$

and defines the probability of scattering or absorption occurring per unit infinitesimal pathlength. The optical penetration depth or mean free path,  $\delta$  [cm], of collimated light can then be defined by inverting equation 2.29 as

$$\delta = 1/\mu_t, \quad 2.30$$

and is the average distance light will travel in tissue before an attenuation event occurs.

## 2.7 Diffusion theory

Diffusion theory is derived from an approximate solution to the radiative transport equation (RTE). The diffusion approximation assumes that the radiance in a high albedo ( $\mu_a \ll \mu_s$ ) scattering medium is nearly isotropic after many scattering events. In addition, it requires that the optical mean free path be much smaller than the physical dimensions of the problem being considered, e.g. the distance to boundaries and sources.

The diffusion equation follows from Fick's law of diffusion and the law of conservation of energy, and is given by [8,9]

$$\frac{1}{c} \frac{\delta \phi(r, t)}{\delta t} = D \nabla^2 \phi(r, t) - \mu_a(r) \phi(r, t) + U(r, t), \quad 2.31$$

where  $\phi$  is the fluence rate  $\text{W/m}^2$ ,  $U$  is the source term,  $c$  [m/s] is the speed of light, and  $r$  and  $t$  are the position and time, respectively.  $D$  is the diffusion constant defined as  $D = 1/(3(\mu_a + \mu'_s))$ . The diffusion equation states that the time rate of change of energy density is equal to the loss of energy per  $\text{m}^3$  per second by diffusion, minus the energy lost through optical absorption, plus the gain in energy from the light source. The solution to the time-resolved diffusion equation for an infinitely short-pulsed point source ( $U(r, t) = \delta(r, t)$ ) is given by

$$\phi(r, t) = cQ \frac{\exp(-r^2/(4cDt))}{(4\pi cDt)^{3/2}} \exp(-\mu_a ct), \quad 2.32$$

where  $Q$  is the point source of radiant energy in Joules [35]. The  $\exp(-\mu_a ct)$  term in equation 2.32 accounts for the reduction in fluence rate due to optical absorption as the light passes through the medium, while the remaining term characterises broadening due to scattering and is an impulse response, known as a Green function. Figure 2.6 shows an example of time-resolved fluence diffusion for a point source in a tissue medium using equation 2.32.

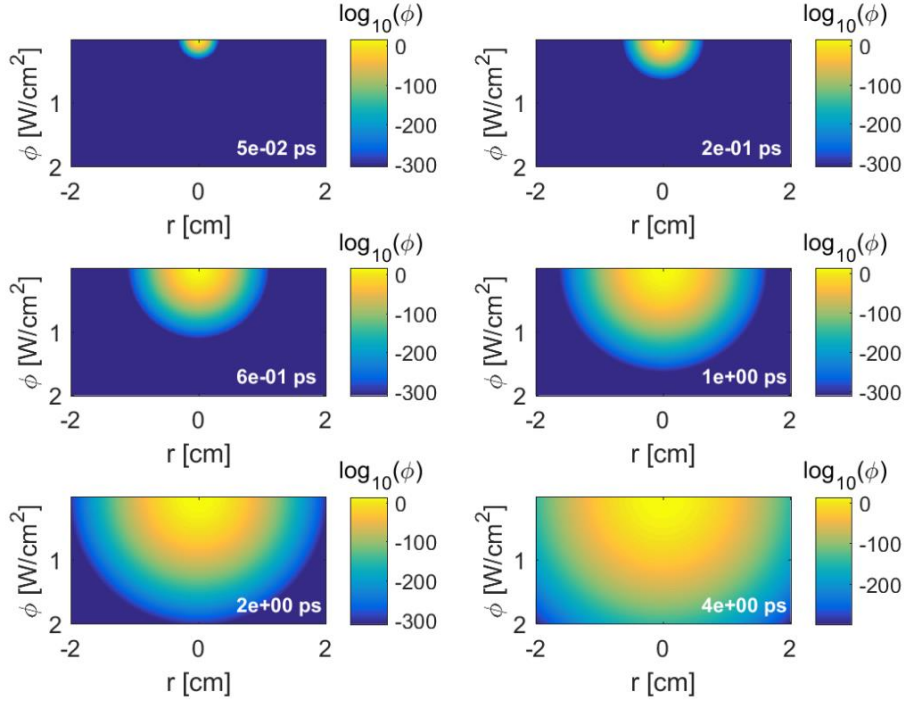


**Figure 2.6.** Time resolved diffusion of fluence rate  $\phi$  [W/cm<sup>2</sup>] after the deposition of a point source of radiant energy of 1 J at  $r = 0$  and  $t = 0$  at various timepoints in an absorbing and scattering tissue medium at 800 nm, with  $\mu_a = 0.017 \text{ cm}^{-1}$  and  $\mu'_s = 14.25 \text{ cm}^{-1}$ .

For stationary situations far from sources ( $\delta\phi(r, t)/\delta t = 0$ ,  $S(r, t) = 0$ ), the time dependency is dropped and equation 2.29 becomes

$$D\nabla^2\phi(r) = \mu_a(r)\phi(r). \quad 2.33$$

For an optically homogenous semi-infinite medium illuminated by a wide-beam light source in the  $z$ -direction, deep inside the medium ( $\sim 10$  penetration depths), equation 2.33 applies with only one variable coordinate  $z$ , which gives the solution

$$\phi(z) = \phi(0) \exp\left(-z\left(\frac{\mu_a}{D}\right)^{\frac{1}{2}}\right) \quad 2.34$$

$$= \phi(0) \exp(z\sqrt{3\mu_a(\mu_a + \mu'_s)}). \quad 2.35$$

where  $\phi(0)$  is the beam fluence at the tissue surface. In the exponential of equation 2.31, the effective attenuation coefficient is defined as  $\mu_{eff} = \sqrt{3\mu_a(\mu_a + \mu'_s)} = \sqrt{\mu_a/D}$ .

## 2.8 Monte Carlo simulations of light transport in biological tissue

Monte Carlo (MC) simulations are a fundamental and versatile approach toward simulating light transport in biological tissue [36–38]. The MC method is a stochastic method of modelling complex physical problems and is considered to be the ‘gold standard’ method of solving the RTE as it (a) converges to exact solutions of the RTE and (b) it can handle a complex range of geometries and illumination patterns. An example MC simulation is illustrated in figure 2.7.

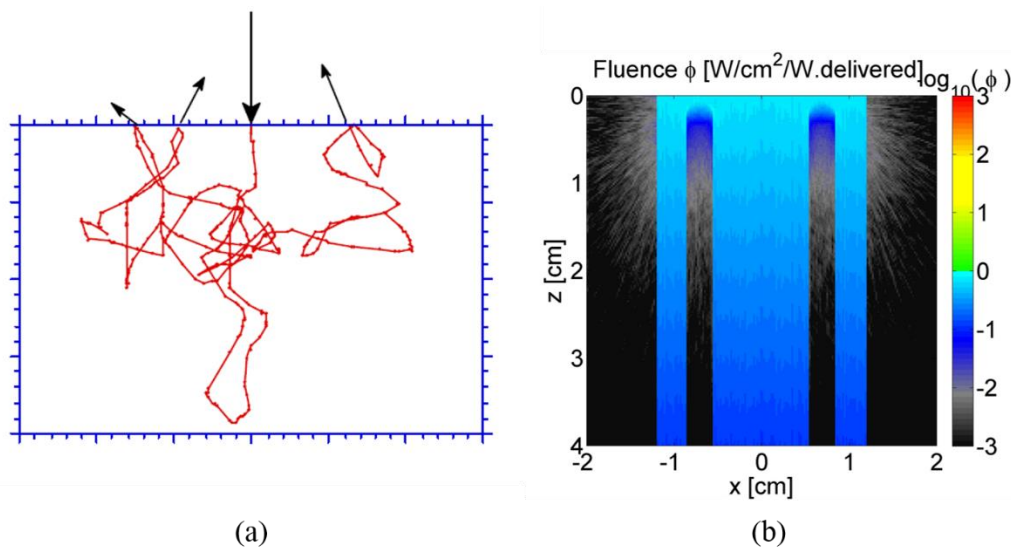


**Figure 2.7.** A MC simulation of light transport. (a) Propagation of a single photon in a light-scattering tissue. When the photon is totally internally reflected at the air/tissue surface, a fraction of the photon weight is allowed to escape as reflectance and the remaining photon weight continues to propagate in the tissue where it can be scattered and absorbed. (b) Example MC simulation of relative fluence rate [W/cm<sup>2</sup>/W delivered] at 800 nm on a tissue phantom composed of two highly absorbing blood vessels with a diameter of 0.25 cm and centred at a depth of 0.3 cm, placed in a medium with low scattering and absorption. The light source is a 2.5 cm diameter collimated circular beam in the +z direction. The low scattering properties of the water results in an extended shadowing underneath the blood vessels.

The general procedure for MC simulations consists of launching a photon packet into a voxelated tissue model at a location defined by  $x, y, z$  coordinates and a trajectory defined by directional cosines (projection of trajectory onto  $x, y,$  and  $z$  axes). The photon packet is given an initial weight (or energy) of 1.0, which is progressively attenuated as the weight is deposited into the voxels as it propagates. The photon travels a random distance into the tissue based on

the selection of a random number [0,1] and the local attenuation coefficient of the medium. At the end of each photon step, the weight of the photon packet is reduced by an amount proportional to the local absorption coefficient. The absorbed weight is then stored in a bin or voxel that encloses the current photon position. The remaining photon weight is then moved again by a random distance and scattered according to a phase function that describes the angular dependence of the single scattering for a particular tissue. The most commonly used function for tissue scattering is the Henyey-Greenstein phase function [39], which is expressed as a function of the scattering deflection angle and the anisotropy. If the photon weight falls below a given threshold, typically  $10^{-4}$ , it has a chance of being terminated. Once the photon is terminated, a new photon is launched and the spatial distribution of the absorbed energy density,  $A(x, y, z)$ , begins to accumulate. After a total of  $N$  photons have been launched,  $A(x, y, z)$  is normalised by the voxel volume and by  $N$  to yield the fractional density matrix of incident light absorbed,  $A$  [ $1/\text{cm}^3$ ] or [ $\text{J}/\text{cm}^3$  per J delivered], in response to one unit of delivered energy. The corresponding radiant energy density matrix in absolute units can be obtained by multiplying  $A$  by the incident beam radiant energy. Photon, transmission, refraction and reflection at index-mismatched boundaries and changes in local optical properties can be included in the simulation.

The MC method for photon transport in biological tissue was first implemented by Adams and Wilson, which considered isotropic scattering [40]. The most widely used MC program for biomedical applications is Monte Carlo Multi-Layered (MCML), developed by Wang and Jacques [41], which stores photon absorption and fluence rate in 2D arrays using a cylindrical coordinate system. In this thesis, a 3D Monte Carlo program, Monte Carlo xyz (MCxyz) [42], is used which uses a 3D Cartesian grid of voxels to save maps of optical absorption and fluence. MCxyz is capable of defining tissue types with a unique set of optical properties (absorption coefficient  $\mu_a[\text{cm}^{-1}]$ , scattering coefficient  $\mu_s[\text{cm}^{-1}]$ , anisotropy of scattering  $g$  and refractive index  $n$ ) appropriate for a given wavelength of light, and can simulate different illumination profiles (e.g. uniform beam, Gaussian, focused, isotropic point source etc.).

## 2.9 Photoacoustic simulations

In this thesis, the generation of time-resolved PA waves is simulated by calculating the velocity potential generated from 3D maps of absorbed optical energy density, or energy deposition, produced by MCxyz [43,44]. The negative of the velocity potential,  $-\Phi_v(t)$ , recorded by a detector at a given position is calculated by implementing equation 2.15 as

$$-\Phi_v(t) = \frac{\beta}{4\pi\rho C_p} \frac{1}{dt} \int_{r-dr/2}^{r+dr/2} \frac{A_{shell}}{r} 4\pi r^2 dr, \quad 2.36$$

where  $A_{shell}$  is a spherical shell of absorbed energy with radius  $r = v_s t$  and thickness  $dr$  centred on the detector position. At each timepoint after the initial deposition of optical energy, each voxel in  $A_{shell}$  emits a stress wave that arrives at the detector at a time  $t$  later (assuming a constant  $v_s$ ). The contribution of each voxel of energy deposition to  $-\Phi_v(t)$  is accounted for by integrating  $A_{shell}$  in equation 2.33. The detector is modelled as a Lambertian detector, i.e. its sensitivity to acoustic waves is proportional to the cosine of the detection angle, which mimics the behaviour of a piezo detector lying flat on the tissue surface. This is achieved by calculating the cosine of the detection angle for each voxel and multiplying it by the corresponding voxel in  $A_{shell}$ . The time-resolved PA pressure  $p(t)$  [Pa per J delivered] is calculated from  $-\Phi_v(t)$  with

$$p(t) = -\rho \frac{d\Phi_v(t)}{dt}. \quad 2.37$$

An example of a coupled MC-PA simulation is shown in figure 2.8. Figure 2.8 (a) shows the tissue model, consisting of a 1 cm diameter blood vessel in a homogenous layer of fat centred at a depth of 1.5 cm from the tissue surface. A MC simulation of the distribution of absorbed energy density,  $A(r)$  [ $\text{W}/\text{cm}^3$  per W delivered], at 800 nm, is shown in panel (b). Panels (c) and (d) show the measured velocity potential and PA pressure recorded by the detector shown on the tissue surface in panels (a) and (b). The time-resolved negative of the velocity potential (which evaluates as a positive quantity) in panel (c) initially increases and then decreases as a progressively larger radius  $A_{shell}$  is integrated at each timepoint and mainly follows the distribution of  $A(r)$  in the  $+z$  direction due to the cosine dependence of the detector. The sudden increase of  $-\Phi_v(t)$  at  $\approx 6.5 \mu\text{s}$  occurs as the shell of integration encounters the highly absorbing blood vessel, which then begins to decrease exponentially from its maximum value as the

magnitude of  $A(r)$  inside the blood vessel decreases due to optical attenuation. The PA pressure in panel (d) is calculated by taking the time derivative of the velocity potential in panel (c). The initial increase in PA signal amplitude from the blood vessel at can be seen at  $\approx 6.5 \mu\text{s}$ , which is proportional to its absorption coefficient. The familiar bipolar shape of the PA waveform can be observed; however, the negative peak is reduced relative to the positive peak due to optical and acoustic attenuation. To obtain PA spectra, multiple MC-PA simulations can be run at different wavelengths.

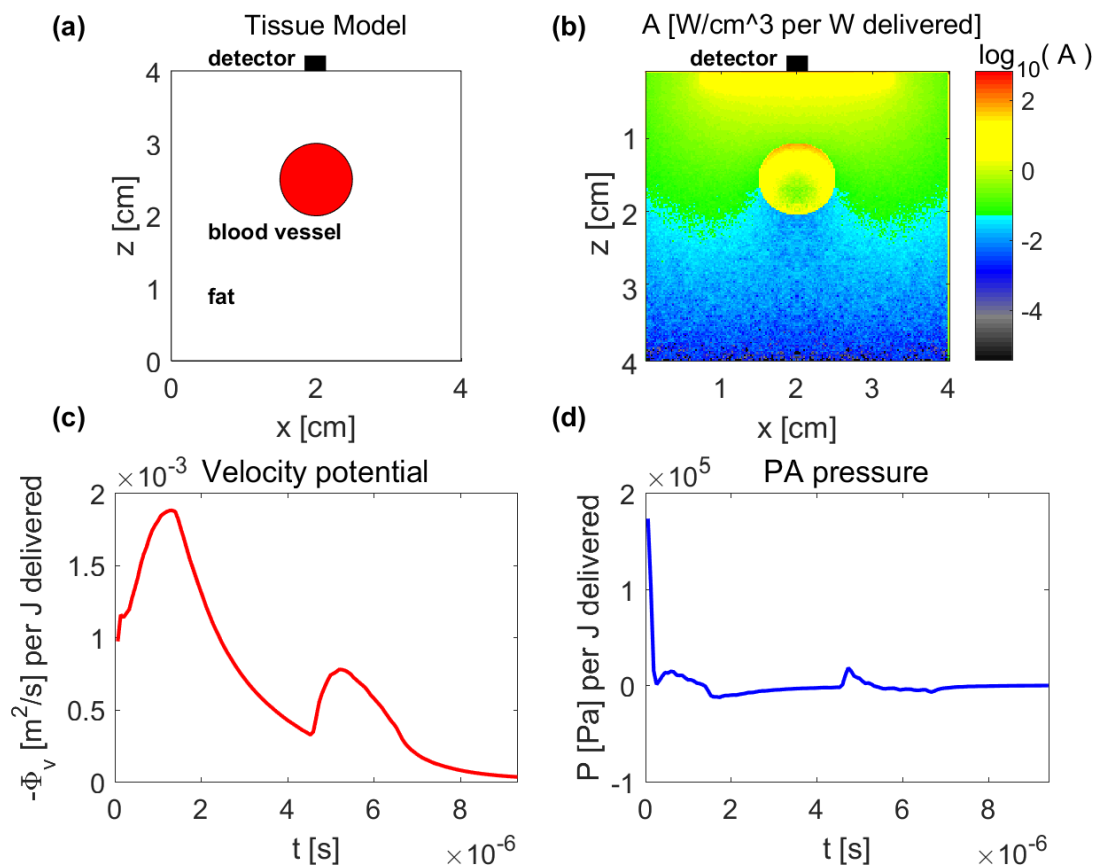


**Figure 2.8.** Example of a coupled MC-PA simulation. (a) Tissue model consisting of a 1 cm diameter blood vessel in a layer of fat centred at a depth of 1.5 cm. (b) MC simulation of optical energy deposition from wide-beam laser source at 800 nm. (c) Velocity potential recorded by detector shown in (a) and (b). (d) PA pressure recorded by detector shown in (a) and (b).

The effects of acoustic attenuation on  $p(t)$  and  $-\Phi_v(t)$  are accounted for using equation 2.18. Figure 2.9 shows the effect of acoustic attenuation on the PA signal amplitude for an acoustic attenuation coefficient of 0.75 dB/cm/MHz, showing that the PA signal amplitude falls by approximately 50% for a tissue depth of 1 cm.

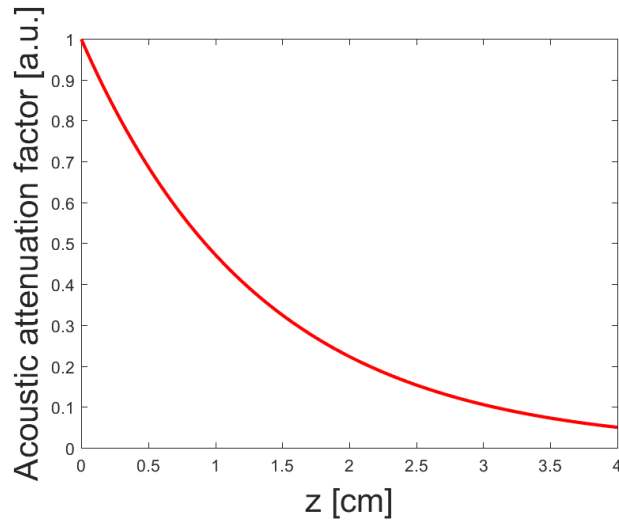


**Figure 2.9.** Acoustic attenuation factor with depth for an acoustic attenuation coefficient of 0.75 dB/cm/MHz.

### ***2.10 Vevo LAZR PAI system.***

The PA imaging system used throughout this thesis was the Vevo® LAZR PA imaging system [45–47] (VisualSonics Inc.), the schematic of which is shown in figure 2.10. The system employed a linear-array PA probe design containing 256 acoustic transducer elements with a given central detection frequency. Two such probes with either a 21 MHz or 40 MHz central frequency were used, depending on the application. The 21 MHz probe had a bandwidth of 52.4% and a transducer element area of 3 mm x 23.4 mm, while the 40 MHz probe had a bandwidth of 55% and a transducer element area of 3 mm x 14 mm. The spatial resolution of each probe was 165  $\mu\text{m}$  and 75  $\mu\text{m}$ , and 90  $\mu\text{m}$  and 44  $\mu\text{m}$ , for the lateral and axial resolutions, for the 21 MHz and 40 MHz probes, respectively.

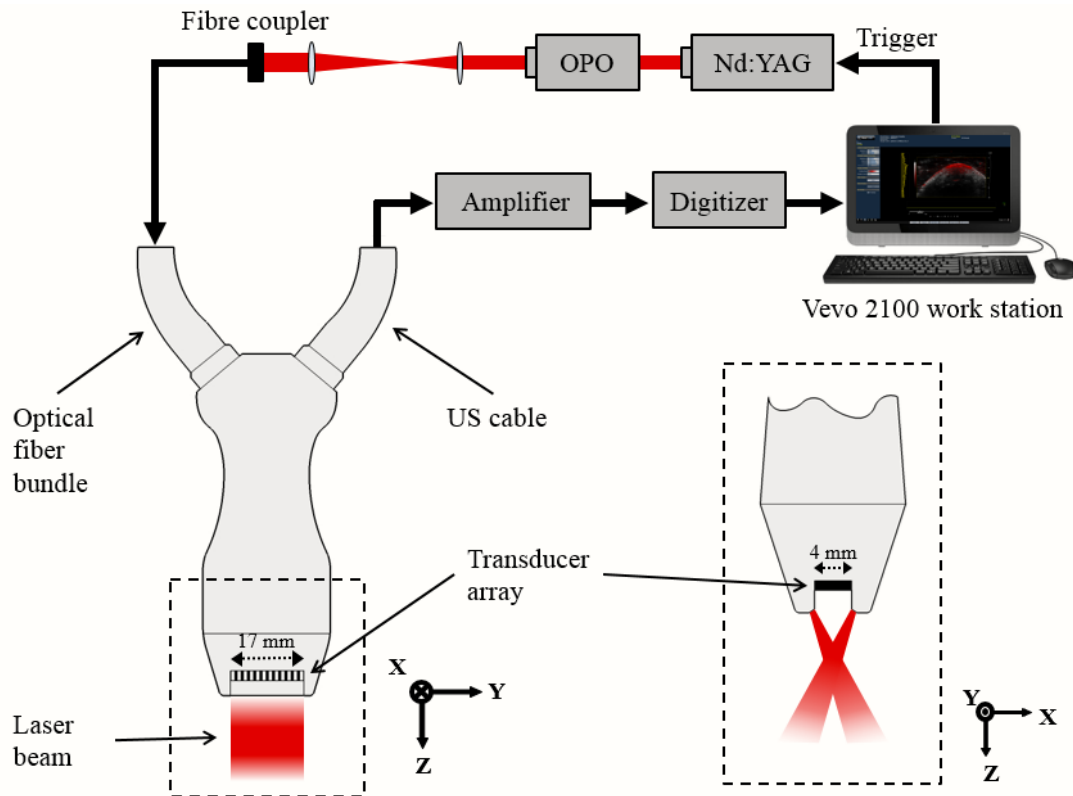


**Figure 2.10.** (Left) Schematic of PA system showing laser source, signal processing procedure, and linear-array PA probe (viewed from elevational direction). (Right) View of the PA probe head (enclosed by dashed box on left) showing crossed laser beam geometry (lateral direction).

Pulsed laser light was delivered through two planar light bars situated on either side of the transducer array, as shown in figure 2.10. The beam focal distance was 7 mm and the beam angle was  $30^\circ$  with respect to the imaging plane for both the 21 MHz and 40 MHz probes, respectively. Figure 2.11 shows an example of the 21 MHz probe illuminating a scattering medium, showing diffusion of the light beam. The laser-source setup is shown in figure 2.12, which consisted of a flashlamp pumped Q-switched ND:YAG laser (20 Hz repetition rate) operating at 1064 nm directed into a second-harmonic generator (SHG) to produce 532 nm light that was subsequently used to pump an optical parametric oscillator (OPO, Opotek Inc.), tunable in the wavelength range of 680-970 nm in steps of 1 nm. The laser light was then coupled to the PA probe with an optical fibre bundle.

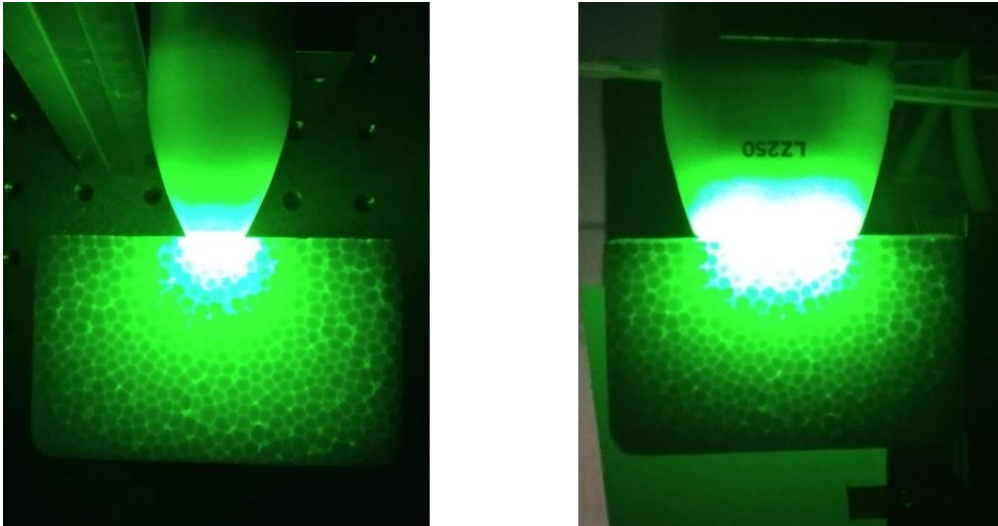


**Figure 2.11.** Photo of the 21 MHz PA probe illuminating a scattering medium (polystyrene insulation) showing diffusion of the light beam in the lateral (left) and elevation (right) directions.

For each laser pulse, the PA signals were captured on a single quadrant of the linear-array consisting of 64 transducer elements. Once all four quadrants were acquired, the full dataset was beamformed to form a PA image using a delay-and-sum back projection algorithm and displayed on an imaging station. Since 4 laser pulses were required to produce a single PA image, the system frame rate was 5 frames per second.

The linear-array probe design allowed for the inherent coregistration of US and PA images that can be displayed in real time, combining the structural imaging capabilities of US with the molecular contrast of PA imaging. To generate 3D images, the linear-array probe was translated across a stepper motor at a given step size to acquire 2D images which can be combined to give a 3D volume. To ensure coupling to the PA probe to the tissue surface, either US gel or water was used as the coupling medium, depending on the application.

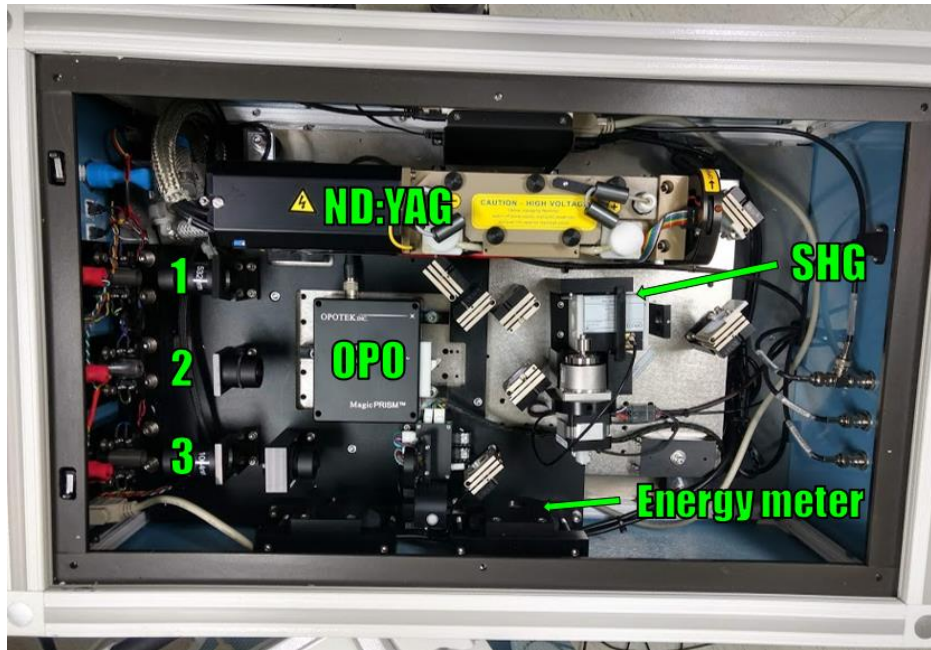


**Figure 2.12.** Laser-source setup, consisting of a flashlamp pumped Q-switched ND:YAG laser operating at 1064 nm directed into the SHG where 532 nm light was produced via frequency doubling. The SHG output was then used to pump the OPO which was tunable in the wavelength range of 680-970 nm. The laser power was measured with an energy meter to ensure the laser energy pulse did not exceed the ANSI standard of 20 mJ/cm<sup>2</sup>. The laser output ports, marked 1, 2, 3, provided 1064 nm light for port 1, the OPO output for port 2, and green 532 nm light for port 3. The laser output source could be changed by manually coupling the probe fibre optical cable to either port. The system configuration allowed for spectroscopic scans to be taken across the OPO output range in steps of 1 nm.

## **Chapter 3: Fluence-corrected venous blood oxygen saturation measurement using arterial fluence calibration.**

### ***3.1 Importance of blood oxygenation measurements: motivation***

Measurement of blood oxygen saturation provides an important physiological indicator of cardiovascular function and the efficiency of the oxygen delivery system. Ensuring an adequate supply of oxygen to the tissues and organs is vital to ensure their function, as hypoxia, the deprivation of an adequate supply of oxygen to biological tissues, can cause irreversible damage to the highly aerobic tissues of the brain and heart in a matter of minutes, which can result in cardiac arrest, brain damage, and death [48–51].

In the human body, blood is circulated via the circulatory system (figure 3.1), carrying oxygen and nutrients to and waste materials away from the tissues and organs. The haemoglobin molecule is the primary transporter of oxygen in the blood, with around 98.5% of oxygen being chemically bound to haemoglobin in arterial blood [52], with the remainder being dissolved in the other blood liquids. Haemoglobin is contained in the red blood cells (erythrocytes), and accounts for 96% of red blood cells dry content and around 35% of total blood content (including water) [53]. Each haemoglobin molecule is capable of binding up to four oxygen molecules ( $O_2$ ) to its heme receptors [50]. When haemoglobin is fully bound with oxygen, it is known as oxyhaemoglobin, and when it is fully unbound it is known as deoxyhaemoglobin. Oxyhaemoglobin is formed in the pulmonary capillaries in the alveoli of the lungs during respiration. The oxygen is transported through the blood stream to the tissues where it is used to fuel metabolism in cells. The capillaries are the primary site of oxygen and nutrient transfer to the cells, where they can diffuse through the thin vessel walls to the surrounding interstitial fluid and subsequently to the intracellular space where they are utilised in metabolism, primarily in the cellular mitochondria [54]. Afterwards, the by-products of cellular metabolism (carbon dioxide, lactic acid, urea etc.) are removed by the capillaries in the same process. As a result, each cell must be located within 100  $\mu m$  of a given capillary to survive, a distance known as the oxygen diffusion limit [55].

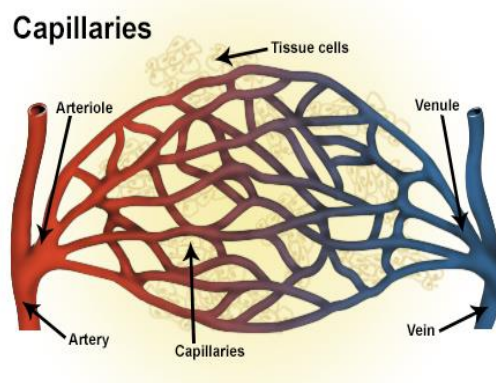


**Figure 3.1.** Blood vessels of the microcirculation. Arterioles extend out from arteries and transition to capillaries. The capillaries convey blood from the arterioles to the venules and are the smallest blood vessels in the body (diameter  $\approx 5\text{-}10\ \mu\text{m}$ ), with vessel walls that are one endothelial cell thick. The thin walls and small diameter of capillaries allow for the exchange of nutrients such as oxygen, water, and glucose, and waste products such as carbon dioxide, with the surrounding interstitial fluid. Cells are typically located within  $100\ \mu\text{m}$  from a capillary, a distance known as the oxygen diffusion limit [55]. The capillary beds then drain into venules and then to veins.

Blood oxygen saturation,  $sO_2$ , is defined as the percentage ratio of oxygen saturated haemoglobin to total haemoglobin (oxyhaemoglobin + deoxyhaemoglobin) in the blood. The human body regulates  $sO_2$  at a very precise level, depending on metabolic activity. Normal arterial oxygen saturation,  $sO_2^A$ , is in the range of 95%-100% [48]. If it falls below 90% it is considered dangerous and can lead to hypoxaemia (insufficient oxygen in arterial blood). If  $sO_2^A$  falls below 80% it can result in serious complications to the heart and brain function that can lead to cardiac or respiratory arrest.  $sO_2^A$  is widely assessed clinically using pulse oximetry [56–58] (figure 3.2). Pulse oximetry is a NIR spectroscopy technique that employs time-gated measurements to distinguish the pulsatile signal from arteries to make  $sO_2^A$  measurements. The main drawback of pulse oximetry is that it is a single point measurement that is only sensitive to arterial blood and lacks spatial resolution. However, it remains the most clinically used method due to its portability and ease of measurement.

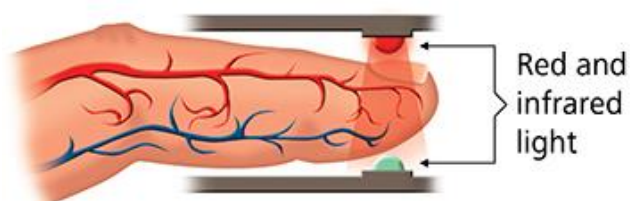


**Figure 3.2.** Schematic of a pulse oximeter. The pulse oximeter revolutionised modern medicine with its ability to noninvasively and transcutaneously measure  $sO_2^A$ . Pulse oximetry is a NIR spectroscopic technique that takes advantage of the spectrally distinct absorption profiles of oxy- and deoxyhaemoglobin to quantify  $sO_2^A$ . Pulse oximeters employ a pair of small light-emitting diodes (LEDs) facing a photo sensor through a translucent part of the patient's body, usually a fingertip or earlobe. The wavelength pair of 660 nm and 940 nm is typically used as the optical absorption difference between oxy- and deoxyhaemoglobin differs significantly at these wavelengths. The sensitivity of pulse oximetry to arterial blood only is based on photoplethysmography (PPG) - the principle that the degree of optical absorption varies due to the cardiac induced changes in blood volume. The arterial blood volume reaches a maximum during systole and reaches a minimum during diastole. In contrast, the blood volume in the capillary beds, veins, and surrounding tissues remains relatively constant. This allows the time-varying portion of the detected signal to be isolated, allowing the oxygenation level of the arterial compartment to be quantified.

Hypoxia [59] is a condition in which biological tissue is deprived of a sufficient supply of oxygen and can be classified as general or local. Hypoxia can result from a variety of conditions which limit the delivery of oxygen to the cells. This can be caused by a decrease in the partial pressure of oxygen (limiting the oxygen-binding ability of haemoglobin), problems with breathing rhythm and oxygen diffusion, deficiency in the availability of haemoglobin, and blood flow problems in the peripheral tissues. Ischemia [60], a restriction of blood flow to a tissue, can also cause hypoxia, which is known as ischemic hypoxia, and can be caused by an embolic event, a myocardial infarction that causes a reduction in blood flow, or trauma to the tissue that results in damage.

Measurement of the oxygenation level in blood and tissue is of major importance for the diagnosis and management of many life-threatening illnesses such as cancer, peripheral vascular disease, sepsis, and shock.

Cerebral oxygenation monitoring is of vital importance during neurosurgery as the brain relies on a carefully regulated and continuous supply of oxygen to maintain its function. If cerebral oxygen supply is sufficiently compromised, loss of consciousness can occur within seconds and serious neuronal damage can result in as little as 3-4 minutes [61]. A reduction in tissue oxygenation is indicative of diseased states such as cerebral ischemia, hypoxia, and brain tumours. Cerebral oxygenation measurements can be used to monitor neuronal function and brain haemodynamics in response to external stimuli. In intensive care patients with traumatic brain injuries, monitoring of cerebral haemodynamics and venous blood oxygenation is used

to detect and minimise additional brain injuries due to secondary mechanisms such as cerebral ischemia, cerebral oedema, hypoxemia, and hypotension [62].

Knowledge of  $sO_2^A$  and venous blood oxygen saturation,  $sO_2^V$ , in the same biological system provides a measure of tissue oxygen extraction [63], which can determine metabolic rate and monitor haemodynamic changes. Oxygen extraction can be monitored on a whole-body or peripheral level. Peripheral venous oxygenation measurements have clinical and physiological significance as lower  $sO_2^V$  values can indicate ischemia, where a reduction in blood flow results in a higher utilisation of oxygen in the body, or circulatory system dysfunction. The monitoring of oxygen consumption in the limbs and extremities provides information on the adequacy of local blood perfusion and can aid in establishing the severity of shock or cardiac failure, in which blood flow is diverted from the peripheral tissues to more vital organs.

Cerebral oxygen consumption or extraction [63–66] is defined as the difference between the measured cerebral venous and arterial oxygen saturations and is a vital parameter for monitoring brain tissue health during neurosurgery and for managing intensive care patients at risk from neurological collapse. The conventional (and gold standard) method for measurement of global cerebral  $sO_2^V$  is central venous catheterisation [65–69], requiring the insertion of a catheter into the jugular bulb of the internal jugular vein. Continuous monitoring of cerebral  $sO_2^V$  allows for the detection of a drop in blood oxygen level that can worsen clinical outcomes.  $sO_2^V$  values that drop below 50% require immediate medical intervention and are associated with a poor prognosis in traumatic brain injury patients and can result in secondary brain insult, permanent disability, and death. Although central venous catheterisation provides valuable information that guides treatment, it is a highly invasive procedure that carries considerable risk, such as bleeding, carotid artery puncture, and infection. As a result, cerebral  $sO_2^V$  is frequently not monitored. In contrast to the routine use and ease of pulse oximetry to monitor arterial blood oxygenation, no accepted method for noninvasively monitoring  $sO_2^V$  is currently available [70].

Tissue oxygenation measurements can be used for the detection of cancerous tumours through the detection of hypoxia [71–76] and an increase in haemoglobin concentration associated with pathological angiogenesis [77–80]. Angiogenesis is the physiological process through which new vasculature is formed and is a vital and normal process in biological growth and development. However, it is also a fundamental mechanism in the growth of tumours and in their transition from a benign state to a malignant one. Tumours depend on a functioning

vascular system to provide oxygen and other essential nutrients. Blood vessel growth in tumours derives from an abnormal increase in the secretion of pro-angiogenic growth factors and proteins from tumour cells. The resulting vasculature is highly chaotic and disorganised, giving rise to a heterogenous delivery of oxygen and nutrients due to variations in blood perfusion level and oxygen consumption, resulting in avascular regions leading to hypoxia. A major driving force behind the development of noninvasive optical imaging technologies using endogenous contrast for cancer detection has been the observed local increase in haemoglobin concentration in malignant tumours, which results in an estimated 4-fold increase in imaging contrast compared with normal tissues [81].

Hypoxia has been found to adversely affect the effectiveness of cancer treatment with radio and chemotherapy [72,82–84]. Breast malignancies have been shown to have a lower median  $sO_2$  level than the healthy breast, and tumour oxygenation levels have been shown to be an indicator of the effectiveness of neoadjuvant chemotherapy [85–88]. Numerous studies have linked tumour oxygenation levels to tumour characteristics. The extent of hypoxia has been linked with tumour aggressiveness and potential to metastasise [89–92]. These findings demonstrate that *a priori* knowledge of tumour oxygenation status can provide important information for diagnostic and therapeutic decision making.

Monitoring for hypoxia in peripheral tissues is also critical for the management of peripheral vascular disease [93–96], which commonly occurs as a result of diabetes mellitus and hypertension, as hypoxia can lead to severe limb dysfunction and necrosis and eventual amputation of the limb [97,98]. In addition, noninvasive measurements of tissue oxygenation level could yield important information to guide treatment and predict the extent of surgery or amputation required.

### ***3.2 Currently available techniques for measuring blood oxygenation***

Due its importance, various imaging technologies have been employed to noninvasively measure tissue oxygenation level, with each having their own advantages and disadvantages.

Diffuse optical methods like near infrared spectroscopy (NIRS) [99,100] and diffuse optical tomography (DOT) [81,101,102] measure diffusely reflected light at multiple wavelengths and

calculate relative haemoglobin concentration using the well-established differences between the specific optical absorption profiles of oxy- and deoxyhaemoglobin (figure 2.2) in the NIR spectral region. However, while they both provide high endogenous optical contrast, the spatial resolution of NIRS and DOT is severely degraded owing to the strong optical scattering in biological tissues. The poor spatial resolution of diffuse optical methods thus limits their potential applications for measuring dynamic and functional parameters of biological tissue, e.g. differentiating heterogeneities in tumour oxygenation.

Magnetic resonance imaging (MRI) has been used to measure tissue oxygenation through the blood oxygen level-dependent (BOLD) effect [103–106], which takes advantage of the fact that the change from diamagnetic oxyhaemoglobin to paramagnetic deoxyhaemoglobin that takes place with neuronal activation results in a decreased intensity of the magnetic resonance signal. BOLD MRI is preferred over other functional MRI techniques as no intravenous contrast medium is required. While BOLD MRI can achieve high spatial resolution (approaching  $1 \text{ mm}^3$ ), it is only sensitive to deoxyhaemoglobin (giving only relative assessments of  $sO_2$ ) and struggles to distinguish between haemodynamic changes and changes in oxygenation level. Its poor signal-to-noise ratio (SNR) also limits its sensitivity. Both of these factors limit its application for longitudinal studies which track changes in oxygenation status in tissue e.g. in cancerous tumours before and after treatment.

Positron emission tomography (PET) [107–109] and single photon emission computed tomography (SPECT) [110–112] can also quantify oxygenation level, however, they require the use of exogenous contrast agents. PET and SPECT are nuclear medicine functional imaging techniques that detect gamma rays emitted from ionising radioligands injected intravenously on a biologically active radioactive tracer. The radiotracer is carried throughout the body by the vasculature system where it accumulates in a targeted tissue. The resulting radioactive isotope decay in the ligand can then be detected by the PET and SPECT sensors. Diagnostic and functional information can be obtained through the selection of an appropriate tracer whose properties can be tuned to bind it to a certain type of tissue, e.g. malignant tumour detection is possible through the use of radiopharmaceuticals that bind to cancer cells, where the higher ligand concentration is detected. Tumour hypoxia can be similarly detected by imaging the increased uptake of radioactive exogenous hypoxic biomarkers, which are sensitive to tissue hypoxia at the cellular level. Additionally, tracers targeted to  $O_2$  and  $CO_2$  can be used to estimate tissue oxygen extraction. PET and SPECT image quality is therefore dependent on the efficiency of the local vascular system to deliver an adequate concentration of tracer, which

can be inadequate in malignant tumours due to the abnormal vasculature microenvironment. Moreover, the maximum permissible radiation dose restricts the amount of radioactive tracer that can be administered. Additional drawbacks include the limited spatial resolution offered by these modalities, high scan time, and cost.

Electron paramagnetic resonance imaging [113–116] (EPRI) can provide quantitative images of  $sO_2$ . EPRI is analogous to MRI in that images are formed with the application of gradient magnetic fields; however, it is electron spins in molecules with unpaired electrons that are excited rather than the spins of atomic nuclei. Tissue oxygenation can be measured with the use of specially designed reagents, or spin probes, that bind to molecular oxygen. The generated EPRI spectra can then give information about the tissue oxygenation level. Since radicals do not naturally occur in high concentrations in biology, potentially toxic free-radical contrast agents are required. EPRI holds potential for spatially resolving hypoxic regions in tumours and studying vascular conditions, however, it offers limited spatial resolution.

### ***3.3 Quantification blood oxygen saturation with PA imaging***

Multiwavelength PAI can extract functional information from tissue and quantify chromophore concentrations [117–120]. The functional measurement capability allows PAI to measure  $sO_2$ , oxygen consumption, monitor for diseased states such as hypoxia and anaemia, and to detect cancerous tumours through the detection of hypoxia associated with abnormal vascular growth.

The PA signal amplitude is proportional to the absorption coefficient of blood, which is in turn sensitive to the concentrations of oxy- and deoxyhaemoglobin (equation 2.24). By monitoring at two or more optical wavelengths,  $sO_2$  and total haemoglobin concentration can be measured. If quantitative measurements are made in each voxel, PAI can create parametric maps showing the spatial distribution of  $sO_2$  and haemoglobin concentration in tissue, which can show hypoxic regions, as shown in figure 3.3.

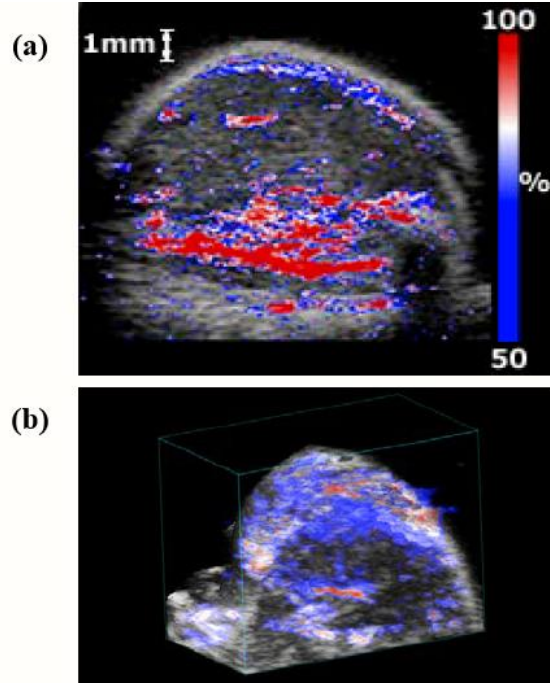


**Figure 3.3.** 2D and 3D parametric  $sO_2$  images. (a) Coupled 2D B-mode US and PA  $sO_2$  scan of a tumour on the hindlimb of a mouse obtained using a linear PA quantification algorithm at two wavelengths (750 and 850 nm). (b) Coupled 3D US and PA  $sO_2$  scan of the tumour volume. Image reproduced from [121] with permission.

The conventional or linear approach for making quantitative measurements of  $sO_2$  assumes that the received PA signal  $S(\lambda, \mathbf{r})$  at wavelength  $\lambda$  from a given voxel at position  $\mathbf{r}$  is linearly proportional to the absorption coefficient, i.e., that it is independent of the local optical fluence. This can be expressed as

$$S(\lambda, \mathbf{r}) = K\mu_a(\lambda), \quad 3.1$$

where  $K$  is the system dependent response, which depends on the detector sensitivity and geometry, the incident fluence, acoustic attenuation, and  $\Gamma$ . Assuming that blood is the dominant absorbing compound in the wavelength range under study, equation 3.1 can be written in terms of the haemoglobin concentrations  $c_{HbO_2}$  and  $c_{Hb}$  as

$$S(\lambda, \mathbf{r}) = K(\varepsilon_{HbO_2}(\lambda)c_{HbO_2} + \varepsilon_{Hb}(\lambda)c_{Hb}). \quad 3.2$$

If scans are taken at multiple wavelengths, a system of linear equations is obtained that can be solved by the method of linear least squares as

$$\begin{bmatrix} c_{HbO_2} \\ c_{Hb} \end{bmatrix} = (M^T M)^{-1} M^T \Phi(\lambda, \mathbf{r}), \quad 3.3$$

where

$$M = \begin{bmatrix} \varepsilon_{HbO_2}(\lambda_1) & \varepsilon_{Hb}(\lambda_1) \\ \cdot & \cdot \\ \cdot & \cdot \\ \cdot & \cdot \\ \varepsilon_{HbO_2}(\lambda_n) & \varepsilon_{Hb}(\lambda_n) \end{bmatrix} \text{ and } \Phi(\lambda, \mathbf{r}) = \begin{bmatrix} S(\lambda_1, \mathbf{r}) \\ \cdot \\ \cdot \\ \cdot \\ S(\lambda_n) \end{bmatrix}, \quad 3.3$$

&  
3.4

and  $n$  is the number of wavelengths measured at.  $sO_2$  can be solved for by inserting the determined values of  $c_{HbO_2}$  and  $c_{Hb}$  into equation 2.22.

The main limitation of equation 3.2 is that it assumes that the local optical fluence remains constant over  $\lambda$ , a condition that is unrealistic in biological tissues. In reality, the local optical fluence is nonlinear and varies according to the wavelength-dependent optical attenuation that occurs as the light propagates through tissue. The degree of optical attenuation is dependent on the concentration of absorbers and scatterers and on the pathlength the light travels. Therefore, in order to accurately quantify  $sO_2$ , wavelength-dependent variations in local optical fluence must be accounted for.

Accounting for heterogeneities in optical fluence at the measuring site is a longstanding problem in quantitative PAI [122]. Many methods of correcting for optical fluence variations have been proposed, with each having various advantages and disadvantages. However, none have been adopted as a standard technique.

The most common method involves constructing a PA forward model that relates the measured PA amplitude spectrum,  $S(\lambda, \mathbf{r})$ , to a theoretical PA model that incorporates a model of optical transport describing the fluence distribution,  $\phi(\lambda, \mathbf{r})$ , as

$$S(\lambda, \mathbf{r}) = K\mu_a(\lambda, \mathbf{r})\phi(\lambda, \mathbf{r}), \quad 3.5$$

where  $\mu_a(\lambda, \mathbf{r})$  is the absorption coefficient at the voxel at position  $\mathbf{r}$ .  $\phi(\lambda, \mathbf{r})$  estimates the local optical fluence in a multilayer or homogenous tissue, depending on the model used. It is expressed in terms of the optical properties of the surrounding media and accounts for the wavelength-dependent optical attenuation effects encountered as the light travels. The forward model is inverted and the right-hand-side of equation 3.5 is iteratively fitted to the left-hand-side by varying the model input parameters until the differences between the model and the

measured data are minimised. The values of the fitted parameters that correspond to the best fit are then assumed to be the “true” values. The model input parameters can include the concentrations of absorbing chromophores in the surrounding tissues (e.g. oxy- and deoxyhaemoglobin, melanin etc.), scattering scaling factors, and  $K$ . In many cases, the scattering properties of the tissue are assumed *a priori* before minimisation. After minimisation,  $\phi(\lambda, \mathbf{r})$  is assumed to be accounted for and fluence-corrected measurements of  $sO_2$  can be made.

Many different optical transport models have been used to account for wavelength dependent changes in the local fluence at the measuring site. Maslov *et al* [123] and Zhang *et al* [124] employed a 1D modified form of the Beer–Lambert law based on optical diffusion to account for fluence attenuation effects in a multilayer rat skin model *in vivo*. The model was iteratively fitted to the PA amplitude spectrum of a spectrally neutral black film inserted underneath the rat skin to yield the blood volume fraction and  $sO_2$  in the dermis. The fitted parameters were then used in the same model to make fluence corrected measurements of  $sO_2$  in arteries and veins at other imaging sites. However, since this method relies on an invasive procedure to optically characterise the skin, it is not desirable. Kim *et al* [125] also used the same optical model on mice, however, the optical properties were assumed *a priori* from literature data, which is not practical as optical properties vary from animal to animal and depend on melanosome concentration, blood concentration (perfusion level), and oxygenation level. Laufer *et al* [126] employed a similar 1D model that incorporated the so-called delta-Eddington approximation of the diffusion equation that increases the model accuracy close to the tissue surface to measure  $sO_2$  on *in vitro* blood samples with high accuracy.

Laufer *et al* [127,128] also employed a more comprehensive 2D finite element method (FEM) diffusion-based model to simulate optical transport in a scattering and absorbing media. The optical model was coupled with a time-domain acoustic model based on equation 2.13 that simulated the PA signal generation from the absorbed energy distribution. The forward model was then inverted and iteratively fitted to experimental PA measurements to recover absolute chromophore concentrations in a tissue phantom composed of a mixture of chromophores in tubes suspended in a homogenous scattering medium. The target geometry used in the FEM grid space was obtained beforehand from the locations of absorbing objects from the reconstructed PA images. The same method was also used in [129] to yield *in vivo* measurements of absolute  $sO_2$  and  $c_{HbT}$  in the digital blood vessels of the human finger, as

well as in the extravascular tissue, which matched reasonably well with literature reported values for same. The main drawback of this method is the considerable computation time (up to 2 hours) required for model inversion, as well as the time taken to setup the spatial geometry of the FEM grid.

So-called calibration-free methods that eliminate optical fluence effects by mathematical cancellation using two wavelengths have also been employed.

Xia *et al* [130] induced a systemic change in the  $sO_2$  in a rat brain model *in vivo* to cancel the fluence dependency on the measured PA signal amplitude at two wavelengths. Changes in the  $sO_2$  state were induced by varying the oxygen level in the inhalation gas. This method assumes that the local fluence at the measuring site is unaffected by the induced  $sO_2$  change, which is unrealistic for systemic  $sO_2$  changes and if the surrounding tissue is highly perfused. Additionally, the requirement of an induced oxygenation change imposes an additional burden.

Guo *et al* [131] used the acoustic frequency spectrum of the detected PA signals from multiple wavelengths to correct for fluence variation effects on  $sO_2$  measurements. Mathematically, based on the system linearity assumption, the received PA signal amplitude spectrum,  $S(\omega, \lambda)$ , can be expressed as

$$S(\omega, \lambda) = \phi(\lambda)O(\omega, \lambda)a(\omega)H(\omega), \quad 3.6$$

where  $\omega$  is the acoustic angular frequency,  $\phi(\lambda)$  is the optical fluence at the target (e.g. a blood vessel) at wavelength  $\lambda$ ,  $O(\omega, \lambda)$  is the “real” frequency spectrum of the target of interest measured with unit fluence,  $a(\omega)$  is the frequency dependent acoustic attenuation, and  $H(\omega)$  is the system dependent response function. For imaging at two wavelengths under the same conditions and with the same imaging system, the last two terms in equation 3.6 can be cancelled, allowing for system dependent and acoustic effects to be eliminated. When using optical-resolution PA microscopy (OR-PAM), in which the incident light is focused onto the imaging point using an objective lens, the method approximates the surface of “large” blood vessels ( $> 30 \mu\text{m}$  in diameter) as roughly flat. The light fluence inside the blood vessel is then described by the Beer–Lambert law for a homogenous optically absorbing medium in which scattering is neglected, and  $\phi_I(t)$  is expressed as

$$\phi_I(t) = \Gamma\mu_a \exp(-\mu_a ct). \quad 3.7$$

For PA signals at two optical wavelengths  $\lambda_1$  and  $\lambda_2$ , the ratio is written as

$$\frac{S_1(\omega, \lambda_1)}{S_2(\omega, \lambda_2)} = \frac{\phi_I(\lambda_1)O_1(\omega, \lambda_1)a(\omega)H(\omega)}{\phi_I(\lambda_2)O_2(\omega, \lambda_2)a(\omega)H(\omega)} = \frac{\phi_I(\lambda_1)\sqrt{(\omega/\mu_{a2})^2 + c^2}}{\phi_I(\lambda_2)\sqrt{(\omega/\mu_{a1})^2 + c^2}} \quad 3.8$$

where  $O(\omega)$  is the Fourier transform of equation 3.7. The right-hand-side of equation 3.8 is then fitted to the ratio of the measured PA frequency spectra on the left-hand-side, and the absorption coefficients  $\mu_{a1}$  and  $\mu_{a2}$  and the fluence ratio  $\phi_I(\lambda_1)/\phi_I(\lambda_2)$  are obtained, from which fluence corrected measurements of  $sO_2$  can be obtained. The main drawback of this method is the assumption that small blood vessels can be approximated as flat surfaces, which is unrealistic in practice. Additionally, it is limited to the penetration depth of OR-PAM.

### ***3.4 Fluence-corrected venous blood oxygen saturation measurement using arterial fluence calibration.***

#### **3.4.1 Method overview**

In this thesis, a method of correcting measured PA spectra for the effects of wavelength-dependent optical fluence attenuation using the method of *arterial fluence calibration* is proposed. The method involves using arteries as an intrinsic optical calibration standard by using the known arterial blood oxygen saturation,  $sO_2^A$ , measured with a pulse oximeter. The measured  $sO_2^A$  value is used to calculate the arterial absorption coefficient,  $\mu_a^A$  (assuming a normal haemoglobin concentration in blood of 150 g/L [18]). With  $\mu_a^A$  known, the arterial fluence spectrum,  $\phi_A(\lambda)$ , can be calculated from the measured arterial PA spectrum,  $S_A(\lambda)$ , by rewriting equation 3.5 as:

$$\phi_A(\lambda) = \frac{S_A(\lambda)}{K\mu_a^A(\lambda)}. \quad 3.9$$

To evaluate  $\phi_A(\lambda)$ , and thus formulate a forward model of arterial fluence, an analytic expression based on the Beer–Lambert law is used. The model, written for a multilayered tissue, composed of an epidermis, dermis, and subcutaneous fat layer, is written as:

$$\begin{aligned} \phi_A(\lambda) = \phi_0(\lambda) \exp \left( -z_E \sqrt{3\mu_a^E(\lambda)(\mu_s'^S(\lambda) + \mu_a^E(\lambda))} \right. \\ \left. - z_D \sqrt{3\mu_a^D(\lambda)(\mu_s'^S(\lambda) + \mu_a^D(\lambda))} - z_F \sqrt{3\mu_a^F(\lambda)(\mu_s'^F(\lambda) + \mu_a^F(\lambda))} \right), \end{aligned} \quad 3.10$$

where  $\phi_0(\lambda)$  is the surface fluence,  $z_E$ ,  $z_D$ , and  $z_F$  are the vertically measured thicknesses, and  $\mu_a^E(\lambda)$ ,  $\mu_a^D(\lambda)$ , and  $\mu_a^F(\lambda)$  are the absorption coefficients, of the epidermis, dermis, and subcutaneous fat, respectively, and  $\mu_s'^S(\lambda)$  and  $\mu_s'^F(\lambda)$  are the reduced scattering coefficients of the skin (averaged epidermis and dermis) and fat, respectively. The absorption coefficients  $\mu_a^E(\lambda)$ ,  $\mu_a^D(\lambda)$ , and  $\mu_a^F(\lambda)$  are given by:

$$\mu_a^E(\lambda) = c_m \cdot \mu_{a.m}(\lambda), \quad 3.11$$

$$\mu_a^D(\lambda) = c_b^D (sO_2^D \cdot \mu_{a.HbO_2}(\lambda) + (1 - sO_2^D) \cdot \mu_{a.Hb}(\lambda)) + c_w^D \cdot \mu_{a.H_2O}(\lambda), \quad 3.12$$

$$\mu_a^F(\lambda) = c_b^F (sO_2^F \cdot \mu_{a.HbO_2}(\lambda) + (1 - sO_2^F) \cdot \mu_{a.Hb}(\lambda)) + c_w^F \cdot \mu_{a.H_2O}(\lambda), \quad 3.13$$

where  $\mu_{a.m}(\lambda)$  and  $c_m$  are the absorption coefficient and volume fraction of melanosome in the epidermis, respectively,  $c_b^D$  and  $c_b^F$  are the blood volume fractions,  $sO_2^D$  and  $sO_2^F$  are the blood oxygen saturations, and  $c_w^D$  and  $c_w^F$  are the water volume fractions, in the dermis and fat layers, respectively, and  $\mu_{a.HbO_2}(\lambda)$ ,  $\mu_{a.Hb}(\lambda)$  and  $\mu_{a.H_2O}(\lambda)$  are the absorption coefficients of oxy- and deoxyhaemoglobin, and water, respectively. The reduced scattering coefficients, in the *in vivo* case,  $\mu_s'^S(\lambda)$  and  $\mu_s'^F(\lambda)$ , are given by the following empirical formulas [34]:

$$\mu_s'^S(\lambda) = 1.1 \times 10^{12} \lambda^{-4} + 73.7^{-0.22}, \quad 3.14$$

$$\mu_s'^F(\lambda) = 1050.6 \lambda^{-0.68}. \quad 3.15$$

Although simplified, the optical model in equation 6 has been shown to give a reasonable approximation for optical fluence in multilayered tissues in *in vivo* and phantom experiments at depths greater than a few optical mean free paths ( $\sim 1$  mm) [2,123–126]. To implement the arterial fluence calibration procedure, equation 3.10 is iteratively fitted to the right-hand side of equation 3.9 by varying the model input parameters,  $K$ ,  $c_m$ ,  $c_b^D$ ,  $sO_2^D$ ,  $c_b^F$ , and  $sO_2^F$ , until the following least squared error is minimised:

$$\sum_N \left( \frac{S_A(\lambda)}{K\mu_a^A(\lambda)} - \phi_A(\lambda, K, c_m, c_b^D, sO_2^D, c_b^F, sO_2^F) \right)^2, \quad 3.16$$

where  $N$  is the number of measurement wavelengths. The uncertainty of the fitted parameters is given by:

$$u_p = \sqrt{\text{var}(X)} = (H^T H)^{-1} \sigma_{p-p}^2, \quad 3.17$$

where  $X$  is a vector of the model input parameters,  $\text{var}$  is the variance,  $H$  is the sensitivity matrix, which is composed of the derivative of the model with respect to the input parameters, and  $\sigma_{p-p}^2$  is the standard deviation of the peak-to-peak PA signal variation, taken from multiple measurements [127,128].

With the values of  $K$ ,  $c_m$ ,  $c_b^D$ ,  $sO_2^D$ ,  $c_b^F$ , and  $sO_2^F$  determined, the fluence model  $\phi_A(\lambda)$  is assumed to be calibrated, allowing for the fluence spectra to be evaluated at other tissue locations (with the model being updated for any changes in the values of  $z_E$ ,  $z_D$ , and  $z_F$  that occur), and used to correct measured PA spectra for the effects of spectral fluence attenuation. In this thesis, the calibrated arterial fluence model is used to correct the measured PA spectra from targeted subcutaneous veins,  $S_V(\lambda)$ , to make fluence-corrected measurements of venous blood oxygen saturation,  $sO_2^V$ . The measured venous PA signal is given by

$$S_V(\lambda) = K \mu_a^V(\lambda) \phi_A(\lambda), \quad 3.18$$

where  $\mu_a^V(\lambda)$  is the venous absorption coefficient (given by equation 2.21).  $S_V(\lambda)$  is divided by  $\phi_A(\lambda)$  to correct for spectral fluence variations and fitted to  $\mu_a^V(\lambda)$  to yield concentrations of venous oxy- and deoxyhaemoglobin,  $c_{HbO_2}$  and  $c_{Hb}$ . Fluence-corrected  $sO_2^V$  is then calculated using equation 2.22.

When calibrating  $\phi_A(\lambda)$ , the distance between the target artery and the vein where  $sO_2^V$  is measured should be kept to a minimum to ensure similar values of  $c_m$ ,  $c_b^D$ ,  $sO_2^D$ ,  $c_b^F$ , and  $sO_2^F$  between measurement sites. Arteries can be distinguished from veins on time-resolved PA images by observation of the arterial pulse. Moreover, since arterial oxygenation level is largely systemic owing to capillaries being the primary site of oxygen diffusion to the tissues and cells, any artery or arteriole that can be resolved on a PA image can potentially be used for calibration.

In this thesis, the proposed method is tested using coupled MC and PA simulations, on tissue-mimicking phantoms, and *in vivo* on the vasculature in the human forearm. The fluence-corrected  $sO_2^V$  are compared with the known values and the values determined using the linear

method. The error in the determined parameters is given by the fractional difference between the determined values and the known values.

## ***3.5 Methodology***

### **3.5.1 Coupled MC-PA simulations**

To initially test the proposed method on a well-controlled data set, coupled MC-PA simulations were carried out. Two tissue models were used, a singlelayer model and a multilayer model, each containing a vein and artery running parallel to the tissue surface. The structure of each model is shown in figure 3.4. The singlelayer model consisted of a vein and artery in a homogenous layer of fat, and the multilayered model consisted of a vein and artery in a multilayered tissue composed of an epidermis, dermis, and subcutaneous fat layer. The dimensions of both models were 2.8 cm × 2.8 cm × 1.4 cm in the x, y, and z directions, respectively, and the bin size was 0.01 cm, giving 10,976,000 bins in total. The epidermis and dermis thicknesses were 0.02 cm 0.2 cm, respectively. The blood vessels were centred at a depth of 0.6 cm and the vessel diameters were 0.3 cm for both tissue models. The blood vessel diameters were given a relatively large value to reduce discretisation errors associated with cubic voxels which resulted in unnecessary noise on the generated PA signals. The optical absorption and reduced scattering coefficients for each tissue type are shown in figure 3.5 (a) and (b), respectively, while the values of  $c_m$ ,  $c_b^D$ ,  $sO_2^D$ ,  $c_b^F$ , and  $sO_2^F$ , used in the tissue layers, are given in table 3.1.

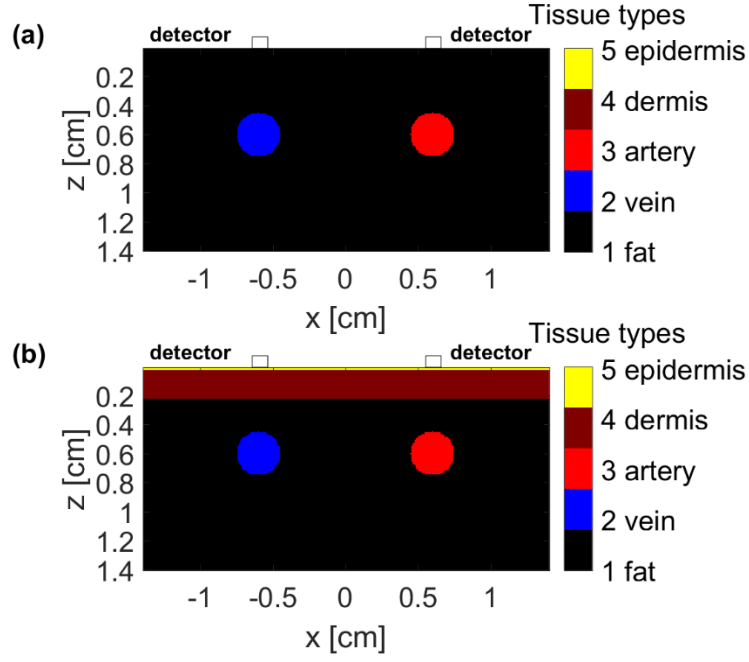


**Figure 3.4.** Tissue models used in MC-PA simulations, showing (a) the singlelayer model and (b) the multilayer model in the  $xz$  plane ( $y=0$ ). Time resolved PA signals were recorded from point detectors placed on the surface of each model directly above the center of the vein and artery, respectively.

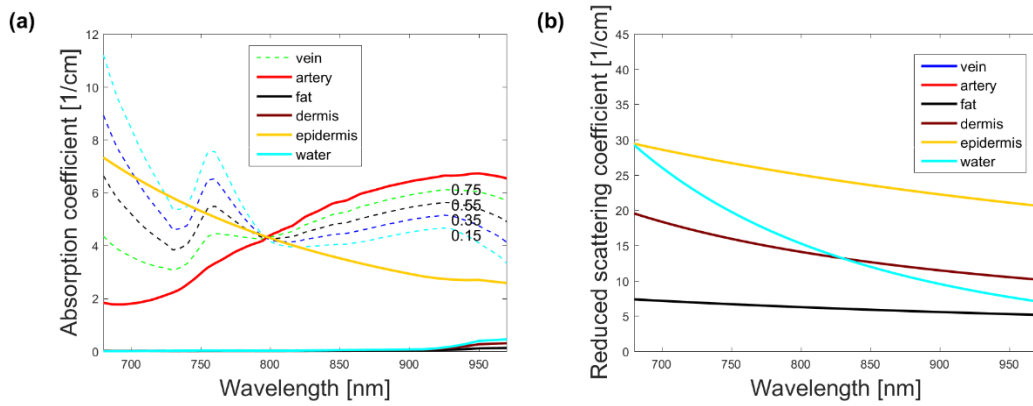


**Figure 3.5.** (a) Optical absorption and (b) reduced scattering coefficients of the tissue types in figure 3.4 (including water). The scattering properties of venous and arterial blood, and fat, are the same. Optical properties are based on data from [26].

**Table 3.1.** Values of  $c_m$ ,  $c_b^D$ ,  $sO_2^D$ ,  $c_b^F$ , and  $sO_2^F$ , used in the tissue models in figure 3.4.

$c_m$	$c_b^D$	$sO_2^D$	$c_b^F$	$sO_2^F$
0.03	0.002	0.67	0.002	0.75

MC simulations were carried out on each model at 19 wavelengths spaced in the 680-970 nm wavelength range for the  $sO_2^A - sO_2^V$  pairs of 15%-97%, 35%-97%, 55%-97%, and 75%-97%. The wavelength range of 680 to 970 nm was chosen to match the wavelength range of the PA system used in the phantom and *in vivo* sections. Within this range, simulations were carried out in 20 nm steps from 690 to 970 nm, as well as at 680, 755, and 760 nm, where haemoglobin has a large sensitivity to oxygen, and also at the haemoglobin isosbestic point of 800 nm. An example MC simulation result on the multilayer model is shown in figure 3.6, showing the optical fluence distribution in the xz and yz planes (panels (a) and (b)) and the distribution of optical energy deposition in the xz plane (panel (c)). The illumination profile in the xy plane is shown in panel (d), which was a rectangular light beam to mimic the rectangular light beam of the LZ250 PA probe. Simulations were carried out for 25 minutes for each wavelength on a 3.2 GHz processor computer, which averaged  $1.2 \times 10^6$  photons for each wavelength.

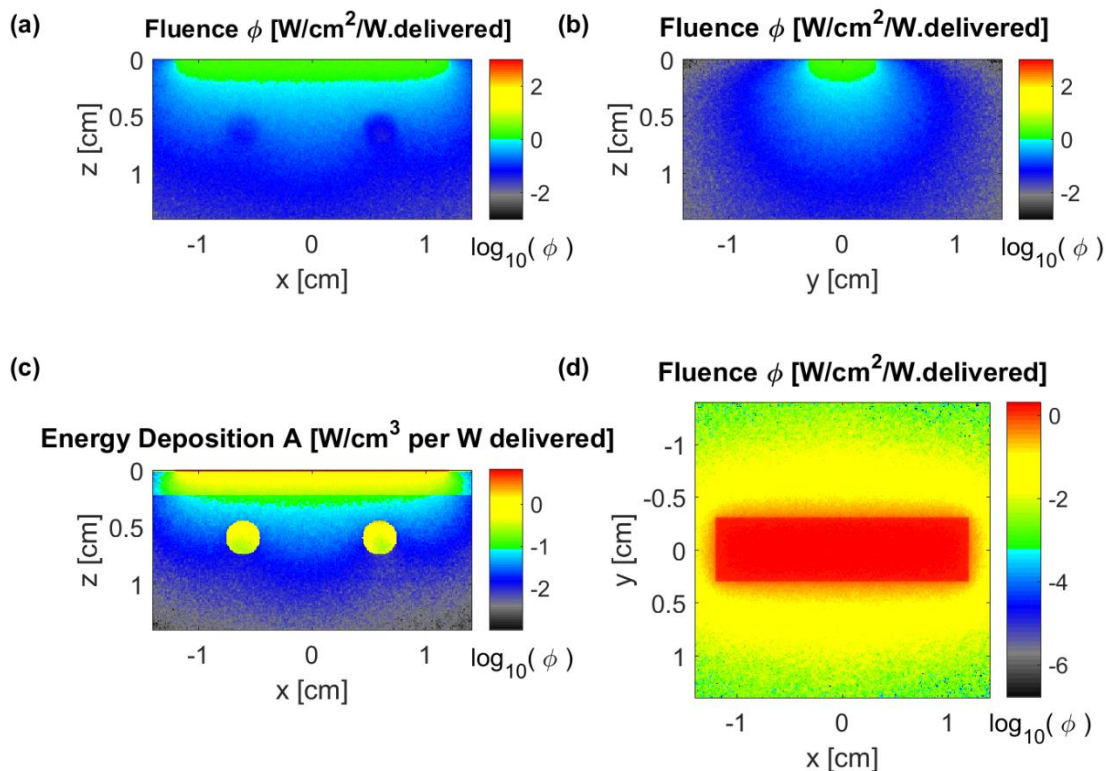


**Figure 3.6.** MC simulation results on the multilayer model at 800 nm. (a) and (b), optical fluence distribution in the xz ( $y=0$ ) and yz ( $x=0$ ) planes, respectively. (c) Optical energy deposition in the xz plane ( $y=0$ ), showing high absorption in the blood vessels compared to the surrounding fat layer. (d) Optical fluence distribution in the xy plane ( $z=0$ ), showing the rectangular-beam illumination profile.

After each MC simulation was completed, the time resolved PA signal generated from the 3D map of absorbed energy was recorded by a pair of surface detectors (shown in figure 3.4), using the method outlined in section 2.9. For the PA simulations, the speed of sound and the acoustic attenuation coefficient were 1500 m/s and 0.75 dB/cm/MHz, respectively. An example set of PA signals plotted against tissue depth recorded by the detectors over the vein and artery at 680 nm are shown in figure 3.7. The difference in the peak PA amplitude between the venous and arterial PA signals can be observed at a depth of  $\approx 0.45$  cm, caused by the different  $sO_2$  levels. The tissue parameters to be fitted for in the arterial fluence calibration procedure were  $c_b^F$  and  $sO_2^F$  for the singlelayer model and  $c_M$ ,  $c_b^D$ ,  $sO_2^D$ ,  $c_b^F$ , and  $sO_2^F$  for the multilayer model. In addition, the scattering properties were assumed to be known *a priori* before applying the method.

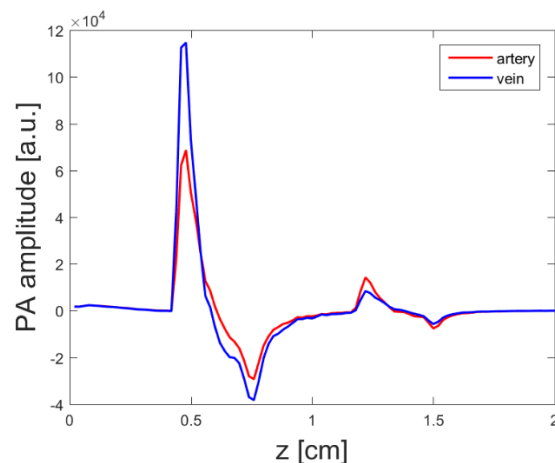


**Figure 3.7.** PA signals plotted against tissue depth for detectors placed over the vein and artery, respectively, for the singlelayer model at 680 nm and with  $sO_2^V = 55\%$  and  $sO_2^A = 97\%$ . The relative difference in PA signal amplitude for the blood vessels can be observed at  $\approx 0.45$  cm, caused by the different oxygenation levels. A secondary set of peaks caused by the blood vessel furthest away from each detector can be observed at  $\approx 1.25$  cm, with a reduced PA amplitude caused by the angular sensitivity of the detector and acoustic attenuation.

### 3.5.2 Phantom experiments

Phantom experiments were performed on tissue-mimicking phantoms composed of polystyrene microspheres and NIR absorbing dyes embedded in an agar background, to simulate optical scattering and absorption, respectively. The phantom structure is shown in

figure 3.8 a, and consisted of two tubes, representing a vein and an artery, embedded in a two-layered cubic volume with dimensions of  $8 \times 8 \times 3$  cm ( $x, y, z$ ). The two layers, termed the upper and lower layers, respectively, represented a skin layer and a lower subcutaneous layer, with the upper layer having an approximate thickness of 0.2 cm. The tubes were made from clear silicon rubber, with an inner diameter of 0.05 cm and an outer diameter of 0.07 cm, and placed in the lower layer at a depth of approximately 0.4 cm from the surface and separated by a distance of 1 cm.

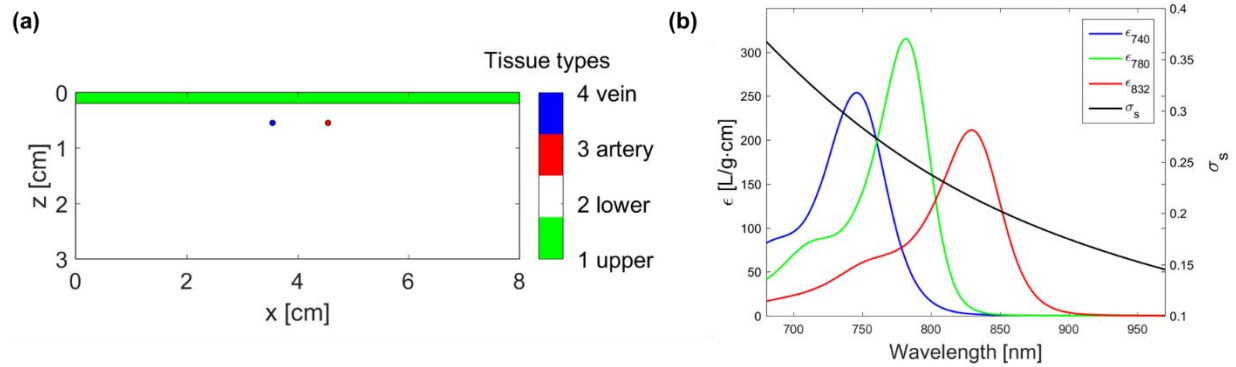


**Figure 3.8.** (a) Schematic of phantom structure. (b) Mass extinction coefficients of the 740, 780, and 832 nm dyes ( $\epsilon_{740}$ ,  $\epsilon_{780}$ ,  $\epsilon_{832}$ ), and scattering efficiency (dimensionless) of polystyrene microspheres contained in the upper and lower layers.

To simulate blood vessels with varying  $sO_2$  levels, the tubes were filled with distilled water containing different concentrations of two NIR absorbing dyes with distinct optical absorption peaks in the NIR. The dyes (American Dye Source Inc.) had absorption peaks at 740 nm and 832 nm, respectively, as shown in figure 3.8 b. The dye concentration ratio,  $R_{dye}$ , was defined analogous to  $sO_2$  as

$$R_{dye} = \frac{c_{832}}{c_{832} + c_{740}} \times 100, \quad 3.19$$

where  $c_{740}$  and  $c_{832}$  are the concentrations of the 740 nm dye and 832 nm dye, respectively. The absorption spectra of the dye mixture is therefore a linear combination of the absorption spectra of the individual dyes.

Phantoms were made with  $R_{dye}$  values of 0%, 25.1%, 55.2%, 74.2% and 87.9% for the venous tube, while the  $R_{dye}$  value of the arterial tube was kept constant at 100% for each case. The dye mixtures for different  $R_{dye}$  values are shown in figure 3.9. The total dye concentration

$(c_{832} + c_{740})$  was 0.031 g/L for each  $R_{dye}$  value, which was calculated to give a peak absorption coefficient of  $15 \text{ cm}^{-1}$  for the 0%  $R_{dye}$  tube, to simulate biologically realistic levels found in the NIR wavelength region.



**Figure 3.9.** Dye mixtures for various  $R_{dye}$  values.

The surrounding tissue layers were composed of a 2% agar-water background containing polystyrene microspheres (Bangs laboratories Inc.) at a concentration of  $3.79 \times 10^{10} \text{ L}^{-1}$ , which was calculated to give a scattering coefficient of  $70 \text{ cm}^{-1}$  at 680 nm. The scattering coefficient was calculated with

$$\mu_s(\lambda) = \rho_s \alpha_s(\lambda), \quad 3.20$$

where  $\rho_s$  is the microsphere concentration, and  $\alpha_s(\lambda)$  is the scattering efficiency (shown in figure 2 b), which was calculated using Mie theory [132] ( $n = 1.58$ ). To account for optical absorption, a 0.021 g/L concentration of a 780 nm peaked dye (figure 3.8 (b)),  $c_{780}^U$ , was added to the upper layer to yield a peak absorption coefficient of  $15 \text{ cm}^{-1}$ . This was done to simulate a highly absorbing skin layer. A  $2.0 \times 10^{-4}$  g/L concentration of the 832 nm dye,  $c_{832}^L$ , was also added to the lower layer to simulate a background absorption with an absorption peak of  $0.1 \text{ cm}^{-1}$ . When applying the method, the  $R_{dye}$  value of the arterial tube was assumed to be known and the parameters to be solved for in the arterial calibration procedure were  $c_{780}^U$  and  $c_{832}^L$ . In addition, the scattering properties were assumed to be known *a priori*.

The phantom manufacture process [133] consisted of heating distilled water to a temperature of  $95^\circ\text{C}$  whereupon 2% agar (Sigma Aldrich) was added under continuous stirring. The solution was allowed to cool to  $40^\circ\text{C}$  whereupon the polystyrene microspheres and absorbing dye were added. The solution was then poured into a 3D-printed phantom mould with the tubes in place and allowed to set for 24 hours, which created the lower layer. A clear plastic film ( $\approx$

10  $\mu\text{m}$  in thickness) was then placed on the surface to prevent bleeding and the upper layer was added using the same process. Figure 3.10 shows the phantom at different stages of manufacture in the 3D mould.



**Figure 3.10.** Tissue phantoms in 3D-printed phantom moulds at different stages of manufacture, in (a) with the lower layer added, and (b) with the upper layer added. The clear silicon tubing can be seen protruding from the mould wall in (a) and (b), as well as the plastic film separating the layers.

PA scans were taken of each phantom with a 256-element linear-array probe (LZ250, VisualSonics Inc.) with a 21 MHz central detection frequency (bandwidth 52.4%), and a lateral and axial resolution of 165  $\mu\text{m}$  and 75  $\mu\text{m}$ , respectively. The scanning setup is shown in figure 3.11. The probe contained two rectangular light bars situated on either side of the transducer array that focused light into the sample at a distance of  $\approx 6$  mm. The laser light source consisted of tunable optical parametric oscillator (OPO, 680 to 970 nm, Oportek Inc.) driven by a frequency-doubled Nd:YAG laser (1064 nm, 20 Hz repetition rate) that was coupled to the probe via a fibre bundle. A 6 mm thick US gel pad (Aquaflex®, Parker Laboratories Inc.) was placed on the probe head to ensure the beam focal point was on the phantom surface and also to ensure reverberation artefacts were pushed below the region of interest on the PA images. The PA probe was aligned so that the imaging plane was perpendicular to the direction of the tubes, and multiwavelength PA scans were acquired on each phantom across the OPO wavelength range of 680-970 nm in steps of 10 nm. The spectral energy variation of the laser was recorded with an energy meter and was used to account for laser energy variation effects on the measured PA spectra.

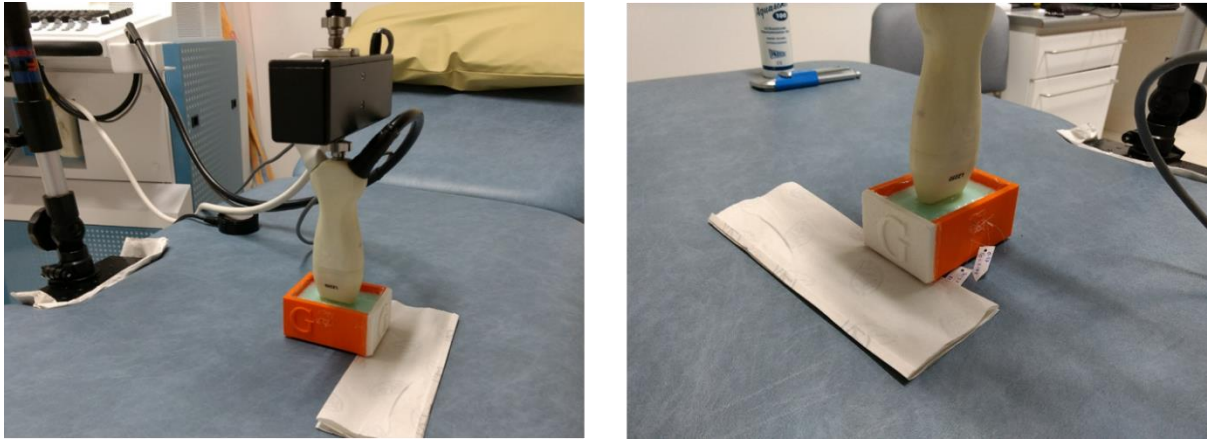


**Figure 3.11.** Scanning setup used for tissue phantom scans (gel pad attachment not shown).

### 3.5.3 *In vivo* experiments

The proposed method was tested *in vivo* on the superficial vasculature of the ventral (inner) aspect of the human wrist on a healthy male volunteer (32-year-old light skinned Caucasian, skin type I-II). The scan region is shown outlined in figure 3.12. The volunteer's arm was placed in a water bath at room temperature to provide acoustic coupling and the 21 MHz PA probe was placed on the scan region. Multiwavelength PA scans were then taken across the OPO range of 680-970 nm in steps of 5 nm. A higher wavelength resolution was used in the *in vivo* case compared to the phantom study to better capture the oxyhaemoglobin peak at  $\approx 755$  nm, which has a high sensitivity to oxygen. During PA scanning, a pulse oximeter was connected to the finger on the opposite hand to monitor  $sO_2^A$ . In addition, the volunteer was required to wear laser safety goggles which blocked light in the 680–970 nm wavelength range under study.

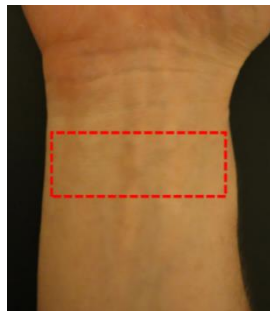


**Figure 3.12.** Scan region on ventral aspect of the wrist.

The ventral aspect of the wrist was chosen to test the method *in vivo* as it is a relatively flat region that contains superficial veins and arteries in close proximity that could be easily resolved with our PAI system. An artery in the scan region was identified for fluence calibration through observation of the arterial pulse on B-mode US. An attempt was made to identify arteries with colour Doppler US by detecting their opposite direction of flow to veins, however, it was found to lack the required spatial resolution. The method was then applied to make  $sO_2^V$  measurements on three targeted subcutaneous veins. The targeted blood vessels were all located beyond 1 mm in depth where light becomes diffuse. After PA scanning, an intravenous catheter was inserted under sterile conditions into a superficial vein on the wrist above the scan region and a blood sample ( $\approx 10$  ml) was collected in a heparinised syringe. The  $sO_2^V$  of the sample was measured with a blood gas analyser and used as a representative value to which the PA measured  $sO_2^V$  was compared. In addition, a correction for acoustic attenuation was applied to each targeted blood vessel using an assumed acoustic attenuation coefficient of  $0.75 \text{ dB cm}^{-1} \text{ MHz}^{-1}$  [6].

## ***3.6 Results and discussion***

### **3.6.1 Coupled Monte Carlo and PA simulation results**

An example set of PA amplitude spectra from the vein and artery from the singlelayer model for each simulated  $sO_2^V$  and  $sO_2^A$  value are shown in figure 3.13.

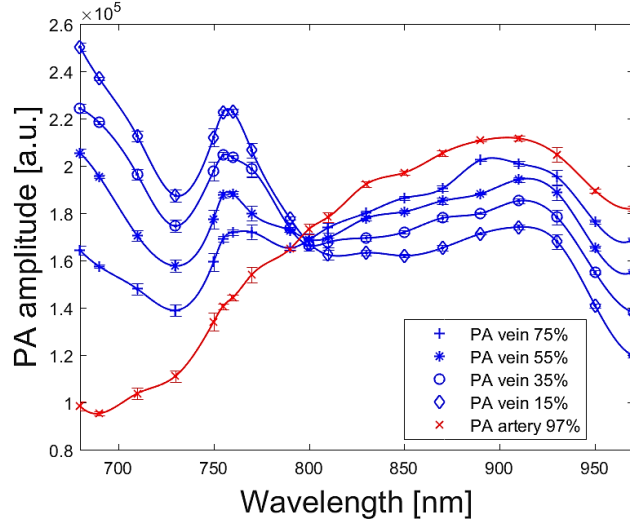


**Figure 3.13.** Peak PA amplitude spectra from the vein and artery from the singlelayer model for each simulated  $sO_2^V$  and  $sO_2^A$  value. The error bars represent the standard deviation of points from repeated simulations.

Table 3.2 shows the average PA determined values of  $c_b^F$  and  $sO_2^F$  from the arterial fluence calibration procedure on the singlelayer model, as well as their respective errors and uncertainties. The results show reasonably good agreement with the known values of 0.002 and 0.75 (table 3.1), however, both  $c_b^F$  and  $sO_2^F$  were overestimated by a factor of 0.3 and 0.083, respectively.

**Table 3.2.** Average values of  $c_b^F$  and  $sO_2^F$  obtained from the arterial fluence calibration procedure for each simulation on the singlelayer model, as well as the corresponding average error and uncertainty.

$c_b^F$	$sO_2^F$	Error		Uncertainty	
		$c_b^F$	$sO_2^F$	$c_b^F$	$sO_2^F$
0.0026	0.83	+0.3	+0.097	$\pm 2.2 \times 10^{-4}$	$\pm 0.082$

**Table 3.3.** Average values of  $c_m$ ,  $c_b^D$ ,  $sO_2^D$ ,  $c_b^F$  and  $sO_2^F$  obtained from the arterial fluence calibration procedure for each simulation on the multilayer model, as well as the corresponding average error and uncertainty for each parameter.

$c_m$	$c_b^D$	$sO_2^D$	$c_b^F$	$sO_2^F$					
0.044	0.014	0.89	0.0046	0.62					
Error			Uncertainty						
$c_m$	$c_b^D$	$sO_2^D$	$c_b^F$	$sO_2^F$	$c_m$	$c_b^D$	$sO_2^D$	$c_b^F$	$sO_2^F$
0.48	6.0	0.33	1.32	-0.17	$\pm 0.0024$	$\pm 0.0016$	$\pm 0.10$	$\pm 0.5 \times 10^{-4}$	$\pm 0.047$

The average values of  $c_m$ ,  $c_b^D$ ,  $sO_2^D$ ,  $c_b^F$  and  $sO_2^F$ , obtained from the arterial fluence calibration procedure on the multilayer model are shown in table 3.3, as well as their respective average error and uncertainties. The determined values show reasonable over all agreement with the known values, however, similarly to the singlelayer model, there is a tendency of the model to overestimate chromophore concentrations in each layer. This is particularly pronounced for  $c_b^D$  and  $c_b^F$ , which are overestimated by an order of magnitude by a factor of 6.0 and 1.32, respectively. The primary reason for the overestimation is due to the one-dimensional nature of the optical model used, as opposed to the MC simulation, which models optical transport in three dimensions. Optical attenuation therefore occurs at a higher rate in the MC simulation and the model input parameters are overestimated in the fitting procedure to account for this. The uncertainty in the determined parameters in tables 3.2 and 3.3 show reasonable sensitivity to each parameter and were found to not have a significant variation for different arterial and venous  $sO_2$  pairs.

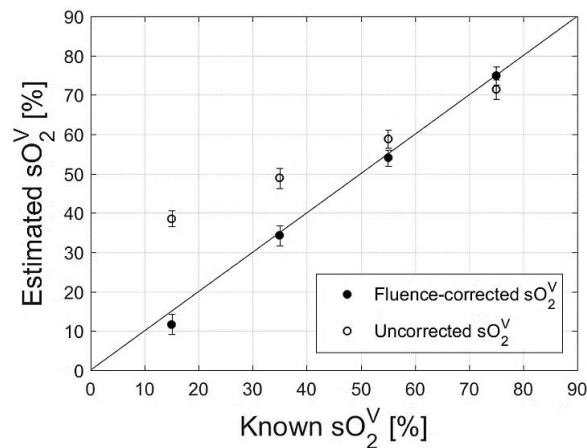


**Figure 3.14.** Fluence-corrected and uncorrected  $sO_2^V$  values plotted against the known values for the singlelayer model.

Figure 3.14 shows the fluence-corrected  $sO_2^V$  values plotted against the known values for the singlelayer model, as well as uncorrected  $sO_2^V$  values determined using the linear method. It can be seen that the fluence-corrected  $sO_2^V$  values increase linearly with the known values and have very good qualitative agreement, with the average absolute error being less than 7% across the whole  $sO_2^V$  range. This is in contrast to the uncorrected values, which have an average error of 50%, mainly caused by the disproportionate overestimation of  $sO_2^V$  for lower values. The disproportionate overestimation is caused by optical attenuation in the fat layer, which scatters light more strongly at lower wavelengths. This results in a comparatively lower fluence in the 680-800 nm wavelength region, which pushes the shape of venous PA spectrum closer to that of oxyhaemoglobin, causing the overestimation. The optical absorption by blood in the fat layer, which has an  $sO_2$  value of 75%, serves to counteract this effect by absorbing comparatively more beyond 800 nm, however, the scattering effect still dominates owing to its higher magnitude.

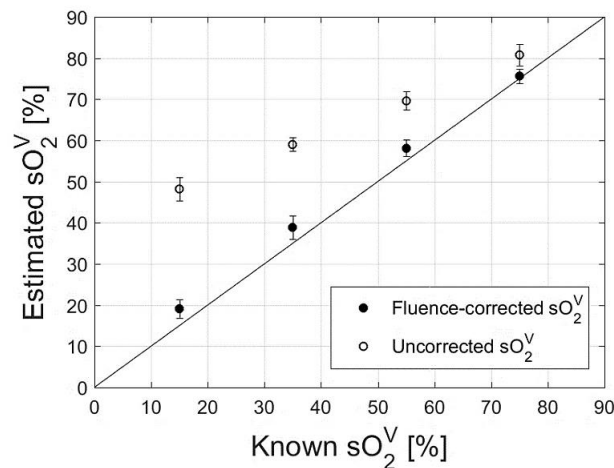


**Figure 3.15.** Fluence-corrected and uncorrected  $sO_2^V$  values plotted against the known values for the multilayer model.

The fluence-corrected  $sO_2^V$  values for the multilayered model are shown plotted against the known values in figure 3.15, as well as the values determined using the linear method. The fluence-corrected  $sO_2^V$  values show good quantitative agreement with the known values, with the average error being 2.7% across the whole  $sO_2^V$  range. This is in contrast to the uncorrected values, which have an average error of 81%, mainly caused by the disproportionate overestimation of  $sO_2^V$  for lower values. The increased overestimation at lower wavelengths compared to the singlelayer case can be explained by considering the optical effects caused by the addition of the dermis and epidermis. Optical scattering in the epidermis, dermis, and fat

layers is higher at lower wavelengths (680-800 nm) compared to longer wavelengths (800-970 nm), while the same is true for optical absorption by melanin in the epidermis (figure 3.5). Concerning the dermis, as is shown in figure 3.5 (b),  $\mu_s'^D$  is over twice the magnitude of  $\mu_s'^F$  across the 680-970 nm wavelength range, with the difference increasing as the wavelength tends toward 680 nm. It is this disproportionate increase in  $\mu_s'^D$  that primarily results in the overestimation of  $sO_2^V$  at lower wavelengths, rather than from optical absorption in the epidermis, due to the longer pathlength in the dermis. The overall resultant increase in optical attenuation in the 680-800 nm region compared with the singlelayer case results in the increased overestimation of  $sO_2^V$  at lower wavelengths. The calibrated fluence model, on the other hand, can accurately predict the shape of the fluence spectrum at the vein and therefore correct  $S_V(\lambda)$  for changes in optical fluence. The uncertainty in the values obtained for  $sO_2^V$ , represented by the error bars in figures 3.14 and 3.15, were found to have no significant variation for different  $sO_2^V$  and  $sO_2^A$  pairs, and for both tissue models, although a higher uncertainty for the multilayer model could be expected due to the decreased SNR caused by the addition of the epidermal and dermal layers.

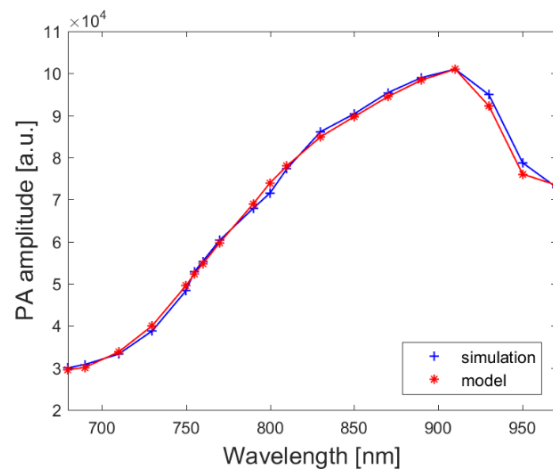


**Figure 3.16.** Simulated arterial PA spectra plotted alongside the arterial spectra calculated using the calibrated fluence model.

Figure 3.16 shows the simulated arterial PA spectrum plotted alongside the predicted PA spectrum calculated using the calibrated fluence model. The close match demonstrates the ability of the model to account for optical fluence attenuation effects from multiple chromophores.

### 3.6.2 Phantom results

A PA scan of the phantom taken at 780 nm with  $R_{dye}$  values of 0% and 100% for the vein and artery, respectively, is shown in figure 3.17 (a), while the average PA amplitude spectra from the marked regions in (a) are shown in figure 3.17 (b). The average values of  $c_{780}^U$  and  $c_{832}^L$ , determined from the arterial fluence calibration procedure for all phantoms, are shown in table 3.4. The results show reasonable agreement with the known values, however, the same tendency of the model to overestimate chromophore concentrations is observed, with  $c_{780}^U$  and  $c_{832}^L$  being overestimated by a factor 0.49 and 2.0, respectively. Possible inhomogeneities in phantom optical properties caused by microsphere or dye sedimentation during fabrication may have contributed to the error.

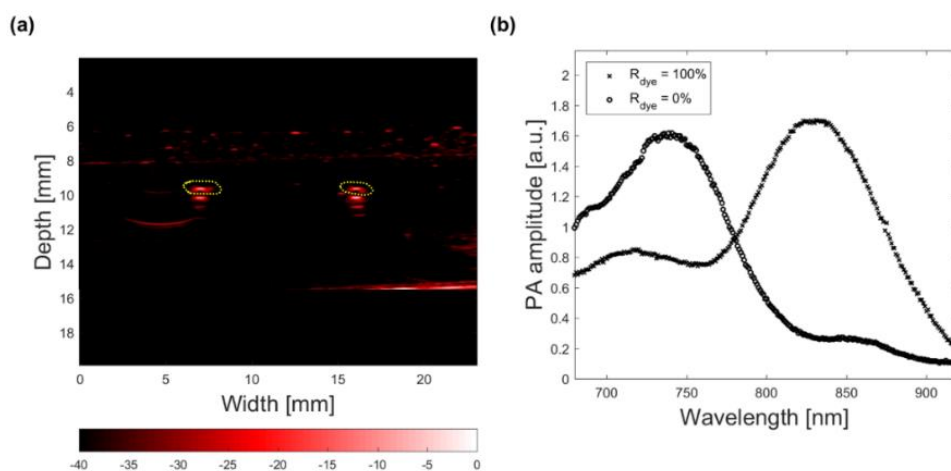


**Figure 3.17.** (a) PA scan of a 0%-100%  $R_{dye}$  phantom taken at 780 nm, showing the 100% tube (left) and 0% dye tube (right), centred at a depth of  $\approx 10$  mm. The upper layer boundaries can be seen between  $\approx 6$ -8 mm. (b) Averaged PA amplitude spectra from the two marked regions in (a).

**Table 3.4.** Average values of  $c_{780}^U$  and  $c_{832}^L$  determined from the arterial fluence calibration procedure on each phantom, as well as the corresponding average error and uncertainty.

$c_{780}^U$ [g/L]	$c_{832}^L$ [g/L]	Error		Uncertainty [g/L]	
		$c_{780}^U$	$c_{832}^L$	$c_{780}^U$	$c_{832}^L$
0.031	0.00060	0.50	2.0	$\pm 0.0037$	$\pm 0.91 \times 10^{-4}$

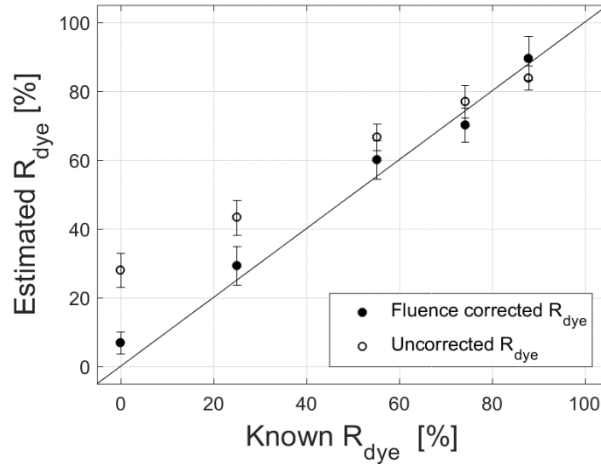


**Figure 3.18.** Fluence-corrected and uncorrected  $R_{dye}$  values plotted against the known values.

The fluence-corrected and linearly determined venous  $R_{dye}$  values are shown plotted against the known values in figure 3.18. The fluence-corrected  $R_{dye}$  values increase linearly with and show good quantitative agreement with the known values, with an average error of 5.6%. This is in contrast to the uncorrected  $R_{dye}$  values which have an average error of 23.2%, which is mainly caused by a disproportionate overestimation of  $R_{dye}$  at lower values. As with the MC-PA simulations, the disproportionate overestimation of  $R_{dye}$  for lower values is caused by an increased optical scattering at lower wavelengths, but also from the greater overlap of the absorption spectrum of the 780 nm dye in the upper layer with the 740 nm peaked dye in the tube (figure 3.8 (b)). The resulting optical attenuation disproportionately decreases the amount of light reaching the tube at lower wavelengths (< 780 nm) compared with longer wavelengths (> 780 nm), resulting in the shape of the PA spectrum being pushed closer to that of the 832 nm dye. The average uncertainty in the determined  $sO_2^V$  values was 5.3%, which was found to have no significant variation for different  $sO_2^V$  levels.

### 3.6.3 *In vivo* results

A coregistered PA-US image of the scan region on the wrist is shown in figure 3.19 (a), showing the targeted subcutaneous veins marked 1, 2, and 3. A nearby artery in the scan region was selected for calibration, which was located approximately 1 cm from the targeted veins. The PA amplitude spectra from each vein and artery are shown normalised at 800 nm in figure 3.19 (b).

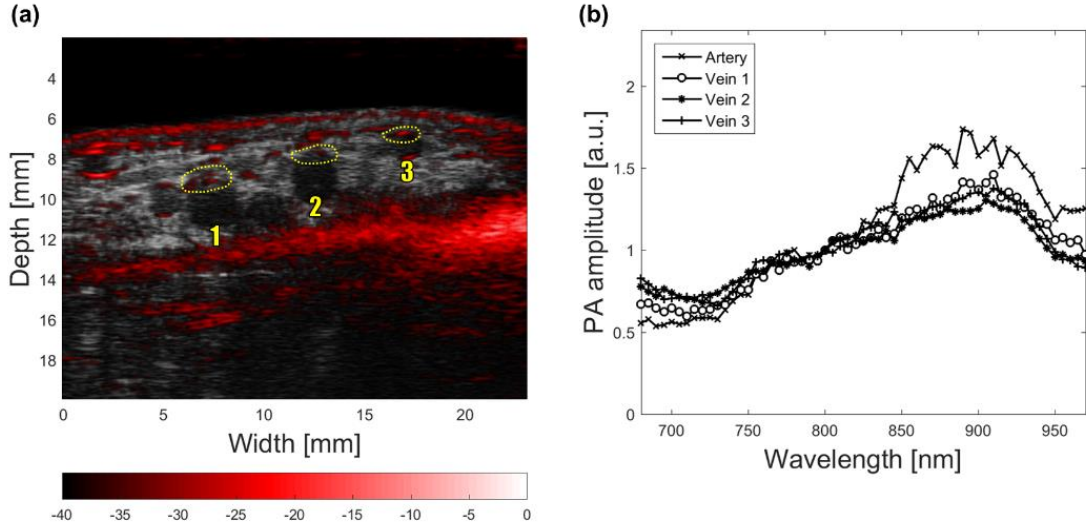


**Figure 3.19.** (a) Coregistered PA-US image at 800 nm of the scan region showing the targeted veins marked 1, 2, and 3. (b) PA amplitude spectra normalised at 800 nm from veins 1, 2, and 3, as well as from the artery used for calibration.

**Table 3.5.** Values of  $c_m$ ,  $c_b^D$ ,  $sO_2^D$ ,  $c_b^F$  and  $sO_2^F$  determined from the arterial fluence calibration procedure, as well as the corresponding average error and uncertainty for each parameter.

$c_m$					$c_b^D$					$sO_2^D$					$c_b^F$					$sO_2^F$				
0.039					0.011					0.46					0.0056					0.54				
Error [%]										Uncertainty														
$c_m$	$c_b^D$	$sO_2^D$	$c_b^F$	$sO_2^F$	$c_m$	$c_b^D$	$sO_2^D$	$c_b^F$	$sO_2^F$	$c_m$	$c_b^D$	$sO_2^D$	$c_b^F$	$sO_2^F$	$c_m$	$c_b^D$	$sO_2^D$	$c_b^F$	$sO_2^F$					
1.49	4.84	-0.30	-0.26	-0.18	$\pm 0.0043$	$\pm 0.0017$	$\pm 0.06$	$\pm 0.0009$	$\pm 0.08$															

The values of  $z_E$ ,  $z_D$ , and  $z_F$ , required as inputs to the forward model, were measured directly from the PA-US scans. The epidermal thickness was measured to have a uniform value of 0.120 mm across the scan region, while the dermis was found to vary slightly with an average value of  $0.718 \pm 0.153$  mm. The thickness of the subcutaneous fat layer overhead each blood vessel was measured from the lower boundary of the dermis to the top of each vessel, and had values of 1.37 mm, 0.478 mm, and 0.299 mm for veins 1, 2, and 3, respectively, and a value of 1.45 mm for the artery. At the time of scanning, an  $sO_2^A$  value of 97% was measured with pulse oximetry. The determined values of  $c_m$ ,  $c_b^D$ ,  $sO_2^D$ ,  $c_b^F$ , and  $sO_2^F$  are shown in table 3.5. Since an independent measurement of these values was not possible, the determined parameters were

compared with the equivalent literature reported values. The  $c_m$  value of 0.049 is possibly high compared with the value reported for the same region in skin type I-II individuals of 0.0156 [18]. The value  $c_b^D$  may also be likewise overestimated compared to the reported values of 0.002. The values of  $c_b^F$ ,  $sO_2^D$ , and  $sO_2^F$ , are, however, underestimated compared with the reported value of 0.0076 for  $c_b^F$  and the reported  $sO_2$  value of 0.66-0.75 for whole skin [134]. Comparison with literature reported values gives only an indication of the accuracy of each parameter, however, the same trend of parameter overestimation observed with the MC-PA simulation and phantom studies is likely continued here.

**Table 3.6.** Fluence corrected and uncorrected  $sO_2^V$  values determined for veins 1, 2, and 3, as well as the corresponding average accuracy and uncertainty.

Vein	Fluence corrected $sO_2^V$ [%]	Linear $sO_2^V$ [%]
1	76.4	83.8
2	72.9	79.6
3	73.1	80.1
Average error		
	Fluence corrected $sO_2^V$ [%]	Linear $sO_2^V$ [%]
	3.3	13.0
Average uncertainty		
	Fluence corrected $sO_2^V$ [%]	Linear $sO_2^V$ [%]
	7.3	7.9

The fluence corrected and linearly determined  $sO_2^V$  values for veins 1, 2, and 3 are given in table 3.6. The determined values were compared with the  $sO_2^V$  value of 71.8%, measured from blood gas analysis on the extracted blood sample. The fluence-corrected  $sO_2^V$  values for vessels 1, 2, and 3 of 76.4%, 72.9% and 73.2%, respectively, matched well with the blood gas measurement with the average error being 3.3%. The values determined with the linear method for the same blood vessels of 83.8%, 79.6% and 80.1%, showed a greater tendency to be overestimated, with the average error being 13.0%. Considering the effects of optical attenuation, it is expected that deeper blood vessels would tend to have a higher  $sO_2^V$  level due

to disproportionate optical attenuation in the 680-800 nm region. However, the  $sO_2^V$  level of blood vessel 2 is slightly less than in blood vessel 3, despite it being deeper in the tissue (as shown in figure 3.19). It is therefore expected that the  $sO_2^V$  level of blood vessel 2 is in fact higher, and that the difference lies within the level of uncertainty. The increased overestimation of the linear  $sO_2^V$  values is likely caused by the disproportionate optical attenuation at lower wavelengths, as outlined in sections 3.6.1 and 3.6.2. Other possible sources of error include movement artefacts which may have corrupted the detected PA spectra, and irregular distribution of tissue optical properties which are modelled as bulk optical properties in the model.

Although the magnitude of the fitted parameters determined in the arterial fluence calibration procedure differed from the reported values by an order of magnitude for  $c_m$  and  $c_b^D$ , the calibrated fluence model was found to provide an accurate prediction of the shape of the fluence spectrum at the vein, as evidenced by the high accuracy of the determined  $sO_2^V$  values. Accurate  $sO_2^V$  measurements are possible as any scaling errors caused by limitations of the optical model used, which effect the accuracy of absolute chromophore concentrations, are cancelled when calculating  $sO_2^V$ . The average uncertainty of 7.3% in the determined  $sO_2^V$  values showed reasonable sensitivity, however, it was affected by the decreased SNR in the measured PA spectra compared to the phantom experiment.

As mentioned in the previous results sections, one of the main limitations of the method with its current implementation is the use of a 1D optical model with which to characterise optical fluence, which resulted in an overestimation of tissue chromophores in the arterial fluence calibration procedure. This limitation could be corrected in subsequent applications of the method by using more complex 3D models. However, general limitations of the method include the necessity of applying a pulse oximeter when making a quantitative measurement, the steps involved in identifying an artery, and delineating and measuring tissue layer thicknesses, which are required as inputs for a multilayered model of optical transport. Despite this, with a fully calibrated optical model, the method holds promise for producing fluence-corrected PA images that enable quantification at any point within the field of view, and has potential applications in clinical situations where accurate  $sO_2^V$  measurements are paramount, such as in cerebral  $sO_2^V$  monitoring.

Another issue with the current implementation of the method is the use of semi-empirical scattering formulas to describe optical scattering in the skin and subcutaneous fat layers. As

was shown in section 3.6.1, optical scattering plays a large role in the corruption of PA spectra due to optical fluence attenuation. Calibrating for optical scattering in the *in vivo* case could therefore help improve the accuracy, as semi-empirical scattering functions give only a general indication of the scattering properties of real biological tissues.

### **3.7 Conclusion**

A method for correcting measured PA spectra for the effects of spectral fluence attenuation based on arterial fluence calibration was proposed. The method involved calibrating a multilayer optical fluence model for the concentrations of tissue chromophores by fitting to the PA measured optical fluence spectrum of an artery. The calibrated fluence model was used to correct measured venous PA spectra for spectral fluence attenuation effects to calculate fluence-corrected  $sO_2^V$ . The method was demonstrated on simulated, phantom, and *in vivo* experiments.

The method was found to give a good match between the fluence-corrected and known  $sO_2^V$  values, despite the tendency of the optical model to overestimate chromophore concentrations in the arterial fluence calibration procedure. Chromophore overestimation was primarily caused by the limitation of the optical model to account for optical fluence attenuation in three dimensions. Accurate  $sO_2^V$  values could be obtained as scaling errors introduced as a result of this were cancelled when calculating  $sO_2^V$ . The high accuracy of the fluence-corrected  $sO_2^V$  measurements demonstrates the ability of the calibrated fluence model to predict the shape of the optical fluence spectrum at the vein under the influence of optical attenuation from multiple chromophores.

To increase the accuracy of the method in determining absolute chromophore concentrations, more complex optical models that can handle 2D or 3D geometries such as FEM methods could be employed. The method has application in clinical settings where accurate quantification of  $sO_2$  is required, such as monitoring cerebral oxygen consumption during surgery, which is currently achieved by invasive central venous catheterisation, or in longitudinal preclinical research studies where accurate absolute quantification at different study timepoints is required.

## **Chapter 4: Preoperative measurement of cutaneous melanoma and nevi thickness with photoacoustic imaging.**

The following chapter is based on publication [135].

### ***4.1 Introduction***

Melanoma is a tumour that results from the malignant transformation of melanocytes and is the most lethal form of skin cancer. Despite accounting for <5% of all skin cancers, it is responsible for 75% of skin-cancer-related deaths [136,137]. Early diagnosis and treatment is essential, with a 98% survival rate for cases discovered before the tumour metastasizes to the sentinel lymph nodes and organs [138]. The histopathologically measured melanoma thickness, known as the Breslow thickness, is the most important clinical indicator for melanoma staging, guiding treatment, and determining prognosis.

Although the recommended technique for diagnosing cutaneous melanoma is excisional biopsy with narrow margins, partial biopsy techniques, such as punch and tangential biopsies, are routinely used to diagnose suspect lesions, particularly in cosmetically sensitive areas, with up to 27% of melanomas being diagnosed with partial biopsy [139,140]. Partial biopsies are associated with an increased risk of inaccurate histopathologic measurement of tumour thickness and misdiagnosis, due to undersampling of the primary lesion [141]. Microstaging inaccuracies for melanoma have been reported in 16% to 43% of non-excisional biopsy techniques [142]. Current guidelines suggest that the most irregular and pigmented part of a suspect lesion is the most favourable for biopsy; however, this does not always correspond to the most histologically advanced area of the lesion [141,143,144], and thus the full lesion thickness may be unavailable to the pathologist. In cases where undersampling occurs, surgeons can be faced with a choice of planning a full surgical excision based on a provisional Breslow thickness, in the hope that it represents the thickest portion of the lesion, or to perform a repeat biopsy to obtain the full lesion thickness prior to definitive surgery [145]. Thus, a preoperative, noninvasive measurement of tumour thickness could guide the surgeon in

determining biopsy depth and sample location and could improve patient management and eliminate the need for additional biopsies.

Many noninvasive imaging modalities have been used for the *in vivo* assessment of melanoma and benign skin lesions, but many have significant limitations. Dermoscopy [146] is routinely used to examine subsurface tumour characteristics and pigmentation and has aided the diagnosis of melanoma. However, its penetration depth is limited by optical diffusion, and it cannot image beyond the papillary dermis. Other optical imaging methods, such as optical coherence tomography [147], confocal microscopy [148,149], and two-photon microscopy [150], while providing good contrast and resolution, are likewise depth limited and do not have sufficient penetration to determine melanoma depth. Magnetic resonance imaging and positron emission tomography [151,152] have been used in the assessment of melanoma, however, they have poor resolution in the skin, are expensive, and are not routinely available for clinical dermatological imaging. Ultrasound (US) imaging has likewise been used to clinically assess cutaneous melanoma. As with photoacoustic imaging (PAI), US image depth and resolution are dependent on the frequency of the sound used. Low frequency US systems in the 3-10 MHz range are used for sentinel lymph node imaging, while systems in the 20-50 MHz range, achieving axial and lateral resolutions greater than 80  $\mu\text{m}$  and 200  $\mu\text{m}$ , respectively, and penetration depths of  $\approx 3.8$  mm, are used for imaging primary lesion architecture with high resolution [153]. Higher frequency US systems in the 50-100 MHz range can increase the axial and lateral resolutions to  $\approx 10$   $\mu\text{m}$  and 30  $\mu\text{m}$ , respectively, however, at the expense of penetration depth ( $\approx 1.1$  mm), and hence are not suited for imaging lesion depth except in the most superficial cases. The main drawback for US imaging for melanoma is its poor image contrast, as the difference in acoustic impedance between melanoma and the surrounding tissue is low [154].

PAI is a noninvasive biomedical imaging modality which combines the advantages of optical and US imaging, namely high optical absorption contrast with high US resolution, for deep tissue imaging in the diffusive regime, while minimizing their disadvantages [155]. In PAI, a pulsed source of electromagnetic energy, typically a short-pulsed laser, is used to heat biological tissue through optical absorption. The resultant thermoelastic expansion generates an acoustic wave that can be detected at the tissue surface in the same way as conventional US imaging. PAI derives its means of contrast from optical absorption and is thus sensitive to endogenous biological absorbers, such as melanin and haemoglobin, allowing it to image

melanin distribution within the skin and pigmented skin lesions, as well as their associated microvasculature networks [156]. By varying the laser wavelength, PAI can acquire functional information such as blood oxygen saturation and haemoglobin concentration measuring angiogenesis—a hallmark of cancer [157,158]. Moreover, since US scattering is 2 to 3 orders of magnitude weaker in biological tissue than optical scattering, PAI can image beyond the optical ballistic regime ( $\sim 1$  mm in soft tissue) while maintaining high spatial resolution.

Several preclinical studies, employing PAI systems with various scanning configurations, have demonstrated its effectiveness in assessing the axial and lateral extent of cutaneous skin lesions, including melanoma, and their associated microvasculature [159–161]. PAI systems with handheld, linear-array probes are most likely to succeed in clinical applications due to their high frame rate, field of view, and ease of application [162,163]. Furthermore, linear-array systems allow for the simultaneous coregistration of PA and B-mode US images, which combine the optical absorption contrast and functional information of PAI with the structural imaging capabilities of US [164].

In this study, we introduce a high-frequency, handheld linear-array PAI system to the clinic to test its feasibility, in terms of ease of application, image quality, scanning time, and accuracy in measuring pigmented skin lesion thickness *in vivo*. To this end, patients with cutaneous lesions suspicious for melanoma were recruited to undergo a preoperative PA scan. PA lesion thickness measurements were compared with the histologically determined thickness measured from resected surgical samples.

## ***4.2 Materials and Methods***

After ethical approval from our institutional review board, 27 patients with pigmented cutaneous lesions that aroused a clinical suspicion of melanoma were recruited to undergo PAI. All patients were informed and gave consent before participation. During scanning, patients were required to wear laser safety goggles for protection from laser radiation.

PA scans were conducted using a 41 MHz linear-array PA probe coupled with a tuneable OPO (680 to 970 nm) laser source, the details of which are outlined in section 2.10. The transducer-

array length (14 mm) allowed for the entire section of most lesions to be assessed in a single scan. If the lesion diameter was greater than the probe length, however, multiple scans were required to capture the full lesion volume. By scanning the linear-array probe along a 1D stepper motor, 3D images of skin lesion morphology could be formed by taking a 2D scan at regular intervals. The frame density of 3D scans was set to 290 frames per scan length, which was varied depending on the lesion diameter. A single 3D scan took ~3 min to acquire, and during scanning the patient was required to keep still to minimise movement artefacts.

The PA probe was coupled to the skin with US gel and scanned laterally across the lesion in several scanning directions to assess its full volume. Single-wavelength PA scans were taken at 680 nm. Care was taken to ensure that the PA probe was placed perpendicular to the skin surface to maximize the amplitude of the detected PA signal. The frame with the deepest portion of the lesion was selected, and the maximum lesion thickness was measured from the top of the epidermis to the deepest discernible lower boundary.

In addition to single-wavelength PA scans, an imaging technique known as spectral unmixing (SU) [165] was employed. SU uses multiwavelength PA scans to produce a PA image that maps the spatial distribution of a selected chromophore, in this case melanin and melanin-containing cells (e.g., melanocytes and basal keratinocytes), by means of their distinct optical absorption spectrum within the near-infrared wavelength region. The SU scanning procedure consisted of first taking a spectroscopic scan of the most pigmented part of the lesion over the wavelength range of 680 to 970 nm in steps of 10 nm, that is used to capture the absorption spectrum of melanin, and a second multiwavelength scan where the laser sequentially switched between 5 wavelengths (680, 700, 750, 850, and 900 nm). The multiwavelength scan is then used to produce a PA image (called an SU image or scan) that exclusively shows pixels which match the absorption spectrum of the lesion taken with the first scan. Since SU separates the absorption signature of melanin-containing cells from other endogenous chromophores in the tissue, it was hypothesized that it may provide a more accurate measure of lesion thickness. To test this, SU thickness measurements were compared with thickness measurements from single-wavelength PA scans. Furthermore, SU scans were used to track the extent of lesion growth along the epithelium in skin adnexa, such as hair follicles and sweat glands, in cases where said measurements were reported by histology. Adnexal depth was measured vertically from the lesion surface to the deepest adnexal structure connected to the primary lesion. On average, the full SU scanning procedure took ~7 min.

The maximum PA lesion thickness, and the depth of lesion extension in the skin adnexa measured with SU, was compared with the histological measurements from resected surgical specimens. PA thickness measurements were made blinded to results of the histological thickness. Correlation between PA measurements and histological measurements was determined by means of the correlation coefficient (CC) obtained from a linear regressive fit. The percentage error between the PA measurements and the histological measurements was equal to the difference between the PA and histology thickness divided by the histological thickness (100×). Two-tailed t-tests were employed to test the statistical significance between results.

### **4.3 Results**

A total of 32 pigmented cutaneous lesions were scanned on 27 patients, with histology confirming a diagnosis of melanoma in six cases. All patients displayed primary tumours, located on the trunk, extremity, head, or neck (lesions immediately adjacent to the eyes were excluded due to laser safety risk), without visible ulceration, which allowed application of the probe. Benign lesions included compound and intradermal melanocytic nevi (8 and 5, respectively), seborrheic keratosis (3), and dysplastic nevi (4), whereas malignant tumours included *in situ* (3) and invasive melanomas (3). Benign lesions were very ill-defined in some cases, with lower structural boundaries being invisible in three cases. Melanoma lower boundaries were determined in all cases.

On the PA images, lesions boundaries could be clearly distinguished from the surrounding soft tissue, with well-demarcated lower boundaries distinguished by high optical absorption. Skin layers, such as the epidermis, dermis, and subcutaneous tissue could be identified (figure 4.1). Superficial lesions, such as compound nevi and thin seborrheic keratoses, appeared as symmetrical masses with well-defined regular borders with no visible presence in the dermis. *In situ* melanomas had more uneven boundaries but were not seen to invade past the basal layer of the epidermis, as confirmed by histopathology (figure 4.2(a)). Invasive lesions, such as intradermal nevi and invasive melanoma, generally had irregular borders, due to uneven proliferations of melanoma cells and melanocytes, and could be distinguished from superficial

lesions through growth of the primary lesion through the dermal–epidermal junction (figure 4.2(d)). SU scans showed the presence of melanin-containing cells extending through skin appendages connected to the primary lesion (figure 4.2(g)).

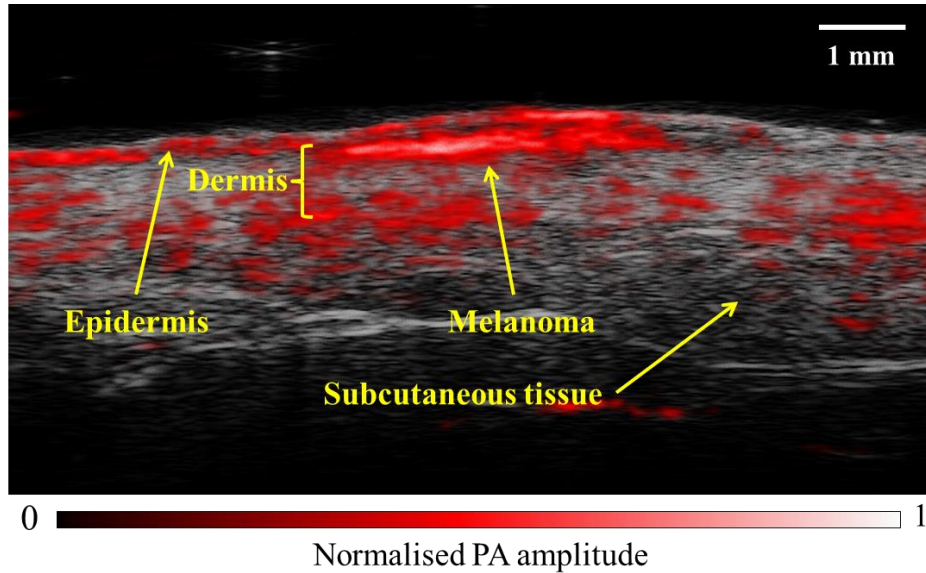


**Figure 4.1.** Coregistered PAI image of *in situ* melanoma on upper left extremity. Handheld linear-array based PAI was able to image pigmented lesion and skin architecture with high contrast, speed, and resolution.

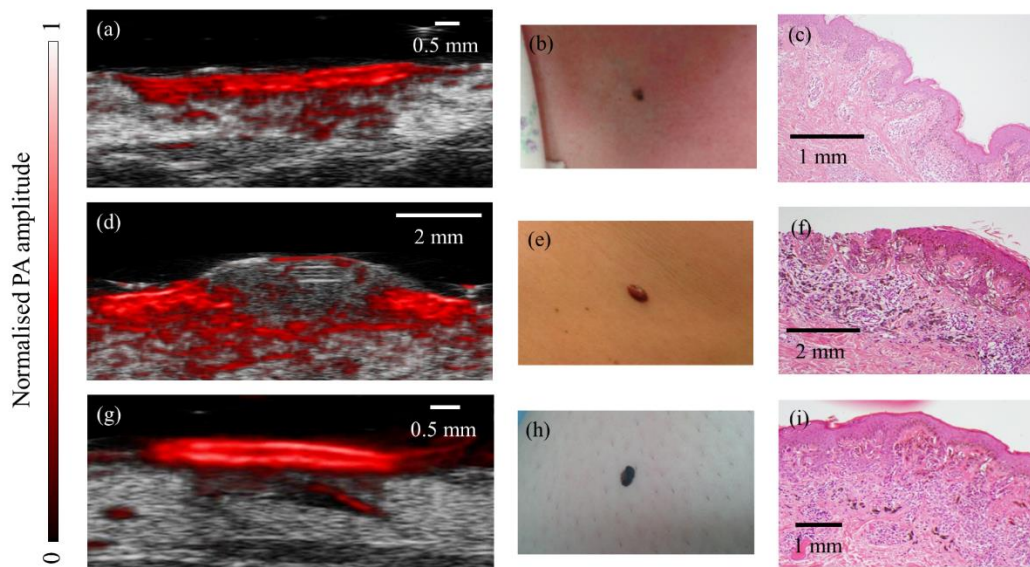


**Figure 4.2.** Coregistered linear-array based PAI of melanoma and benign skin lesions. (a) Coregistered PAI image of *in situ* melanoma with a PA depth of 0.3 mm. (b) *In situ* melanoma on chest. (c) Histology

of excised melanoma, with Breslow depth of 0.15 mm. Original magnification  $\times 4$ . (d) Coregistered PAI image of invasive melanoma on back, showing signs of dermal invasion, with a PA depth of 1.85 mm. (e) Invasive melanoma on back. (f) Histology after full excision, with a Breslow depth of 1.6 mm and Clarke level IV. Original magnification  $\times 4$ . (g) SU image of dysplastic nevus showing adnexal extension, with a PA depth of 0.36 mm and adnexal depth of 1.6 mm. (h) Dysplastic nevus on lower left extremity. (i) Histology of excised nevus, with a histological depth of 0.39 mm and adnexal depth of 2.08 mm. Original magnification  $\times 4$ .

Statistical analysis and plots of *in vivo* thickness measurements against histological thickness are shown in table 4.1 and figure 4.3. In figure 4.3, the slope of the linear fit indicates the sensitivity of the imaging system in estimating lesion depth. For PA and SU, the slope was found to be  $>1.1$ , indicating a tendency to over-estimate lesion thickness.

**Table 4.1.** CC, median percentage errors, and statistical significance of PAI and SU measurements of lesion thickness and adnexal depths, for melanomas and benign lesions.

Imaging modality	N	CC	Mean % error	t-test P value
PA benign	23	0.98 P < 0.001	13.4 %	0.60
SU benign	23	0.98 P < 0.001	13.1 %	0.67
PA melanoma	6	0.99 P < 0.001	22.3 %	0.76
SU melanoma	6	0.99 P < 0.001	22.1 %	0.80
SU adnexae	10	0.93 P < 0.001	37.8 %	0.44

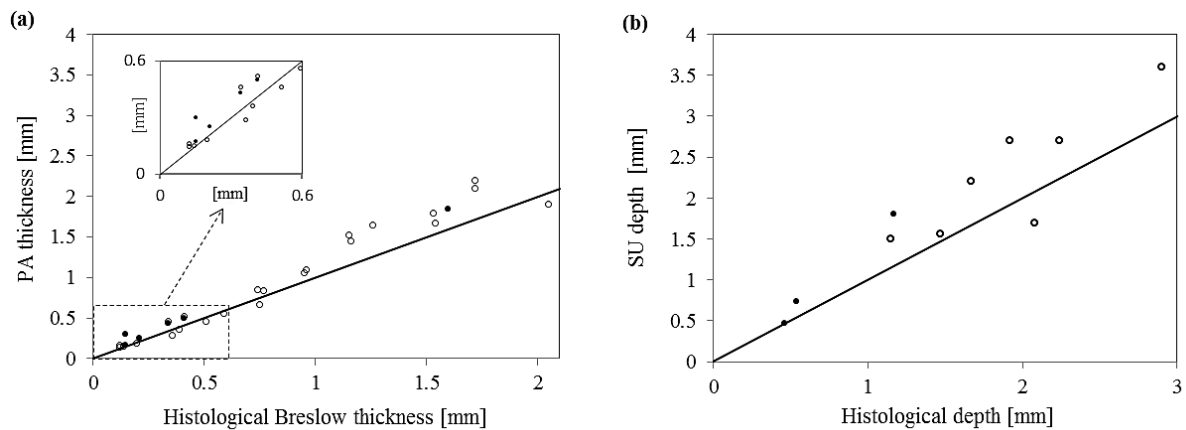


**Figure 4.3.** Correlation between *in vivo* measurements of melanomas (black circles) and benign lesions (clear circles) and histological measurements from biopsied samples (black line shows 1:1 agreement for PAI measurements and histological measurements). (a) Plot of primary lesion thickness measured with PAI against histological thickness. (b) Plot of adnexal tumour extension measured with SU against histological depths.

For benign lesions, PAI and SU gave a high correlation with the histological thickness, with a CC of 0.98 ( $P < 0.001$ ) for both. For cases where an *in vivo* measurement was possible, the mean PA thickness was 0.96 mm (range, 0.14 to 2.2 mm), giving a 13.4% error with the histological thickness of 0.84 mm (0.12 to 2.05 mm), whereas the mean SU thickness was 0.86 mm (0.13 to 2.0 mm), with a percentage error of 13.1%. Benign lesions thickness was overestimated in 69% of cases. For melanomas, a CC of 0.99 ( $P < 0.001$ ) was obtained for both PAI and SU. The mean percentage error for PA was 22.3%, for a mean PA thickness of 0.58 mm (0.17 to 1.85 mm) and mean Breslow thickness of 0.47 mm (0.15 to 1.6 mm). For SU, the mean percentage error was 22.1%, with a mean thickness of 0.56 mm (0.17 to 1.74 mm). Both PA and SU overestimated melanoma thickness in all cases. Adnexal measurements were reported in histology for 12 lesions, with SU depth measurement being possible in 10 cases. The CC between SU adnexal depth and histology was 0.93 ( $P < 0.001$ ). Mean histological depth was 1.56 mm (0.46 to 2.9 mm) compared with a mean SU depth of 2.15 mm (0.47 to 3.6 mm), with a percentage error of 37.8%. Two-tailed t-test analysis yielded no statistically significant differences between results for all measurement groups.

3D rendered scans of an *in situ* melanoma and benign lesion are shown in figure 4.4. 3-D PA scans provided a map of the overall lesion architecture, allowing for the thickest point to be

identified and correlated to the surface topography, which can be difficult with 2-D images. However, in some cases, 3-D scans had to be discarded due to movement artefacts.

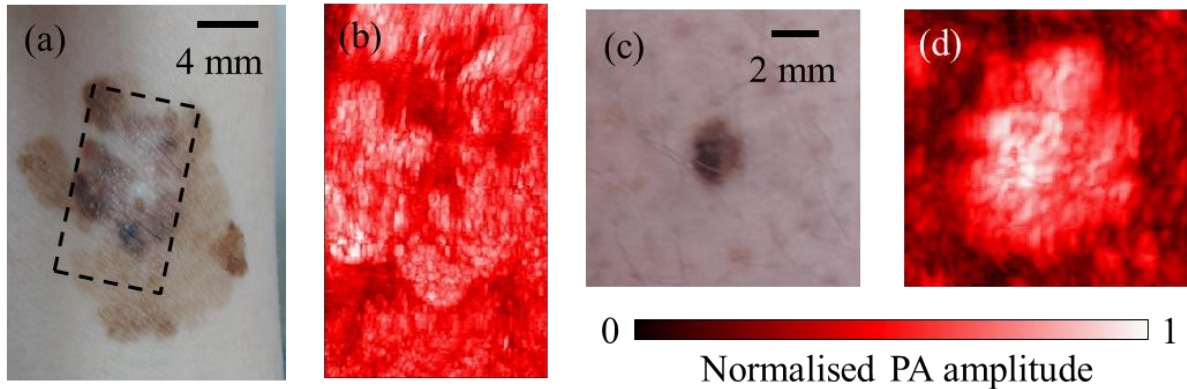


**Figure 4.4.** Rendered 3-D PA images of pigmented skin lesions taken using a stepper motor. (a) Large diameter melanoma *in situ* located on ventral aspect of wrist. (b) 3-D PAI scan (area 14 mm × 235 mm) of dashed region in (a) showing complex pigmentation pattern. (c) Compound melanocytic nevus located on lower left extremity. (d) 3-D PAI scan (area 4 mm × 4 mm) of lesion in (c). 3-D PA scans assessed lesion volume and allowed for the thickest portion to be registered to the surface, which can potentially guide incisional biopsy location and depth.

#### 4.4 Discussion

PAI represents a new technique for the *in vivo* evaluation of melanoma and benign skin lesions in dermatology. The main strength of PAI is its ability to image molecular changes at clinically significant depths. In this study, we have demonstrated the feasibility of PAI in measuring the *in vivo* depth of pigmented melanocytic nevi and melanomas on patients in the clinic. The use of a handheld, linear-array PA probe provided an easily applicable means of imaging the entire lesion architecture with high contrast, speed, and resolution.

PAI was found to accurately measure primary lesion thickness, for both melanocytic nevi and melanomas, as evidenced by the high CC obtained. In general, PAI, tended to overestimate lesion thickness compared with the histologically measured thickness. This was expected, as

dehydration of the resected samples in the histological sectioning process results in sample shrinkage, which is further compounded by loss of *in vivo* skin tension [166]. Although care was taken to ensure registration of the PAI measurement location with the histological sections obtained from biopsy, this cannot be guaranteed and could therefore effect measurement correlation. Moreover, unlike histology, handheld B-mode and 3D scans allow for the entire lesion volume to be assessed, and the deepest portion to be selected for measurement.

Lower lesion boundaries could not be determined for nevi in three cases, possibly due to strong optical attenuation from absorption in highly pigmented lesions or possible suboptimal directional placement of the PA probe.

PAI's ability to image the skin layers and lesion architecture with high contrast enabled it to distinguish between invasive and superficial lesions by their penetration through the dermal–epidermal boundary. Benign intradermal lesions were identified as such in all cases; however, epidermal lesions were misread as having a dermal presence in two cases due to irregular border profiles. For melanomas, PAI was able to structurally distinguish *in situ* melanomas from invasive melanomas in all cases. In cases where a melanoma diagnosis is made with an undersampled biopsy, preoperative knowledge of lesion penetration through the dermal–epidermal boundary could expedite and inform the treatment process, as this is a critical step in the metastatic development of melanoma.

SU had a slightly lower measurement error for primary lesion thickness; however, since the contrast ratio between the background tissue and pigmented lesions is high in the NIR, its accuracy over single-wavelength PAI at 680 nm was negligible. It is therefore recommended that single wavelength PAI is sufficient for imaging lesion lower boundaries. SU was able to track lesion extension in skin appendages in most cases and can potentially guide the surgical management of adnexal-based malignant tumours [167,168]. However, it had a large measurement error due to difficulty ensuring registration between *in vivo* sections and histology, and in the case of hair follicles, melanin presence in hair shaft made it difficult to determine where lesion extension ended.

The high correlation between PAI depth measurements and histopathology allows for the establishment of a linear depth index [166], which accounts for measurement errors, such as shrinkage effects. While PAI is more suited to imaging pigmented melanomas (>90% of cases),

it can potentially be used to image amelanotic melanomas as they still contain a low concentration of melanin. Our results show that handheld linear-array PAI could help guide biopsy depth and sample location, and thus improve staging and diagnostic accuracy and prevent the need for additional biopsies. Demonstrating the staging potential of PAI in the clinic is important, as it has the potential to diagnose melanoma and other skin cancers with the injection of targeted antibodies coupled with PA sensitive contrast agents [169]. While PAI shares the same means of detection and associated electronics as US imaging, it can have a considerably higher cost if pulsed nanosecond lasers are employed as the excitation source. However, it is still relatively inexpensive when compared with PET and MRI. PAI systems which employ inexpensive laser diode sources as the excitation means can significantly reduce costs, rendering PAI on the same cost level as US imaging [170].

#### ***4.5 Acknowledgements***

This research was supported by the Science Foundation Ireland (SFI) under Grant No. 12/RI/2338(4).

# **Chapter 5: Photoacoustic imaging of tumour oxygenation level in breast cancer and neoadjuvant chemotherapy patients.**

## ***5.1 Introduction***

Breast cancer is the most frequently occurring malignancy in women worldwide and is the leading cause of cancer mortality, resulting in up to half a million women dying of the disease in 2008 alone [171]. In the United States, breast cancer is the second most common cause of death among women after lung cancer [172]. Early detection and accurate diagnosis of breast cancer is vital to ensure patient survival, with imaging technologies playing a crucial role. Imaging methods for breast cancer detection have made significant advances in recent years, however, there currently exists no imaging modality with sufficient sensitivity and specificity to enable it to be sufficient for standalone application [173–175].

Currently, X-ray mammography is the gold standard for screening asymptomatic women for breast cancer and has been shown to decrease mortality [176–178]. In screening, X-ray mammography demonstrates an overall sensitivity and specificity of 80% and 90%, respectively [19]. However, sensitivity has repeatedly been shown to decrease for younger age groups and for denser breasts [179]. The sensitivity of X-ray mammography in dense breasts containing a high fraction of fibroglandular tissue, more common in younger women (<50 yr), can fall as low as 45%, in comparison to near 100% sensitivity in predominantly fatty breasts, more common in older women [179–181]. This decreased sensitivity is caused by the increased radiographic absorption of fibrous and glandular breast tissue compared to fat, which obscures tumours on X-ray images. In addition, fibroglandular tissue may have similar X-ray absorption properties to breast tumours [182,183]. To overcome these limitations, optical imaging methods employing lasers are being investigated to detect lesions obscured by overlapping breast tissue common in women with dense breasts. X-ray mammography has the additional drawbacks of using ionizing radiation and involves painful breast compression during scanning.

US imaging is usually employed alongside mammography in breast cancer screening and has an important role in lesion detection, image-guided biopsy, and lymph node diagnosis [184,185]. US images differences in tissue density and can distinguish between a solid tumour and fluid filled cysts by the difference in echogenicity. However, it suffers from suboptimal sensitivity and specificity in many cases and has poor contrast in soft tissue. In addition, it is limited by inter-operator dependence.

Diffuse optical imaging (DOI) technologies using NIR light have been applied to quantitatively characterise the optical absorption and scattering properties of breast tissue in either transmission or reflectance modes [186–188]. DOI has reported average levels of haemoglobin in malignant tumours to be a factor of two higher than breast parenchyma [189]. The main drawback of DOI is its poor spatial resolution owing to the highly scattering nature of tissue in the NIR, which can mask heterogenous distributions of blood and obscure tumour morphology for all but the largest of tumours.

MRI can detect the increased microvascular density and haemoglobin concentration associated with malignant tumours for high-sensitive imaging of cancer by imaging the extravasation of contrast agent from the blood vessels. MRI demonstrates higher sensitivity to breast lesions than mammography (at the expense of specificity) and has been explored as an alternative to improve diagnostic accuracy in dense breasts [190,191]. The American Cancer Society has recommended that MRI be used as an annual screening test for women with a greater than 20% risk of breast cancer development in their lifetime [192]. Dynamic contrast enhanced MRI is the most widely used MRI technique for breast cancer detection, employing gadolinium-based exogenous contrast agents [193]. While it has many advantages, MRIs drawbacks include the requirement of exogenous contrast agents, its expense, and the fact that it is not routinely available for clinical screening.

When malignant breast tumours reach approximately 1-2 mm in diameter ( $\approx 10^6$  cells) the inner core can no longer be sustained by nutrient diffusion, resulting in hypoxia [194]. The hypoxia causes the increased secretion of pro-angiogenic growth factors from tumour cells such as vascular endothelial growth factor, leading to the formation of new microvasculature characterised by its chaotic structure and leaky capillaries [195]. The formation of new tumour vasculature in this manner is referred to as pathological angiogenesis. The chaotic distribution of the new vasculature leads to heterogenous perfusion and avascular regions, resulting in further hypoxia. Total haemoglobin concentration has been shown to be higher in malignant

tumours compared with the surrounding healthy breast tissue, which enables their detection with optical imaging technologies due to the increased optical contrast [187].

Haemoglobin is the primary endogenous biological component that is evaluated by NIR optical imaging techniques due to its high optical absorption and tissue concentration. Increased haemoglobin concentration at tumour sites has been shown to correlate with abnormal angiogenesis and an increase in microvascular density [189], a hallmark of cancer. The absorption coefficient of haemoglobin in whole blood (150 g/L) is  $\approx 0.62 \text{ cm}^{-1}$  at 756 nm, whereas the absorption coefficient of haemoglobin-free breast tissue parenchyma at this wavelength has been reported to be much lower, in the range of  $0.04\text{-}0.05 \text{ cm}^{-1}$ , and the reduced scattering coefficient of all breast tissue lies in the range of 8 and  $12 \text{ cm}^{-1}$  [196]. The average breast effective optical attenuation coefficient is therefore in the range of  $1.0\text{-}1.3 \text{ cm}^{-1}$ , which is not much greater than the reported range for X-rays at mammographic energies of  $0.5\text{-}0.8 \text{ cm}^{-1}$  [196]. However, the optical contrast difference between highly perfused tissues (e.g. a malignant tumour) and less perfused tissues (e.g. fat, glandular tissue) is estimated to differ by a factor of 4, which is significantly greater than the same contrast difference observed with mammographic X-rays. This fact is the basis for the belief that PAI at NIR wavelengths can be used to detect breast cancer lesions using nothing more than endogenous contrast associated with the increased haemoglobin concentration due to pathological angiogenesis observed in tumours.

In contrast to X-ray mammography, it has been reported that PAI shows no significant difference in image contrast between high and low density breasts, which is very promising for its application in breasts with a high fraction of radiodense glandular tissue, where the sensitivity of X-ray mammography is reduced [197]. In addition, PAI has been shown to have a very good to excellent correspondence with MRI for the detection of breast malignancies [197].

PA imaging of the breast was first proposed in 1994 and since then several breast imaging prototypes have been developed [198]. Dedicated PA mammography systems are generally designed with a large field of view, with spatial resolution being sacrificed in favour of increased penetration depth (up to 5 cm) with the selection of lower central frequency transducers ( $< 2 \text{ MHz}$ ).

The laser optoacoustic imaging system (LOIS) for the detection of breast cancer was proposed over two decades ago by Oraevsky *et al* [199], and since then has gone through considerable

development. A more recent publication describes a system designed to image a single breast in a hemispherical volume using an arc-shaped array of 64 ultrawide-band acoustic transducers [200]. The LOIS system schematic is shown in figure 5.1. A Q-switched alexandrite laser (75 ns, 750 mJ/pulse, 10 Hz) operating at 757 nm irradiates the breast with a 70 mm beam diameter incident normal to the imaging plane and a single frame can be captured in the craniocaudal or mediolateral projections. The system spatial resolution in the imaging plane on breast phantoms was reported to be at least 0.5 mm, a considerable improvement over DOI, however, cross-plane spatial resolution was relatively poor. 3D images can be acquired by rotating the imaging device around the breast; however, cross-plane resolution is relatively poor.

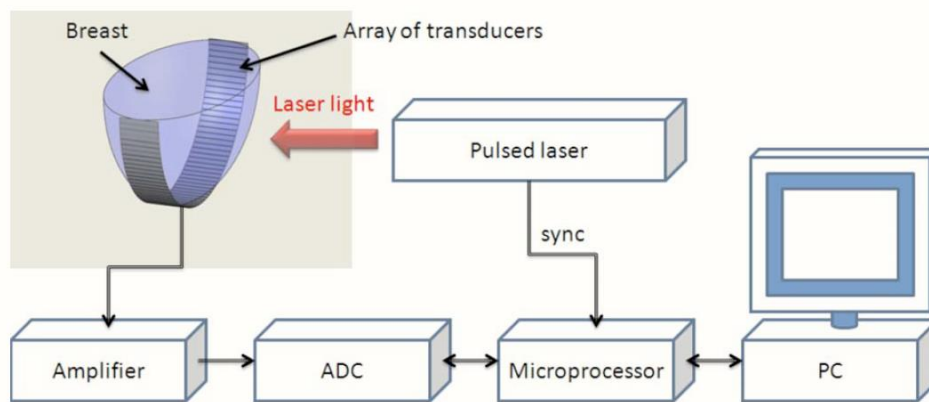


**Figure 5.1.** Schematic diagram of LOIS optoacoustic imaging system. Reproduced with permission from [200].

The Twente photoacoustic mammoscope, developed by Manohar *et al* in 2004 [201,202], employed a parallel plate geometry in which a single breast is placed for transmission mode imaging. The system schematic diagram is shown in figure 5.2. The detection mechanism consisted of a flat high-density ultrasound detector matrix composed of 590 PVDF transducers with an individual transducer detection frequency of 0.5 MHz (80% bandwidth). A 1064 nm Q-switched Nd:YAG laser (5 ns, 50 mJ/pulse, 10 Hz) with a 16 mm beam diameter served as the excitation source. Scans are acquired by translating the light-coupled scanning mechanism across the breast, with the total scan time reported to be 20 minutes and a spatial resolution of 3.5 mm. Clinical studies with this system have shown promising results, with 32 of 33 measured breast malignancies being imaged with high contrast and good co-localisation with conventional breast imaging techniques (X-ray mammography and ultrasonography) [203]. The drawbacks of the system include the need for breast compression, long scan time, and the limited field of view which prevents whole-breast coverage in a single scan.

Recently the Twente photoacoustic mamoscope 2 was introduced, which overcomes the limitations of the previous system [204]. The new system employs a tomographic imaging configuration which images the breast pendant inside an imaging tank filled with water while the woman lies on a bed in the prone position. The imaging tank configuration is depicted in figure 5.3. The breast is illuminated with a large laser beam directed at the nipple and through nine optical fibre bundles positioned around the breast near the chest wall. The light source consisted of a dual laser system comprising an Nd:YAG and an alexandrite Q-switched laser operating at 1064 nm and 755 nm, respectively. US signals are detected with 12 arc-shaped detection arrays, each curving along the pendant breast. Each array contained 32 piezocomposite elements with a central frequency of 1 MHz. During scanning, the imaging tank rotates in steps around the breast for a tomographic scan. The systems *in vivo* performance was tested on the breasts of two healthy volunteers, with the resulting images showing the breast vasculature, breast contour, and nipple anatomy with high optical contrast. The system resolution was estimated to be 0.96 mm and 1.06 mm in the elevational and lateral directions, respectively.

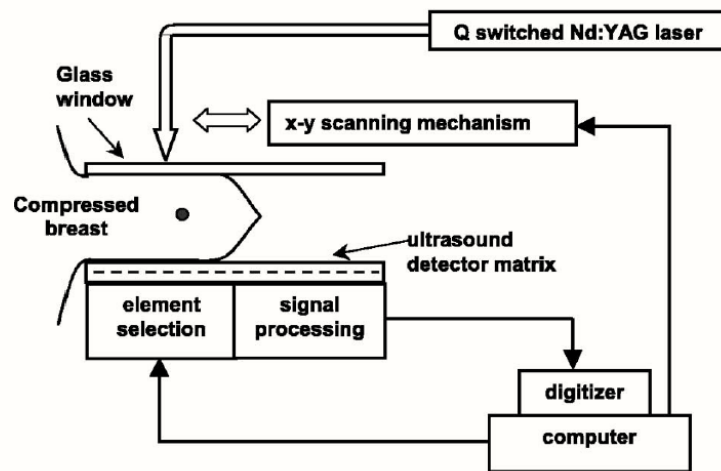


**Figure 5.2.** Schematic diagram of the Twente photoacoustic mamoscope showing parallel plate geometry. Reproduced from [201] with permission.

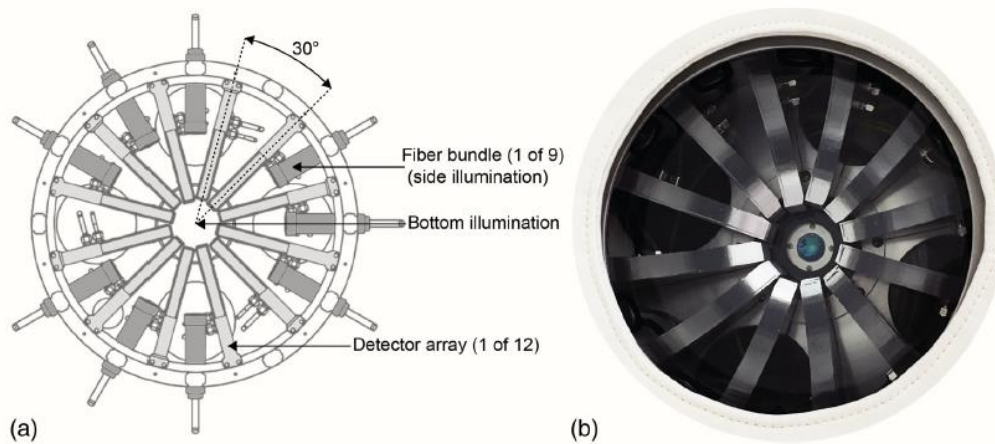


**Figure 5.3.** (a) Top view drawing of the imaging tank and (b) photograph of the imaging tank. Figure reproduced with permission from [204].

Kruger *et al* [196] developed a PA mammography system employing a hemispherical detection aperture in which the breast is placed with the patient lying in the prone position. Water is used in the hemispherical cup as the means of acoustic coupling. The hemispherical detection array (shown in figure 5.4) contains 512 discrete ultrasonic transducer elements, each having a 2 MHz central detection frequency and a 70% bandwidth. The excitation source consisted of a 7-mm beam diameter, pulsed alexandrite laser (75 ns, 300 mJ/pulse, 10 Hz) operating at 756 nm, and was directed vertically upward through the center of the array and focused on the breast with a converging lens with a beam diameter of 60 mm, resulting in a surface fluence of  $10 \text{ mJ/cm}^2$  at the beam center. The detection array is scanned in a spiral shape with a radius varying from 24 to 96 mm, creating a field of view that can accommodate a wide range of breast sizes. Imaging depth was reported to be 53 mm. The system spatial resolution was reported at 0.42 mm with a maximum imaging depth of 53 mm. Demonstrations showed the system capable of imaging breast vasculature as far as the chest wall, showing promise for future clinical applications.

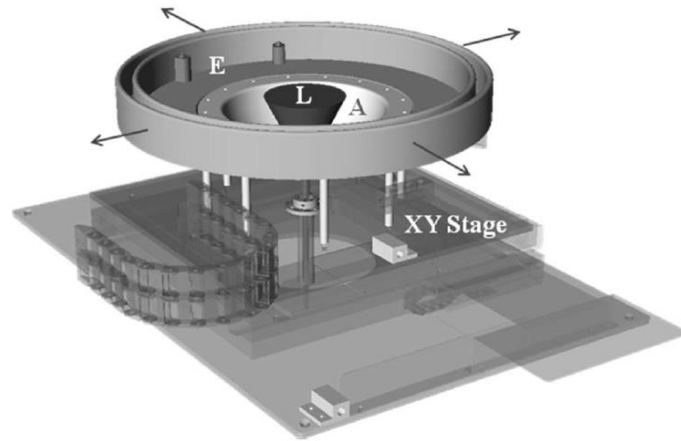


**Figure 5.4.** Drawing of 3D PA mammography system hemispherical detection array mounted on an XY translation stage. Reproduced from [196] with permission.

In recent years NIR optical imaging techniques have been used to monitor neoadjuvant chemotherapy response in breast cancer tumours [186,205,206]. Neoadjuvant chemotherapy, or preoperative systemic therapy, is in widespread use as a standard treatment for locally advanced breast cancer and is used on breast cancer patients with operable tumours prior to definitive surgery [207]. One of the main goals of neoadjuvant chemotherapy is to achieve a reduction in tumour volume via regression prior to lumpectomy, thereby allowing smaller surgeries and less tissue damage, potentially conserving the functional and cosmetic aspect of the breast. Another main objective is to combat or reduce the probability of tumour metastases prior to either lumpectomy or mastectomy. Patients who display a pathologically complete response to neoadjuvant chemotherapy have a higher probability of overall survival and a reduction in disease reoccurrence. Unfortunately, however, between 8 and 20% of women with locally advanced breast cancer experience no clinical or pathological response despite undergoing months of treatment and thus endure toxic side effects with no therapeutic benefit [85,86]. It is therefore of critical importance to determine which patients are responding and which are not so that alterations to treatment strategy can be made. One way this is achieved is by monitoring for non-invasive biomarkers indicative of treatment response that would enable physicians to make evidence-based decisions to change treatment to improve therapeutic outcome.

Previous neoadjuvant studies with DOI monitoring for pathological complete response in breast cancer tumours have shown reductions in concentrations of oxy- and

deoxyhaemoglobin, as well as water, within the first week of treatment and continuing until definitive surgery [86]. The results indicate a consistent response between different tumour types and chemotherapy regimens. A clinical study by Tromberg *et al* [85] showed that functional biomarkers measured with quantitative DOI on the first day after neoadjuvant chemotherapy administration correlated with non-responding patients. In the study, 23 patients with 24 primary breast cancer tumours in total underwent quantitative DOI to measure absolute concentrations of oxy- and deoxyhaemoglobin, water, and lipid in the tumours and normal breast tissue. Measurements were made immediately before the start of chemotherapy, 1 day after, and at various other timepoints over a 7-day period. The DOI measurements were compared with postsurgical pathological response for each patient, where it was observed that:

1. a statistically significant oxyhaemoglobin flair was observed in partially responding or pathologically complete responding tumours on day 1 of treatment.
2. Non-responding patients showed no oxyhaemoglobin flair and a subsequent decrease in oxyhaemoglobin concentration in tumours on day 1.
3. The observed differential in oxyhaemoglobin concentration was enough to distinguish responding from non-responding tumours.

The results are shown in figure 5.5. represented as oxyhaemoglobin percentage, or sO<sub>2</sub> level. The results demonstrate that an early indication of non-responding patients is possible on the first day of treatment, potentially allowing treatment strategy to be altered and needless patient trauma to be avoided.

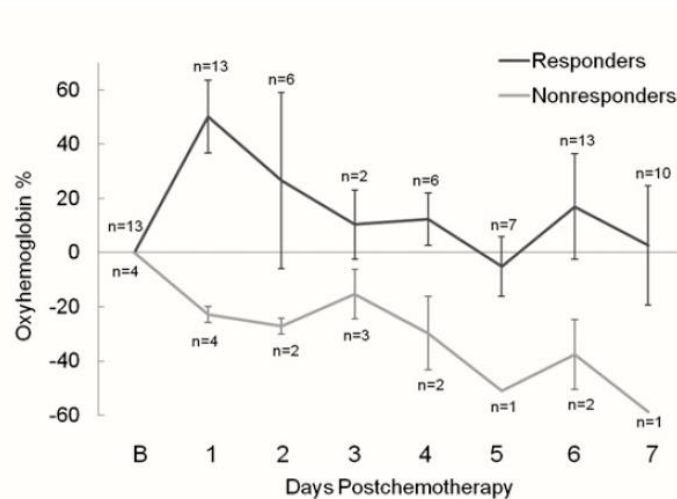


**Figure 5.5.** Change in oxygenation level of responding and non-responding tumours on days 1-7. Reproduced from [85] with permission.

## ***5.2 Materials and methods.***

The aim of the study was to investigate the efficacy of handheld linear-array PAI in the management of breast cancer in the following areas:

- (a) Image breast lesion morphology.
- (b) Predict tumour malignancy by measuring intratumoural hypoxia.
- (c) Monitor for changes in intratumoural oxygen level post administration of neoadjuvant chemotherapy to determine responding from non-responding patients.

To achieve this, 31 patients with breast lesions suspicious of malignancy were recruited from the symptomatic breast unit (SBU) in Galway University Hospital to undergo a PA scan of the suspect lesion. Before recruitment, each patient was informed of the nature of the study and signed a consent form. Ethical approval for the study was granted by the Clinical Research and Ethics Committee of Galway University Hospital. During scanning, the patient and PAI system operators were required to wear laser safety goggles that blocked light in the wavelength ranges under study.

The criteria for inclusion in the study were that the patient was (1), over 18 years of age, (2), capable of providing written and informed consent, and (3), that the suspect lesion be relatively superficial i.e., within 2-3 cm from the skin surface in order to be within the imaging depth range of the system. The latter was determined before scanning from physical examination of the patient by a breast surgeon and/or from conventional imaging (US or X-ray mammography) by a consultant radiologist.



**Figure 5.6.** Vevo® LAZR PAI system setup in the SBU, showing laser cart, computer station, and examination table.

The PAI system setup in the SBU is shown in figure 5.6. The scanning procedure consisted of lying the patient in the supine position on the examination table and then applying the linear-array probe to the breast to take coregistered PA and US scans of the tumour mass and control breast (contralateral breast). Each scanning session took approximately 15-20 minutes to complete. The tumour mass in the suspect breast was initially located using B-mode US. Following this, coregistered PA and US scans were taken of the lesion with single-wavelength mode at 800 nm, followed by an sO<sub>2</sub> and relative haemoglobin concentration (HbT) scan using the in-built algorithm in the Vevo® LAZR system (VisualSonics Inc.). The system algorithm employed two wavelengths, 750 nm and 850 nm, to produce parametric maps of absolute sO<sub>2</sub> and relative HbT (figure 3.3), and was based on the following equations developed by Wang *et al* [208]:

$$\mu_a^{\lambda_1}(r) = \frac{P^{\lambda_1}(r)}{\Gamma F^{\lambda_1}(r)}, \quad 5.1$$

$$\mu_a^{\lambda_2}(r) = \frac{P^{\lambda_2}(r)}{\Gamma F^{\lambda_2}(r)}, \quad 5.2$$

$$HbT(r) = \frac{a_1\mu_a^{\lambda_1}(r) - a_2\mu_a^{\lambda_2}(r)}{a_3}, \quad 5.3$$

$$sO_2(r) = \frac{a_4\mu_a^{\lambda_2}(r) - a_5\mu_a^{\lambda_1}(r)}{a_6\mu_a^{\lambda_1}(r) - a_7\mu_a^{\lambda_2}(r)}, \quad 5.4$$

where  $\mu_a^{\lambda_1}(r)$  and  $\mu_a^{\lambda_2}(r)$  are the absorption coefficients,  $P^{\lambda_1}(r)$  and  $P^{\lambda_2}(r)$  are the peak photoacoustic pressures,  $F^{\lambda_1}(r)$  and  $F^{\lambda_2}(r)$  are the optical fluences, at wavelengths  $\lambda_1$  and  $\lambda_2$  (750 nm and 850 nm, respectively), and at the voxel at position  $r$ , respectively, and  $a_{1-7}$  are coefficients. As can be seen from equations 5.1 and 5.2, the method assumes a linear relationship between optical absorption and the peak photoacoustic amplitude for a given voxel, and no correction for optical fluence attenuation of the incident light is made. The system allows for the average  $sO_2$  and HbT values within a region of tissue defined by the user to be calculated. For the choice of wavelength selection, 800 nm was chosen for single wavelength scans as here the optical scattering is relatively low while sensitivity to haemoglobin is relatively high, while for the  $sO_2$  algorithm, 750 nm and 850 nm were used due to the high sensitivity of haemoglobin to oxygen at 750 nm and 850 nm, respectively. In addition to measuring  $sO_2$  and HbT within the tumour (termed the intratumoural space), the same measurements were carried out in a region outside the tumour (termed the extratumoural space) at the same depth, and in the contralateral breast. The scanning procedure for any patients recruited that were scheduled to begin neoadjuvant chemotherapy was to carry out single wavelength,  $sO_2$ , and HbT scans immediately pre-treatment (day -1), and post treatment at days 1-7. However, follow-up scans post treatment for these patients was not possible due to logistical reasons, as will be discussed later.

Scans were initially carried out using US gel as the acoustic coupling medium, however, in most cases the reflection artefact, caused by US wave reverberation between the skin surface and the transducer surface, appeared at the tumour depth which caused it to be obscured. To correct for this, an ultrasound gel pad (Aquaflex® Ultrasound Gel Pad, Parker Laboratories, USA), shaped to fit the probe shape, was placed on the end of the probe (shown in figure 5.7).

The gel pad was secured to the probe head with clear plastic film, which was then taped to the body of the probe. This allowed for a constant distance between the probe head and the skin surface to be maintained and resulted in the reflection artefact being pushed below the imaging depth range.

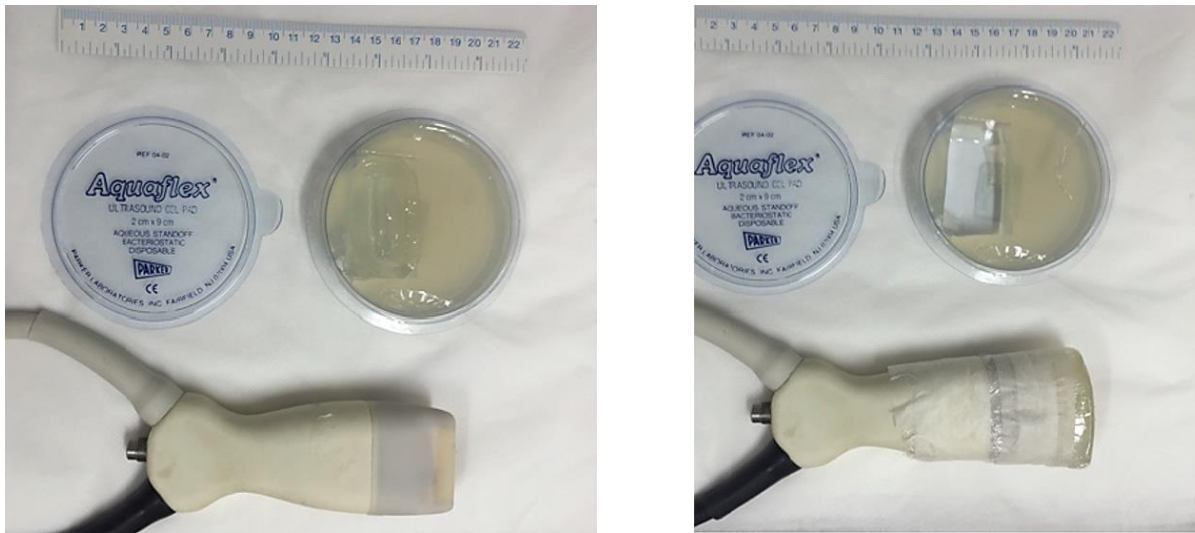


**Figure 5.7.** (Left) PA imaging probe (15 MHz) with US gel pad showing a section of the pad cut out to fit the shape of the probe head. (Right) PA probe with Gel pad attached at the head and held in place with clear plastic film wrapped over the probe and secured with tape on the body of the probe.

At the beginning of the study PA scans were carried out using the 21 MHz linear-array probe (outlined in section 2.10), which was the lowest frequency probe available at the time. However, it was found that the maximum achievable penetration depth ( $\approx 5$  mm) in breast tissue *in vivo* was not sufficient to image superficial breast lesions. Other factors that negatively affected image quality at this time included suboptimal laser energy caused by optical misalignment when moving the PAI system to the SBU, and the use of US gel as the coupling medium instead of the gel pad. In total, 16 patients were scanned with the 21 MHz probe, however, due to the above listed reasons, image quality was poor, and it was not possible to image lesion morphology.

To improve image quality, a lower-frequency, prototype 15 MHz probe was acquired from VisualSonics Inc. The 15 MHz probe followed the same design as the 21 MHz and 40 MHz probes outlined in section 2.10, and had a 5 x 32 mm transducer element array, bandwidth range of 8-19 MHz, lateral and axial resolutions of 250  $\mu$ m and 100  $\mu$ m, respectively, and a

focal depth of 13 mm. When the probe was initially obtained it was found to have severe reverberation artefacts caused by the lack of a spectrally neutral acoustic covering on the transducer surface. Upon reporting this, the probe was returned to the manufacturer to allow for said covering to be added. In addition, to improve the laser pulse energy the system was realigned by a laser technician from VisualSonics Inc. With these changes made, image quality and penetration depth ( $\approx 13$  mm) improved, and the first PA images of lesion morphology were obtained. In total, 15 patients were scanned with the 15 MHz probe, which included 6 benign lesions (4 fibroadenomas and 2 cysts), 5 malignant lesions (including 2 neoadjuvant chemotherapy patients), and 4 healthy breast patients scanned as a control. For the 2 neoadjuvant patients scanned, follow-up scans were not possible post administration of chemotherapy due logistical reasons, as outlined in section 5.2.3. The data taken from these patients was instead added to the malignant tumour group. The mean age of patients scanned was 46 with a range of 19-77 years. Since the scans taken with the 21 MHz probe were suboptimal, only the scan results from the 15 MHz probe are presented here.

## ***5.3 Results and discussion***

### **5.3.1 Benign lesions**

Excisional biopsy confirmed 6 out of the 11 lesions scanned with the 15 MHz probe to be benign. This included 4 fibroadenomas and 2 breast cysts. In addition, 4 scans were taken of healthy breasts (with no lesions) to establish a baseline  $sO_2$  reading for the system, this was done to see if any differences in tissue oxygenation level were found between these and the control breasts on the suspect lesions. The healthy breast scans were performed on healthy women who were consented after screening.

Of the 6 benign lesions scanned, 3 were found to be too deep to scan ( $> 1.3$  mm in depth), which included 1 fibroadenoma and 2 breast cysts. PA absorption contrast was visible on the upper surface of each fibroadenoma within the system depth range. The average intratumoural  $sO_2$  values measured within the 3 fibroadenomas scanned (patients 1-3), as well as in the

control breasts, are shown in table 5.1, while the average sO<sub>2</sub> within the healthy breast tissue is shown in table 5.2 (patients 4-7).

**Table 5.1.** Average sO<sub>2</sub> values measured from within the fibroadenomas (intratumoural) and from the contralateral breasts (control), for patients 1-3.

Patient no.	Average intratumoural sO <sub>2</sub>	Average control sO <sub>2</sub>
1	68.3 ± 2.1%	66.1 ± 1.9%
2	65.0 ± 2.0%	69.8 ± 2.1%
3	70.1 ± 2.1%	66.3 ± 1.8%

**Table 5.2.** Average sO<sub>2</sub> values measured from within healthy breasts for patients 4-7.

Patient no.	Average sO <sub>2</sub>
4	70.3 ± 2.4%
5	67.6 ± 1.1%
6	65.9 ± 1.7%
7	69.5 ± 1.4%

An example side-by-side PA and US scan of a fibroadenoma on patient 1 is shown in figure 5.8. The fibroadenoma can be seen circled as the dark anechogenic region in the US image at an image depth of ≈ 21 mm. The surface of the lesion can be seen circled in the corresponding PA scan at ≈ 6 mm from the tissue surface. Figure 5.9. shows a parametric sO<sub>2</sub> map of the fibroadenoma on the same patient. Regions of high tissue oxygenation are indicated in red, lower oxygenation in blue, and regions of very low oxygenation in black. The scan shows the oxygenation level is approximately constant with depth and no significant difference in sO<sub>2</sub> is

observed between the intratumoural and extratumoural tissue. The average  $sO_2$  level within the intratumoural region outlined in figure 5.9 was measured at  $68.3 \pm 2.1\%$ . For the 3 benign lesions scanned thus far, no signs of tumour hypoxia or difference in oxygenation level was observed between the intra and extratumoural regions. In addition, no significant difference in  $sO_2$  was found between the intratumoural regions (mean  $sO_2 = 67.8 \pm 2.6\%$ ) and the control breasts (mean  $sO_2 = 67.4 \pm 2.1\%$ ).

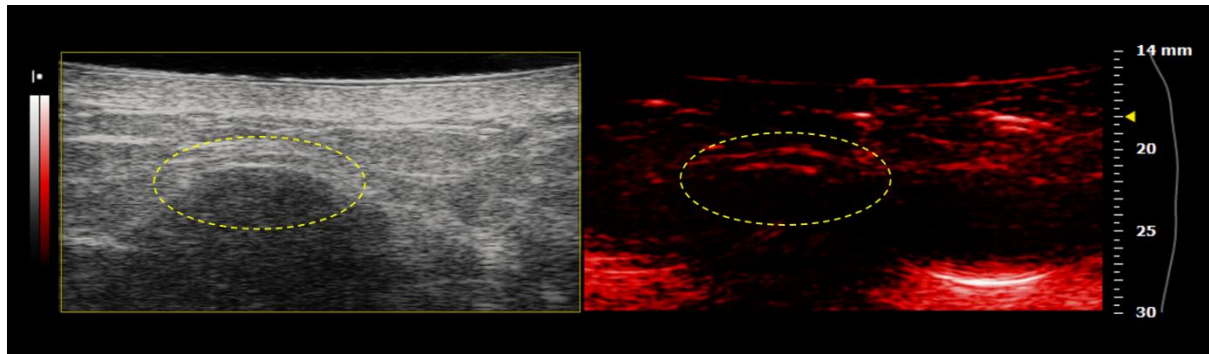


**Figure 5.8.** Coregistered US image (left) and PA image (right) of a fibroadenoma (shown marked) at an image depth of  $\approx 21$  mm. The highly absorbing region on the PA image at an image depth of  $\approx 27$  mm is an image artefact caused by an air bubble in the gel pad.

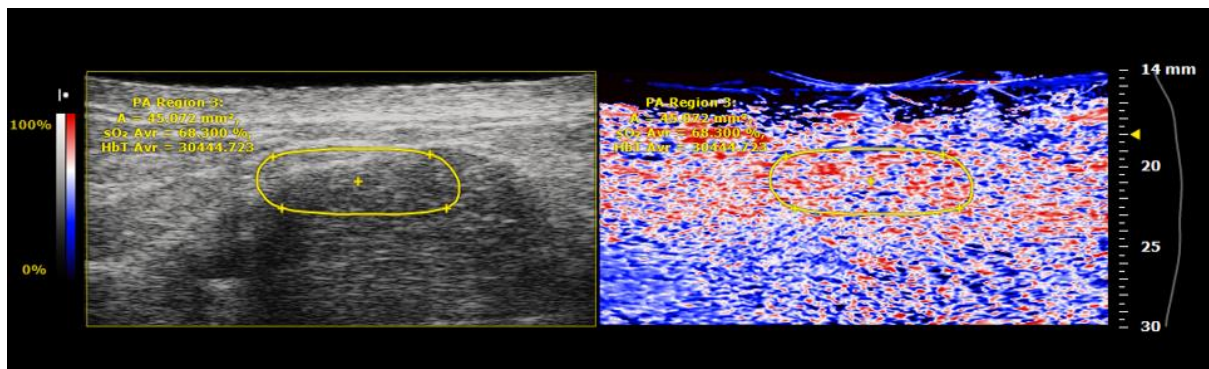


**Figure 5.9.** Coregistered US image (left) and PA image (right) of the fibroadenoma shown in figure 5.8. The average intratumoural  $sO_2$  is measured in the yellow region.

The  $sO_2$  values measured in the 4 healthy breast patients (mean  $sO_2 = 68.3 \pm 1.97\%$ ) also showed no significant difference compared with the values measured in the benign lesions or the control breasts. An example  $sO_2$  and US scan of a healthy breast patient, patient 4, is shown in figure 5.10. The average  $sO_2$  in the marked region was measured at  $70.3 \pm 2.4\%$ . No significant variation in  $sO_2$  was found between the 4 healthy patients scanned.

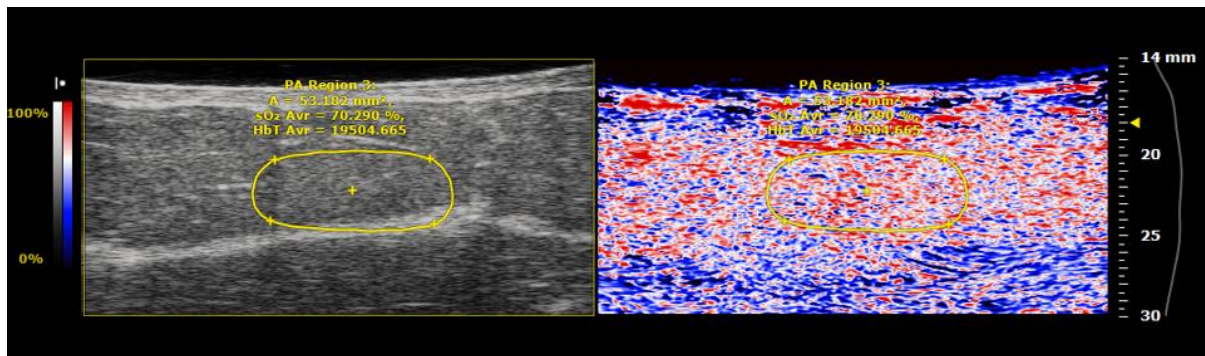


**Figure 5.10.** Coregistered US image (left) and parametric  $sO_2$  map (right) of a healthy breast patient. The average tissue  $sO_2$  is measured in the yellow region.

### 5.3.2. Malignant tumours and NAC patients

In total 5 consenting patients with malignant tumours, as confirmed via excisional biopsy, were scanned using the 15 MHz probe. Of the 5 that were scanned, 1 was too deep to be imaged ( $> 1.3$  mm), while the upper boundary of the tumour morphology on the remaining lesions was visible on the PA scans at 800 nm. Two of the 5 patients with malignant tumours were scheduled to begin neoadjuvant chemotherapy soon after the scan date, however, due to logistical issues caused by the patients undergoing treatment at their regional facilities, it was not possible to conduct further PA scans. The  $sO_2$  data obtained from these patients was to be used as the baseline  $sO_2$  measurement in a longitudinal study monitoring  $sO_2$  status within the tumour post treatment, but since this was not possible, the  $sO_2$  data is best interpreted as a sign of tumour hypoxia which may indicate malignancy. The average  $sO_2$  values measured in the intratumoural and extratumoural regions in the same breast, and in the control breast, for the malignant tumour patients (patients 8-11) are shown in table 5.3.

**Table 5.3.** Average sO<sub>2</sub> values measured from within the tumour (intratumoural), outside the tumour in the same breast (extratumoural), and from the contralateral breast (control) for patients 8-11.

Patient no.	Average intratumoural sO <sub>2</sub>	Average extratumoural sO <sub>2</sub>	Average control sO <sub>2</sub>
8	48.3 ± 4.9%	66.1 ± 4.5%	69.8 ± 1.3%
9	49.3 ± 6.3%	66.2 ± 3.9%	71.5 ± 2.1%
10	55.5 ± 3.8%	63.3 ± 3.0%	66.7 ± 2.9%
11	69.6 ± 1.1%	71.1 ± 1.6%	NA

Figure 5.11 shows a side-by-side PA and US image of a malignant breast tumour in the 1 o'clock position, with the tumour region circled. The patient in question (patient 8) was a 48-year-old woman that was scheduled to begin neoadjuvant chemotherapy soon after scanning. The tumour can be seen as the dark, anechogenic region in the US image, at a depth of  $\approx 8$  mm from the tissue surface. A region of high optical contrast at the same depth can be seen on the corresponding PA image matching the morphology observed on the US, which is assumed to be from the tumour surface.

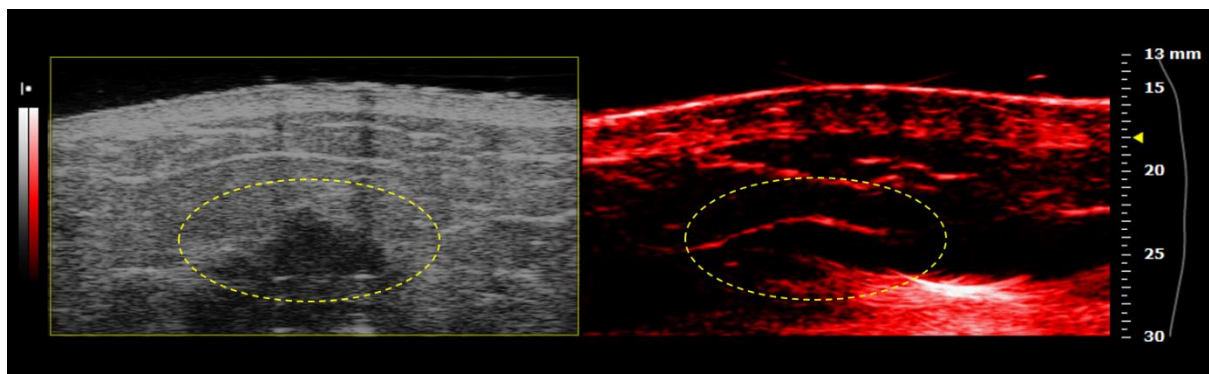


**Figure 5.11.** Coregistered US image (left) and PA image (right) of a malignant breast tumour (shown marked) in patient 8 at an image depth of  $\approx 22$  mm. The highly absorbing region on the PA image at an image depth of  $\approx 27$  mm is an image artefact caused by an air bubble in the gel pad.

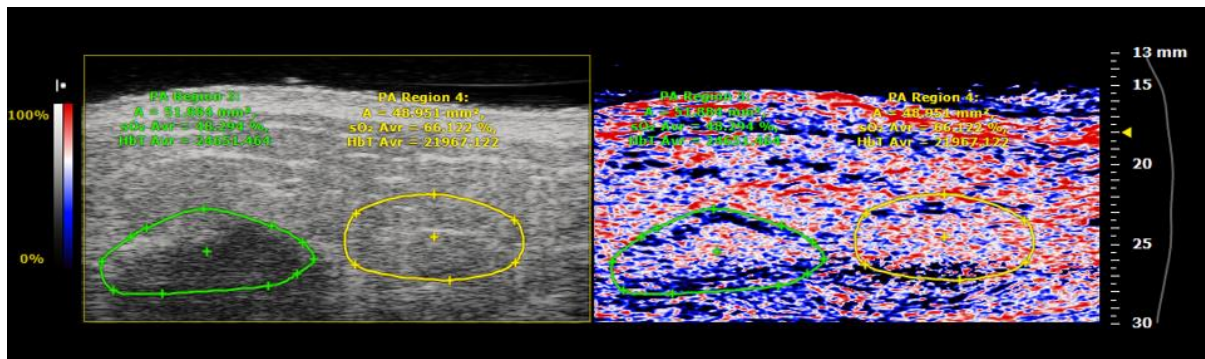


**Figure 5.12.** Coregistered US image (left) and parametric sO<sub>2</sub> map (right) of the same malignant breast tumour shown in figure 5.11. The green and yellow regions show the average sO<sub>2</sub> and average haemoglobin concentrations (relative units) in the intertumoural and extratumoural regions, respectively.

Figure 5.12 shows a parametric sO<sub>2</sub> map of the tumour from the same patient in figure 5.11. The average sO<sub>2</sub> was measured within the tumour and a region of normal breast tissue at the same depth, shown marked in the green and yellow regions in figure 5.12, respectively. A dark region of low oxygenation level can be seen outlining the tumour surface in the green region, as well as areas within the tumour, which appear lower than the surrounding tissue. The average sO<sub>2</sub> in the tumour region was measured at  $48.3 \pm 4.9\%$ , while the average sO<sub>2</sub> in the tissue outside the tumour was  $66.1 \pm 4.5\%$ . Additionally, the sO<sub>2</sub> in the control breast was as  $69.8 \pm 1.3\%$ . The absolute sO<sub>2</sub> difference between the intratumoural and extratumoural regions within the same breast of 17.9%, and the same difference between the tumour region and the control breast of 23.1%, may indicate tumour hypoxia and possible malignancy. The average haemoglobin concentration measured in the intratumoural region in figure 5.12 was also 112.2% greater than in the extratumoural region, which may indicate increased vascular density.

A coregistered PA and US scan of a malignant breast tumour in the 2 o'clock position on a 61-year-old woman (patient 9), not set to undergo neoadjuvant chemotherapy, is shown in figure 5.13. The tumour can be seen circled in the US scan as the slightly darker, anechogenic region. The corresponding PA image appears to show the tumour surface at an image depth of  $\approx 20$  mm, denoted by a region of high optical absorption. Increased PA absorption contrast is also visible within the tumour area. Figure 5.14 shows the corresponding sO<sub>2</sub> scan of the same region. The intratumoural region shows a reduced oxygenation level compared to the rest of the breast and is delineated by regions of low oxygenation level on the upper and lower boundaries. The average sO<sub>2</sub> in the intratumoural region (green area) was measured at  $49.3 \pm 6.3\%$ , while the average sO<sub>2</sub> was  $66.2 \pm 3.9\%$  in the extratumoural region (yellow area) at the

same depth and  $70.1 \pm 2.1\%$  in the control breast. The absolute  $sO_2$  difference between the intra- and extratumoural regions is therefore 16.9%, and 20.8% between the intratumoural region and the control, respectively. As in the previous case, the lower oxygenation level in the tumour may indicate hypoxia and could indicate tumour malignancy. The average total haemoglobin concentration in the intratumoural region was 135.8% greater than in the extratumoural region, which may also indicate an increased vascular density.

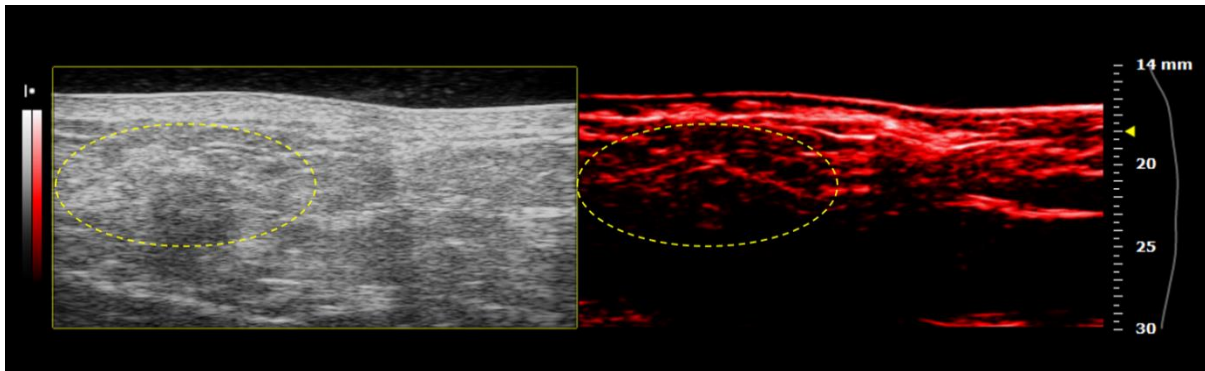


**Figure 5.13.** Coregistered US image (left) and PA image (right) of a malignant breast tumour (shown marked) in patient 9 at an image depth of  $\approx 20$  mm.

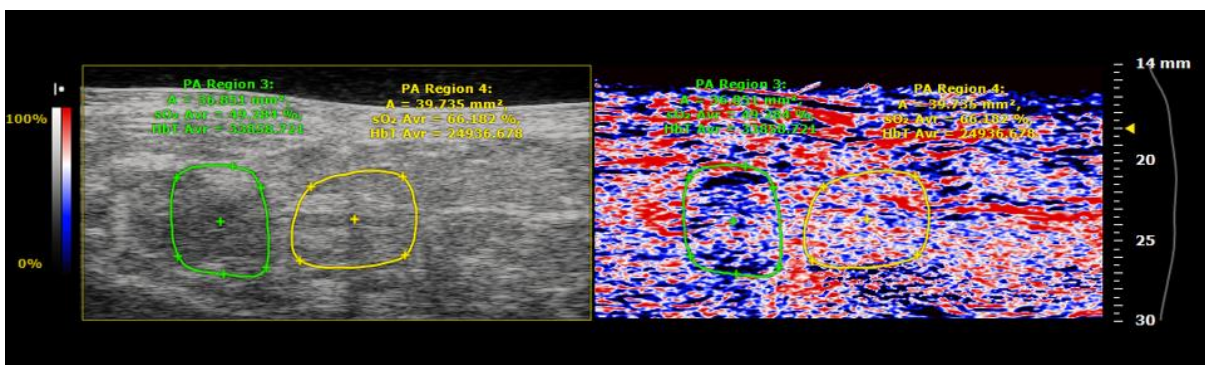


**Figure 5.14.** Coregistered US image (left) and parametric  $sO_2$  map (right) of the same malignant breast tumour shown in figure 5.13. The green and yellow regions show the average  $sO_2$  and average haemoglobin concentrations (relative units) in the intertumoural and extratumoural regions, respectively.

Figure 5.15 shows a US and  $sO_2$  scan of patient 10, a 50-year-old woman with a malignant breast tumour in the 10 o'clock position. The average  $sO_2$  was measured at  $55.5 \pm 3.8\%$  within the tumour (green region),  $63.3 \pm 3.0\%$  in the extratumoural tissue (average of both yellow regions in figure 5.15), and  $66.7 \pm 2.9\%$  in the control breast. Although not as large as in patients 1 and 2, the absolute  $sO_2$  difference between the intertumoural regions and extratumoural and control regions of 7.8% and 11.2%, respectively, may still be evidence of tumour hypoxia and malignancy. The dark region at the top of the  $sO_2$  scan in figure 5.15 from

≈ 14-17 mm, indicating a lack of blood, is likely caused by excessive pressure by the probe on the skin surface. Examining the total haemoglobin level in each of the three regions beneath provides evidence for this, which shows a 423% increase in relative haemoglobin concentration in the extratumoural region on the right-hand-side (region 2) compared with the intratumoural region, while the extratumoural region on the left-hand-side (region 3) shows a 20% reduction for same. This indicates increased blood perfusion in the areas directly below the dark region caused by blood being pushed out of the tissue close to the surface by the application of the probe. Care is therefore needed in future scans to avoid applying excessive pressure on the probe and any signs of vascular occlusion should be corrected for.

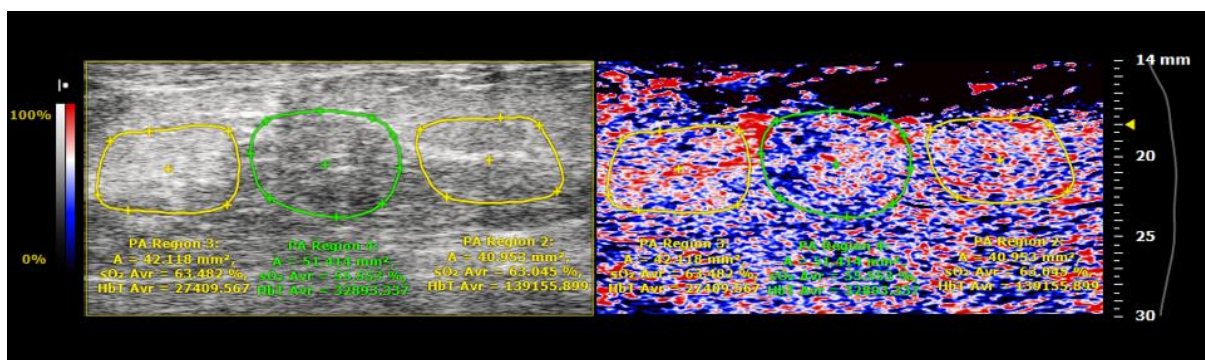


**Figure 5.15.** Coregistered US image (left) and parametric sO<sub>2</sub> map (right) of a malignant breast tumour in patient 10. The green and yellow regions show the average sO<sub>2</sub> and average haemoglobin concentrations (relative units) in the intertumoural and extratumoural regions, respectively

Figure 5.16 shows the coregistered US and sO<sub>2</sub> scan of patient 11, a 41 year-old-woman with a malignant tumour in the 1 o'clock position. The sO<sub>2</sub> scan shows no discernible difference in tissue oxygenation level within the tumour compared with the surrounding tissue. This was confirmed by sO<sub>2</sub> measurements from the intra- and extratumoural regions of  $69.6 \pm 1.1\%$  and  $71.1 \pm 1.6\%$ , respectively, which show no significant difference in sO<sub>2</sub>. No data was collected from the control breast due to time constraints on the scanning day. Total haemoglobin concentration in the tumour region was found to be 26% less than in the intratumoural region, which may indicate a decreased vascular density in this part of the tumour.

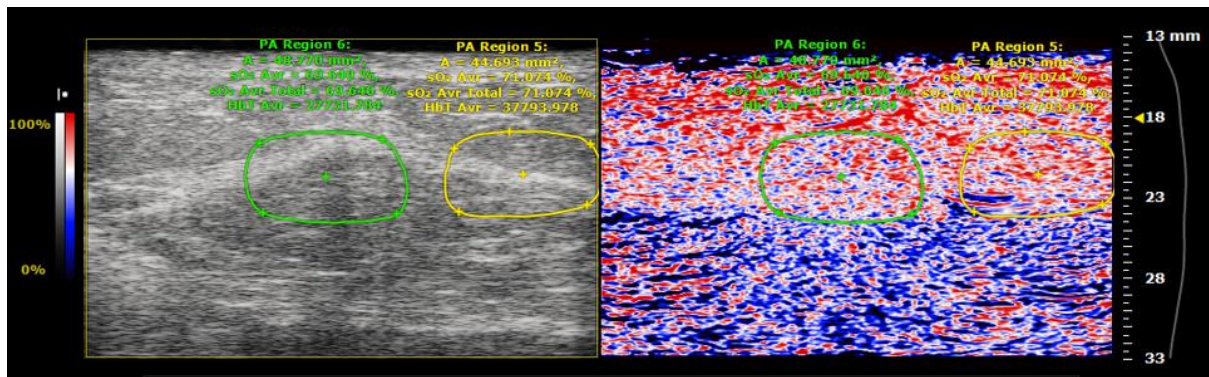


**Figure 5.16.** Coregistered US image (left) and parametric sO<sub>2</sub> map (right) of a malignant breast tumour in patient 11. The green and yellow regions show the average sO<sub>2</sub> and average haemoglobin concentrations (relative units) in the intertumoral and extratumoural regions, respectively.

Of the 4 malignant tumours where sO<sub>2</sub> measurements were possible, 3 showed possible evidence of tumour hypoxia indicating malignancy, while 1 did not. The results of the study thus far show that diagnosis of tumour malignancy with handheld linear-array PAI may be possible for superficial breast lesions that meet the study criteria. However, thus far the number of patients scanned with the 15 MHz probe is low and additional data is needed for a more robust validation.

Given that the sO<sub>2</sub> algorithm employed by the system does not account for optical fluence attenuation effects on the measured PA signal amplitude, the absolute sO<sub>2</sub> values may have questionable accuracy, especially in deep tissue. However, it has been demonstrated that even in cases where no spectral fluence compensation is applied to measured PA spectra, the absolute difference in sO<sub>2</sub> between neighbouring measurement sites is minimally affected [123]. This fact indicates that the absolute differences in tissue oxygenation between the intratumoural regions and the extratumoural and control regions, respectively, are valid despite the error in the overall sO<sub>2</sub> magnitude. This fact was the basis for not applying the fluence compensation method developed in chapter 3 in this study.

The ability to image changes in intratumoural oxygenation level holds promise for the eventual monitoring of oxyhaemoglobin concentration within the tumour after the administration of neoadjuvant chemotherapy. Confirmation of the diagnostic potential of PAI relying on endogenous contrast alone may lead to its eventual incorporation with US imaging in breast cancer screening. Incorporation may be relatively easy to achieve given that US and PAI can be performed simultaneously with the same probe and without much additional effort or change

in protocol, with the major differences being the requirement of a laser source and the need for laser safety goggles to be worn by the patient and clinical staff.

In terms of the future development of linear-array PAI systems for use in breast imaging, replacing nano-second pumped laser systems with high-energy pulsed laser diodes would serve to reduce the system cost, bringing PAI systems more in line with current US systems, and would also reduce the bulk of the system. The PAI system used in this study, which employed a flashlamp pumped Q-switched ND:YAG laser, was quite bulky and as a result was found to be difficult to manoeuvre around the bedside, and took up a large space in the examination room (see figure 5.6). Furthermore, Q-switched ND:YAG laser systems require regular maintenance, which gives them a disadvantage for regular clinical use. Diode lasers, on the other hand, are virtually maintenance free, requiring little to no servicing. In addition, laser diodes are available in a broad range of wavelengths in the NIR and would therefore not compromise the functional aspect of the system. The main drawback of laser diodes for PAI is the lower achievable pulse energy (typically  $> 100 \mu\text{J}$ ) as they are limited by the catastrophic optical damage peak power limit that affects semiconductor devices. To overcome this, laser diode arrays can be constructed which stack individual laser diode bars together to achieve pulses in the mJ range while maintaining nanosecond pulse durations [209]. PAI systems employing such arrays have been employed for wide-field PAI illuminating large tissue volumes, and could potentially be applied for breast imaging [210].

## ***5.4 Conclusion***

In this study hand-held, linear-array PAI was introduced to the breast clinic in order to assess its efficacy in the areas of: (1) imaging the morphology of suspect breast lesions, (2) measuring the oxygenation status of suspect lesions with a view to predicting malignancy, and (3), assessing the intratumoural oxygenation changes that may be characteristic of patients responding or non-responding to neoadjuvant chemotherapy. Linear-array PAI at 15 MHz was found to be able to image the upper boundary of the lesion morphology for superficial lesions ( $< 13 \text{ mm}$ ) in most cases. US imaging, however, was still used as the primary means of locating the lesion position. No identifiable structural differences in lesion morphology were observed between benign and malignant lesions. Due to logistical issues, no follow up scans on the

neoadjuvant chemotherapy patients recruited were possible post administration of treatment. For malignant breast lesions,  $sO_2$  and relative HbT scans at two wavelengths (750 nm and 850 nm) showed differences in oxygenation level between the intratumoural tissue and the extratumoural tissue and control breast, respectively, in 3 of the 4 cases where a scan was possible. These results provide an early indication that the oxygenation differences measured within the tumour region may show the efficacy of linear-array PAI in predicting lesion malignancy *in vivo*. However, at this stage the number of patients scanned is low and further recruitment is required to provide a more robust validation. Handheld linear-array PAI was found to be easily applicable to the breast and allowed for real-time assessment. To increase image depth, transducer arrays with lower central frequencies could be employed, however, this would have to be scaled with the available laser power and resultant SNR to ensure PA signals are detectable.

## **Chapter 6: Silica enhanced dual plasmonic gold nanostars for photoacoustic imaging and photothermal therapy**

The following chapter is based on publications [211,212].

### ***6.1 Introduction***

Gold nanoparticles (GNPs) are extensively used in many biomedical applications, including imaging, diagnostics, and therapy [213–215]. GNPs are favourable over other metal nanoparticles due to their unique properties of small size to volume ratio, thermal stability, inertness, and general nontoxicity [216]. GNPs can be easily synthesised into a variety of sizes (1-100 nm) and shapes that control their optical and electronic properties and can be tuned to absorb in the NIR wavelength region, which has important significance for biomedical imaging applications. When coupled to various biomolecules and ligands, GNPs enable the development of new biomedical applications for the treatment and diagnosis of disease and can be used for targeted delivery to specific tissues [217–221]. Applications include their use as molecular imaging contrast agents [222–225], disease biomarkers [226], vehicles for drug and gene delivery [227,228], and therapeutic agents [229,230], due to their favourable properties.

The optical properties of GNPs depend on the property of surface plasmon resonance (SPR), whereby an incident EM field of specific frequency induces the resonant oscillation of conduction band electrons on the metallic surface [231]. The resonant photons can be confined by the GNPs, which results in a large increase in the EM field and subsequently enhances all of the nanoparticles optical properties, such as scattering and absorption. The size and shape of the nanoparticle also influences the nature of the SPR and consequently can be varied or tuned to produce absorption bands in different regions of the EM spectrum. The phase of the electron oscillations are predominantly dipolar in nature and are approximately constant over the nanoparticle's volume, however, as the nanoparticle's size become comparable to the wavelength of the incident EM wave, higher order modes of oscillation can be produced such as quadrupole, octapole etc., which have specific effects on the optical properties [232].

One such plasmonic near-field enhanced process is surface-enhanced Raman scattering (SERS) [233,234], where the cross-section of Raman scattering from molecular vibrations is proportional to the square of the intensity of the electric field, which results in an amplification of the Raman scattering by several orders of magnitude (typically 5 to 6) due to the enhancement of the electric field resonant with the particles local SPR frequency. The amplification is mostly from enhanced-field hotspots – regions of intense localised surface plasmon electric fields at the nanoparticle crevices and interstices [235]. Aggregated GNPs (such as spheres and rods) and similar metal nanoparticles owe the majority of their local SERS enhancement from hotspots located at the interparticle junction. The local SERS enhancement, however, decreases rapidly with increasing interparticle distance, as is the case in isolated colloidal suspensions of GNPs. An alternative method to enhance the local plasmonic EM field is to increase the complexity of the nanoparticle geometry via the creations of nanoprotusions on the particle surface. The rough surface topography creates localised gaps that allows for EM field enhancement, eliminating the need for particle aggregation. Gold nanostars (GNS), with their complex multibranch topography, can produce significant SERS enhancement at the points due to the ‘lightning rod’ effect [236,237]. The development of dual-plasmonic gold nanostars (DPGNS) that contain much longer branches and sharper tips than previously developed nanostars has been reported [211]. The longer, sharper tips allow for enhanced hotspots, producing localised SPR absorption at longer wavelengths (1000-1200 nm), while maintaining the previously reported absorption peaks in the visible/NIR region of  $\approx 700$  nm. Importantly for photothermal conversion efficiency, DPGNS efficiently convert the absorbed EM radiation by the localised surface plasmons at the tips into thermal energy through phonon-phonon and electron-phonon processes.

Previous studies employing GNP-based contrast agents for biomedical imaging applications typically used nanoparticles tuned to absorb at approximately 800 nm [238–240]. Currently, however, there is a lack of GNPs designed to operate at longer wavelengths (beyond 1000 nm). Imaging in the 1000-1350 nm wavelength region, termed the *second biological window*, has specific advantages due to the nature of the optical properties of biological tissue [241,242]. Optical scattering decreases by up to two orders of magnitude compared with the visible-NIR (700-1000 nm) region, depending on the tissue type [18], allowing for increased penetration depth and SNR. For example, the reduced scattering mean free path ( $1/\mu'_s$ ) in human skin increases from 0.35 mm at 700 nm to 1.4 mm at 1064 nm, with a further increase to 1.7 mm at 1200 nm, with a similar pattern being reported for other tissues such as the breast and brain.

Light penetration is therefore mainly limited by absorption, however, oxy- and deoxyhaemoglobin absorption is low ( $\mu_a = 0.1 \text{ mm}^{-1}$  and  $0.02 \text{ mm}^{-1}$  for oxy- and deoxyhaemoglobin at  $\approx 1100 \text{ nm}$ , respectively). Absorption by water can severely degrade optical penetration depth due to the increase in absorption after  $900 \text{ nm}$ , and due to the high water concentration in biological tissues, however, this is minimised to similar levels as in the visible-NIR outside of the absorption peaks at  $950 \text{ nm}$  and  $1450 \text{ nm}$ .

Photoacoustic imaging (PAI) is a novel, hybrid biomedical imaging technology that combines US detection with optical contrast for deep tissue imaging in the diffusive regime and has been shown to achieve an imaging depth of  $5\text{-}6 \text{ cm}$  in the visible-NIR wavelength region [20,240]. PAI relies on several major endogenous biological chromophores, including haemoglobin, melanin, lipids, and water, to provide image contrast. In situations where the PA signal is depth limited or there is a lack of endogenous contrast available, exogenous contrast agents, either oral or injectable, can be used to enhance optical contrast and potentially break through the imaging depth limit. Furthermore, receptor-targeted contrast agents can be used for many clinical applications, such as cancer diagnosis, molecular typing of disease, and lesion localisation, potentially broadening the applications of PAI [243,244]. Targeted contrast agents can also function as dual contrast agents and photoabsorbers in photothermal therapy (PTT), allowing for simultaneous imaging, monitoring, and targeted therapy [211,245].

GNPs serve as excellent PA contrast agents due to their high optical-to-acoustic conversion efficiency (representing the fraction of incident photons that are converted to heat and how efficiently this heat is diffused to the surrounding tissue during thermoelastic expansion and PA wave generation) [246]. These nanoparticles can exist in a variety of shapes, including nanospheres, rods, shells, cages, and stars. The PA imaging contrast of gold nanorods, tuned to produce an SPR absorption peak beyond  $1000 \text{ nm}$ , has been demonstrated in phantom studies, however, the same has not been done *in vivo* in the same wavelength region [247]. This may be due to the blue-shifting tendency of the SPR peak when the GNRs become aggregated in clusters within cells [248,249]. Single-walled carbon nanotubes (SWNT) can also be used in the second biological window and exhibit good PA image contrast [250], however, the nonbiodegradable nature of SWNTs and their needle-like structure has been reported to cause chronic toxicity in lung tissue [251]. DPGNS have been shown to produce strong PA image contrast in agar phantoms in the visible and NIR ranges [212], due to their high photothermal efficiency and heat dissipation. The heat disputation efficiency and PA signal amplitude of the

particles can be further increased with the addition of a material with a high thermal conductance, such as silica [252,253]. Silica is also favourable since it is a non-absorbing material and thus does not interfere with the PA absorption profile. PA image contrast for silica-coated DPGNS was also displayed *in vivo* at 1064 nm. Due to their high photothermal conversion efficiency, silica-coated DPGNS were used as theranostic nanoprobe for dual PAI monitoring and PTT therapy *in vivo* [254,255].

In this study, the increased PAI contrast and photothermal transfer of silica-coated DPGNS, synthesised to produce absorption bands in the visible and NIR wavelength regions, is first demonstrated in optical phantoms. Next, the efficacy of silica-coated DPGNS mediated PTT, with PAI monitoring, is investigated on MDA-MB-231 tumours in mice in a longitudinal study. PAI is used to estimate the relative nanoparticle concentration at different study time points through analysis of the intratumoural PA signal amplitude. The effect of the PTT treatment is assessed through the change in total tumour volume, histological analysis of the excised tumours, and comparison with untreated control groups.

## ***6.2 Materials and Methods***

All the chemicals used in this study were obtained from Sigma Aldrich (Dublin, Ireland). All of the water used in this study was obtained from Milli-Q ultrapure-water purification system by Merck Millipore Limited (Dublin, Ireland). All glasswares used were washed with aquaregia (mixture of 3:1 ratio of concentrated hydrochloric and nitric acid, respectively) and rinsed with deionized water.

### **6.2.1 Synthesis & surface modification of DPGNS**

The synthesis procedure for producing PEGylated DPGNS has previously been reported in [232]. To produce a local SPR absorption peak to match the PA laser excitation wavelength of 1064 nm, DPGNS were synthesised with a gold precursor (hydrogen tetrachloroaurate (HAuCl<sub>4</sub>)) and reducing agent (ascorbic acid) ratio of 2:1. Silica coating of the PEGylated DPGNS, to enhance the photothermal conversion efficiency and thus the PA signal amplitude,

was performed using the Stöber method [252,253,256–258] for the production of silica nanoparticles. The procedure consisted of adding 1.2 ml of PEGylated DPGNS to 1.8 ml of isopropanol under vigorous shaking, with 2 M ammonia in isopropanol solution then being added dropwise until the PH of the reaction solution reached 11. To complete the procedure, 400 ml tetraethyl orthosilicate in isopropanol solution was added under gentle stirring and the reaction solution was allowed to settle for 2 hours. The DPGNS absorption spectrum is shown in figure 6.1, showing the absorption peaks in the 650–700 nm and 1000-1350 nm wavelength ranges.

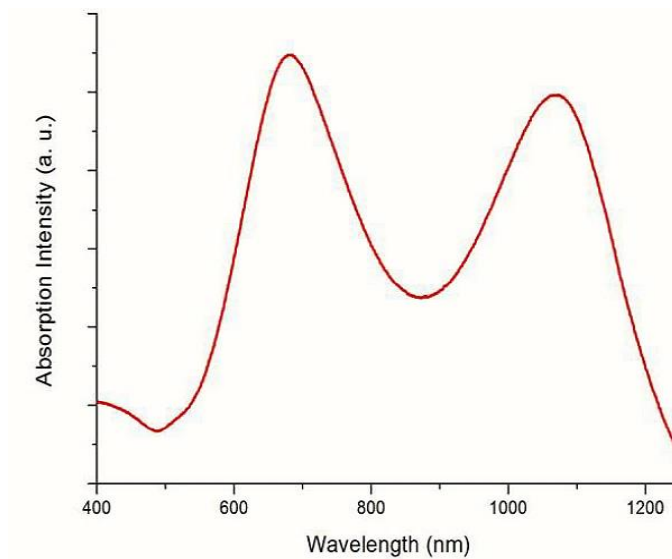


**Figure 6.1.** Absorption spectrum (a.u.) of DPGNS tuned to absorb in the 650–700 nm and 1000-1350 nm wavelength ranges.

### 6.2.2 PAI of phantoms

Details of the PAI system used in this study can be found in section 2.10. The PAI contrast capabilities of non-silica coated DPGNS at 700 and 1064 nm were first tested on agarose phantoms containing different nanoparticle concentrations, and in mouse tissue *ex vivo*. The phantom consisted of 4 agarose tubes with DPGNS concentrations ranging from 0, 17, 33, and 50  $\mu\text{M}$ , for each tube, respectively, while the *ex vivo* imaging was performed on the thigh tissue of a mouse sacrificed immediately prior to imaging. To compare the difference in PA signal amplitude between the silica-coated and non-silica-coated DPGNS, and to test the PA signal in the DPGNS absorption peak ranges of 650–700 nm and 1050–1200 nm, PA scans were taken

on a tissue phantom containing each particle type at the same concentration. The phantom consisted of two capillary tubes embedded side-by-side in an agarose-intralipid background, with each tube containing either 400 µg/ml of aqueous DPGNS or silica-coated DPGNS, respectively. The agarose and intralipid were added to water at a 2% and 1% volume fraction, respectively. PA scans were taken with a 21 MHz linear-array PA probe at 700 nm and 1064 nm, respectively, with the PA probe being coupled to the phantoms with US gel.

### 6.2.3 *In vivo* PAI of DPGNS

To test the PA contrast *in vivo*, scans were taken of silica-coated DPGNS injected in a mouse-tumour model. Prior to the study commencement, ethical approval was granted from our local ethical approval board (Animal Care Research Ethics Committee) and national authorization (The Health Products Regulatory Authority) for all procedures performed. 7 to 8-week-old female athymic nude mice (Charles River, UK) were subcutaneously injected with MDA-MB-231 tumour cells into the hind legs to induce tumour growth. A 200 µl suspension of  $1 \times 10^7$  cells in a 50:50 mix of RPMI:Matrigel were initially injected. When the tumour volume (measured with US) reached 100 mm<sup>3</sup>, 50 µl of DPGNS at a 400 µg/ml concentration were injected intratumourally. Baseline PA images of the tumour volume were taken before and after the commencement of laser treatment (PTT), at days -1, 3, 7, 14, and 21. For each PA scan, care was taken to align the center PA probe with the center of the tumour and to ensure the PA probe was the same distance from the tumour surface to ensure similar experimental conditions at each timepoint. VevoLab software (VisualSonics Inc. Toronto, Canada) was used to analyse the US, PA and the coregistered PA-US images.

The MDA-MB-231 cell line is commonly used to model late-stage breast cancer. It was originally isolated from a pleural effusion of a patient with invasive ductal carcinoma and is a highly aggressive, invasive, and poorly differentiated triple-negative breast cancer with limited treatment options [259,260]. As such, it was chosen as a good model on which to test the current treatment.

#### 6.2.4 PTT of tumours *in vivo*

Mice with the MDA-MB-231 tumour xenografts were separated into four groups, with 7 tumours (n=7) in total in each group, and with each tumour having a volume of 100 mm<sup>3</sup> at the beginning of the study. Prior to PTT (day 0), each group had 50 µl of 400 µg/ml silica-coated DPGNS injected intratumorally (as per previous PTT protocols [254,261]). Group 1, the treatment group had tumours administered with DPGNS and underwent PTT. Group 2, used as a control group for PTT, contained no DPGNS, but instead had tumours injected with phosphate buffered saline (PBS) before undergoing PTT. Group 3 had DPGNS administered but did not undergo PTT, and group 4 contained the untreated control group, with tumours that contained no DPGNS, PBS, or underwent PTT.

Although subcutaneous injection of the DPGNS inevitably results in an inhomogeneous particle distribution, the absolute PA signal amplitude has been shown to be higher from intratumoural injection compared with intravenous administration [262]. The injection of DPGNS was guided by US to ensure that the tip of the needle was inserted just beyond the tumour epicenter. The needle was then slowly drawn out while simultaneously pressing down on the syringe plunger, releasing the DPGNS solution gradually. This was done to maximise the DPGNS particle distribution within the necrotic core of the tumour.

A schematic of the experimental setup and study timeline is shown in figure 6.2. To initiate PTT, the tumours were irradiated with a 1064 nm continuous-wave (CW) DPSS laser (Dragon Lasers, China) with a radiant flux of 0.5 W/cm<sup>2</sup> for 10 minutes. During PTT, the surface temperature of the tumours was monitored using an FLIR A325 infrared thermal camera (FLIR Systems, Inc. OR, USA) with a spectral range of 7.5–13 µm. A photo of the experimental setup is shown in figure 6.3, showing the PAI system, PTT laser, animal stage (with mouse) and thermal camera. Coregistered PA-US scans at the 700 and 1064 nm wavelengths were taken just before PTT treatment commenced, and afterwards on days -1, 3, 7, 14, and 21. On day 21, the mice in each study group were sacrificed by CO<sub>2</sub> inhalation. The tumours were then excised and sent for histological analysis. The excised samples were fixed in 4% paraformaldehyde and embedded in paraffin blocks, where they were subsequently sectioned and stained with haematoxylin and eosin (H&E) to enable the tumour cellular damage as a result of the treatment to be assessed.

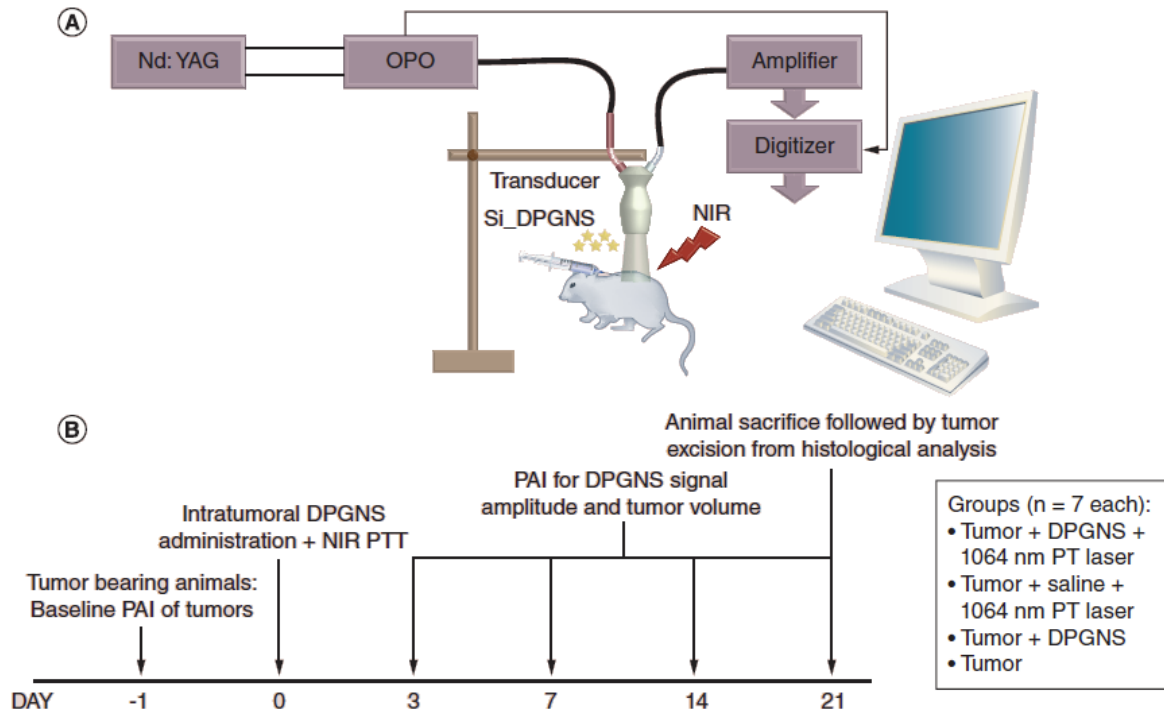


**Figure 6.2.** (A) Schematic of PTT and PAI experimental setup. (B) Timeline of the *in vivo* study.



**Figure 6.3.** Experimental setup, showing the PAI system, consisting of the PA laser source, imaging station, and PA imaging probe. Also shown is the PTT laser source (right), thermal camera, and animal stage with mouse attached. During treatment/PAI, the mouse vital signs, including heart rate, respiration

rate, and temperature, were monitored. The 1064 nm PTT laser source is shown directed onto the target with a fibre optical cable.

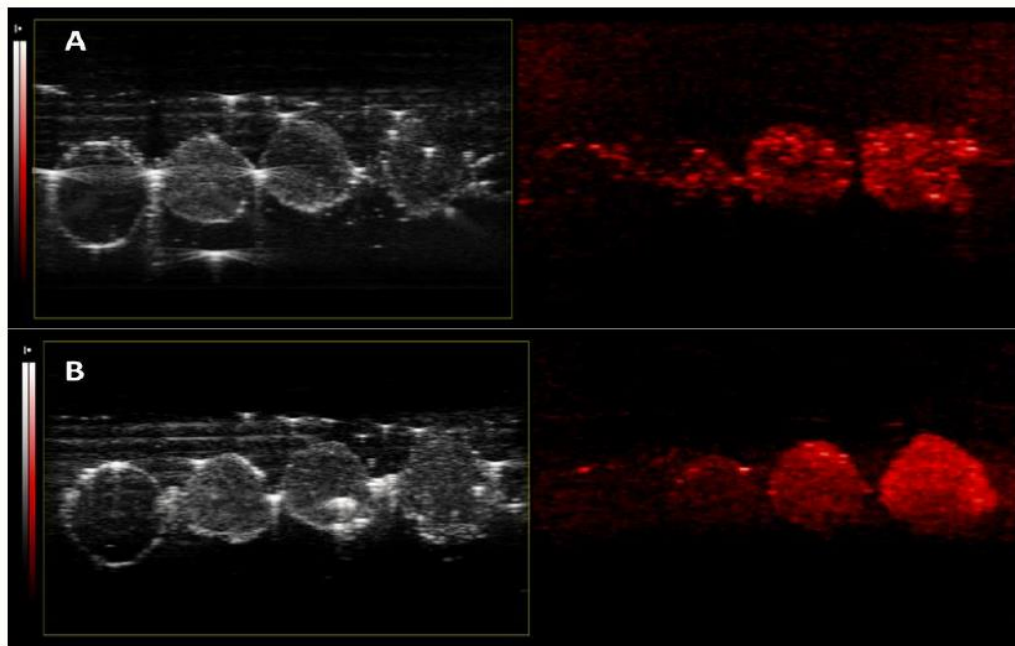
Statistical analysis for all data was performed using Graph-Pad PRISM (GraphPad Software Inc., USA). The PA amplitude data from the tumours was measured from the PA images reconstructed in MATLAB using a delay-and-sum beamforming algorithm. The images were reconstructed using the raw PA data exported from the Vevo LAZR system. Pearson's  $R^2$  correlation was used to analyse the relationship between the PA signal amplitude and the concentration of DPGNS within the tumours. One-way analysis of variance (ANOVA) was used to compare the PA signal amplitude at 700 and 1064 nm. The percent tumour tissue area on the 40x histological slides was measured using ImageJ (National Institutes of Health (NIH), USA), with the tumour cells (alive and dead) being identified by their positive reaction to H&E staining. The mean percentage of tumour tissue area between groups was calculated using a one-way ANOVA. Student Newman-Keuls Multiple Comparisons post-hoc test was used for all post-hoc analysis.

## ***6.3 Results and Discussion***

### **6.3.1 Initial PA characterisation of DPGNS.**

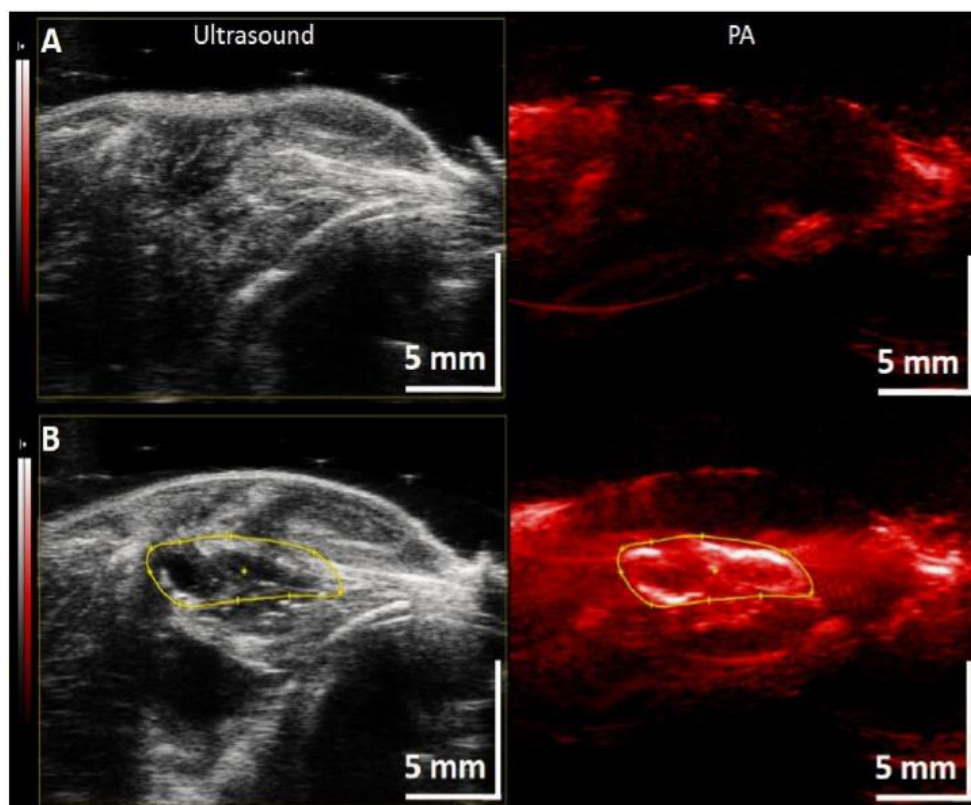
To initially demonstrate the PA absorption contrast of the non-silica-coated DPGNS, tuned to produce a SPR absorption peaks in the wavelength ranges of 650–700 nm and 1050–1200 nm, an optical phantom containing different concentrations of DPGNS particles was made. The phantom consisted of 4 agarose tubes approximately 5 mm in diameter, placed side-by-side with DPGNS concentrations ranging from 0, 17, 33, and 50  $\mu\text{M}$ , for each tube, respectively. PA scans were taken at 700 and 1064 nm to demonstrate the PA sensitivity at each of the DPGNS SPR absorption. The PA and US scan results are shown in figure 6.4, with the PA image being on the right-hand-side and the US image being on the left, and with panels (A) and (B) showing scans taken at 700 and 1064 nm, respectively. Both panels (A) and (B) show the PA image contrast in each tube increasing with increasing DPGNS concentration (from left to right). Analysis of the PA amplitude in each tube showed a linear relationship between the PA

amplitude and the DPGNS concentration for both the 700 and 1064 nm laser excitations ( $R^2 = 0.923$ ,  $p < 0.001$ ).



**Figure 6.4.** B-mode PA and US scans of an optical phantom consisting of 4 agarose tubes ( $\approx 5$  mm in diameter) arranged from left to right in order of increasing concentration of DPGNS. Panels (A) and (B) show PA scans taken at 700 and 1064 nm, respectively. The agarose tubes were placed in US gel to provide coupling to the PA-US probe.

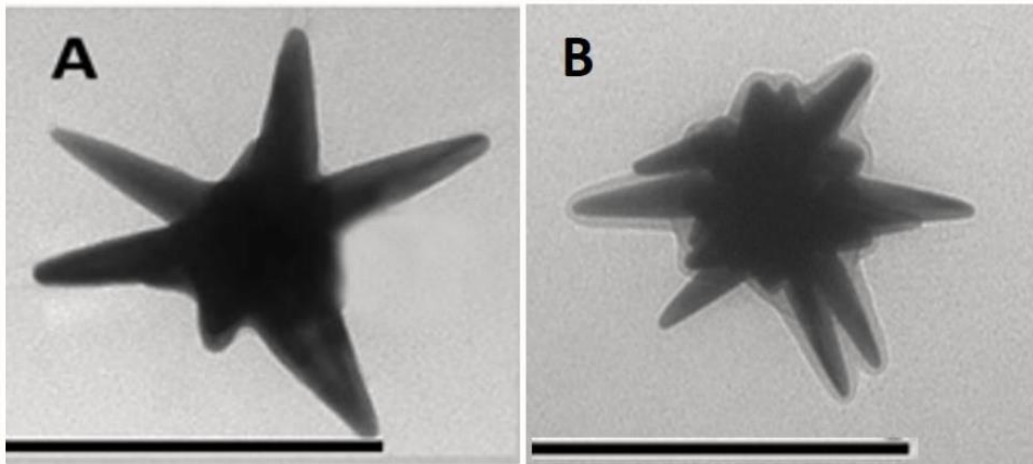
Based on the strong PA signal observed in the phantom study, the PA image contrast was then tested in an animal model. To this end, 10  $\mu$ L of DPGNS at a concentration of 50  $\mu$ M was injected intramuscularly into the thigh of a euthanised mouse, using US as a guide. Figure 6.5 shows a PA and US image of the mouse before (panel A) and after injection (panel B) of the DPGNS solution. The PA scan was taken at 1064 nm. As can be seen in figure 6.5, a large rise in the PA signal due to the introduction of the DPGNS is observed post injection. Correspondingly, the resulting cavity caused by the injection of the DPGNS solution can be seen in the US image.



**Figure 6.5.** B-mode PA and US scans of a euthanised mouse thigh taken at 1064 nm, showing the injection of 10  $\mu\text{L}$  of DPGNS at a concentration of 50  $\mu\text{M}$ . Panel A and panel B show the mouse thigh before injection and post injection, respectively.

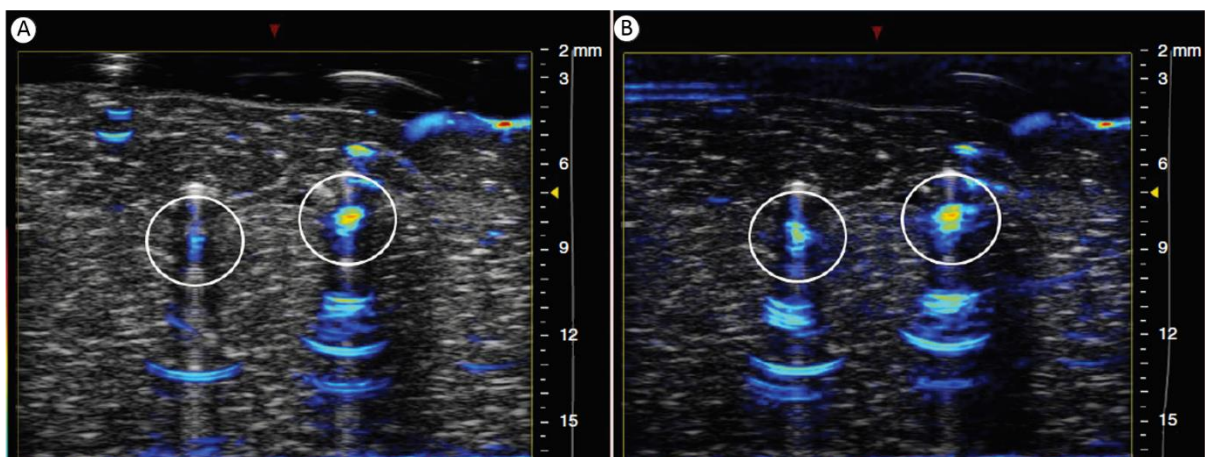
### 6.3.2 Initial PA and photothermal characterisation of silica-coated DPGNS

Figure 6.6 shows a transmission electron microscopy (TEM) image of silica-coated and non-silica-coated DPGNS in panels (B) and (A), respectively. The silica coating observed on the DPGNS in figure 6.6 (B) is approximately 10 nm on average. The silica coating of the DPGNS is designed to increase the PA signal generation through the increase in the photothermal efficiency, or heat transfer, to the surrounding environment, as the gold-water interface exhibits high thermal resistance [252,253]. To test this, PA scans on a phantom containing silica-coated and non-silica-coated DPGNS were taken.



**Figure 6.6.** TEM image of non-silica-coated and silica-coated DPGNS in panels A and B, respectively. The silica coating in panel B is approximately 10 nm on average. The scale bar in both panels is 100 nm.

The phantom consisted of two capillary tubes embedded in an agarose-intralipid background tissue, with each tube containing an aqueous solution of either silica-coated or non-silica-coated of DPGNS. Figure 6.7 shows two coregistered PA-US scans of the phantom, taken at 700 and 1064 nm, respectively. The scans show the increased PA contrast of the silica-coated DPGNS compared to the non-silica-coated DPGNS, confirming the photothermal enhancement properties of the silica coating.



**Figure 6.7.** Coregistered PA-US scans of an agarose-intralipid phantom containing two capillary tubes filled with an aqueous solution of silica-coated DPGNS (right) and non-silica-coated DPGNS (left). Panels A and B show scans taken at 700 and 1064 nm, respectively.

The aqueous solution of DPGNS is particularly suited for PA signal generation as the thermal expansion coefficient of water at atmospheric pressure is drastically reduced at 3.98°C [263]. At temperatures above this, PA signals due to the thermal expansion of water vanish. The amplitude of the PA signal from the DPGNS depends on its photothermal efficiency and the thermal conductivity of the surrounding media, water in the case of an aqueous solution. The compressibility of water is negligible at room temperature and therefore any PA waves generated in the solution come from the DPGNS themselves. Since all other factors influencing the generation of PA waves in the phantom were kept constant (e.g. Grüneisen parameter, illumination profile etc.), the observed increase in PA signal amplitude between the two tubes can only result from the interfacial heat resistance changes caused by the silica coating. The silica coating reduces the interfacial thermal resistance between the gold-silica and silica-water interfaces and results in a higher temperature gradient, increasing the PA signal.

To test the ability of both variants of DPGNS to generate heat under laser illumination, cuvettes containing aqueous solutions of silica-coated and non-silica-coated DPGNS were illuminated with a 1064 nm laser, with the laser power ranging from 0.5 to 2 W/cm<sup>2</sup>. The temperature of the DPGNS was measured using a FLIR A325 infrared thermal camera (FLIR Systems, Inc. OR, USA). The thermal images are shown in figure 6.8 (A) and (B). The temperature of the silica-coated DPGNS (panel A) increased from room temperature to 45°C in under 10 minutes with increasing laser power, while the non-silica-coated DPNGNS (panel B) reached ≈ 42°C under the same conditions. The addition of silica increases the thermal transfer from the nanoparticle's surface to the aqueous solution due to the higher emissivity (0.9) and thermal conductance of silica [252,264]. This is verified by the temperature plot in figure 6.8 C, which shows a higher temperature increase of 2-3°C for the silica-coated DPGNS.

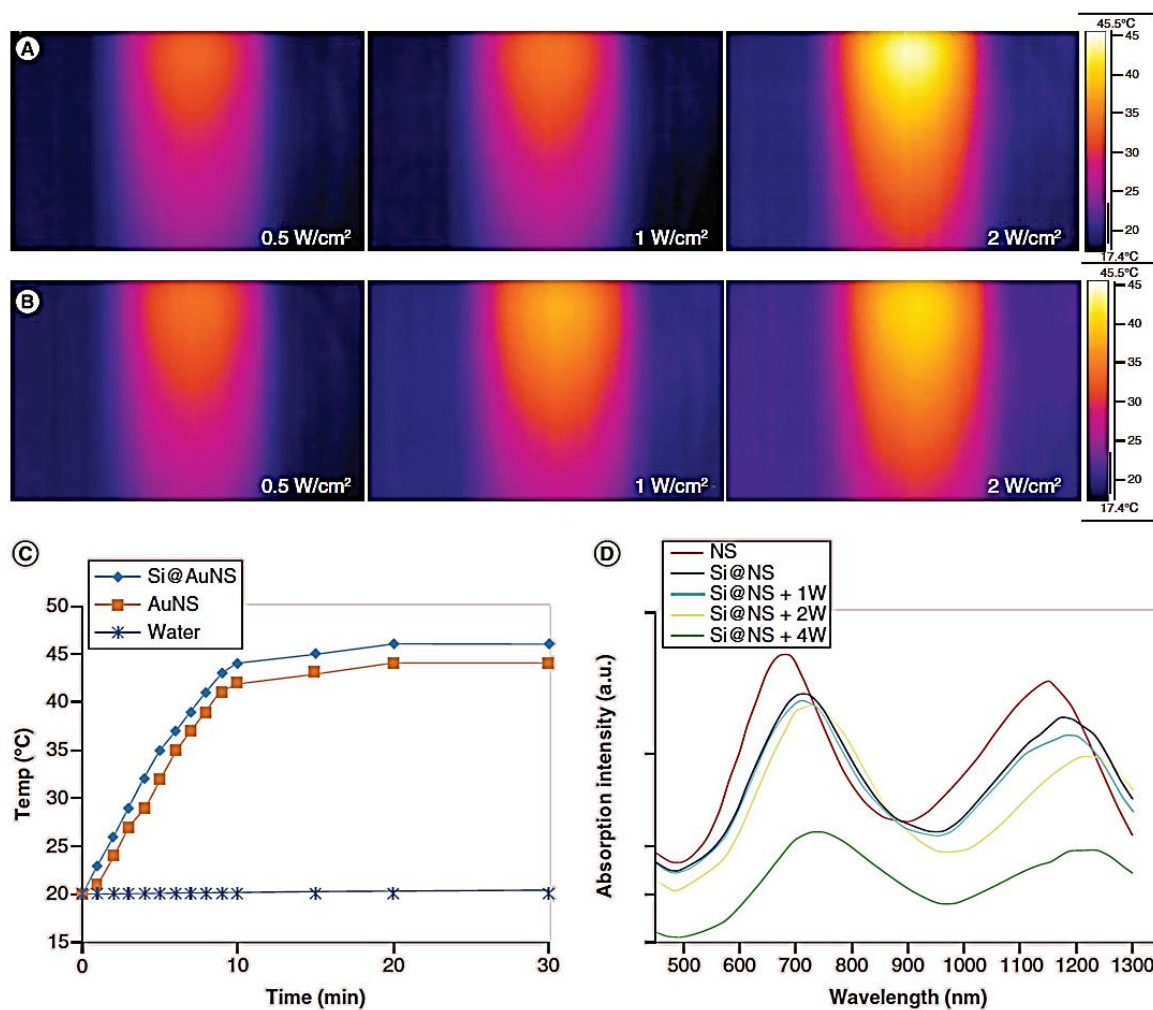


**Figure 6.8.** Photothermal efficiency of DPGNS. Thermal camera images of cuvettes filled with aqueous solutions of silica-coated (A) and non-silica-coated (B) DPGNS, irradiated by a 1064 nm laser with an irradiance ranging from 0.5 to 2 W/cm<sup>2</sup>. (C) Temperature plot vs time of the cuvettes undergoing laser heating in (A) and (B), as well as water. (D) Absorption spectra (via spectrophotometer) of non-silica coated DPGNS, as well as silica-coated DPGNS after exposure to laser irradiation ranging from 1 to 4 W/cm<sup>2</sup> (spot size 1 mm<sup>2</sup>).

Figure 6.8 (D) shows the absorption spectra of both variants of DPGNS. It can be seen that the 10 nm silica coating resulted in a 30 nm redshift of the absorption spectra. This is due the change in the dielectric constant of the surrounding medium which has a direct effect on the local SPR absorption of the nanoparticle [257,265]. Figure 6.8 (D) also shows the effect of laser heating on the absorption spectra of the silica-coated DPGNS, which were exposed to a 1064 nm laser with an irradiance ranging from 1 to 4 W/cm<sup>2</sup>. An amplitude reduction in the absorption spectrum with increasing laser energy can be observed, however the spectrum shape

and position of the absorption peaks remained mostly unchanged, which indicates the preservation of the aspect ratio of the nanostar branches. This is likely caused by the thermal stability added to the DPGNS from the silica coating, which protects their shape.

### 6.3.3 PA monitoring of PTT in a mouse-tumour model

The *in vivo* PAI contrast ability of silica-coated DPGNS and the efficacy of PAI for monitoring PTT treatment with silica enhanced DPGNS in mice tumours was next investigated. Adult athymic mice were injected with MDA-MB-213 tumour cells on both the left and right flanks to initiate tumour growth. When each tumour volume had grown to a volume of 100 mm<sup>3</sup> (day -1), baseline PA images were acquired. Aqueous colloidal solutions of silica-coated DPGNS were injected intratumourally into the relevant treatment groups, and PA scans at 700 and 1064 nm were when acquired on day 0.

The initial demonstration of silica-coated DPGNS PAI contrast *in vivo* is shown in figure 6.9. The PA signal amplitude within the tumour (not including the skin) was found to be higher at 1064 nm (C) compared with excitation at 700 nm (B), demonstrating the higher PA amplitude at longer wavelengths. This is quantified in figure 6.9 (D), where the average PA signal amplitude at 1064 nm was nearly twice that at 700 nm. Contrasting with this, the average PA signal from the untreated tumour (A) was minimal. The higher PA signal amplitude at 1064 nm is caused in part by the fact that the absorption coefficient of plasmonic GNPs increases when in resonance with the incident light at longer wavelengths [22], producing a greater photothermal conversion and subsequent thermoelastic expansion. In addition, it has been reported that the lower background signal from the surrounding tissue at longer wavelengths can result in a 50-70% increase in PA signal amplitude from GNPs when excited at 1064 nm compared with 700-800 nm [22]. The increased tissue penetration depth at 1064 nm also serves to increase the local fluence rate and hence DPGNS absorption and PA signal amplitude.

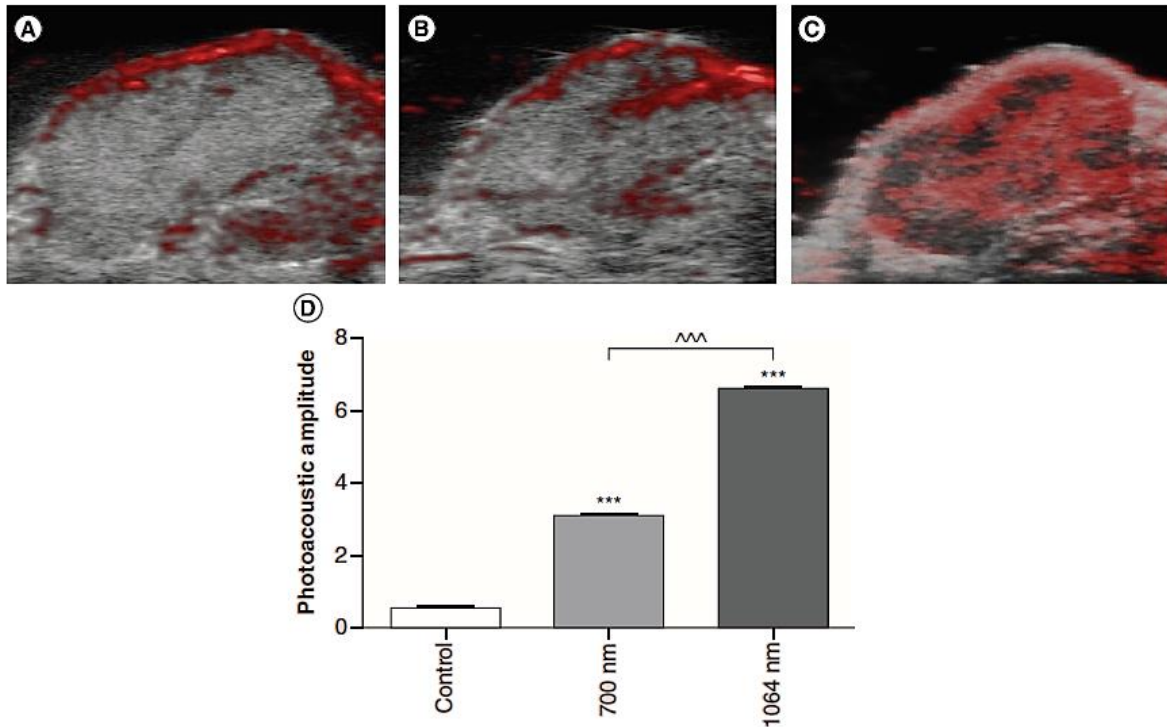


**Figure 6.9.** *In vivo* PAI of silica-coated DPGNS. Coregistered PA-US images of mice tumours for (A) untreated tumour at 700 nm, while (B) and (C) show tumours injected with silica-coated DPGNS imaged at 700 and 1064 nm, respectively. (D) Plot of the relative, average PA amplitude inside the tumour volume corresponding to the images (A), (B), and (C). Student Newman-Keuls Multiple Comparison post hoc test found an increase in laser wavelength to cause a significant difference in PA amplitude at 700 and 1064 nm ( $p < 0.001$ ). Data are expressed as means and SDs. \*\*\* $p < 0.001$  versus control; ^^ $p < 0.001$  versus 1064 nm wavelength.

Thermal imaging was used to monitor the photothermal efficacy of the DPGNS during PTT *in vivo* for the relevant study groups, which included the PTT treatment and PTT control groups. PTT therapy commenced after the intratumoural injection of the aqueous solution of silica-coated DPGNS on day 0, and consisted of irradiating the treatment area with a 1064 nm CW laser operating at  $0.5 \text{ W/cm}^2$  for 10 minutes. The laser irradiance used was kept lower than the maximum permissible exposure (MPE) safety level for skin as specified by ANSI [12] for the 700-1100 nm wavelength range. Figure 6.10 shows thermal images of mice in the treatment and control groups whilst undergoing laser irradiation, as well as a plot of the relative change in tumour volume at the study time points. Following laser irradiation, the surface temperature of the tumours with silica-coated DPGNS, as recorded by the thermal camera (figure 6.10 (B)), rose rapidly by  $8\text{-}9^\circ\text{C}$ , while the tumours containing SBP or no DPGNS rose on average by  $1^\circ\text{C}$  (figure 6.10 (C)). The  $8\text{-}9^\circ\text{C}$  temperature rise from the baseline tumour temperature of

35°C put the treatment group into the hyperthermia range (41-48°C), the clinically relevant range for PTT [238,266,267]. This laser-induced temperature rise and subsequent heating of the surrounding tissue was predicted to result in cellular destruction through protein denaturation and aggregation, and cell membrane destruction. Laser heating produced no significant temperature rise in any other parts of the animal. Note that the high temperature observed at the base of the animal in figure 6.10 (B) and (C) is from a heating pad used to keep the animal warm whilst undergoing laser treatment.

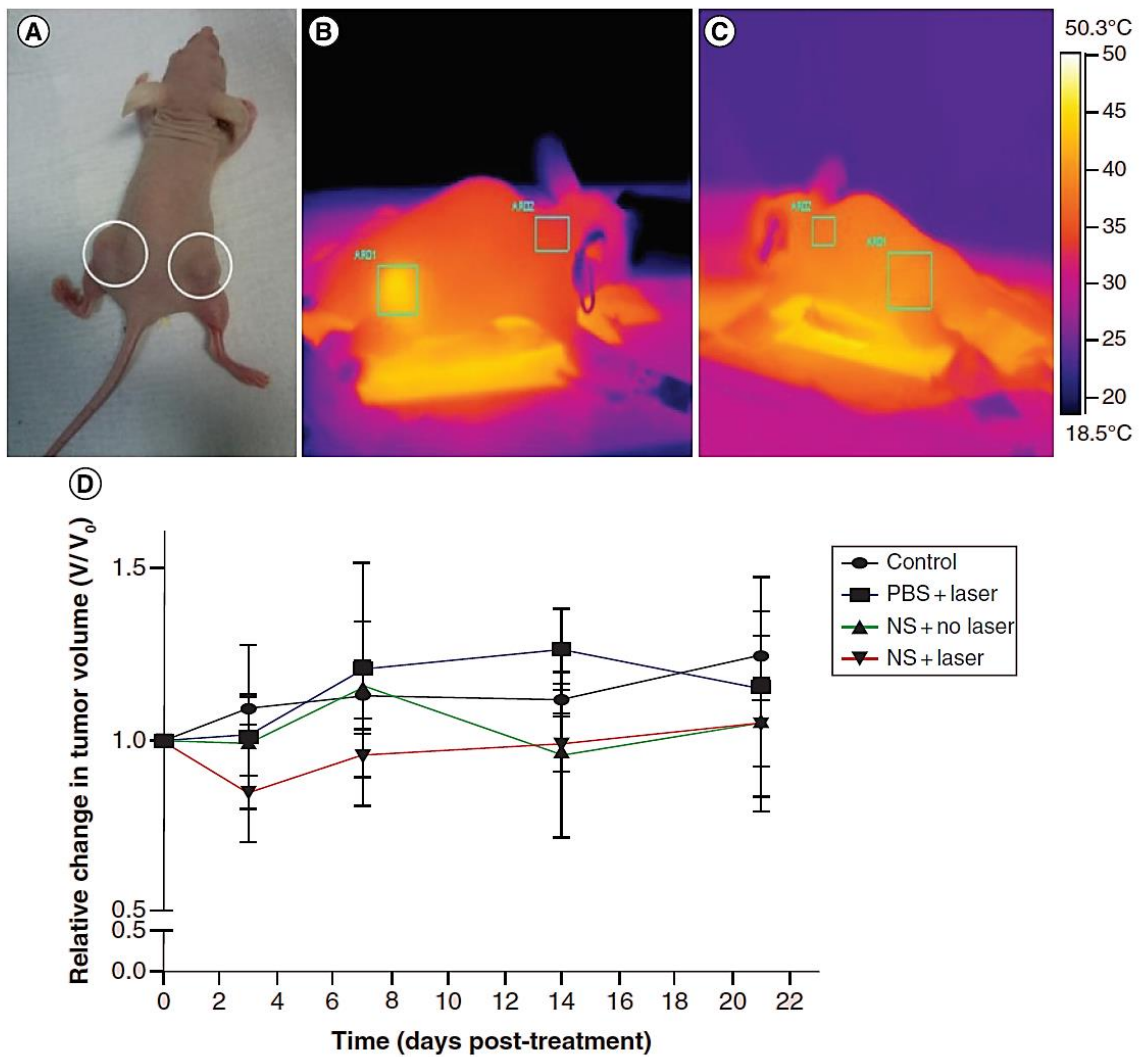


**Figure 6.10.** PTT treatment of mice tumours. (A) photo of mouse with tumours on each flank circled. (B) Thermal image of mouse in the treatment group (with tumours containing silica-coated DPGNS) undergoing laser irradiation (CW laser operating at 1064 nm and 0.5 W/cm<sup>2</sup> for 10 minutes), where a rapid increase in temperature of 8-9°C in the tumour (marked area) was observed compared with the surrounding tissue (baseline temperature 35°C). (C) Thermal image of control group mouse undergoing laser treatment showing no temperature increase in the tumour (marked area). (D) Tumour-growth curve

of the 4 different study groups, consisting of: treatment group containing DPGNS and undergoing PTT, tumours containing DPGNS but without PTT, tumours containing PBS and given laser irradiation, and the untreated control group. No significant difference in mean relative tumour volume was found for the treatment group ( $F(3, 24) = 0.397, p > 0.05$ ) or measurement day ( $F(3, 72) = 1.581, p > 0.05$ ). Error bars represent the standard deviation ( $n = 7$ ). (NS = nanostars).

The tumour growth curve shown in figure 6.10 (D) shows an initial reduction in the relative tumour volume after PTT for the treatment group (NS + laser) at day 3, followed by a gradual increase in tumour volume up to day 21. This suggests that the tumours initially regressed soon after PTT, but that tumour-growth recovered after day 3. It can also be seen that the presence of DPGNS or laser irradiation alone own did not produce an initial reduction in tumour volume. The recommencement of tumour growth after day 3 can be explained by the thermo-resistance exhibited by cells after heating to approximately 41°C, resulting in protein denaturation and cell inactivation. Cells that survive inactivation develop temporary thermal resistance and can begin to proliferate again [238]. This resistance to heat-induced apoptosis may be due to the increased expression of a class of proteins called heat shock proteins which occurs during PTT [268]. The heat shock proteins prevent the aggregation of denatured proteins and initiate protein refolding [269,270]. Cellular thermal resistance can be overcome by increasing the temperature over a longer period of time, causing more severe hyperthermia inducing longer-term cell inactivation. The effected cells become unable to cope with the increased thermal stress and can undergo thermal-induced cellular necrosis or apoptosis [269]. The effectiveness of PTT in this study could therefore be increased by increasing the laser irradiance used ( $0.5 \text{ W/cm}^2$ ), which was much lower than the ANSI standard safety limit for MPE at 1064 nm of  $1 \text{ W/cm}^2$  [12]. An increase of laser irradiance from between  $0.6\text{-}1 \text{ W/cm}^2$  and conducting multiple PTT treatment sessions could help increased the effectiveness of PTT in future studies.

A PA amplitude spectrum taken across the OPO range of 680-970 nm of an absorbing region of a silica-coated DPGNS administered tumour (in the treatment group) is shown in figure 6.11 (A). The PA spectrum shows a distinct absorption peak at approximately 700 nm, matching the first local SPR peak of the DPGNS, and also shows a second absorption band beginning to form beyond the OPO range, which is likely due to the second SPR absorption peak beyond 1000 nm. Since the PA system used does not enable a spectral scan outside of the OPO range, this was unable to be verified. Figure 6.11 (B-D) shows coregistered PA-US scans of a tumour from the treatment group at days 3, 7, and 14, where it can be seen that the DPGNS

concentration decreases over time, indicating that the DPGNS were gradually diffused out of the tumour and were almost completely removed by day 14 (as verified by the spectral scans).

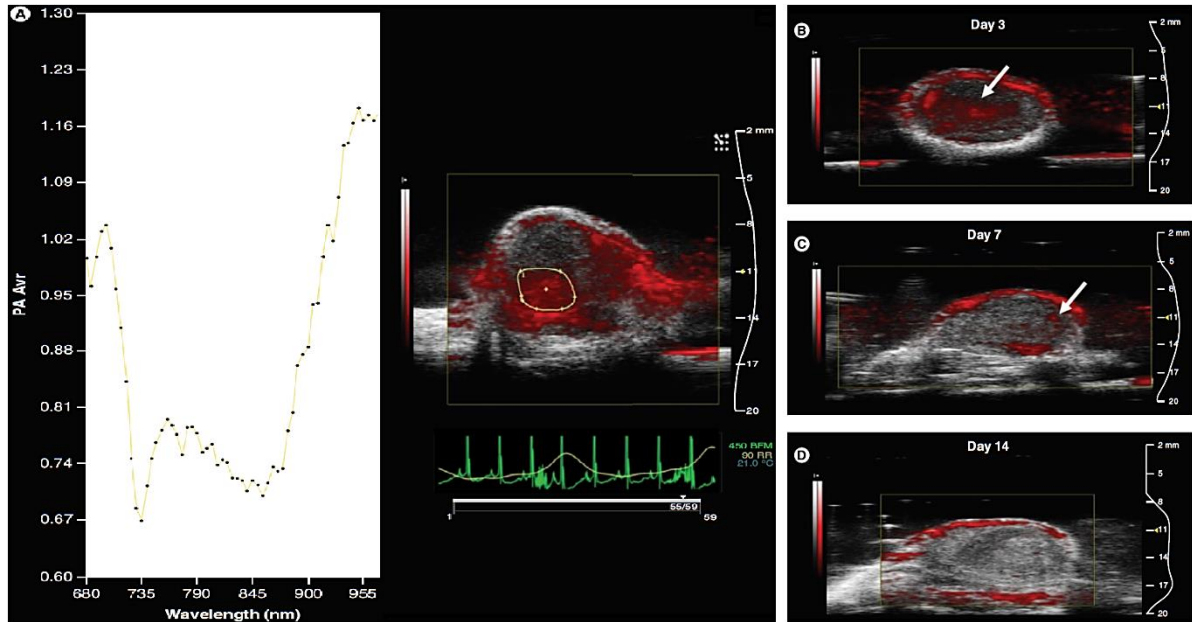


**Figure 6.11.** *In vivo* PA spectra of silica-coated DPGNS. (A) Average photoacoustic amplitude spectra (680-970 nm, relative units) from DPGNS administered tumour from scan region marked in yellow. (B-D) Coregistered PA-US images (700 nm) of a DPGNS administered tumour (from treatment group) at days 3, 7, and 14 post-treatment, respectively.

Figure 6.12 shows the comparison of relative PA amplitude from silica-coated DPGNS administered tumours at different study timepoints for the treatment group and the group that received DPGNS but no PTT. Figure 6.12 (A) shows the PA-US scans (1064 nm) from a representative tumour from the treatment group at the study baseline (day -1) and post-treatment on days 3, 7, 14, and 21, while panel (B) shows the same for a DPGNS administered tumour only. A strong increase in the PA signal from within the tumour can be observed on the PA-US scans on day 3 for both groups, which can visually be seen to diminish as the study progressed. This is quantified in panel (C) where the relative PA amplitude from within the tumours is plotted at each study timepoint. It can be seen in panel (C) that the PA signal amplitude for both groups strongly diminishes after day 3, indicating the gradual removal of the DPGNS. However, there is a noticeable reduction in PA amplitude of the treatment group compared with the untreated group on days 3 and 7.

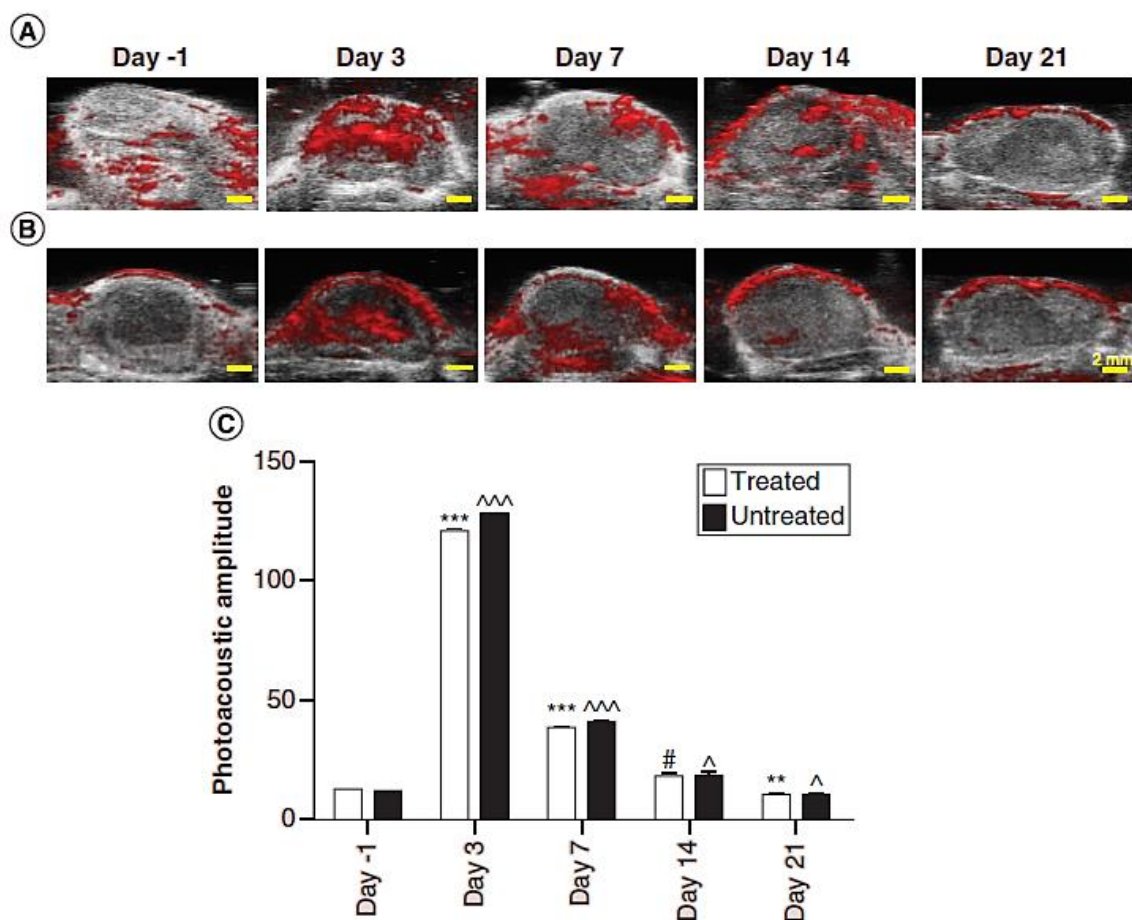


**Figure 6.12.** (A-B) Coregistered PA-US scans taken at 1064 nm of a representative silica-coated DPGNS administered tumour from the treatment group (A) and the untreated group (no PTT) (B). (C) Plot of average PA signal amplitude from inside the tumours shown in (A) and (B) at each study timepoint. Post hoc analysis of PA signal amplitudes using a two-sided dependent samples t-test found a significant difference in PA signal amplitude for all measurement days post DPGNS administration compared with the baseline measurement (Day -1) for both the treated and untreated group ( $p < 0.05$ ). Data are presented as means and standard error of mean. \*\* $p < 0.01$  vs Day -1, \*\*\* $p < 0.001$  vs Day -1, # $p = 0.066$  vs Day -1, ^ $p < 0.05$  vs Day -1, ^^ $p < 0.001$  vs Day -1.

Contrasting with the PA scans taken at 700 nm (figure 6.12 (B)), the DPGNS signal can still be seen on the 1064 nm scan past day 7. The PA signal amplitude on day 14 is also noticeably higher than on day -1, which may indicate the presence of deep-lying DPGNS which have yet to be removed, showing the potential of silica-coated DPGNS for deep tissue imaging applications at longer wavelengths. The similar PA amplitude from the tumours in both groups indicates the strong photo-stability properties of the silica-coated DPGNS and shows the

potential for further PTT sessions and the use of a higher laser irradiance to achieve a more favourable therapeutic outcome.

Following animal sacrifice on day 21, the tumours were excised and sent for histological analysis, where H&E staining was performed on the histological sections. The histological sections were assessed for evidence of changes in cellular morphology or damage as a result of treatment. Histological sections of tumours from all 4 study groups at magnifications of x10 and x40 are shown in figure 6.13. Histological results showed apoptotic-like cells in the treatment group (figure 6.13 (A)), with shrunken cell sizes and increased intercellular distance compared with the other groups (figure 6.13 (B-D)) (similar to findings from other nanoparticle-mediated PTT studies [254,271,272]). The histological sections from the remaining groups (figure 6.13 (B-D)) showed typical MDA-MB-231 tumour morphology and showed no signs of treatment-induced cell destruction.

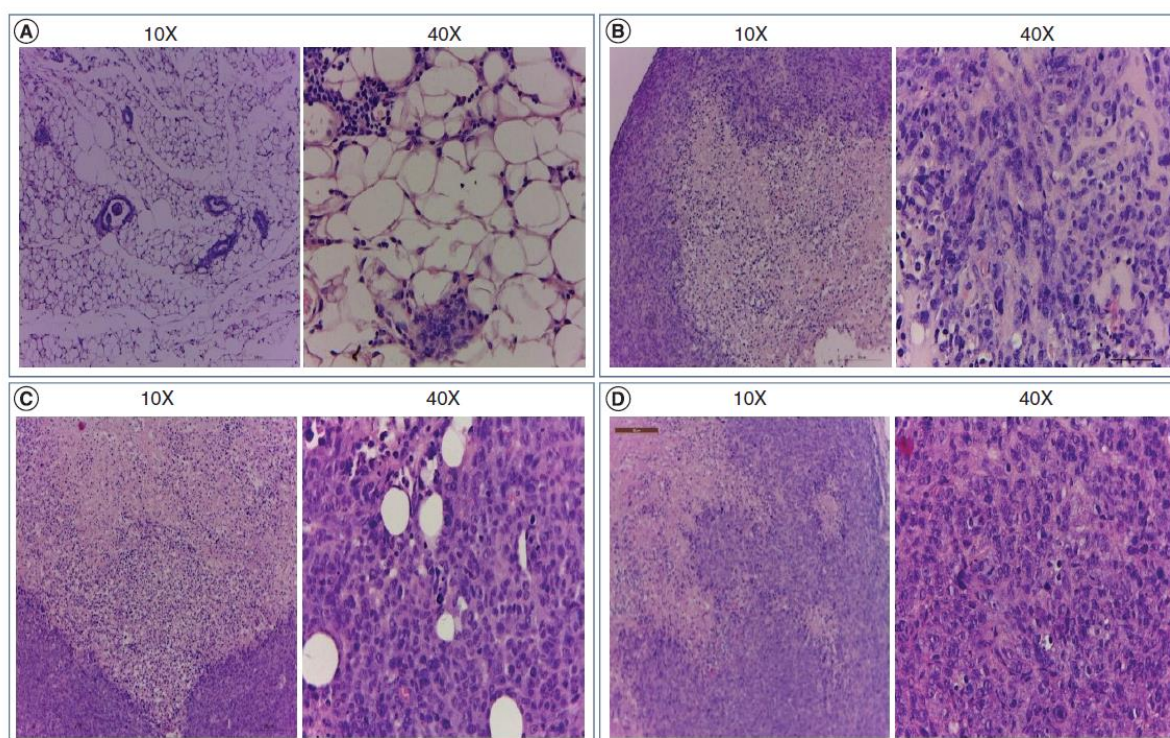


**Figure 6.13.** Histological sections with H&E staining from tumours from each study group at magnifications of x10 and x40, respectively, for (A) the treatment group (DPGGS + PTT), (B) DPGNS and no PTT, (C) PBS and PTT, and (D) control group (no DPGNS, PBS, or PTT).

The extent of tissue abnormality on the histological sections was quantified by calculating the percentage area of H&E stained cellular tissue. No distinction was made between live and dead

cellular tissue and only H&E positive stained tissue was used for quantification. The quantification results are shown in figure 6.14, which show a noticeable decrease in the percentage area of cellular tissue in the treatment group, at 39.8%, compared with the other study groups, which had values of 75.3% for the control group, 77.2% for the DPGNS alone group, and 82.1% for the PBS + PTT group. A one-way ANOVA statistical analysis found the percentage mean cellular area to be significantly different between the treatment groups ( $F_{(3,7)} = 21.75$ ,  $p < 0.01$ ). Although the tumours in the treatment group began to regrow after day 3, histological analysis confirmed the destruction of tumour cellular tissue as a result of treatment. The morphological features found in the treatment group from histology, such as fragmentation of the nucleus and blebbing of the cells (marked in figure 6.14 (B)), indicates apoptosis as a result of thermal-induced stress, as has been previously reported [271,272].

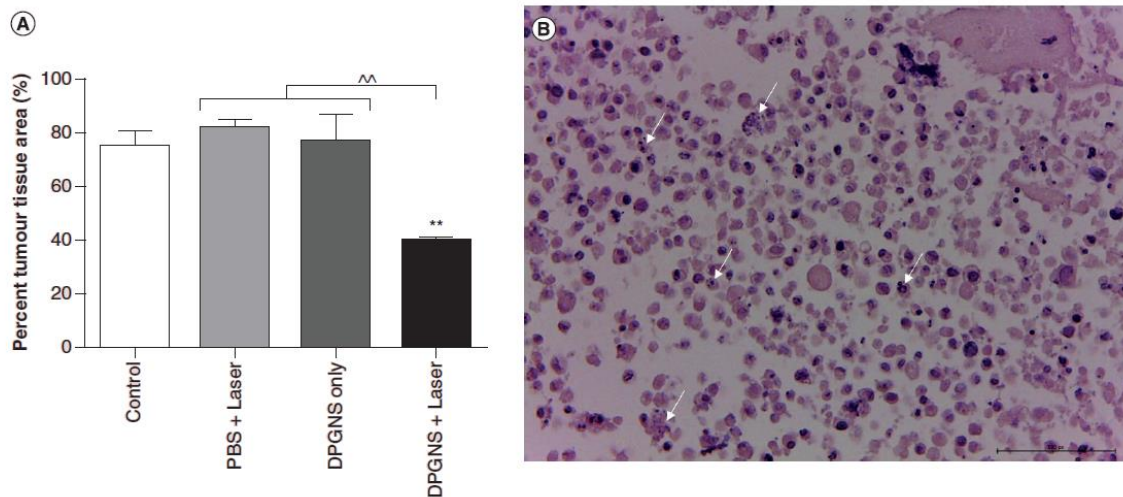


**Figure 6.14.** Quantification of tumour cellular area post treatment. (A) A one-way ANOVA test found the percentage difference in total cellular area to be significant between different groups ( $F_{(3,7)} = 21.75$ ,  $p < 0.01$ ). A student's Newman-Keuls Multiple Comparisons post hoc test found the tumours in the treatment group to a significantly lower cellular area compared to the other groups. Data are expressed as means and SDs. \*\* $p < 0.01$  vs control, ^^ $p < 0.01$  DPGNS + Laser; (B) H&E stained histological section from a tumour in the treatment group with apoptotic cells with fragmented nuclei marked with arrows.

The results indicate that a single silica-coated DPGNS mediated PTT session was sufficient to cause cell damage and/or death. However, in order to increase the therapeutic outcome, it is proposed that multiple PTT sessions (and an increase in laser power) be carried out in future studies. Such an approach may yield an increase in tumour cell death and an overall reduction

in tumour volume. Future studies could also utilise targeted nanoparticles injected intravenously to study particle biodistribution, as monitored with PAI.

## **6.4 Conclusion**

DPGNS were synthesised to produce absorption bands in the 650–700 nm and 1000–1350 nm wavelength ranges. The unique multi-branched structure of DPGNS serves to enhance the localised SPR effect compared with other nanoparticles and results in enhanced photothermal transfer capabilities. The addition of a 10 nm silica layer on DPGNS was found to further increase the photothermal conversion efficiency by 2–3°C. This results in an increase in the PA image contrast, as confirmed in phantom studies. Since photothermal conversion efficiency is the mechanism which decides PA contrast and the effectiveness of PTT, silica-coated DPGNS can be used as a dual-modal nanoprobe for simultaneous PTT and monitoring with PAI. The photothermal capabilities of silica-coated DPGNS were demonstrated *in vivo* in a mouse tumour, where a 8–9°C localised rise in temperature was recorded when irradiated with a 0.5 W/cm<sup>2</sup> laser at 1064 nm during PTT.

The effectiveness of DPGNS mediated PTT was investigated in a longitudinal study on MDA-MB-231 mice tumours, where the mice were divided into a treatment group (DPGNS+PTT) and various control groups. PAI was used to image the distribution of DPGNS and calculate their relative concentration at different study timepoints and between different groups. The results found a reduction in tumour volume in the treatment group on day 3 post-treatment, likely caused by PTT induced hyperthermia. However, tumour growth recovered post day 3, resulting in no overall loss in tumour volume by the study's conclusion on day 21. The tumour regrowth can be explained by thermal resistance developed by tumour cells due to heat induced stress causing inactivation, with the surviving cells becoming able to proliferate again. Histological analysis on the excised tumours revealed a significant percentage decrease in tumour cellular area from the treatment group compared with the control groups. PAI of the treatment group and the DPGNS administered only group at different study timepoints showed a very similar PA signal amplitude, indicating the photostability of the DPGNS under PTT. The results showed that a single DPGNS mediated PTT session was enough to bring about

tumour cell death, however, in order to increase the therapeutic outcome, additional PTT sessions and an increase in the incident laser power are recommended.

## Chapter 7: Conclusion and future work

PAI is an emerging modality that has broad applications in biology and medicine. It has the potential to revolutionise the screening, diagnosis, and management of metabolic diseases, particularly cancer, and is already playing an increasingly important role in basic physiological research and pre-clinical studies. Many new developments are happening in this fast-growing field, with major prospects on the horizon, and also many challenges.

PAI can provide *in vivo* molecular and functional imaging using endogenous optical contrast alone. Exogenous contrast agents extend the capabilities of PAI to targeted molecular and genetic imaging. The scalability of PAI allows it to image on multiple length scales, from organelles to whole bodies, and from superficial structures to internal organs, giving it the unprecedented ability to link macroscopic and microscopic domains using the same optical contrast mechanism.

Clinical and preclinical applications have been widely studied in the past decade. PAI is beginning to find clinical application in several major areas, including melanoma imaging, breast cancer detection, guided sentinel lymph node needle biopsy for cancer staging, chemotherapeutic response imaging, blood oxygenation and perfusion imaging, and metabolic imaging. Several preclinical PAI systems have been commercialised, however, few systems have been approved for clinical use due to the need to pass rigorous validation and regulatory approval.

The clinical applications of this thesis serve to further the integration of PAI in clinical practice with positive results in the areas of melanoma and breast imaging, while the quantitative method proposed offers a solution to correcting for the effects of wavelength-dependent fluence variations in soft tissue. In addition, the PA contrast capabilities of novel gold nanoparticles were demonstrated *in vivo*, showing their potential for targeted molecular imaging applications.

In this thesis, handheld linear-array PAI was introduced to the clinic for breast and melanoma imaging applications. For the breast imaging study, patients were recruited to assess the capability of PAI to image suspect breast lesion morphology and to measure intratumoural oxygenation level. The results showed that linear-array PAI at 15 MHz was capable of imaging

the upper surface of lesions within a depth of 13 mm from the skin surface for both benign and malignant lesions. More significantly, the intratumoural oxygenation measurements from malignant lesions showed strong indication of malignant status in the majority of cases, where clear differences in  $sO_2$  were observed between the intra- and extratumoural spaces and control breast. However, it is noted that the number of patients scanned is low and therefore additional recruitment is planned to obtain a more robust validation. For future studies, it is recommended that lower-frequency PAI probes be used to improve imaging depth. Handheld linear-array PAI could be incorporated in breast cancer screening with conventional US imaging given that both modalities can be performed simultaneously with and with the same probe. PAI can potentially provide an early, point-of-care diagnosis that could expediate patient treatment. Validation of the diagnostic potential of handheld linear-array PAI using endogenous optical contrast alone could therefore increase the effectiveness of breast cancer screening and improve patient therapeutic outcome.

The study criteria also included for PA scans to be performed on women undergoing neoadjuvant chemotherapy to monitor for changes in intratumoural oxygenation level before and after treatment, with a view to predict responding from nonresponding patients. Baseline oxygenation measurements were taken on 2 neoadjuvant patients recruited, however, follow up scans were not possible due to logistical reasons. Confirmation that an easily applicable handheld PA probe can detect changes in intratumoural oxygen level as a predictive biomarker to determine responding from non-responding patients early in treatment would greatly improve neoadjuvant chemotherapy patient management and therapeutic outcome. It is therefore planned to recommence neoadjuvant patient recruitment in the near future, under the same study protocol, to test linear-array PAI's efficacy for this application.

In the melanoma imaging study, patients with suspect cutaneous lesions were recruited to undergo preoperative PAI with a 40 MHz probe to measure lesion thickness. PAI was found to be effective at imaging lesion architecture with high contrast and resolution. The PAI measured lesion thickness was found to correlate strongly with histological thickness for both benign and malignant lesions. The results found that handheld PAI could be used to guide sample depth and location for partial biopsies which have a high rate of undersampling, thereby increasing microstaging accuracy and preventing the need for repeat biopsies in many cases. Additionally, it could be used to guide surgical safety margins for full excisional biopsies.

The invasion of cutaneous melanoma through the basement layer of the epidermis into the blood rich dermis greatly increases the risk of melanoma metastases to the sentinel lymph nodes and organs. In such cases, treatment strategy must be altered to improve patient prognosis. Since PAI can potentially diagnose melanoma using exogenous contrast agents, its ability to detect intradermal lesion growth was tested. Benign intradermal lesions were identified as such in all cases, however epidermal lesions were misread as having a dermal presence in two cases due to irregular border profiles. Notably, *in situ* melanomas were distinguished from invasive melanomas in all cases. The results indicate the efficacy of linear-array PAI in imaging intradermal lesion invasion *in vivo*, thereby increasing staging accuracy and informing treatment strategy if a melanoma diagnosis were possible.

A method to correct for the effects of optical fluence attenuation on measured PA spectra based on the method of arterial fluence calibration was proposed and implemented. The method involves fitting a PA forward model incorporating a model of optical diffusion to the measured arterial signal and solving for the concentrations of the various chromophores that govern the extent of optical attenuation encountered as the light propagates. The determined parameters were used in the same model to correct the venous PA spectrum for optical fluence variation effects and subsequently to make fluence-corrected venous sO<sub>2</sub> measurements. The method was tested on coupled MC-PA simulations, phantoms, and *in vivo* in the human forearm. The parameters determined in the arterial calibration procedure, namely the melanosome volume fraction, blood volume fraction and sO<sub>2</sub> level (in the dermis and subcutaneous fat) were found to be overestimated in each case, which was caused by the 1D nature of the optical model used. However, the determined parameters when used in the venous forward model were found to accurately match its shape and therefore a good correlation between the measured and known venous sO<sub>2</sub> values was obtained. For future studies, the accuracy of the method could be increased by incorporating a more robust optical model that models light in 3D into the forward model, such as an MC model.

The problem of compensating for spectral fluence variations is a longstanding problem in quantitative PAI and solving it is essential for obtaining accurate quantitative measurements. Many different corrective methods have been proposed, however, no one method currently has universal applicability. The method proposed here has the advantage of being able to be applied virtually anywhere in soft tissue due to the ubiquity of arteries and arterioles (depending on if they can be resolved), and the fact that oxygen diffusion primarily takes place in the capillary network, meaning arterial sO<sub>2</sub> level is systemic. Moreover, it can account for differences in

blood perfusion, oxygenation level, and melanosome volume fraction at different measuring sites.

For fluence compensation in tissue environments with complex geometries containing multiple tissue types with variations in tissue density, such as from bones or cartilage, we are currently investigating the use of an MC-PA lookup table method. The method involves performing MC simulations on a tetrahedral-based MC solver [273] coupled with a PA wave simulator that allows for changes in tissue density and speed of sound to be accounted for [274]. The experimentally measured PA signals are fitted to the simulated PA data to account for fluence attenuation effects and solve for the concentrations of given chromophores *in vivo*. The method has the additional benefit of being able to account for complex illumination patterns.

The PA image contrast capabilities of silica-coated DPGNS were tested in phantom and *in vivo* studies. DPGNS are novel nanoparticles that can be tuned to produce SPR absorption bands in the second biological window (1000-1350 nm) by extending the branch-tip length. Moreover, the addition of a nonabsorbing silica coating increases the photothermal efficiency and enhances PA image contrast. This was demonstrated in phantom studies where an increase in the PA signal amplitude was observed in silica-coated DPGNS compared to non-silica-coated DPGNS. The distribution and relative concentration of DPGNS in a mouse-tumour model after DPGNS-mediated PTT was also measured. PAI scans on each study group were taken before PTT treatment on day -1 and after treatment on days 3, 7, 14, and 21. The results showed the *in vivo* concentration of DPGNS in the treatment group and control group to be very similar on each scan day, indicating the photostability of the particles and showing that additional PTT sessions using a higher laser power were possible. In addition, the scans showed a significant DPGNS presence in the tumour on day 7 indicating relatively slow tissue clearance.

Exogenous contrast agents can increase the sensitivity and specificity of PAI and allow for deeper imaging. DPGNS and other gold nanoparticle variants have the distinct advantage over other exogenous contrast agents (e.g. organic dyes) of being optically tunable to a specific wavelength range, in this case the 1000-1350 nm range where optical penetration depth in biological tissue is increased. Bioconjugation of DPGNS with various ligands allows for targeted molecular imaging, therapy monitoring, and drug delivery, giving them many potential applications. Our group is currently investigating the efficacy of the DPGNS reported in this thesis for use as a PA contrast agent coupled with stem cells for the treatment of osteoarthritis.

The study involves imaging the uptake and distribution of DPGNS tagged stems cells in the knee joint in a longitudinal study using PAI in the 1000-1350 nm wavelength range.

In light of the uniqueness and versatility of PAI, its continued development, of which this thesis contributes in part, is expected to lead to more high-impact applications in biomedical studies and clinical practice.

## Chapter 8: References

- [1] M. Xu, L.V. Wang, Photoacoustic imaging in biomedicine, *Review of Scientific Instruments*. 77 (2006) 041101.
- [2] C. Li, L.V. Wang, Photoacoustic tomography and sensing in biomedicine, *Physics in Medicine & Biology*. 54 (2009) R59.
- [3] L.V. Wang, S. Hu, Photoacoustic tomography: *in vivo* imaging from organelles to organs, *Science*. 335 (2012) 1458–1462.
- [4] J. Xia, J. Yao, L.V. Wang, Photoacoustic tomography: principles and advances, *Electromagnetic Waves (Cambridge, Mass.)*. 147 (2014) 1.
- [5] J. Yao, L.V. Wang, Photoacoustic tomography: fundamentals, advances and prospects, *Contrast Media & Molecular Imaging*. 6 (2011) 332–345.
- [6] P. Beard, Biomedical photoacoustic imaging, *Interface Focus*. (2011) rfs20110028.
- [7] S. Manohar, D. Razansky, Photoacoustics: a historical review, *Advances in Optics and Photonics*. 8 (2016) 586–617.
- [8] L.V. Wang, H.I. Wu, *Biomedical Optics: Principles and Imaging 2007*, Hoboken: John Wiley & Sons. (n.d.).
- [9] A.J. Welch, M.J. Van Gemert, *Optical-thermal response of laser-irradiated tissue*, Springer, 2011.
- [10] E. De Montigny, *Photoacoustic Tomography: Principles and applications*, Department of Physics Engineering, Polytechnic School Montreal. (2011).
- [11] K. Giering, I. Lamprecht, O. Minet, A. Handke, Determination of the specific heat capacity of healthy and tumorous human tissue, *Thermochimica Acta*. 251 (1995) 199–205.
- [12] A.N.S. Institute, *American national standard for safe use of lasers*, Laser Institute of America, 2007.
- [13] D.-K. Yao, C. Zhang, K.I. Maslov, L.V. Wang, Photoacoustic measurement of the Grüneisen parameter of tissue, *Journal of Biomedical Optics*. 19 (2014) 017007.
- [14] I.V. Larina, K.V. Larin, R.O. Esenaliev, Real-time optoacoustic monitoring of temperature in tissues, *Journal of Physics D: Applied Physics*. 38 (2005) 2633.
- [15] P.M. Morse, K.U. Ingard, *Theoretical acoustics*, Princeton university press, 1986.
- [16] M.J.C. Van Gemert, S.L. Jacques, H. Sterenborg, W.M. Star, Skin optics, *IEEE Transactions on Biomedical Engineering*. 36 (1989) 1146–1154.

- [17] R.R. Anderson, J.A. Parrish, The optics of human skin, *Journal of Investigative Dermatology*. 77 (1981) 13–19.
- [18] S.L. Jacques, Optical properties of biological tissues: a review, *Physics in Medicine & Biology*. 58 (2013) R37.
- [19] R.A. Kruger, R.B. Lam, D.R. Reinecke, S.P. Del Rio, R.P. Doyle, Photoacoustic angiography of the breast, *Medical Physics*. 37 (2010) 6096–6100.
- [20] G. Ku, L.V. Wang, Deeply penetrating photoacoustic tomography in biological tissues enhanced with an optical contrast agent, *Optics Letters*. 30 (2005) 507–509.
- [21] C. Kim, T.N. Erpelding, L. Jankovic, M.D. Pashley, L.V. Wang, Deeply penetrating *in vivo* photoacoustic imaging using a clinical ultrasound array system, *Biomedical Optics Express*. 1 (2010) 278–284.
- [22] K. Homan, S. Kim, Y.-S. Chen, B. Wang, S. Mallidi, S. Emelianov, Prospects of molecular photoacoustic imaging at 1064 nm wavelength, *Optics Letters*. 35 (2010) 2663–2665.
- [23] M. Xu, L.V. Wang, Analytic explanation of spatial resolution related to bandwidth and detector aperture size in thermoacoustic or photoacoustic reconstruction, *Physical Review E*. 67 (2003) 056605.
- [24] M. Xu, L.V. Wang, Universal back-projection algorithm for photoacoustic computed tomography, *Physical Review E*. 71 (2005) 016706.
- [25] Y. Xu, L.V. Wang, Time reversal and its application to tomography with diffracting sources, *Physical Review Letters*. 92 (2004) 033902.
- [26] Scott Prael, Oregon Medical Laser Center, spectra: <https://omlc.org/spectra/>, (2019). <https://omlc.org/spectra/>.
- [27] H.J. Van Staveren, C.J. Moes, J. van Marie, S.A. Prael, M.J. Van Gemert, Light scattering in Intralipid-10% in the wavelength range of 400–1100 nm, *Applied Optics*. 30 (1991) 4507–4514.
- [28] S.L. Jacques, C.A. Alter, S.A. Prael, Angular dependence of HeNe laser light scattering by human dermis, *Lasers Life Sci*. 1 (1987) 309–333.
- [29] Q. Fu, W. Sun, Mie theory for light scattering by a spherical particle in an absorbing medium, *Applied Optics*. 40 (2001) 1354–1361.
- [30] T. Vo-Dinh, *Biomedical photonics handbook: biomedical diagnostics*, CRC press, 2014.
- [31] W.-F. Cheong, S.A. Prael, A.J. Welch, A review of the optical properties of biological tissues, *IEEE Journal of Quantum Electronics*. 26 (1990) 2166–2185.

- [32] G. Marquez, L.V. Wang, S.-P. Lin, J.A. Schwartz, S.L. Thomsen, Anisotropy in the absorption and scattering spectra of chicken breast tissue, *Applied Optics*. 37 (1998) 798–804.
- [33] S.L. Jacques, Origins of tissue optical properties in the UVA, visible, and NIR regions, *OSA TOPS on Advances in Optical Imaging and Photon Migration*. 2 (1996) 364–369.
- [34] A.N. Bashkatov, E.A. Genina, V.I. Kochubey, V.V. Tuchin, Optical properties of human skin, subcutaneous and mucous tissues in the wavelength range from 400 to 2000 nm, *Journal of Physics D: Applied Physics*. 38 (2005) 2543.
- [35] S.L. Jacques, B.W. Pogue, Tutorial on diffuse light transport, *Journal of Biomedical Optics*. 13 (2008) 041302.
- [36] S.L. Jacques, L. Wang, Monte Carlo modeling of light transport in tissues, in: *Optical-Thermal Response of Laser-Irradiated Tissue*, Springer, 1995: pp. 73–100.
- [37] C.M. Gardner, S.L. Jacques, A.J. Welch, Light transport in tissue: Accurate expressions for one-dimensional fluence rate and escape function based upon Monte Carlo simulation, *Lasers in Surgery and Medicine: The Official Journal of the American Society for Laser Medicine and Surgery*. 18 (1996) 129–138.
- [38] C. Zhu, Q. Liu, Review of Monte Carlo modeling of light transport in tissues, *Journal of Biomedical Optics*. 18 (2013) 050902.
- [39] D. Toubanc, Henyey–Greenstein and Mie phase functions in Monte Carlo radiative transfer computations, *Applied Optics*. 35 (1996) 3270–3274.
- [40] B.C. Wilson, G. Adam, A Monte Carlo model for the absorption and flux distributions of light in tissue, *Medical Physics*. 10 (1983) 824–830.
- [41] L. Wang, S.L. Jacques, L. Zheng, MCML—Monte Carlo modeling of light transport in multi-layered tissues, *Computer Methods and Programs in Biomedicine*. 47 (1995) 131–146.
- [42] S.L. Jacques, T. Li, Monte Carlo simulations of light transport in 3D heterogenous tissues (mcxyz. c), See [Http://Omlc.Org/Software/Mc/Mcxyz/Index.Html](http://Omlc.Org/Software/Mc/Mcxyz/Index.Html) [Accessed 30.01. 2017]. (2013).
- [43] S.L. Jacques, Coupling 3D Monte Carlo light transport in optically heterogeneous tissues to photoacoustic signal generation, *Photoacoustics*. 2 (2014) 137–142.
- [44] S.L. Jacques, G. Paltauf, Modeling pressure waves generated by pulsed laser irradiation of irregularly shaped absorbing objects within media, in: *Biomedical Optoacoustics II*, International Society for Optics and Photonics, 2001: pp. 90–101.

- [45] A. Needles, A. Heinmiller, J. Sun, C. Theodoropoulos, D. Bates, D. Hirson, M. Yin, F.S. Foster, Development and initial application of a fully integrated photoacoustic micro-ultrasound system, *IEEE Transactions on Ultrasonics, Ferroelectrics, and Frequency Control*. 60 (2013) 888–897.
- [46] H. Zafar, A. Breathnach, H.M. Subhash, M.J. Leahy, Linear-array-based photoacoustic imaging of human microcirculation with a range of high frequency transducer probes, *Journal of Biomedical Optics*. 20 (2014) 051021.
- [47] A. Needles, A. Heinmiller, P. Ephrat, C. Bilan-Tracey, A. Trujillo, C. Theodoropoulos, D. Hirson, F.S. Foster, Development of a combined photoacoustic micro-ultrasound system for estimating blood oxygenation, in: *2010 IEEE International Ultrasonics Symposium*, IEEE, 2010: pp. 390–393.
- [48] S.I. Fox, *Human Physiology 9th Edition*, McGraw-Hill press, New York, USA, 2006.
- [49] C.A. Finch, Oxygen transport in man, *Chest*. 61 (1972) 12S-13S.
- [50] L.S. Costanzo, *Physiology*, Elsevier, 2014.
- [51] R.N. Pittman, Regulation of tissue oxygenation, in: *Colloquium Series on Integrated Systems Physiology: From Molecule to Function*, Morgan & Claypool Life Sciences, 2011: pp. 1–100.
- [52] F. Martini, *Fundamentals of anatomy & physiology*, 8th ed., Pearson/Benjamin Cummings, p. 657, 2009.
- [53] R.I. Weed, C.F. Reed, G. Berg, Is hemoglobin an essential structural component of human erythrocyte membranes?, *The Journal of Clinical Investigation*. 42 (1963) 581–588.
- [54] S. Sukriti, M. Tauseef, P. Yazbeck, D. Mehta, Mechanisms regulating endothelial permeability, *Pulmonary Circulation*. 4 (2014) 535–551.
- [55] R.N. Pittman, The circulatory system and oxygen transport, in: *Regulation of Tissue Oxygenation*, Morgan & Claypool Life Sciences, 2011.
- [56] K.K. Tremper, Pulse oximetry, *Chest*. 95 (1989) 713–715.
- [57] E.D. Chan, M.M. Chan, M.M. Chan, Pulse oximetry: understanding its basic principles facilitates appreciation of its limitations, *Respiratory Medicine*. 107 (2013) 789–799.
- [58] S.L. Schutz, Oxygen saturation monitoring by pulse oximetry, *AACN Procedure Manual for Critical Care*. (2005) 101–107.
- [59] J. Samuel, C. Franklin, Hypoxemia and hypoxia, in: *Common Surgical Diseases*, Springer, 2008: pp. 391–394.

- [60] C. Iadecola, M. Alexander, Cerebral ischemia and inflammation, *Current Opinion in Neurology*. 14 (2001) 89–94.
- [61] T.Q. Duong, C. Iadecola, S.-G. Kim, Effect of hyperoxia, hypercapnia, and hypoxia on cerebral interstitial oxygen tension and cerebral blood flow, *Magnetic Resonance in Medicine: An Official Journal of the International Society for Magnetic Resonance in Medicine*. 45 (2001) 61–70.
- [62] S.H. Haddad, Y.M. Arabi, Critical care management of severe traumatic brain injury in adults, *Scandinavian Journal of Trauma, Resuscitation and Emergency Medicine*. 20 (2012) 12.
- [63] M. Khan, C.G. Pretty, A.C. Amies, J. Balmer, H.E. Banna, G.M. Shaw, J.G. Chase, Proof of concept non-invasive estimation of peripheral venous oxygen saturation, *Biomedical Engineering Online*. 16 (2017) 60.
- [64] H.-Y. Tsai, K.-C. Huang, H.-C. Chang, J.-L.A. Yeh, C.-H. Chang, A Noncontact Skin Oxygen-Saturation Imaging System for Measuring Human Tissue Oxygen Saturation., *IEEE Trans. Instrumentation and Measurement*. 63 (2014) 2620–2631.
- [65] P. van Beest, G. Wietasch, T. Scheeren, P. Spronk, M. Kuiper, Clinical review: use of venous oxygen saturations as a goal-a yet unfinished puzzle, *Critical Care*. 15 (2011) 232.
- [66] J.M. Lynch, E.M. Buckley, P.J. Schwab, D.R. Busch, B.D. Hanna, M.E. Putt, D.J. Licht, A.G. Yodh, Noninvasive optical quantification of cerebral venous oxygen saturation in humans, *Academic Radiology*. 21 (2014) 162–167.
- [67] C. Higgins, *Central venous blood gas analysis*, 2011.
- [68] K.R. Walley, Use of central venous oxygen saturation to guide therapy, *American Journal of Respiratory and Critical Care Medicine*. 184 (2011) 514–520.
- [69] Z. Walton, *Measuring Venous Oxygen Saturation Using the Photoplethysmograph Waveform*, (2010).
- [70] M. Nitzan, A. Babchenko, B. Khanokh, H. Taitelbaum, Measurement of oxygen saturation in venous blood by dynamic near IR spectroscopy, *Journal of Biomedical Optics*. 5 (2000) 155–163.
- [71] D.M. Gilkes, G.L. Semenza, D. Wirtz, Hypoxia and the extracellular matrix: drivers of tumour metastasis, *Nature Reviews Cancer*. 14 (2014) 430–439.
- [72] M.C. Brahim-Horn, J. Chiche, J. Pouysségur, Hypoxia and cancer, *Journal of Molecular Medicine*. 85 (2007) 1301–1307.

- [73] M.-L. Li, J.-T. Oh, X. Xie, G. Ku, W. Wang, C. Li, G. Lungu, G. Stoica, L.V. Wang, Simultaneous molecular and hypoxia imaging of brain tumors *in vivo* using spectroscopic photoacoustic tomography, *Proceedings of the IEEE*. 96 (2008) 481–489.
- [74] I.N. Fleming, R. Manavaki, P.J. Blower, C. West, K.J. Williams, A.L. Harris, J. Domarkas, S. Lord, C. Baldry, F.J. Gilbert, Imaging tumour hypoxia with positron emission tomography, *British Journal of Cancer*. 112 (2015) 238–250.
- [75] K. Brindle, New approaches for imaging tumour responses to treatment, *Nature Reviews Cancer*. 8 (2008) 94.
- [76] L. Ziemer, S. Evans, A. Kachur, A. Shuman, C. Cardi, W. Jenkins, J. Karp, A. Alavi, W. Dolbier, C. Koch, Noninvasive imaging of tumor hypoxia in rats using the 2-nitroimidazole 18 F-EF5, *European Journal of Nuclear Medicine and Molecular Imaging*. 30 (2003) 259–266.
- [77] F. Spill, D.S. Reynolds, R.D. Kamm, M.H. Zaman, Impact of the physical microenvironment on tumor progression and metastasis, *Current Opinion in Biotechnology*. 40 (2016) 41–48.
- [78] R.L. Jensen, Brain tumor hypoxia: tumorigenesis, angiogenesis, imaging, pseudoprogression, and as a therapeutic target, *Journal of Neuro-Oncology*. 92 (2009) 317–335.
- [79] J.G. Rajendran, K.A. Krohn, Imaging hypoxia and angiogenesis in tumors, *Radiologic Clinics*. 43 (2005) 169–187.
- [80] N.G. Costouros, F.E. Diehn, S.K. Libutti, Molecular imaging of tumor angiogenesis, *Journal of Cellular Biochemistry*. 87 (2002) 72–78.
- [81] T.O. McBride, B.W. Pogue, E.D. Gerety, S.B. Poplack, U.L. Österberg, K.D. Paulsen, Spectroscopic diffuse optical tomography for the quantitative assessment of hemoglobin concentration and oxygen saturation in breast tissue, *Applied Optics*. 38 (1999) 5480–5490.
- [82] J. Kim, P. Gao, C.V. Dang, Effects of hypoxia on tumor metabolism, *Cancer and Metastasis Reviews*. 26 (2007) 291–298.
- [83] O. Trédan, C.M. Galmarini, K. Patel, I.F. Tannock, Drug resistance and the solid tumor microenvironment, *Journal of the National Cancer Institute*. 99 (2007) 1441–1454.
- [84] P. Vaupel, A. Mayer, Hypoxia in cancer: significance and impact on clinical outcome, *Cancer and Metastasis Reviews*. 26 (2007) 225–239.
- [85] D. Roblyer, S. Ueda, A. Cerussi, W. Tanamai, A. Durkin, R. Mehta, D. Hsiang, J.A. Butler, C. McLaren, W.-P. Chen, Optical imaging of breast cancer oxyhemoglobin flare

- correlates with neoadjuvant chemotherapy response one day after starting treatment, *Proceedings of the National Academy of Sciences*. 108 (2011) 14626–14631.
- [86] S. Ueda, D. Roblyer, A. Cerussi, A. Durkin, A. Leproux, Y. Santoro, S. Xu, T.D. O’Sullivan, D. Hsiang, R. Mehta, Baseline tumor oxygen saturation correlates with a pathologic complete response in breast cancer patients undergoing neoadjuvant chemotherapy, *Cancer Research*. 72 (2012) 4318–4328.
- [87] B.J. Tromberg, Z. Zhang, A. Leproux, T.D. O’Sullivan, A.E. Cerussi, P.M. Carpenter, R.S. Mehta, D. Roblyer, W. Yang, K.D. Paulsen, Predicting responses to neoadjuvant chemotherapy in breast cancer: ACRIN 6691 trial of diffuse optical spectroscopic imaging, *Cancer Research*. 76 (2016) 5933–5944.
- [88] D.B. Jakubowski, A.E. Cerussi, F. Bevilacqua, N. Shah, D. Hsiang, J. Butler, B.J. Tromberg, Monitoring neoadjuvant chemotherapy in breast cancer using quantitative diffuse optical spectroscopy: a case study, (2004).
- [89] S.M. Evans, K.D. Judy, I. Dunphy, W.T. Jenkins, W.-T. Hwang, P.T. Nelson, R.A. Lustig, K. Jenkins, D.P. Magarelli, S.M. Hahn, Hypoxia is important in the biology and aggression of human glial brain tumors, *Clinical Cancer Research*. 10 (2004) 8177–8184.
- [90] P. Vaupel, D.K. Kelleher, M. Höckel, Oxygenation status of malignant tumors: pathogenesis of hypoxia and significance for tumor therapy, in: *Seminars in Oncology*, Elsevier, 2001: pp. 29–35.
- [91] O. Hashimoto, K. Shimizu, S. Semba, S. Chiba, Y. Ku, H. Yokozaki, Y. Hori, Hypoxia induces tumor aggressiveness and the expansion of CD133-positive cells in a hypoxia-inducible factor-1 $\alpha$ -dependent manner in pancreatic cancer cells, *Pathobiology*. 78 (2011) 181–192.
- [92] J. Chiche, M.C. Brahimi-Horn, J. Pouyssegur, Tumour hypoxia induces a metabolic shift causing acidosis: a common feature in cancer, *Journal of Cellular and Molecular Medicine*. 14 (2010) 771–794.
- [93] W.K. Stadelmann, A.G. Digenis, G.R. Tobin, Impediments to wound healing, *The American Journal of Surgery*. 176 (1998) 39S-47S.
- [94] R.S. Kirsner, A.C. Vivas, Lower-extremity ulcers: diagnosis and management, *British Journal of Dermatology*. 173 (2015) 379–390.
- [95] D. Mathieu, J.-C. Linke, F. Wattel, Non-healing wounds, in: *Handbook on Hyperbaric Medicine*, Springer, 2006: pp. 401–428.

- [96] B.T. Ngo, K.D. Hayes, D.J. DiMiao, S.K. Srinivasan, C.J. Huerter, M.S. Rendell, Manifestations of cutaneous diabetic microangiopathy, *American Journal of Clinical Dermatology*. 6 (2005) 225–237.
- [97] J.L. Mills Sr, M.S. Conte, D.G. Armstrong, F.B. Pomposelli, A. Schanzer, A.N. Sidawy, G. Andros, S. for V.S.L.E.G. Committee, The society for vascular surgery lower extremity threatened limb classification system: risk stratification based on wound, ischemia, and foot infection (WIFI), *Journal of Vascular Surgery*. 59 (2014) 220–234.
- [98] P. Burns, S. Gough, A.W. Bradbury, Management of peripheral arterial disease in primary care, *Bmj*. 326 (2003) 584–588.
- [99] S.J. Matcher, P.J. Kirkpatrick, K. Nahid, M. Cope, D.T. Delpy, Absolute quantification methods in tissue near-infrared spectroscopy, in: *Optical Tomography, Photon Migration, and Spectroscopy of Tissue and Model Media: Theory, Human Studies, and Instrumentation*, International Society for Optics and Photonics, 1995: pp. 486–496.
- [100] D.T. Delpy, M. Cope, Quantification in tissue near-infrared spectroscopy, *Philosophical Transactions of the Royal Society of London. Series B: Biological Sciences*. 352 (1997) 649–659.
- [101] J.P. Culver, T. Durduran, D. Furuya, C. Cheung, J.H. Greenberg, A.G. Yodh, Diffuse optical tomography of cerebral blood flow, oxygenation, and metabolism in rat during focal ischemia, *Journal of Cerebral Blood Flow & Metabolism*. 23 (2003) 911–924.
- [102] T. Durduran, G. Yu, M.G. Burnett, J.A. Detre, J.H. Greenberg, J. Wang, C. Zhou, A.G. Yodh, Diffuse optical measurement of blood flow, blood oxygenation, and metabolism in a human brain during sensorimotor cortex activation, *Optics Letters*. 29 (2004) 1766–1768.
- [103] W. Utz, J. Jordan, T. Niendorf, M. Stoffels, F.C. Luft, R. Dietz, M.G. Friedrich, Blood oxygen level-dependent MRI of tissue oxygenation: relation to endothelium-dependent and endothelium-independent blood flow changes, *Arteriosclerosis, Thrombosis, and Vascular Biology*. 25 (2005) 1408–1413.
- [104] J. Neugarten, Renal BOLD-MRI and assessment for renal hypoxia, *Kidney International*. 81 (2012) 613–614.
- [105] M.C. Krishna, S. Subramanian, P. Kuppusamy, J.B. Mitchell, Magnetic resonance imaging for *in vivo* assessment of tissue oxygen concentration, in: *Seminars in Radiation Oncology*, Elsevier, 2001: pp. 58–69.
- [106] S.C. Textor, J.F. Glockner, L.O. Lerman, S. Misra, M.A. McKusick, S.J. Riederer, J.P. Grande, S.I. Gomez, J.C. Romero, The use of magnetic resonance to evaluate tissue

- oxygenation in renal artery stenosis, *Journal of the American Society of Nephrology*. 19 (2008) 780–788.
- [107] A.K. Gupta, P.J. Hutchinson, T. Fryer, P.G. Al-Rawi, D.A. Parry, P.S. Minhas, R. Kett-White, P.J. Kirkpatrick, J.C. Mathews, S. Downey, Measurement of brain tissue oxygenation performed using positron emission tomography scanning to validate a novel monitoring method, *Journal of Neurosurgery*. 96 (2002) 263–268.
- [108] M.N. Diringier, V. Aiyagari, A.R. Zazulia, T.O. Videen, W.J. Powers, Effect of hyperoxia on cerebral metabolic rate for oxygen measured using positron emission tomography in patients with acute severe head injury, *Journal of Neurosurgery*. 106 (2007) 526–529.
- [109] Y.-C.T. Huang, Monitoring oxygen delivery in the critically ill, *Chest*. 128 (2005) 554S–560S.
- [110] A. Shiino, Y. Morita, A. Tsuji, K. Maeda, R. Ito, A. Furukawa, M. Matsuda, T. Inubushi, Estimation of cerebral perfusion reserve by blood oxygenation level—dependent imaging: Comparison with single-photon emission computed tomography, *Journal of Cerebral Blood Flow & Metabolism*. 23 (2003) 121–135.
- [111] S.I. Chefer, A.G. Horti, K.S. Lee, A.O. Koren, D.W. Jones, J.G. Gorey, J.M. Links, A.G. Mukhin, D.R. Weinberger, E.D. London, *In vivo* imaging of brain nicotinic acetylcholine receptors with 5-[123I] iodo-A-85380 using single photon emission computed tomography, *Life Sciences*. 63 (1998) PL355–PL360.
- [112] Y. Shen, Z. Kou, C.W. Kreipke, T. Petrov, J. Hu, E.M. Haacke, *In vivo* measurement of tissue damage, oxygen saturation changes and blood flow changes after experimental traumatic brain injury in rats using susceptibility weighted imaging, *Magnetic Resonance Imaging*. 25 (2007) 219–227.
- [113] M. Elas, B.B. Williams, A. Parasca, C. Mailer, C.A. Pelizzari, M.A. Lewis, J.N. River, G.S. Karczmar, E.D. Barth, H.J. Halpern, Quantitative tumor oxymetric images from 4D electron paramagnetic resonance imaging (EPRI): methodology and comparison with blood oxygen level-dependent (BOLD) MRI, *Magnetic Resonance in Medicine: An Official Journal of the International Society for Magnetic Resonance in Medicine*. 49 (2003) 682–691.
- [114] J. Shen, R. Sood, J. Weaver, G.S. Timmins, A. Schnell, M. Miyake, J.P. Kao, G.M. Rosen, K.J. Liu, Direct visualization of mouse brain oxygen distribution by electron paramagnetic resonance imaging: application to focal cerebral ischemia, *Journal of Cerebral Blood Flow & Metabolism*. 29 (2009) 1695–1703.

- [115] S.S. Velan, R.G. Spencer, J.L. Zweier, P. Kuppusamy, Electron paramagnetic resonance oxygen mapping (EPRM): direct visualization of oxygen concentration in tissue, *Magnetic Resonance in Medicine*. 43 (2000) 804–809.
- [116] D.S. Vikram, J.L. Zweier, P. Kuppusamy, Methods for noninvasive imaging of tissue hypoxia, *Antioxidants & Redox Signaling*. 9 (2007) 1745–1756.
- [117] B.T. Cox, J.G. Laufer, P.C. Beard, S.R. Arridge, Quantitative spectroscopic photoacoustic imaging: a review, *Journal of Biomedical Optics*. 17 (2012) 061202.
- [118] A.V. Mamonov, K. Ren, Quantitative photoacoustic imaging in radiative transport regime, *ArXiv Preprint ArXiv:1207.4664*. (2012).
- [119] Z. Yuan, H. Jiang, Quantitative photoacoustic tomography: Recovery of optical absorption coefficient maps of heterogeneous media, *Applied Physics Letters*. 88 (2006) 231101.
- [120] J.R. Cook, W. Frey, S. Emelianov, Quantitative photoacoustic imaging of nanoparticles in cells and tissues, *ACS Nano*. 7 (2013) 1272–1280.
- [121] Imaging of Vasculature with the Vevo LAZR Photoacoustic Imaging System, Application Note Ver1.1, VisualSonics Inc., (2010).
- [122] B.T. Cox, J.G. Laufer, P.C. Beard, The challenges for quantitative photoacoustic imaging, in: *Photons Plus Ultrasound: Imaging and Sensing 2009*, International Society for Optics and Photonics, 2009: p. 717713.
- [123] K. Maslov, H.F. Zhang, L.V. Wang, Effects of wavelength-dependent fluence attenuation on the noninvasive photoacoustic imaging of hemoglobin oxygen saturation in subcutaneous vasculature *in vivo*, *Inverse Problems*. 23 (2007) S113.
- [124] H.F. Zhang, K. Maslov, M. Sivaramakrishnan, G. Stoica, L.V. Wang, Imaging of hemoglobin oxygen saturation variations in single vessels *in vivo* using photoacoustic microscopy, *Applied Physics Letters*. 90 (2007) 053901.
- [125] S. Kim, Y.-S. Chen, G.P. Luke, S.Y. Emelianov, *In vivo* three-dimensional spectroscopic photoacoustic imaging for monitoring nanoparticle delivery, *Biomedical Optics Express*. 2 (2011) 2540–2550.
- [126] J. Laufer, C. Elwell, D. Delpy, P. Beard, In vitro measurements of absolute blood oxygen saturation using pulsed near-infrared photoacoustic spectroscopy: accuracy and resolution, *Physics in Medicine & Biology*. 50 (2005) 4409.
- [127] J. Laufer, D. Delpy, C. Elwell, P. Beard, Quantitative spatially resolved measurement of tissue chromophore concentrations using photoacoustic spectroscopy: application to the

- measurement of blood oxygenation and haemoglobin concentration, *Physics in Medicine & Biology*. 52 (2006) 141.
- [128] J. Laufer, B. Cox, E. Zhang, P. Beard, Quantitative determination of chromophore concentrations from 2D photoacoustic images using a nonlinear model-based inversion scheme, *Applied Optics*. 49 (2010) 1219–1233.
- [129] J. Laufer, E. Zhang, P. Beard, Quantitative in-vivo measurements of blood oxygen saturation using multiwavelength photoacoustic imaging, in: *Photons Plus Ultrasound: Imaging and Sensing 2007: The Eighth Conference on Biomedical Thermoacoustics, Optoacoustics, and Acousto-Optics*, International Society for Optics and Photonics, 2007: p. 64371Z.
- [130] J. Xia, A. Danielli, Y. Liu, L. Wang, K. Maslov, L.V. Wang, Calibration-free quantification of absolute oxygen saturation based on the dynamics of photoacoustic signals, *Optics Letters*. 38 (2013) 2800–2803.
- [131] Z. Guo, S. Hu, L.V. Wang, Calibration-free absolute quantification of optical absorption coefficients using acoustic spectra in 3D photoacoustic microscopy of biological tissue, *Optics Letters*. 35 (2010) 2067–2069.
- [132] C. Maetzler, S. Jaques, <https://omlc.org/software/mie/>, (2018). <https://omlc.org/software/mie/>.
- [133] R. Cubeddu, A. Pifferi, P. Taroni, A. Torricelli, G. Valentini, A solid tissue phantom for photon migration studies, *Physics in Medicine & Biology*. 42 (1997) 1971.
- [134] S.-H. Tseng, P. Bargo, A. Durkin, N. Kollias, Chromophore concentrations, absorption and scattering properties of human skin in-vivo, *Optics Express*. 17 (2009) 14599–14617.
- [135] A. Breathnach, E. Concannon, J.J. Dorairaj, S. Shaharan, J. McGrath, J. Jose, J.L. Kelly, M.J. Leahy, Preoperative measurement of cutaneous melanoma and nevi thickness with photoacoustic imaging, *Journal of Medical Imaging*. 5 (2018) 015004.
- [136] D. Braithwaite, J. Demb, L.M. Henderson, American Cancer Society: Cancer Facts and Figures 2016, Atlanta, GA: American Cancer Society. (2016).
- [137] A.F. Jerant, J.T. Johnson, C. Demastes Sheridan, T.J. Caffrey, Early detection and treatment of skin cancer., *American Family Physician*. 62 (2000).
- [138] J. Jose, D.J. Grootendorst, T.W. Vijn, T.G. van Leeuwen, W. Steenbergen, S. Manohar, M. Wouters, T.J. Ruers, H. van Boven, Initial results of imaging melanoma metastasis in resected human lymph nodes using photoacoustic computed tomography, *Journal of Biomedical Optics*. 16 (2011) 096021.

- [139] J.W. Kelly, M.A. Henderson, V.J. Thursfield, J. Slavin, J. Ainslie, G.G. Giles, The management of primary cutaneous melanoma in Victoria in 1996 and 2000, *Medical Journal of Australia*. 187 (2007) 511–514.
- [140] T.J. Hieken, R. Hernández-Irizarry, J.M. Boll, J.E. Jones Coleman, Accuracy of diagnostic biopsy for cutaneous melanoma: implications for surgical oncologists, *International Journal of Surgical Oncology*. 2013 (2013).
- [141] J.C. Ng, S. Swain, J.P. Dowling, R. Wolfe, P. Simpson, J.W. Kelly, The impact of partial biopsy on histopathologic diagnosis of cutaneous melanoma: experience of an Australian tertiary referral service, *Archives of Dermatology*. 146 (2010) 234–239.
- [142] O.A. Orzan, A. Şandru, C.R. Jecan, Controversies in the diagnosis and treatment of early cutaneous melanoma, *Journal of Medicine and Life*. 8 (2015) 132.
- [143] C.K. Bichakjian, A.C. Halpern, T.M. Johnson, A.F. Hood, J.M. Grichnik, S.M. Swetter, H. Tsao, V.H. Barbosa, T.-Y. Chuang, M. Duvic, Guidelines of care for the management of primary cutaneous melanoma, *Journal of the American Academy of Dermatology*. 65 (2011) 1032–1047.
- [144] V.H. Stell, H.J. Norton, K.S. Smith, J.C. Salo, R.L. White, Method of biopsy and incidence of positive margins in primary melanoma, *Annals of Surgical Oncology*. 14 (2007) 893–898.
- [145] D.J. Karimipour, J.L. Schwartz, T.S. Wang, C.K. Bichakjian, J.S. Orringer, A.L. King, C.C. Huang, T.M. Johnson, Microstaging accuracy after subtotal incisional biopsy of cutaneous melanoma, *Journal of the American Academy of Dermatology*. 52 (2005) 798–802.
- [146] C. Benvenuto-Andrade, S.W. Dusza, A.L.C. Agero, A. Scope, M. Rajadhyaksha, A.C. Halpern, A.A. Marghoob, Differences between polarized light dermoscopy and immersion contact dermoscopy for the evaluation of skin lesions, *Archives of Dermatology*. 143 (2007) 329–338.
- [147] T. Gambichler, P. Regeniter, F.G. Bechara, A. Orlikov, R. Vasa, G. Moussa, M. Stücker, P. Altmeyer, K. Hoffmann, Characterization of benign and malignant melanocytic skin lesions using optical coherence tomography *in vivo*, *Journal of the American Academy of Dermatology*. 57 (2007) 629–637.
- [148] S. Segura, S. Puig, C. Carrera, J. Palou, J. Malvehy, Development of a two-step method for the diagnosis of melanoma by reflectance confocal microscopy, *Journal of the American Academy of Dermatology*. 61 (2009) 216–229.

- [149] M. Rajadhyaksha, M. Grossman, D. Esterowitz, R.H. Webb, R.R. Anderson, *In vivo* confocal scanning laser microscopy of human skin: melanin provides strong contrast, *Journal of Investigative Dermatology*. 104 (1995) 946–952.
- [150] E. Dimitrow, M. Ziemer, M.J. Koehler, J. Norgauer, K. König, P. Elsner, M. Kaatz, Sensitivity and specificity of multiphoton laser tomography for *in vivo* and *ex vivo* diagnosis of malignant melanoma, *Journal of Investigative Dermatology*. 129 (2009) 1752–1758.
- [151] J. Bittoun, B. Querleux, L. Darrasse, Advances in MR imaging of the skin, *NMR in Biomedicine: An International Journal Devoted to the Development and Application of Magnetic Resonance In vivo*. 19 (2006) 723–730.
- [152] T.Z. Belhocine, A.M. Scott, E. Even-Sapir, J.-L. Urbain, R. Essner, Role of nuclear medicine in the management of cutaneous malignant melanoma, *Journal of Nuclear Medicine*. 47 (2006) 957–967.
- [153] L. Smith, S. MacNeil, State of the art in non-invasive imaging of cutaneous melanoma, *Skin Research and Technology*. 17 (2011) 257–269.
- [154] W. Dummer, H.-J. Blaheta, B.C. Bastian, T. Schenk, E.-B. Bröcker, W. Remy, Preoperative characterization of pigmented skin lesions by epiluminescence microscopy and high-frequency ultrasound, *Archives of Dermatology*. 131 (1995) 279–285.
- [155] L.V. Wang, Prospects of photoacoustic tomography, *Medical Physics*. 35 (2008) 5758–5767.
- [156] X. Wang, G. Ku, X. Xie, Y. Wang, G. Stoica, L.V. Wang, Noninvasive functional photoacoustic tomography of blood-oxygen saturation in the brain, in: *Photons Plus Ultrasound: Imaging and Sensing*, International Society for Optics and Photonics, 2004: pp. 69–77.
- [157] M. Mehrmohammadi, S. Joon Yoon, D. Yeager, S. Y Emelianov, Photoacoustic imaging for cancer detection and staging, *Current Molecular Imaging*. 2 (2013) 89–105.
- [158] S. Mallidi, G.P. Luke, S. Emelianov, Photoacoustic imaging in cancer detection, diagnosis, and treatment guidance, *Trends in Biotechnology*. 29 (2011) 213–221.
- [159] J.-T. Oh, M.-L. Li, H.F. Zhang, K. Maslov, L.V. Wang, Three-dimensional imaging of skin melanoma *in vivo* by dual-wavelength photoacoustic microscopy, *Journal of Biomedical Optics*. 11 (2006) 034032.
- [160] Y. Wang, D. Xu, S. Yang, D. Xing, Toward *in vivo* biopsy of melanoma based on photoacoustic and ultrasound dual imaging with an integrated detector, *Biomedical Optics Express*. 7 (2016) 279–286.

- [161] C.P. Favazza, L.V. Wang, O.W. Jassim, L.A. Cornelius, *In vivo* photoacoustic microscopy of human cutaneous microvasculature and a nevus, *Journal of Biomedical Optics*. 16 (2011) 016015.
- [162] Y. Zhou, G. Li, L. Zhu, C. Li, L.A. Cornelius, L.V. Wang, Handheld photoacoustic probe to detect both melanoma depth and volume at high speed *in vivo*, *Journal of Biophotonics*. 8 (2015) 961–967.
- [163] Y. Zhou, S.V. Tripathi, I. Rosman, J. Ma, P. Hai, G.P. Linette, M.L. Council, R.C. Fields, L.V. Wang, L.A. Cornelius, Noninvasive determination of melanoma depth using a handheld photoacoustic probe, *The Journal of Investigative Dermatology*. 137 (2017) 1370.
- [164] M. Lakshman, A. Needles, Screening and quantification of the tumor microenvironment with micro-ultrasound and photoacoustic imaging, *Nature Methods*. 12 (2015) 372.
- [165] S. Morscher, J. Glatz, N.C. Deliolanis, A. Buehler, D. Razansky, V. Ntziachristos, Blind spectral unmixing to identify molecular signatures of absorbers in multispectral optoacoustic tomography, in: *Photons Plus Ultrasound: Imaging and Sensing 2011*, International Society for Optics and Photonics, 2011: p. 78993D.
- [166] M. Crisan, D. Crisan, G. Sannino, M. Lupsor, R. Badea, F. Amzica, Ultrasonographic staging of cutaneous malignant tumors: an ultrasonographic depth index, *Archives of Dermatological Research*. 305 (2013) 305–313.
- [167] N.A. Obaidat, K.O. Alsaad, D. Ghazarian, Skin adnexal neoplasms—part 2: an approach to tumours of cutaneous sweat glands, *Journal of Clinical Pathology*. 60 (2007) 145–159.
- [168] O. Pozdnyakova, J. Grossman, B. Barbagallo, S. Lyle, The hair follicle barrier to involvement by malignant melanoma, *Cancer*. 115 (2009) 1267–1275.
- [169] C. Kim, E.C. Cho, J. Chen, K.H. Song, L. Au, C. Favazza, Q. Zhang, C.M. Cobley, F. Gao, Y. Xia, *In vivo* molecular photoacoustic tomography of melanomas targeted by bioconjugated gold nanocages, *ACS Nano*. 4 (2010) 4559–4564.
- [170] W.-S. Wu, W.-W. Liu, P.-C. Li, Cost-effective design of a concurrent photoacoustic-ultrasound microscope using single laser pulses, in: *Photons Plus Ultrasound: Imaging and Sensing 2016*, International Society for Optics and Photonics, 2016: p. 97081O.
- [171] R. Siegel, D. Naishadham, A. Jemal, Cancer statistics, 2012, *CA: A Cancer Journal for Clinicians*. 62 (2012) 10–29.
- [172] R.L. Siegel, K.D. Miller, A. Jemal, Cancer statistics, 2015 *CA Cancer J Clin* 2015; 65: 5-29, External Resources Pubmed/Medline (NLM) Crossref (DOI). (n.d.).

- [173] J.A. Smith, E. Andreopoulou, An overview of the status of imaging screening technology for breast cancer, *Annals of Oncology*. 15 (2004) i18–i26.
- [174] L. Irwig, N. Houssami, C. Van Vliet, New technologies in screening for breast cancer: a systematic review of their accuracy, *British Journal of Cancer*. 90 (2004) 2118–2122.
- [175] I. Khalkhali, I. Mena, L. Diggles, Review of imaging techniques for the diagnosis of breast cancer: a new role of prone scintimammography using technetium-99m sestamibi, *European Journal of Nuclear Medicine*. 21 (1994) 357–362.
- [176] L. Tabár, B. Vitak, T.H.-H. Chen, A.M.-F. Yen, A. Cohen, T. Tot, S.Y.-H. Chiu, S.L.-S. Chen, J.C.-Y. Fann, J. Rosell, Swedish two-county trial: impact of mammographic screening on breast cancer mortality during 3 decades, *Radiology*. 260 (2011) 658–663.
- [177] N. Prasad, D. Houserkova, The role of various modalities in breast imaging., *Biomedical Papers of the Medical Faculty of Palacky University in Olomouc*. 151 (2007).
- [178] N.G. Coburn, M.A. Chung, J. Fulton, B. Cady, Decreased breast cancer tumor size, stage, and mortality in Rhode Island: an example of a well-screened population, *Cancer Control*. 11 (2004) 222–230.
- [179] R.W. Pinsky, M.A. Helvie, Mammographic breast density: effect on imaging and breast cancer risk, *Journal of the National Comprehensive Cancer Network*. 8 (2010) 1157–1165.
- [180] P.A. Carney, D.L. Miglioretti, B.C. Yankaskas, K. Kerlikowske, R. Rosenberg, C.M. Rutter, B.M. Geller, L.A. Abraham, S.H. Taplin, M. Dignan, Individual and combined effects of age, breast density, and hormone replacement therapy use on the accuracy of screening mammography, *Annals of Internal Medicine*. 138 (2003) 168–175.
- [181] C.H. Van Gils, J.D. Otten, A.L. Verbeek, J.H. Hendriks, R. Holland, Effect of mammographic breast density on breast cancer screening performance: a study in Nijmegen, The Netherlands., *Journal of Epidemiology & Community Health*. 52 (1998) 267–271.
- [182] K. Kerlikowske, D. Grady, J. Barclay, E.A. Sickles, V. Ernster, Effect of age, breast density, and family history on the sensitivity of first screening mammography, *Jama*. 276 (1996) 33–38.
- [183] I. Persson, E. Thurfjell, L. Holmberg, Effect of estrogen and estrogen-progestin replacement regimens on mammographic breast parenchymal density., *Journal of Clinical Oncology*. 15 (1997) 3201–3207.

- [184] R. Guo, G. Lu, B. Qin, B. Fei, Ultrasound imaging technologies for breast cancer detection and management: A review, *Ultrasound in Medicine & Biology*. 44 (2018) 37–70.
- [185] E.A.M. O’Flynn, A.R.M. Wilson, M.J. Michell, Image-guided breast biopsy: state-of-the-art, *Clinical Radiology*. 65 (2010) 259–270.
- [186] B.J. Tromberg, A. Cerussi, N. Shah, M. Compton, A. Durkin, D. Hsiang, J. Butler, R. Mehta, Imaging in breast cancer: diffuse optics in breast cancer: detecting tumors in premenopausal women and monitoring neoadjuvant chemotherapy, *Breast Cancer Research*. 7 (2005) 279.
- [187] B.J. Tromberg, B.W. Pogue, K.D. Paulsen, A.G. Yodh, D.A. Boas, A.E. Cerussi, Assessing the future of diffuse optical imaging technologies for breast cancer management, *Medical Physics*. 35 (2008) 2443–2451.
- [188] D.R. Leff, O.J. Warren, L.C. Enfield, A. Gibson, T. Athanasiou, D.K. Patten, J. Hebden, G.Z. Yang, A. Darzi, Diffuse optical imaging of the healthy and diseased breast: a systematic review, *Breast Cancer Research and Treatment*. 108 (2008) 9–22.
- [189] B.W. Pogue, S.P. Poplack, T.O. McBride, W.A. Wells, K.S. Osterman, U.L. Osterberg, K.D. Paulsen, Quantitative hemoglobin tomography with diffuse near-infrared spectroscopy: pilot results in the breast, *Radiology*. 218 (2001) 261–266.
- [190] W.A. Berg, L. Gutierrez, M.S. NessAiver, W.B. Carter, M. Bhargavan, R.S. Lewis, O.B. Ioffe, Diagnostic accuracy of mammography, clinical examination, US, and MR imaging in preoperative assessment of breast cancer, *Radiology*. 233 (2004) 830–849.
- [191] M. Kriege, C.T. Brekelmans, I.M. Obdeijn, C. Boetes, H.M. Zonderland, S.H. Muller, T. Kok, R.A. Manoliu, A.P.E. Besnard, M.M. Tilanus-Linthorst, Factors affecting sensitivity and specificity of screening mammography and MRI in women with an inherited risk for breast cancer, *Breast Cancer Research and Treatment*. 100 (2006) 109–119.
- [192] D. Saslow, C. Boetes, W. Burke, S. Harms, M.O. Leach, C.D. Lehman, E. Morris, E. Pisano, M. Schnall, S. Sener, American Cancer Society guidelines for breast screening with MRI as an adjunct to mammography, *CA: A Cancer Journal for Clinicians*. 57 (2007) 75–89.
- [193] E.V. Heiberg, W.H. Perman, V.M. Herrmann, C.G. Janney, Dynamic sequential 3D gadolinium-enhanced MRI of the whole breast, *Magnetic Resonance Imaging*. 14 (1996) 337–348.

- [194] S.R. McDougalla, A.R.A. Andersonb, M.A.J. Chaplain, Mathematical modeling of dynamic adaptive tumor-induced angiogenesis: Clinical implications and therapeutic targeting strategies, *Journal of Theoretical Biology*. 241 (2006) 564–589.
- [195] M.A.J. Chaplain, Avascular growth, angiogenesis and vascular growth in solid tumours: The mathematical modelling of the stages of tumour development, *Mathematical and Computer Modelling*. 23 (1996) 47–87.
- [196] R.A. Kruger, C.M. Kuzmiak, R.B. Lam, D.R. Reinecke, S.P. Del Rio, D. Steed, Dedicated 3D photoacoustic breast imaging, *Medical Physics*. 40 (2013) 113301.
- [197] M. Heijblom, W. Steenbergen, S. Manohar, Clinical photoacoustic breast imaging: the Twente experience., *IEEE Pulse*. 6 (2015) 42–46.
- [198] A.A. Oraevsky, S.L. Jacques, R.O. Esenaliev, F.K. Tittel, Laser-based optoacoustic imaging in biological tissues, in: *Laser-Tissue Interaction V; and Ultraviolet Radiation Hazards*, International Society for Optics and Photonics, 1994: pp. 122–128.
- [199] A.A. Oraevsky, R.O. Esenaliev, S.L. Jacques, F.K. Tittel, D. Medina, Breast cancer diagnostics by laser optoacoustic tomography, *Trends in Optics and Photonics*. 2 (1996) 316–321.
- [200] S.A. Ermilov, T. Khamapirad, A. Conjusteau, M.H. Leonard, R. Lacewell, K. Mehta, T. Miller, A.A. Oraevsky, Laser optoacoustic imaging system for detection of breast cancer, *Journal of Biomedical Optics*. 14 (2009) 024007.
- [201] S. Manohar, A. Kharine, J.C.G. van Hespén, W. Steenbergen, T.G. van Leeuwen, Photoacoustic mammography laboratory prototype: imaging of breast tissue phantoms, *Journal of Biomedical Optics*. 9 (2004) 1172–1182.
- [202] S. Manohar, A. Kharine, J.C. van Hespén, W. Steenbergen, T.G. van Leeuwen, The Twente Photoacoustic Mammoscope: system overview and performance, *Physics in Medicine & Biology*. 50 (2005) 2543.
- [203] M. Heijblom, D. Piras, F.M. van den Engh, M. van der Schaaf, J.M. Klaase, W. Steenbergen, S. Manohar, The state of the art in breast imaging using the Twente Photoacoustic Mammoscope: results from 31 measurements on malignancies, *European Radiology*. 26 (2016) 3874–3887.
- [204] S.M. Schoustra, D. Piras, R. Huijink, T.J. Op't Root, L. Alink, W.M.F. Kobold, W. Steenbergen, S. Manohar, Twente Photoacoustic Mammoscope 2: system overview and three-dimensional vascular network images in healthy breasts, *Journal of Biomedical Optics*. 24 (2019) 121909.

- [205] A. Cerussi, D. Hsiang, N. Shah, R. Mehta, A. Durkin, J. Butler, B.J. Tromberg, Predicting response to breast cancer neoadjuvant chemotherapy using diffuse optical spectroscopy, *Proceedings of the National Academy of Sciences*. 104 (2007) 4014–4019.
- [206] Q. Zhu, S. Tannenbaum, P. Hegde, M. Kane, C. Xu, S.H. Kurtzman, Noninvasive monitoring of breast cancer during neoadjuvant chemotherapy using optical tomography with ultrasound localization, *Neoplasia* (New York, NY). 10 (2008) 1028.
- [207] J. Specht, J.R. Gralow, Neoadjuvant chemotherapy for locally advanced breast cancer, in: *Seminars in Radiation Oncology*, Elsevier, 2009: pp. 222–228.
- [208] X. Wang, X. Xie, G. Ku, L.V. Wang, G. Stoica, Noninvasive imaging of hemoglobin concentration and oxygenation in the rat brain using high-resolution photoacoustic tomography, *Journal of Biomedical Optics*. 11 (2006) 024015.
- [209] K. Daoudi, P.J. Van Den Berg, O. Rabot, A. Kohl, S. Tisserand, P. Brands, W. Steenbergen, Handheld probe integrating laser diode and ultrasound transducer array for ultrasound/photoacoustic dual modality imaging, *Optics Express*. 22 (2014) 26365–26374.
- [210] J. Jo, G. Xu, Y. Zhu, M. Burton, J. Sarazin, E. Schiopu, G. Gandikota, X. Wang, Detecting joint inflammation by an LED-based photoacoustic imaging system: a feasibility study, *Journal of Biomedical Optics*. 23 (2018) 110501.
- [211] V. Raghavan, C. O’Flatharta, R. Dwyer, A. Breathnach, H. Zafar, P. Dockery, A. Wheatley, I. Keogh, M. Leahy, M. Olivo, Dual plasmonic gold nanostars for photoacoustic imaging and photothermal therapy, *Nanomedicine*. 12 (2017) 457–471.
- [212] V. Raghavan, H. Subhash, A. Breathnach, M. Leahy, P. Dockery, M. Olivo, Dual plasmonic gold nanoparticles for multispectral photoacoustic imaging application, in: *Photons Plus Ultrasound: Imaging and Sensing 2014*, International Society for Optics and Photonics, 2014: p. 89434J.
- [213] P. Ghosh, G. Han, M. De, C.K. Kim, V.M. Rotello, Gold nanoparticles in delivery applications, *Advanced Drug Delivery Reviews*. 60 (2008) 1307–1315.
- [214] R.A. Sperling, P.R. Gil, F. Zhang, M. Zanella, W.J. Parak, Biological applications of gold nanoparticles, *Chemical Society Reviews*. 37 (2008) 1896–1908.
- [215] J.F. Hainfeld, D.N. Slatkin, T.M. Focella, H.M. Smilowitz, Gold nanoparticles: a new X-ray contrast agent, *The British Journal of Radiology*. 79 (2006) 248–253.

- [216] A.F. Versiani, L.M. Andrade, E.M. Martins, S. Scalzo, J.M. Geraldo, C.R. Chaves, D.C. Ferreira, M. Ladeira, S. Guatimosim, L.O. Ladeira, Gold nanoparticles and their applications in biomedicine, *Future Virology*. 11 (2016) 293–309.
- [217] M.H. Jazayeri, H. Amani, A.A. Pourfatollah, H. Pazoki-Toroudi, B. Sedighimoghaddam, Various methods of gold nanoparticles (GNPs) conjugation to antibodies, *Sensing and Bio-Sensing Research*. 9 (2016) 17–22.
- [218] P.M. Tiwari, K. Vig, V.A. Dennis, S.R. Singh, Functionalized gold nanoparticles and their biomedical applications, *Nanomaterials*. 1 (2011) 31–63.
- [219] L. Dykman, N. Khlebtsov, Gold nanoparticles in biomedical applications: recent advances and perspectives, *Chemical Society Reviews*. 41 (2012) 2256–2282.
- [220] P.M. Tiwari, S.S. Bawage, S.R. Singh, Gold nanoparticles and their applications in photomedicine, diagnosis and therapy, in: *Applications of Nanoscience in Photomedicine*, Elsevier, 2015: pp. 249–266.
- [221] N. Khlebtsov, V. Bogatyrev, L. Dykman, B. Khlebtsov, S. Staroverov, A. Shirokov, L. Matora, V. Khanadeev, T. Pylaev, N. Tsyganova, Analytical and theranostic applications of gold nanoparticles and multifunctional nanocomposites, *Theranostics*. 3 (2013) 167.
- [222] T. Curry, R. Kopelman, M. Shilo, R. Popovtzer, Multifunctional theranostic gold nanoparticles for targeted CT imaging and photothermal therapy, *Contrast Media & Molecular Imaging*. 9 (2014) 53–61.
- [223] T. Reuveni, M. Motiei, Z. Romman, A. Popovtzer, R. Popovtzer, Targeted gold nanoparticles enable molecular CT imaging of cancer: an *in vivo* study, *International Journal of Nanomedicine*. 6 (2011) 2859.
- [224] R.G. Rayavarapu, W. Petersen, C. Ungureanu, J.N. Post, T.G. van Leeuwen, S. Manohar, Synthesis and bioconjugation of gold nanoparticles as potential molecular probes for light-based imaging techniques., *International Journal of Biomedical Imaging*. (2007).
- [225] J.A. Copland, M. Eghtedari, V.L. Popov, N. Kotov, N. Mamedova, M. Motamedi, A.A. Oraevsky, Bioconjugated gold nanoparticles as a molecular based contrast agent: implications for imaging of deep tumors using optoacoustic tomography, *Molecular Imaging & Biology*. 6 (2004) 341–349.
- [226] G. Peng, U. Tisch, O. Adams, M. Hakim, N. Shehada, Y.Y. Broza, S. Billan, R. Abdah-Bortnyak, A. Kuten, H. Haick, Diagnosing lung cancer in exhaled breath using gold nanoparticles, *Nature Nanotechnology*. 4 (2009) 669.

- [227] G. Han, P. Ghosh, M. De, V.M. Rotello, Drug and gene delivery using gold nanoparticles, *Nanobiotechnology*. 3 (2007) 40–45.
- [228] D. Pissuwan, T. Niidome, M.B. Cortie, The forthcoming applications of gold nanoparticles in drug and gene delivery systems, *Journal of Controlled Release*. 149 (2011) 65–71.
- [229] X. Huang, M.A. El-Sayed, Gold nanoparticles: Optical properties and implementations in cancer diagnosis and photothermal therapy, *Journal of Advanced Research*. 1 (2010) 13–28.
- [230] X. Huang, P.K. Jain, I.H. El-Sayed, M.A. El-Sayed, Plasmonic photothermal therapy (PPTT) using gold nanoparticles, *Lasers in Medical Science*. 23 (2008) 217.
- [231] V. Amendola, R. Pilot, M. Frasconi, O.M. Maragò, M.A. Iati, Surface plasmon resonance in gold nanoparticles: a review, *Journal of Physics: Condensed Matter*. 29 (2017) 203002.
- [232] V. Raghavan, H.M. Fan, E.K. McCarthy, P. Dockery, A. Wheatley, I. Keogh, M. Olivo, Synthesis and characterisation of dual plasmonic gold nanostars as high-performance surface-enhanced Raman spectroscopy substrate, *Micro & Nano Letters*. 11 (2016) 769–774.
- [233] S.-Y. Ding, E.-M. You, Z.-Q. Tian, M. Moskovits, Electromagnetic theories of surface-enhanced Raman spectroscopy, *Chemical Society Reviews*. 46 (2017) 4042–4076.
- [234] E. Nalbant Esenturk, A.R. Hight Walker, Surface-enhanced Raman scattering spectroscopy via gold nanostars, *Journal of Raman Spectroscopy: An International Journal for Original Work in All Aspects of Raman Spectroscopy, Including Higher Order Processes, and Also Brillouin and Rayleigh Scattering*. 40 (2009) 86–91.
- [235] Y. Oh, W. Lee, D. Kim, Colocalization of gold nanoparticle-conjugated DNA hybridization for enhanced surface plasmon detection using nanograting antennas, *Optics Letters*. 36 (2011) 1353–1355.
- [236] C.L. Nehl, H. Liao, J.H. Hafner, Optical properties of star-shaped gold nanoparticles, *Nano Letters*. 6 (2006) 683–688.
- [237] A. Samanta, K.K. Maiti, K.-S. Soh, X. Liao, M. Vendrell, U.S. Dinis, S.-W. Yun, R. Bhuvanewari, H. Kim, S. Rautela, Ultrasensitive near-infrared Raman reporters for SERS-based *in vivo* cancer detection, *Angewandte Chemie International Edition*. 50 (2011) 6089–6092.

- [238] D. Jaque, L.M. Maestro, B. Del Rosal, P. Haro-Gonzalez, A. Benayas, J.L. Plaza, E.M. Rodriguez, J.G. Sole, Nanoparticles for photothermal therapies, *Nanoscale*. 6 (2014) 9494–9530.
- [239] X. Yang, E.W. Stein, S. Ashkenazi, L.V. Wang, Nanoparticles for photoacoustic imaging, *Wiley Interdisciplinary Reviews: Nanomedicine and Nanobiotechnology*. 1 (2009) 360–368.
- [240] G.P. Luke, D. Yeager, S.Y. Emelianov, Biomedical applications of photoacoustic imaging with exogenous contrast agents, *Annals of Biomedical Engineering*. 40 (2012) 422–437.
- [241] E. Hemmer, A. Benayas, F. Légaré, F. Vetrone, Exploiting the biological windows: current perspectives on fluorescent bioprobes emitting above 1000 nm, *Nanoscale Horizons*. 1 (2016) 168–184.
- [242] S. Wang, H. Xu, J. Ye, Plasmonic rod-in-shell nanoparticles for photothermal therapy, *Physical Chemistry Chemical Physics*. 16 (2014) 12275–12281.
- [243] J. Weber, P.C. Beard, S.E. Bohndiek, Contrast agents for molecular photoacoustic imaging, *Nature Methods*. 13 (2016) 639.
- [244] D. Wu, L. Huang, M. Jiang, H. Jiang, Contrast agents for photoacoustic and thermoacoustic imaging: a review, *International Journal of Molecular Sciences*. 15 (2014) 23616–23639.
- [245] Y. Shi, D. Peng, K. Wang, X. Chai, Q. Ren, J. Tian, C. Zhou, Targeted Au-core-Ag-shell nanorods as a dual-functional contrast agent for photoacoustic imaging and photothermal therapy, *Biomedical Optics Express*. 7 (2016) 1830–1841.
- [246] S. Manohar, C. Ungureanu, T.G. Van Leeuwen, Gold nanorods as molecular contrast agents in photoacoustic imaging: the promises and the caveats, *Contrast Media & Molecular Imaging*. 6 (2011) 389–400.
- [247] Y.-S. Chen, K. Homan, D. Xu, W. Frey, S. Emelianov, Feasibility of contrast-enhanced photoacoustic liver imaging at a wavelength of 1064 nm, in: *Biomedical Optics*, Optical Society of America, 2012: pp. BM2B-7.
- [248] R. Kanjanawarut, B. Yuan, S. XiaoDi, UV-vis spectroscopy and dynamic light scattering study of gold nanorods aggregation, *Nucleic Acid Therapeutics*. 23 (2013) 273–280.
- [249] P.K. Sudeep, S.S. Joseph, K.G. Thomas, Selective detection of cysteine and glutathione using gold nanorods, *Journal of the American Chemical Society*. 127 (2005) 6516–6517.
- [250] Y. Zhang, H. Hong, W. Cai, Photoacoustic imaging, *Cold Spring Harbor Protocols*. 2011 (2011) pdb-top065508.

- [251] A.M. Smith, M.C. Mancini, S. Nie, Bioimaging: second window for *in vivo* imaging, Nature Nanotechnology. 4 (2009) 710.
- [252] Y.-S. Chen, W. Frey, S. Kim, P. Kruizinga, K. Homan, S. Emelianov, Silica-coated gold nanorods as photoacoustic signal nanoamplifiers, Nano Letters. 11 (2011) 348–354.
- [253] Y.-S. Chen, P. Kruizinga, P.P. Joshi, S. Kim, K. Homan, K. Sokolov, W. Frey, S. Emelianov, On stability of molecular therapeutic agents for noninvasive photoacoustic and ultrasound image-guided photothermal therapy, in: Photons Plus Ultrasound: Imaging and Sensing 2010, International Society for Optics and Photonics, 2010: p. 75641Q.
- [254] P. Huang, J. Lin, W. Li, P. Rong, Z. Wang, S. Wang, X. Wang, X. Sun, M. Aronova, G. Niu, Biodegradable gold nanovesicles with an ultrastrong plasmonic coupling effect for photoacoustic imaging and photothermal therapy, Angewandte Chemie International Edition. 52 (2013) 13958–13964.
- [255] Z. Liu, J. Liu, R. Wang, Y. Du, J. Ren, X. Qu, An efficient nano-based theranostic system for multi-modal imaging-guided photothermal sterilization in gastrointestinal tract, Biomaterials. 56 (2015) 206–218.
- [256] L.M. Liz-Marzán, P. Mulvaney, The assembly of coated nanocrystals, The Journal of Physical Chemistry B. 107 (2003) 7312–7326.
- [257] I. Pastoriza-Santos, J. Pérez-Juste, L.M. Liz-Marzán, Silica-coating and hydrophobation of CTAB-stabilized gold nanorods, Chemistry of Materials. 18 (2006) 2465–2467.
- [258] Y. Kobayashi, H. Katakami, E. Mine, D. Nagao, M. Konno, L.M. Liz-Marzán, Silica coating of silver nanoparticles using a modified Stöber method, Journal of Colloid and Interface Science. 283 (2005) 392–396.
- [259] E.C. Cruz, Cell line profile MDA-MB-231 (ECACC catalogue no. 92020424), Eur. Collect. Authenticated Cell Cult. (2017).
- [260] J. Welsh, Animal models for studying prevention and treatment of breast cancer, in: Animal Models for the Study of Human Disease, Elsevier, 2013: pp. 997–1018.
- [261] S. Liang, C. Li, C. Zhang, Y. Chen, L. Xu, C. Bao, X. Wang, CD44v6 monoclonal antibody-conjugated gold nanostars for targeted photoacoustic imaging and plasmonic photothermal therapy of gastric cancer stem-like cells, Theranostics. 5 (2015) 970.
- [262] L. Cheng, J. Liu, X. Gu, H. Gong, X. Shi, T. Liu, C. Wang, X. Wang, G. Liu, H. Xing, PEGylated WS2 nanosheets as a multifunctional theranostic agent for *in vivo* dual-modal CT/photoacoustic imaging guided photothermal therapy, Advanced Materials. 26 (2014) 1886–1893.

- [263] Y.-S. Chen, W. Frey, S. Aglyamov, S. Emelianov, Environment-dependent generation of photoacoustic waves from plasmonic nanoparticles, *Small*. 8 (2012) 47–52.
- [264] M.G. Cerruti, M. Sauthier, D. Leonard, D. Liu, G. Duscher, D.L. Feldheim, S. Franzen, Gold and silica-coated gold nanoparticles as thermographic labels for DNA detection, *Analytical Chemistry*. 78 (2006) 3282–3288.
- [265] P.K. Jain, M.A. El-Sayed, Plasmonic coupling in noble metal nanostructures, *Chemical Physics Letters*. 487 (2010) 153–164.
- [266] J.A. Webb, R. Bardhan, Emerging advances in nanomedicine with engineered gold nanostructures, *Nanoscale*. 6 (2014) 2502–2530.
- [267] P. Shi, Z. Liu, K. Dong, E. Ju, J. Ren, Y. Du, Z. Li, X. Qu, A Smart “Sense-Act-Treat” System: Combining a Ratiometric pH Sensor with a Near Infrared Therapeutic Gold Nanocage, *Advanced Materials*. 26 (2014) 6635–6641.
- [268] M.R. Ali, H.R. Ali, C.R. Rankin, M.A. El-Sayed, Targeting heat shock protein 70 using gold nanorods enhances cancer cell apoptosis in low dose plasmonic photothermal therapy, *Biomaterials*. 102 (2016) 1–8.
- [269] B. Hildebrandt, P. Wust, O. Ahlers, A. Dieing, G. Sreenivasa, T. Kerner, R. Felix, H. Riess, The cellular and molecular basis of hyperthermia, *Critical Reviews in Oncology/Hematology*. 43 (2002) 33–56.
- [270] A.S. SREEDHAR, Hyperthermia and pharmacological intervention of heat shock proteins in anticancer treatments, *Thermal Medicine (Japanese Journal of Hyperthermic Oncology)*. 22 (2006) 211–227.
- [271] J.R. Melamed, R.S. Edelstein, E.S. Day, Elucidating the fundamental mechanisms of cell death triggered by photothermal therapy, *ACS Nano*. 9 (2015) 6–11.
- [272] J. Yu, B.-D. Tang, W.K. Leung, K.-F. To, A.H. Bai, Z.-R. Zeng, P.-K. Ma, M.Y. Go, P.-J. Hu, J.J. Sung, Different cell kinetic changes in rat stomach cancer after treatment with celecoxib or indomethacin: implications on chemoprevention, *World Journal of Gastroenterology: WJG*. 11 (2005) 41.
- [273] Q. Fang, Mesh-based Monte Carlo method using fast ray-tracing in Plücker coordinates, *Biomedical Optics Express*. 1 (2010) 165–175.
- [274] B.E. Treeby, B.T. Cox, k-Wave: MATLAB toolbox for the simulation and reconstruction of photoacoustic wave fields, *Journal of Biomedical Optics*. 15 (2010) 021314.